Nanoparticle formation and dynamics in a complex (dusty) plasma : from the plasma ignition to the afterglow.

Lénaïc Couëdel

UNIVERSITÉ D'ORLÉANS
ÉCOLE DOCTORALE SCIENCES ET TECHNOLOGIES
LABORATOIRE GREMI

THE UNIVERSITY OF SYDNEY
FACULTY OF SCIENCE, SCHOOL OF PHYSICS
COMPLEX PLASMA LABORATORY

THÈSE/THESIS présentée par/presented by :
Lénaïc Gaël Hervé Fabien COUËDEL
soutenue le /defended on : **11**th **septembre 2008**
pour obtenir les grades de/to obtain the titles of :
Docteur de l'Université d'Orléans
Doctor of Philosophy of the University of Sydney
Spécialité/Specialty : Physique des Plasmas/Physics of Plasmas

NANOPARTICLE FORMATION AND DYNAMICS IN A COMPLEX (DUSTY) PLASMA : FROM THE PLASMA IGNITION TO THE AFTERGLOW.

FORMATION ET DYNAMIQUE DE NANOPARTICULES DANS UN PLASMA COMPLEXE (POUSSIÉREUX) : DE L'ALLUMAGE DU PLASMA À LA PHASE POST-DÉCHARGE.

THÈSE en COTUTELLE INTERNATIONALE dirigée par/supervised by :
Monsieur Laïfa BOUFENDI Professeur, Université d'Orléans, France
Monsieur Alexandre SAMARIAN Doctor, University of Sydney, Australia

RAPPORTEURS/EXAMINERS :
Monsieur Gregor E. MORFILL Professor, Max Planck Institute, Germany
Monsieur Vladimir E. FORTOV Professor academician, Russian academy of science, Russia

JURY :
Monsieur Jean-Michel POUVESLE Docteur, CNRS, France, Président du jury
Monsieur Gregor E. MORFILL Professor, Max Planck Institute, Germany
Monsieur Vladimir E. FORTOV Professor academician, Russian academy of science, Russia
Monsieur Brian W. James Associate Professor, University of Sydney, Australia
Monsieur Jean-Pierre BOEUF Docteur, CNRS, France
Monsieur Christian STENZ Professeur, Université Bordeaux 1, France
Monsieur Laïfa BOUFENDI Professeur, Université d'Orléans, France
Monsieur Alexandre SAMARIAN Doctor, University of Sydney, Australia

Declaration of Originality

To the best of my knowledge, this thesis contains no copy or paraphrase of work published by another person, except where duly acknowledged in the text. This thesis contains no material which has been presented for a degree at the University of Sydney, the University of Orléans or another university.

Lénaïc Couëdel

Acknowledgments

Les travaux présentés dans cette thèse ont été effectués au laboratoire GREMI (CNRS/Université d'Orléans, France) et au laboratoire CPL (School of Physics of the University of Sydney, Australia). Il n'auraient pu être menés à terme sans l'aide et le soutien de plusieurs personnes que je souhaite remercier.

Je souhaite remercier Monsieur Jean-Michel Pouvesle, directeur du laboratoire GREMI, pour avoir accepté de présider mon jury de thèse.

I would like to thank Prof. Gregor Morfill (Max Planck Institute, Garching, Germany) and Prof. academician Vladimir Fortov (Russian academy of science) who accepted to be my thesis examiners.

I would also like to thank A/Prof. Brian James (University of Sydney), Dr. Jean-Pierre Boeuf (Laplace, Toulouse) and Prof. Christian Stenz (Université Bordeaux 1) who accepted to be part of my thesis jury.

Je remercie mes directeurs de thèse Prof Laïfa Boufendi (Université d'Orléans) et Dr. Alexandre Samarian (University of Sydney) qui ont rendu cette thèse en Cotutelle possible en facilitant la collaboration entre mes deux laboratoires d'accueil ainsi que pour la qualité de leur encadrement. Je souhaite particulièrement remercier Dr. Maxime Mikikian pour son encadrement, ses compétences, ses conseils et sa confiance durant toute la durée de ma thèse.

Je remercie également Dr. Pascal Brault pour ses conseils sur les techniques de simulation.

I would like to thank Dr. Joe Kachan (University of Sydney) and A/Prof. Brian James (again) for their useful advices and corrections when I was writing my thesis manuscript.

Je souhaite remercier Yves Tessier, notre ingénieur au GREMI pour son aide sans faille durant toute la durée de mon séjour au GREMI. Je voudrais aussi adresser un grand merci à Philippe, Guy, Sébastien, Bernard, Jacky, Sylvie, Evelyne et Christophe pour leur aide précieuse durant mon séjour au GREMI.

I would like to thank Robert Davies, our engineer in Sydney Uni who helped me with my experiment and his faithful attendance to Monday soccer. I would like to give special thanks to the Plasma group (Ian, Richard, Joe, Brian, Oded, Vanessa, Michael, John, Roberto, Alex) for those very useful wednesday plasma group meetings.

Je veux aussi remercier tous les amis, collègues thésards et postdocs passés et présents du GREMI ou d'ailleurs (Thomas, Marjorie, Xavier, Corinne, Gareth, Laurianne, Amaël, Maria, Thierry, Maxime, Alain, Clément, Gaëtan, Elise, Fakhri, Edward, Sylvain, Binjie, Sébastien,

Hervé, Jérémy, Catherine, Arnaud, Xeniya, ...pardon à ceux que j'oublie) grâce à qui j'ai eu des fous rires mémorables et passé des soirées inoubliables. Merci Thomas, Edward et Amaël pour ces tournées "Rue de Bourgogne" (ainsi qu' à Sydney et à Canberra pour le "Master of BBQs") permettant d'oublier un peu la thèse. Catherine, nous nous sommes connus que sur la fin de ma thèse mais tu as une place spéciale dans mon coeur.

I would like to thank all my friends in Sydney: Fitz, Katherine, John, Oded, Roberto, Mark, Chanokporn, Alexey, Garth, Scott, Chris, Wojciech, Skander, the "physicist" soccer team, Daren, Bill, Michael, Mike, Vanessa, Brett, Nick, Eve, Sebastien and all other mates attending to the "Last Friday of the Month" drinks.

I would like to thank all my housemate in Sydney (Ollie, Kate, Laurie, Michelle, Luke, Charlotte, Bjorn) who survived in the same house as me. I had good fun with you and I hope we will meet again someday.

I would like to thank Véronique for the "Paddy McGuires" tours and other parties in Sydney.

Un grand merci aux amis nantais et assimilés: Maxime, Nathalie, Pascal, Pierre, Tiburce, Yaël, Vincent, Fafane, etc.

I want also to give a special "thank you" to Marko and Heidi Lang with whom I became very good friends during the past two years. I spent very good time with you and I will miss those evenings at the Royal "living room" Hotel.

Je veux aussi adresser un grand merci à Christelle Monat et Christian Grillet pour toutes ces après-midis "Coinche" endiablées, Boston Legal, les soirées chansons françaises-cigares-whisky. Grâce à vous, je garde de merveilleux souvenirs de mon séjour à Sydney et je pense pouvoir dire que nous sommes devenus de très bons amis.

Enfin, je remercie ma famille pour leur soutien sans faille durant ces trois dernières années.

Mersi bras deoc'h

Contents

List of Figures

List of Constants

ϵ_0	$8.85419{\cdot}10^{-12}$ A$\cdot$ s$\cdot$V$^{-1}\cdot$m^{-1}
π	3.14159265
c	$2.99792458{\cdot}10^{8}$ m$\cdot$s^{-1}
e	$1.60218{\cdot}10^{-19}$ C
h	$6.626076{\cdot}10^{-34}$ J$\cdot$s
k_B	$1.38066{\cdot}10^{-23}$ J$\cdot$K^{-1}

List of Symbols

A	probe area
A_{kj}	transition probability for $k \rightarrow j$ $(j < k)$ radiative transition
Ar	argon
C	dust particle capacitance
CH_4	methane
C_c	dust particle charge corrective factor
C_{abs}	absorption coefficient
C_{ext}	extinction parameter
C_{sca}	scattering coefficient
D_a	ambipolar diffusion coefficient
D_e	electron diffusion coefficient
D_i	ion diffusion coefficient
D_{eff}	effective electron diffusion coefficient
E	electric field
F_T	thermophoretic force
F_e	electric force
F_{di}	ion drag force
F_{dn}	neutral drag force
F_g	gravitational force
He	helium
I_a	current absorbed by the dust particle
I_e	electron current
I_i	ion current
I_j	$j-$species current
I_l	current emitted by the dust particle
I_t	transmitted laser light
I_{kj}	power radiated per unit of volume for $k \rightarrow j$ radiative transition
N	number of bounded electrons
N_2	nitrogen

N_d	number of dust particles
P	pressure
P_H	Havnes parameter
P_W	RF power
P_{Ar}	argon pressure
P_{He}	helium pressure
Q	quality factor of the microwave resonant cavity
Q_d	dust particle charge
$Q_{d_{res}}$	residual dust particle charge
Q_{mean}	mean dust particle charge
S_e	electron source term
S_i	ion source term
SiH_4	silane
T	neutral gas temperature
T_e	electron temperature
T_i	ion temperature
T_{eff}	effective electron temperature
V	probe potential
V_f	floating potential
V_p	plasma potential
V_s	sheath-presheath edge potential
V_{RF}	RF voltage
V_{dc}	self-bias voltage
V_{pp}	peak to peak RF voltage
W	probability for a dust particle to carry the charge Q_d
Z	atomic number
Z_d	dust charge number
Z_{eff}	effective atomic number
Γ	flux
Γ_c	Coulomb logarithm
Γ_e	electron flux
Γ_i	ion flux
Λ	diffusion length
α_{ac}	accommodation coefficient
δ	dust charge distribution width parameter
ϵ_r	cavity dielectric constant
λ_D	linearised Debye length

λ_{De}	electron Debye length
λ_{Di}	ion Debye length
λ_{mfp}	electron or ion-neutral collisional mean free path
λ_{rad}	radiation wavelength
μ_e	electron mobility
μ_i	ion mobility
μ_r	cavity relative permeability
ν_e	electron collision frequency
ν_{en}	electron-neutral collision frequency
ν_{kj}	radiation frequency between levels k and j
ω	angular frequency
ω_{pd}	dust angular frequency
ω_{pe}	electron angular frequency
ω_{pi}	ion angular frequency
ϕ_d	dust surface potential with respect to the plasma potential
ϕ_g	dust surface potential
ρ	mass density
σ	standard deviation of the dust charge distribution
σ_j^d	cross section for a j particle-dust grain collision
σ_{nd}	dust-neutral collision cross section
τ_A	dust particle absorption time
τ_D	diffusion time
τ_L	plasma decay time
τ_Q	charge fluctuation time
τ_T	electron temperature relaxation time
τ_{D_e}	electron diffusion time
τ_{D_i}	ion diffusion time
$\tilde{T}_e$	T_e/T_i
$\tilde{n}$	$n_{i,e}/n_0$
φ	dimensionless dust particle surface potential
b_c	OML maximum impact parameter
b_j	j-species impact parameter
$b_{\pi/2}$	impact parameter for 90° deflection
f	frequency
f_e	electron velocity distribution function
f_j	j-species velocity distribution function
f_{1k}	absorption oscillator strength of the transition $1 \rightarrow k$

g_e	electron energy distribution function
k_{1k}	electron impact excitation rate coefficient from the ground state
k_{tr}	translational part of the thermal conductivity
l_{en}	electron-neutral collision mean free path
l_{in}	ion-neutral collision mean free path
m	complex refractive index
m_e	electron mass
m_i	ion mass
m_j	j-species mass
m_n	neutral atom mass
n	cavity refractive index
n_0	plasma density
n_1	ground state density
n_d	dust particle density
n_e	electron density
n_i	ion density
n_j	j-species density
p_e	probability per unit of time for absorbing an electron
p_i	probability per unit of time for absorbing an ion
p_{tot}	probability per unit of time for absorbing a plasma particle
q_j	j-species charge
r_d	dust particle radius
v	velocity
v_d	dust particle velocity
v_i	ion drift velocity
v_s	mean velocity of the ions approaching a dust particle
v_{Te}	electron thermal speed
v_{Ti}	ion thermal speed
v_{Tn}	neutral thermal speed

List of Abbreviations

ABR	Allen-Boyd-Reynolds
ComPLExS	Complex PLasma Experiment in Sydney
DA	dust acoustic
DC	direct current
DCD	Dust charge distribution
DIA	dust-ion acoustic
DPGI	dust particle growth instabilities
EEDF	electron energy distribution function
EMD	empirical mode decomposition
fps	frames per second
GREMI	Groupe de Recherches sur l'Énergétique des Milieux Ionisés
HH	Hilbert-Huang
HRR	high repetition rate
IHED	Institute for High Energy Density
IMF	intrinsic mode function
ISS	International Space Station
LRR	low repetition rate
MMO	mixed-mode oscillation
MPE	Max Planck Institute for Extraterrestrial Physics
OML	orbital motion limited
PKE	Plasma Kristall Experiment
RF	Radio-frequency
SEM	scanning electron microscopy
TEM	transmission electron microscopy

« La science consiste à passer d'un étonnement à un autre. »
Aristote

« The most exciting phrase to hear in science, the one that heralds new discoveries, is not "Eureka", but "That's funny"... »
Isaac Asimov

Chapter 1

Introduction

Smoke, fog, soot, mist, dust all refer to particles that can be suspended in a liquid or a gas. Dusty media have always been of considerable interest. The Egyptians used dust particles suspended in a liquid to make ink, the Chinese discovered their explosive properties. Dust particles are still of major interest in a wide range of applications from dry powder coatings [1], atmospheric research [2, 3], to the microelectronics industry [4, 5]. In any cases, these particles can be useful or harmful and consequently a lot of studies are devoted to them.
Dusty (or complex) plasmas are ionised gases in which there are some charged macroscopic dust particles. They are very common media and can be found in nature such as in an astrophysical environment (planetary nebula, planetary rings [6–8]) or planetary upper atmosphere [3, 9] as well as in human made plasma (laboratory or industrial discharges [4], fusion plasmas [10, 11], etc).

1.1 A selective history of complex (dusty) plasma

1.1.1 The early age

Before the XXth century, dusty plasmas were known as the zodiacal light (described and interpreted by Cassini in the late 17th century) and the noctilucent clouds (discovered about a century ago). However, the physics of dusty plasmas did not start before the observation of dust particles in a laboratory discharge (hot cathode cylindrical positive column) by Irvin Langmuir in the 1920's [12]. Constriction and instabilities of the plasma were observed and assigned to the presence of small dust particles coming from the sputtered tungsten cathode. From this time to the 1960's, the effect of dust and/or aggregates in low pressure plasmas was sporadically studied (see for examples [13]).
The effect of dust particles in combustion plasmas (such as combustion products of solid rockets, combustion products of hydrocarbon flames in which carbon particles may have formed, wake of a re-entry body) was studied in the 1950's and 1960's (see for example Ref. [14] and references therein). In most of these cases, the dust particles emit electrons thermionically (due a high

dust particle surface temperature), and therefore, their effects on the plasma are different from the non-emiting dust particles that can be found in most low pressure and low temperature plasmas.
In the late 1960's, the effect of dust on DC positive columns gained attention again. The effect of negatively charged large dust particles in a DC positive column was investigated. It was found that the dust particle effect can be compared to the effect of negative ions in electronegative discharges [15–19]. These results can be summarised as followed:

- When the dust density is not too high and when each dust particle can be considered as isolated, electron and ion densities (n_e and n_i respectively) can be deduced from the basic plasma equations [20] in which a term corresponding to volume losses on dust particle surfaces is added (dust particles act as surface ionization sinks [17]). Moreover, the electron temperature and the axial electric field were found to be higher than in a dust-free column.

- When the dust density is high, the dust particles replace the walls of the discharge and the plasma can be roughly treated as a set of parallel plasma filaments between absorbing walls with a radius about the order of the half of the mean interparticle distance [19].

- The dust particle surface temperature will be greater than that of the gas due to its heating by surface recombination.

- The radial distribution of dust particles varies from one discharge to another and is a compromise between a Maxwell-Boltzmann distribution, the effect due to local or large scale gas movement, the chemical destruction of the particle and the ion drag force in a strongly inhomogeneous discharge.

At the same time, Dimoff and Smy reported independantly that the dust particles act to remove free electrons in low temperature plasmas [21]: they showed experimentally that the rate of de-ionisation can be increased by the presence of dust particles. This result was obtained by measuring the plasma decay time in the afterglow of a linear pulsed discharge. Nevertheless, the theoretical explanation they provided was not satisfactory.

Meanwhile, the use of dust particles as a plasma diagnostic was also proposed [22, 23]:

- In Ref.[22], dust particles were observed between the capillary discharge and the Brewster window during investigations on a He-Ne laser. It was proposed to use these dust particles to locate potential local maxima in the discharge.

- In Ref.[23], it was proposed to inject dust particles inside a plasma and then, by measuring their charges, to deduce the electron temperature. The injected dust particles were uniform spherical alcohol droplets; then, by measuring the deflection of the dust particles in an electric field, the charge carried by the dust particles was measured and the electron temperature deduced.

1.1.2 And it came from the sky ...

The studies of plasma-dust interactions are of major interest for astrophysics as dusty plasmas can be found almost everywhere in a space environment (comet tails, planetary nebulae, planet atmospheres, planetary rings) and their physical properties need to be understood to explain observations.

Thus, a boost to the physics of dusty plasma came from astrophysics with the discovery of

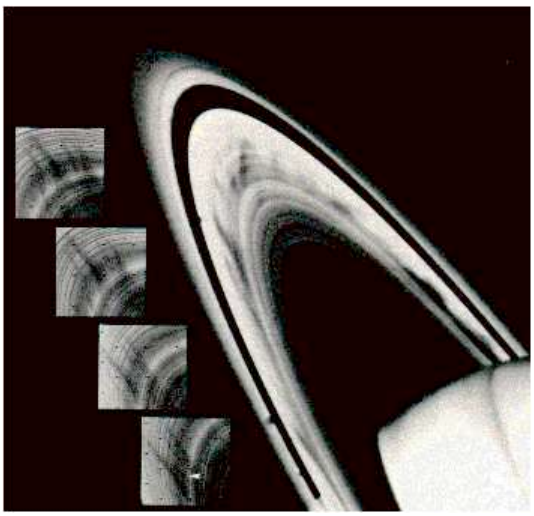

Figure 1.1: "spokes" on Saturn's B ring

nearly radial ghostly-like "spokes" in the outer portion of Saturn's B ring in the early 1980's by the Voyager space probes (Fig.1.1). It brought forward a lot of theoretical works about plasma-dust interactions in astrophysical environments. It was proposed that the spokes might be dust particles charged to a sufficiently large negative potential, through electron collection in transient dense plasmas, that they lift off from the ring and enter the permanently present background plasma environment. The sufficiently dense short-lived transient plasma can be created immediately above the ring by meteorite impacts [24, 25] or high energy auroral electron beams [26]. The spokes are then sculpted by electrostatic forces. This theory led to a large number of studies about the dust particle-plasma interactions and the charging processes of dust particles in space plasmas (see for example Refs.[27, 28]).

However, the spokes in Saturn's ring appear intermittently. Indeed, the spokes disappeared from October 1998 to September 2005 when the Cassini spacecraft saw them reappear [29]. It is suggested that, because the rings were more open to the sun than during Voyager missions and, because the spokes depend critically on the background plasma density above the rings which is a function of the solar angle, the charging environment prevented the formation of spokes. Recently, it has been proposed that, due their localised formation, their seasonality and their morphology, the *"spokes are caused by lightning-induced electron beams striking the rings, at locations magnetically-connected to thunderstorms"* [30].

1.1.3 The industrial era

In the late 1980's, dust particle formation was observed in laboratory and industrial chemically active discharges (Fig.1.2) [4, 31]. Dust particle formation in an industrial reactor can be a significant problem: dust particles falling on wafers (when the discharge is turned off) can adversely affect the performance of semiconductor devices or the quality of thin films. Consequently the mechanism of growth of dust particles in plasmas needed to be actively studied. It was indeed a major issue to understand how dust particles were formed in the plasma and how to inhibit their growth in order to avoid problems during industrial processes.

For this purpose, a lot of works has been carried out to understand the dust growth mechanism

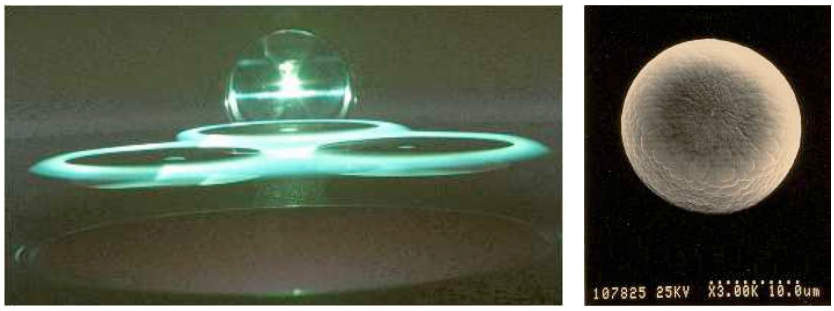

(a) (b)

Figure 1.2: (a) Photograph of Laser Light Scattering during plasma operation from particle structures suspended above a planar graphite electrode covered with three 82 mm diameter Si wafers [32]. (b) SEM photo of a typical plasma-generated particulate on a wafer surface after 12 hours exposure at a 200 mTorr, 10% CCl_2F_2 in Ar plasma during Si etching [4].

in silane discharges which are commonly used in the industry (see Ref.[5] and references therein). In Ref.[33–41], the dust particle growth mechanism and the dust cloud behaviour were studied in argon-silane discharges. It was shown that dust growth occurs following a well defined pattern:

1. Formation of molecular precursors from gas dissociation
2. Formation and accumulation of nanocrystallites from these precursors
3. Aggregation of the nanocrystallites
4. Growth by molecular sticking

The transport of dust particles in the discharge has also been well studied (see for example Refs.[10, 42]). Since the dust particles are generally charged in plasmas, they are subject to different forces (ion drag force, neutral drag force, electrostatic force, gravity, thermophoresis) which can confine or expel the particles from the discharge. Consequently it is possible to manipulate the dust particles, which can have strong industrial applications [5].

1.1.4 Modern times

The additional dust component of complex plasmas offers a unique opportunity to study strongly coupled systems as the coupling parameter Γ_c (representing the ratio of the potential electrostatic energy over the dust thermal energy) can be very large. It has indeed been shown that the dust particle density can reach very high values and that the total charge carried by the dust particles can exceed the one carried by the electrons. The coupling parameter Γ_c can be much greater than one and the dust particle cloud can be considered as a Coulomb liquid [33, 38] or even as Coulomb crystals [43–45].

As the dust particles interact strongly with each other, complex plasmas can be seen as self-organising systems. Dust plasma crystals have been discovered in the near sheath areas of capacitively coupled radio-frequency (RF) discharges [43–45]. The discovery of dust plasma crystals gave a real boost to the investigations of dusty plasmas. Many experiments were designed to study complex plasmas with an added micrometer-sized dust component and the formation of ordered structures were reported in DC discharges [46], Q-machines [47], thermal plasmas operated at atmospheric pressures [48, 49], UV-induced plasmas [50] and nuclear-induced plasmas [51].

Many studies (experimental and theoretical) are now devoted to the investigation of the dust charging process, dust-dust interactions, dust-plasma interactions and the forces acting on the dust particles (ion drag force, thermophoresis, neutral drag force, etc). For example, complex plasmas allow the studies of phenomena such as wave propagation [52, 53], crystal melting and phase transitions [54–56], and cluster motion to the kinetic level [57]. Formation of intriguing dust structures such as the dust "void" (the region totally free of dust in the core of the plasma) and its instabilities have been reported under microgravity conditions [58] and in discharges where high densities of grown particles can be achieved [59, 60].

The recent advances of experimental research under microgravity gave new opportunities to study the properties of complex plasmas [61–64]. Indeed, under typical laboratory conditions, the dust particles usually levitate in the sheath region where the electric field is strong enough to balance the gravitational force and gravity thus limits the range of parameters that can be studied. However, under microgravity conditions, a much wider range of parameters can be studied and bigger dust particle sizes can be used.

Experiments under microgravity conditions were first considered in the beginning of the 90's. Experiments were done at the end of the 90's on board parabolic flights, with rocket launches (TEXUS) and on board the MIR space station [65], mainly by two laboratories: the Max Planck Institute for Extraterrestrial Physics (MPE) in Garching (Germany) and the Institute for High Energy Density (IHED) in Moscow (Russia). These laboratories decided at the end of 1998 to collaborate through the program PKE (Plasma Kristall Experiment). PKE-Nefedov was the first plasma experiment designed for use on board the International Space Station (ISS). It was built to study dusty (complex) plasmas under microgravity conditions to avoid problems associated with the weight of the dust particles in ground-based experiments. As a result, it was possible to directly study plasma-dust particle interactions and dust particle-dust particle inter-

actions without gravitational perturbations. At the beginning of 2001, the first experiment with the PKE-Nefedov apparatus was made on board the ISS. Micrometer size melamine formaldehyde dust particles were injected directly into the plasma in order to study phenomena such as Coulomb crystals.
In December 2000, the GREMI laboratory (Orléans, France) joined the collaboration. The aim was to study the growth of particles created by sputtering of the previously injected dust particles. These grown dust particles are much smaller than the injected ones and can fill the whole chamber, even in ground-based experiments. At the end of 2001, the astronaut C. Haigneré made the first experiment of dust particle growth in the PKE-Nefedov reactor during the Andromeda mission. Some results obtained under microgravity conditions have been partially reproduced in ground-based experiments [61, 66–68]. Since that time, dust particle growth in the PKE-Nefedov reactor and phenomena such as growth instabilities and the void "heartbeat" oscillations are under active investigation. Complex plasmas under microgravity conditions are still intensively studied with the PK3+ experiment (an improved version of the PKE-Nefedov experiment) on board the ISS [69], and the PK4 experiment (a DC discharge) is under active development [70].

Meanwhile, the research on dust plasma interaction and particle growth is still motivated by strong technological challenges. For example, dust particles created by plasma-wall interactions in thermonuclear fusion devices are actively studied as the dust particles can be very harmful (lowering of plasma temperature, safety, transport of impurities, radioactivity) and lead to the malfunction of the fusion reactor [10, 11]. On the other hand, nanoparticles grown in the plasma phase can have very interesting and useful properties. For example, the electronic properties of polymorphous silicon (amorphous silicon with embedded crystalline silicon nanoparticles) created in silane-based discharges are of major interest for the manufacture of solar cells [71, 72].

1.2 Overview of this thesis

1.2.1 Aim of this thesis

Until now, the different studies on complex/dusty plasmas have focussed on few aspects of the new physics resulting from the presence of dust in the plasma. However, it is obvious that a complete picture from the plasma ignition to the discharge afterglow has to be built as every industrial or laboratory discharge has to be turned on and turned off. Consequently, in this thesis, phenomena arising from the growth of the dust particles at plasma ignition to the discharge afterglow are investigated.

1.2.2 Organisation of this thesis

Chapter 2 and chapter 3 are devoted to the basics of complex (dusty) plasma physics and the description of the experiments. Then, this thesis is centred around three major issues:

1. Growth of dust particles by sputtering in capacitively coupled RF discharges and associated instabilities (Chapter 4)

2. Instabilities of dust particle clouds in a complex plasma (Chapter 5)

3. Influence of dust particles on complex plasma decay and dust particle residual charges (Chapter 6)

As can be seen, the main goal of this thesis is to give a complete picture of a complex plasma from its beginning until it is extinguished. However, the work in each part of this thesis has been motivated by previous results that needed to be further investigated:

1. The first issue (Chapter 4) is devoted to the dust particle growth by sputtering in a RF discharge and its influence on the plasma and discharge parameters. This work was motivated by the activities of Goree's group [59, 73, 74] and is in the continuity of Mikikian's experiments at the GREMI laboratory [61, 66, 68, 75]. Its main goal is a better understanding of the effect of dust particle growth on the discharge and plasma parameters. For this reason, dust particle growth by RF sputtering has been investigated in two different RF discharges: the PKE-Nefedov reactor and the ComPLExS reactor. The diagnostics that have been used are electrical measurements (self bias voltage and current amplitude), optical measurements (high speed video imaging, spectroscopy) and Langmuir probe measurements. It is reported that the self bias voltage decreases in absolute value during the dust particle growth and that the current amplitude decreases at the same time. It is attributed to the loss of free electrons to the growing dust particle surfaces. It is also reported that the electron energy distribution function EEDF is greatly affected by the growth of the dust particles (increase of the electron temperature but loss of the energetic tail of the EEDF). It is also reported that the dust particle growth is greatly affected by the gas purity in the discharge. Finally, dust particle growth instabilities (DPGI) have been observed. It is shown that these instabilities follow a defined evolution pattern.

2. The second issue (Chapter 5) focusses on dust particle cloud instabilities in a complex plasma. We focus on the instabilities of the void region. Our results are concerned with the heartbeat instability (regular contractions and expansions of the void size) which has been studied theoretically [58, 76] and experimentally [60, 61] and void instabilities due to the growth of a new generation of dust particles inside the void: the "delivery instability" (which is accompanied by low frequency and large amplitude contraction and expansion of the void region and that ends with a new generation of dust particles inside the former void region), and the rotating void (which is characterised by a rotation of the void region

around the central axis of the chamber). In these studies, we focus particularly on measurements of some discharge parameters (discharge current) as well as spatially resolved measurements of the plasma glow (high speed video imaging, spatially focussed optical fibres coupled to photomultiplier tube (PMT) array) and observations of the dust cloud motion (high speed video imaging). Correlations between the different measurements led to a better understanding of the physical phenomena involved in the instabilities of dusty plasmas. It has been found that the dust void contraction is preceded by a strong increase of the plasma glow inside the void and hence the ionisation. Moreover, failed or aborted contraction can occur in between the main contraction-expansion sequences of the heartbeat instability. The evolution kinetics of the delivery instability is found to be linked to the growth kinetics of the new dust particle generation.

3. The third and last issue (Chapter 6) focusses on the study of dusty plasma afterglow and the residual electric charge on the dust particles when the plasma has disappeared. This work emerged as a result of the discovery of residual electric charge on dust particles after the power of an RF discharge was switched off during microgravity experiments [77]. Before this result, it was commonly believed that dust particles do lose their electric charge during the afterglow and remain neutral in the surrounding gas. Hence more investigations were necessary.

   It naturally led to the study of dusty afterglow plasma in order to understand the decharging process of the dust particles. Since the dust particle (de)charging process is strongly linked to the diffusion of the charge carriers in the afterglow plasma, theoretical investigations about the influence of the dust particle in the plasma loss processes in discharge afterglow have been made. Comparison with the available data [21] shows that the measurement of decay time in the afterglow plasma may be used as a complementary diagnostic. Furthermore, measurements of the electron density decay in various dust-free and dusty afterglow plasmas have been performed. The results confirm that dust particles influence substantially the diffusion of electrons in afterglow plasma.

   In order to further investigate the dust residual charges in the late plasma afterglow, ground-based measurements on dust residual charge in the PKE-Nefedov reactor have been performed. The dust particles were directly grown in the plasma chamber by sputtering of polymer materials previously deposited on the electrodes. The dust particles were sustained in the chamber volume after the discharge was switched off by a system creating an upward thermophoretic force inspired by Rothermel's experiments [78]. We confirm that the dust particles do carry residual electric charges and we show that this charge can be either positive or negative. Dust charge distributions (DCDs) have been reconstructed from measurements of many dust particle charges and show that the width of the dust charge distribution is larger than the one expected for the running discharge. Simulations of the decharging process show that the residual dust charge distribution is very sensitive to the ion and electron diffusion losses and especially the transition from ambipolar to free diffusion.

To conclude, in this thesis, we focus on the influence of dust particles on RF discharges from the plasma ignition to the discharge afterglow. It allows us to perform a detailed analysis of the effect the dust particles can have on a RF discharge at different instants during its lifetime. The main results are centred around the different stages of the lifetime of the discharge:

1. The effect of dust particle growth at plasma ignition and its effect on the plasma and discharge parameters and the related instabilities
2. The instabilities of the void region in a well established dust cloud in a discharge
3. The effect of dust particles on afterglow plasma and the influence of the plasma diffusion losses on the particle decharging and the residual charges.

1.3 Introduction en Français

La fumée, le brouillard, la suie, la brume, la poussière sont autant de termes qui renvoient à des particules en suspension dans des liquides ou des gaz. Les milieux poussiéreux ont toujours été très intéressants pour l'homme. Les égyptiens ont utilisé des poudres en suspension dans un liquide pour créer l'encre ; les chinois ont découvert leurs propriétés explosives. Les poudres restent aujourd'hui intéressantes pour une grande variété d'applications allant des enduits secs [1] aux recherches sur l'atmosphère [2, 3] en passant par l'industrie de la microélectronique [4, 5]. Dans tous les cas, les poudres peuvent être soit utiles, soit nuisibles et, par conséquent, de nombreuses études leur sont consacrées.
Les plasmas poussiéreux (ou complexes) sont des gaz ionisés contenant des poudres macroscopiques chargées. Ce sont des milieux communément rencontrés dans l'espace (nébuleuses planétaires, anneaux planétaires [6–8]), les hautes atmosphères [3, 9] et dans les plasmas créés par l'homme (décharges industrielles ou de laboratoire [4], plasmas de fusion [10, 11], etc).

Histoire sélective des plasmas poussiéreux

La préhistoire

A l'aube du $XX^{ème}$ siècle, les plasmas poussiéreux n'étaient connus que sous la forme de lueurs zodiacales (correctement décrites et interprétées par Cassini à la fin du $XVII^{ème}$ siècle) et de nuages noctilucents (découverts il y a environ un siècle). Leur étude physique n'a cependant pas commencé avant l'observation de poudres dans une décharge de laboratoire (colonne positive cylindrique à cathode chaude) par Irvin Langmuir dans les années 1920 [12]. Des constrictions et des instabilités du plasma furent observées et attribuées à la présence des petites poudres provenant de la pulvérisation de la cathode de tungstène. En revanche, jusqu'aux années 1960, l'impact de la présence de poudres dans les plasmas basse pression ne fut que sporadiquement étudié (voir par exemple la Réf.[13]).
L'effet des poudres dans les plasmas de combustion (comme les produits de combustion des fusées à combustible solide, les produits de combustion de flammes d'hydrocarbures dans lesquelles des suies de carbone peuvent être créés, le sillage d'objets entrant dans l'atmosphère) fut étudié dans les années 1950 et 1960 (voir par exemple la Réf.[14] et ses références). Dans la majorité de ces études, les poudres sont émettrices d'électrons thermoioniques (à cause d'une importante température de surface) et, par conséquent, doivent avoir un impact différent sur les plasmas de celles non-émettrices que l'on peut trouver dans la plupart des plasmas basse pression et basse température.
A la fin des années 1960, l'influence des poudres sur les colonnes positives à courant continu connut un regain d'attention. L'effet de poudres massives chargées négativement sur des colonnes positives à courant continu fut étudié. Il a été montré qu'elles ont un effet comparable à celui des ions négatifs dans les décharges électronégatives [15–19]. Ces résultas peuvent être résumés de la manière suivante :

- *Quand la densité de poussières n'est pas trop importante et quand chaque poudre peut être considérée comme isolée, les densités d'ions et d'électrons (respectivement n_i et n_e) peuvent être déduites des équations plasmas classiques [20] dans lesquelles un terme correspondant aux pertes en volume dues aux recombinaisons à la surface des poudres a été ajouté. De plus, il a été observé que la température électronique ainsi que le champ électrique axial sont plus importants que dans une colonne sans poudre.*
- *Quand la densité de poussières est importante, les poudres remplacent les parois de la décharge et le plasma peut être approximativement vu comme un jeu de filaments de plasma parallèles entre des parois absorbantes, chacun avec un rayon de l'ordre de la moitié de la distance moyenne entre deux poudres.*
- *La température de surface des poudres est plus élevée que celle du gaz environnant à cause de l'échauffement dû aux recombinaisons de surface.*

- *La distribution radiale des poussières varie d'une décharge à l'autre et est un compromis entre une distribution de Maxwell-Boltzmann, l'effet des mouvements locaux et à grande échelle du gaz environnant, de la destruction chimique des poudres et de la force de friction des ions dans les décharges fortement inhomogènes.*

A la même époque, Dimoff and Smy rapportèrent indépendamment que les poudres ont tendance à capturer les électrons libres dans les plasmas basse température [21] : ils montrèrent expérimentalement que le taux de dé-ionisation peut être accru par la présence des poussières. Ce résultat fut obtenu en mesurant le temps de décroissance du plasma dans la phase post-décharge d'une décharge linéaire pulsée. Leur explication théorique n'était néanmoins pas satisfaisante.
Pendant ce temps, l'utilisation de poudres comme moyen de diagnostic pour les plasmas a aussi été suggérée :

- *Dans la Réf.[22], des poussières furent observées entre la décharge capillaire et la fenêtre de Brewster lors d'études sur les lasers He-Ne. Ils proposèrent d'utiliser ces poussières pour localiser les maxima locaux de potentiel dans la décharge.*
- *Dans la Réf.[23], il fut proposé de mesurer la température électronique d'un plasma en mesurant les charges électriques de particules injectées à l'intérieur de celui-ci : les particules injectées étaient des gouttes d'alcool qui ont la propriété d'être sphériques et uniformes ; ensuite, en mesurant la déflexion de leurs trajectoires dans un champ électrique, leurs charges électriques étaient mesurées et la température électronique déduite.*

Et cela vint du ciel ...

L'étude des interactions entre les poudres et les plasmas est d'un grand intérêt pour l'astrophysique. En effet, les plasmas poussiéreux peuvent être rencontrés un peu partout dans l'espace (queues des comètes, nébuleuses planétaires, atmosphères planétaires, anneaux planétaires) et leurs propriétés physiques ont besoin d'être comprises afin d'expliquer les observations.
Ainsi, un coup d'accélérateur à la physique des plasmas poussiéreux vint de l'astrophysique grâce à la découverte de « stries »(« spokes ») pratiquement radiales sur la partie extérieure de l'anneau B de Saturne par la sonde Voyager au début des années 1980 (Fig.1.1). Cela a engendré un grand nombre de travaux sur les interactions plasmas-poudres dans les milieux astrophysiques. Il fut proposé que ces stries soient composées de poussières chargées à des potentiels négatifs suffisamment importants, par collection d'électrons dans des plasmas transitoires denses, afin de les élever au dessus de l'anneau et de les faire entrer dans le plasma environnant. Des plasmas denses transitoires peuvent être créés juste au dessus des anneaux lors d'impacts avec des météorites [24, 25] ou par des faisceaux auroraux d'electrons de hautes énergies [26]. Les stries sont ensuite sculptées par les forces électrostatiques. De nombreuses études furent ensuite consacrées aux interactions plasmas-poussières et aux processus de chargement des poudres (voir par exemples les Réfs.[27, 28]).
Les stries sur les anneaux de Saturne apparaissent cependant par intermittence. En effet, aucune strie ne fut observée d'octobre 1998 à septembre 2005 au moment où la sonde Cassini les a vues réapparaître [29]. L'hypothèse proposée est que, parce que les anneaux étaient plus exposés au soleil que pendant les missions Voyager et parce que les stries sont très dépendantes de la densité du plasma environnant, la formation des stries fut inhibée par les conditions ambiantes. Il a récemment été suggéré que, en raison de leur formation localisée, leur saisonnalité et leur morphologie, les stries sont générées par des faisceaux d'electrons induits par la foudre et atteignant les anneaux en des domaines connectés magnétiquement aux orages [30].

L'ère industrielle

A la fin des années 1980, la formation de poussières fut observée dans des décharges chimiquement actives industrielles et de laboratoire (Fig.1.2) [4, 31]. La formation de poudres dans les réacteurs industriels peut être un gros problème : les particules tombant sur les substrats peuvent réduire la performance des circuits intégrés ou la qualité des couches minces. Par conséquent, les mécanismes de croissance de poudres dans les plasmas devaient être étudiés finement. Il était

en effet vital de comprendre comment les poussières se forment dans les plasmas et comment inhiber leur formation afin d'éviter les problèmes dans les processus industriels.
Pour ces raisons, de nombreux travaux ont été menés pour comprendre les mécanismes de croissance de poudres dans les décharges à base de silane très largement utilisées dans l'industrie (voir la Réf.[5] et ses références). Dans les Réfs.[33–41], la croissance et le comportement de nuages de poudres dans des décharges argon-silane ont été étudiés. Il a ainsi été montré que la croissance des poussières suit le modèle suivant :

1. *Précurseurs moléculaires provenant de la dissociation du gaz*
2. *Formation et accumulation de nanocristallites*
3. *Agglomération des nanocristallites*
4. *Croissance par attachement moléculaire*

Le transport des particules dans les décharges a aussi été étudié (voir par exemple les Réfs.[10, 42]). Les poudres étant généralement chargées dans les plasmas, elles sont soumises à différentes forces (force de friction des ions, force de friction des neutres, forces électrostatiques, gravité, thermophorèse) qui peuvent les confiner ou les expulser de la décharge. Il est par conséquent possible de manipuler les particles, ce qui peut avoir d'importantes applications industrielles [5].

Les temps modernes

La composante additionnelle de poudres chargées dans les plasmas poussiéreux donne l'opportunité unique d'étudier les systèmes fortement couplés en raison du paramètre de couplage Γ_c (qui représente le rapport entre l'énergie potentielle électrostatique des poudres et leur énergie d'agitation thermique) pouvant être très grand. Il a en effet été rapporté que la densité de poussières dans un plasma peut être extrêmement élevée et que la charge globale portée par celles-ci peut donc excéder celle portée par les électrons. La paramètre de couplage Γ_c peut être alors largement supérieur à un et le nuage de poudres considéré comme un liquide coulombien [33, 38], voire même un cristal coulombien [43–45].
En raison des fortes interactions des poudres entre elles, les plasmas poussiéreux peuvent être vus comme des milieux auto-organisés. Des cristaux coulombiens furent ainsi découverts dans les zones aux alentours des gaines dans des décharges radio-fréquences (RF) capacitives [43–45]. Cette découverte créa un réel engouement pour les recherches sur les plasmas poussiéreux. De nombreuses expériences, dans lesquelles des poudres micrométriques étaient ajoutées, furent conçues pour ces travaux et la formation de structures ordonnées fut observée dans des décharges à courant continu [46], des machines Q [47], des plasmas thermiques à pression atmosphérique [48, 49], des plasmas induits par rayonnement ultraviolet [50], et des plasmas créés par des réactions nucléaires [51].
De nombreuses études (expérimentales et théoriques) sont dorénavant consacrées aux processus de chargement des poudres, aux interactions poudre-poudre, aux interactions poudre-plasma et aux forces agissant sur les poussières (force de friction des ions, force de friction des neutres, thermophorèse, etc). Les plasmas poussiéreux permettent par exemple d'analyser certains phénomènes comme la propagation d'ondes [52, 53], la fusion des cristaux et les transitions de phases [54–56], et la dynamique des clusters au niveau le plus élémentaire [57]. La formation de structures singulières comme le « void »(région vide de poudres au centre du plasma) et ses instabilités ont été observées lors d'expériences en microgravité [58] et dans des décharges où la densité de poudres formées dans le plasma peut être très élevée [59, 60].
Les récentes avancées aux niveaux des recherches en microgravité ont ouvert de nouvelles perspectives pour l'étude des propriétés des plasmas poussiéreux [61–64]. En effet, durant les expériences en laboratoire, les poudres lévitent généralement dans les gaines du plasma où le champ électrique est suffisamment puissant pour compenser leur poids. L'éventail de paramètres qui peuvent être explorés est alors restreint. Au contraire, lors d'expériences en microgravité, la gamme peut être étendue et des poudres plus grosses peuvent être utilisées.
Les expériences en microgravité ont d'abord été envisagées au début des années 1990. Les premières furent réalisées à la fin des années 1990 à bord de vols paraboliques et de fusées, et

à bord de la station spatiale MIR par principalement deux laboratoires : le Max-Planck-Institut für Extraterrestrische Physik (Allemagne) et l'Institut for High Energy Density (IHED, Russie). Ces laboratoires décidèrent à la fin de l'année 1998 de collaborer et créèrent le programme PKE (Plasma Kristall Experiment). PKE-Nefedov fut ainsi la première expérience plasma conçue pour fonctionner à bord de la station spatiale internationale (ISS). Elle a été construite afin d'étudier les plasmas poussiéreux en microgravité et ainsi éviter les problèmes dus au poids des poudres. Il fut ainsi possible d'étudier directement les interactions plasma-poudre et poudre-poudre sans les perturbations liées à la gravité. Au début de l'année 2001, les premières expériences à bord de l'ISS furent réalisées. Des poudres de mélamine formaldéhyde de quelques micromètres furent injectées dans le plasma afin d'étudier les structures ordonnées comme les cristaux coulombiens. En décembre 2000, le laboratoire GREMI (France) joignit la collaboration afin d'étudier la croissance de poudres par pulvérisation des poudres précédemment injectées dans le réacteur. Ces poussières sont bien plus petites que les poudres injectées et peuvent remplir la décharge même en laboratoire. Fin 2001, l'astronaute C. Haigneré fit les premières expériences sur la croissance de poudres dans le réacteur PKE-Nefedov durant la mission Andromède. De plus, certains résultats obtenus en microgravité furent partiellement reproduits en laboratoire [61, 66–68]. Depuis cette époque, la croissance de poudres dans le réacteur PKE-Nefedov et les phénomènes comme les instabilités de croissance et les battements du « void »sont intensivement étudiés. Les plasmas poussiéreux en microgravité sont toujours étudiés grâce à l'expérience PK3+ (une version améliorée de PKE-Nefedov) à bord de l'ISS [69], et le développement de l'expérience PK4 (une décharge à courant continu) [70].

Pendant ce temps, les recherches sur les plasmas poussiéreux sont toujours motivées par d'importants défis technologiques. Par exemple, les poussières créées lors des interactions du plasma avec les parois des tokamaks pour la fusion nucléaire sont fortement étudiées car elles peuvent être extrêmement nuisibles (réduction de la température du plasma, sécurité, transport d'impuretés, radioactivité) et entraîner un dysfonctionnement du réacteur [10, 11]. D'un autre côté, les nanopoudres formées dans les plasmas peuvent avoir des propriétés très intéressantes. Par exemple, les propriétés du silicium polymorphe (silicium amorphe incrusté de nanocristaux de silicium créé dans des décharges à base de silane) sont très intéressantes pour la fabrication de panneaux solaires [71, 72].

Présentation de la thèse

But de la thèse

Jusqu'à maintenant, les différentes recherches sur les plasmas poussiéreux se sont focalisées sur certains aspects de la nouvelle physique due à la présence des poudres. Cependant, il est évident qu'un panorama complêt depuis l'allumage du plasma jusqu'à la phase post-décharge doit être construit car chaque décharge industrielle ou de laboratoire doit être allumée mais aussi éteinte. Par conséquent, dans cette thèse, les phénomènes liés à la croissance de poudres dans le plasma depuis l'allumage jusqu'à la phase post-décharge sont étudiés.

Organisation de la thèse

Les chapitres 2 et 3 sont dédiés aux bases de la physique des plasmas poussiéreux et à la description des expériences. Ensuite, la thèse s'articule autour de trois grands thèmes :

1. *Croissance de poudres par pulvérisation dans des décharges RF capacitives et les instabilités associées (Chapitre 4).*
2. *Les instabilités des nuages de poussières dans les plasmas complexes (Chapitre 5).*
3. *L'influence des poudres sur la décroissance du plasma durant la phase post-décharge et les charges résiduelles des poussières (Chapitre 6).*

Le but principal de cette these est donc de donner une image complète d'un plasma poussiéreux depuis sa création jusqu'à son extinction. Cependant, les travaux effectués dans chaque thème ont été motivés par des résultats antérieurs qui méritaient d'être approfondis :

1. *Le premier thème (Chapitre 4) est consacré à la croissance de poudres par pulvérisation dans des décharges RF capacitives et à son influence sur les paramètres du plasma. Ce travail est influencé par les activités du groupe du Prof. Goree [59, 73, 74] et est dans la continuité des expériences menées par Dr. Mikikian au GREMI [61, 66, 68, 75]. Son principal but est la compréhension de l'influence de la croissance de poudres sur les paramètres du plasma et de la décharge. Pour cela, la formation de poussières par pulvérisation a été étudiée dans deux réacteurs différents : le réacteur PKE-Nefedov et le réacteur ComPLExS. Des diagnostics électriques (tension d'autopolarisation et amplitude du courant), des diagnostiques optiques (imagerie video rapide, spectroscopie, luminosité du plasma) et des mesures de sondes de Langmuir ont été utilisés. Les résultats montrent que la tension d'autopolarisation décroît en valeur absolue durant la croissance des poudres et que l'amplitude du courant diminue. Cela est attribué à la perte des électrons libres du plasma à la surface des poussières en formation. La fonction de distribution en énergie des électrons (FDEE) est profondément modifiée par la présence des poudres (accroissement de la température électronique mais perte des électrons très énergétiques). La pureté du gaz de la décharge affecte énormément la croissance des poussières. Finalement, des instabilités du plasma durant la croissance des poudres ont été observées. Celles-ci suivent un schéma d'évolution temporel bien précis.*
2. *Le deuxième thème (Chapitre 5) est centré autour des instabilités d'un nuage de poussières dans un plasma complexe et plus particulièrement les instabilités du « void ». Nos résultats s'intéressent plus particulièrement aux battements (heartbeat) du « void »(dilatations et contractions régulières de la taille du « void »), qui ont été étudié théoriquement [58, 76] et expérimentalement [60, 61], et aux instabilités dues à la croissance d'une nouvelle génération de poudres à l'intérieur du « void » : dilatations et contractions de la taille du void de grande amplitude et basse fréquence et qui se terminent par l'apparition d'un nouveau nuage de poussières dans l'ancien « void », et le « void »en rotation (révolution du « void »autour de l'axe de symétrie du réacteur). Pour ces différentes études, nous avons particulièrement mis l'accent sur la mesure de certains paramètres de la décharge (courant) ainsi que sur des mesures spatialement résolues de la luminosité du plasma (imagerie vidéo rapide, fibres optiques focalisées et couplées à des photomultiplicateurs) et de la dynamique du nuage de poudres (imagerie vidéo rapide). La corrélation entre ces différentes mesures a permis une meilleure compréhension des phénomènes physiques impliqués dans ces instabilités. Les contractions du « void »sont accompagnés d'un fort accroissement de la luminosité au centre du plasma et donc de l'ionisation. De plus, des contractions avortées du « void »ont été observées entre les séquences principales de contraction-expansion. La cinétique d'évolution des dilatations et contractions de la taille du void de grande amplitude et basse fréquence est liée à la cinétique de croissance du nouveau nuage de poudres.*
3. *Le troisième thème (Chapitre 6) est consacré aux études sur la phase post-décharge des plasmas complexes et sur la charge électrique résiduelle des poudres quand le plasma a complètement disparu. Ce travail fut initié par la découverte de la charge électrique résiduelle des poussières après l'arrêt d'une décharge RF capacitive lors d'expériences en microgravité [77]. Avant ce résultat, on pensait que les poudres perdaient toutes leurs charges pendant la phase post-décharge et devenaient électriquement neutres. Par conséquent, des études complémentaires étaient nécessaires.*
   Cela a naturellement donné lieu à des recherches sur la phase post-décharge des plasmas complexes afin de comprendre les processus de déchargement des poudres. Comme la charge des poudres est fortement liée à la diffusion des porteurs de charge dans la phase post-décharge, des études théoriques sur l'influence des poussières sur la perte des ions et des électrons ont été menées. La comparaison avec les résultats expérimentaux disponibles [21] montre que la mesure du temps de disparition du plasma durant la post-décharge peut être

utilisée comme un diagnostic complémentaire. Des mesures de la décroissance de la densité électronique dans différents plasmas avec ou sans poudres ont montré que ces dernières ont un effet conséquent sur la diffusion des électrons durant la phase post-décharge.
Afin d'approfondir les connaissances sur la charge résiduelle des poudres, des expériences au sol ont été réalisées dans le réacteur PKE-Nefedov. Les poudres ont été formées directement dans le plasma et maintenues entre les deux électrodes, après que la décharge a été éteinte, par une force de thermophorèse compensant la force de gravité et engendrée par un système inspiré des expériences de Dr. Rothermel [78]. Nous avons confirmé que les poudres portent bien une charge électrique résiduelle après l'arrêt de la décharge et avons découvert que cette charge peut être positive ou négative. Des fonctions de distribution des charges résiduelles ont été reconstruites en mesurant les charges d'un grand nombre de poudres. Leur variance est plus grande que celle attendue pour la fonction de distribution de charges des poussières dans un plasma allumé. Les simulations du processus de déchargement ont montré que la fonction de distribution des charges résiduelles est très sensible à la diffusion des ions et des électrons et plus précisément à la transition de la diffusion ambipolaire vers la diffusion libre.

En conclusion, cette thèse s'intéresse à l'influence des poudres sur des décharges RF depuis leur allumage jusqu'à leur extinction. Une analyse détaillée de l'effet des poussières aux différents instants de la vie du plasma est réalisée. Les principaux résultats s'articulent autour des différentes étapes de la vie de la décharge :

1. *L'effet de la croissance des poudres à l'allumage de la décharge et son influence sur les paramètres du plasma ainsi que les instabilités associées.*
2. *Les instabilités du « void »dans un nuage de poudres bien établi.*
3. *L'effet des poussières sur la phase post-décharge et l'influence de la diffusion du plasma sur le déchargement des poudres et les charges résiduelles.*

Chapter 2

Review of complex plasma physics

Dusty or complex plasmas are partially ionized gases composed of neutral species, ions, electrons and charged dust particles. Dust particles are electrically charged due to their interactions with ions and electrons of the surrounding plasma [28, 79, 80]. In this chapter, the charging process of the dust particles and the forces acting on them are described. New phenomena due to the presence of dust particles in a plasma are also discussed.

2.1 Charge and charge distribution

The particle charge controls the dust dynamics both in laboratory and industrial plasma reactors, and also in space plasmas. Thus one of the main challenges in dusty plasma is to understand the charging of dust particles in a wide range of experimental conditions, which includes industrial and space plasmas. For example, in most industrial processes in the microelectronics industry, which uses silane as the reactive gas, dust contamination is a vital problem [5]. The dust dynamics and coagulation in space plasma are also phenomena governed by dust particle charges [81, 82].

Elementary processes leading to dust particle charging are the collection of the ions and the electrons of the surrounding plasma, the interactions with photons, secondary electron emission due to collisions with energetic particles, thermionic emission, etc. In laboratory plasmas, charging by ion and electron collection is the prevalent effect.

Two extreme cases can be considered. When the Debye length λ_D of the dusty plasma is much smaller than the intergrain distance a, the dust particles can be considered as isolated in the plasma. When the Debye length λ_D is larger than the intergrain distance a, the dust particles interact with each other and have a collective behaviour. The size of the dust particle compared to the Debye length also has an influence. Here, we consider only the case where $r_d \ll \lambda_D$ where r_d is the radius of the dust particles.

2.1.1 The Debye length

A fundamental characteristics of plasmas is the screening of electric field created by individual charged particles (ions, electrons and dust particles) or by a surface with a potential that is different to the plasma potential. This screening effect has a characteristic length: the Debye length. This is the length below which the electric field of a charged particles can influence the other charged particle. In dusty plasmas, the linearised Debye length is [5, 83]:

$$\lambda_D = \frac{\lambda_{De}\lambda_{Di}}{\sqrt{\lambda_{De}^2 + \lambda_{Di}^2}} \tag{2.1}$$

where $\lambda_{Di(e)}$ is the ion (electron) Debye length defined as:

$$\lambda_{Di(e)} = \sqrt{\frac{\epsilon_0 k_B T_{i(e)}}{n_{i(e)0} e^2}} \tag{2.2}$$

with ϵ_0 the vacuum permittivity, k_B the Boltzmann constant, $T_{i(e)}$ the ion (electron) temperature, $n_{i(e)0}$ the ion (electron) density and e the elementary charge.
For typical plasmas with $T_e \sim 3\ eV$, $T_i \sim 0.03\ eV$ and $n_{i0} \simeq n_{e0} \sim 10^{15}\ m^{-3}$, the Debye length is $\lambda_D \sim 40\ \mu m$

2.1.2 Isolated dust grains

Orbital motion limited (OML) theory for a spherical dust grain

The charging (decharging) process of dust particles in a plasma is governed by the contributions of all currents entering (or leaving) the dust surface, involving plasma electron and ion currents, photoemission and thermionic emission currents, etc.

$$\frac{dQ_d}{dt} = \sum_a I_a + \sum_l I_l \tag{2.3}$$

where Q_d is the charge of the dust particle and I_a and I_l are currents absorbed and emitted by the dust particle (with appropriate signs). For discharge plasmas we can ignore the emission current in most cases. The plasma ions and electrons are collected by the grain, which acts like a floating probe. Dust particles are consequently electrically charged by accumulation of plasma particles "falling" onto their surfaces. Dust particle electric charge is determined by:

$$\frac{dQ_d}{dt} = \sum_j I_j \tag{2.4}$$

where I_j is the current associated with the plasma $j-$species.

Let's consider a spherical dust grain with radius r_d immersed in an ion and electron plasma. It is obvious that when $v_{Te} \gg v_{Ti}$ where $v_{Te(i)} = \sqrt{8k_B T_{e(i)}/\pi m_{e(i)}}$ is the electron (ion) thermal speed with $m_{e(i)}$ the electron (ion) mass, the electrons reach the dust grain surface at a greater

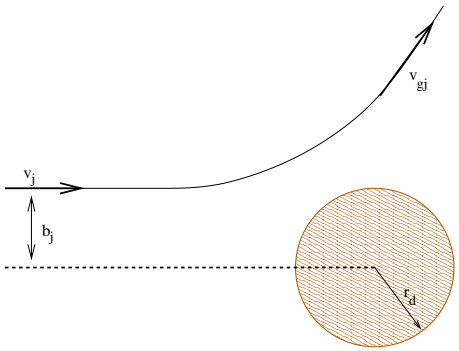

Figure 2.1: Schematic of interaction of a particle j with a dust grains of the same charge

rate. Consequently, more electrons are collected and dust grain surface potential ϕ_g is negative. Ion and electron currents are of course affected by the dust surface potential. Thus, when it is too repulsive for the $j-$species, the current from the oppositely-charged plasma particle is favoured which modifies, in proportion, the dust surface potential.

When $r_d \ll \lambda_{Di} \ll \lambda_{mfp}$ where λ_{mfp} is either the electron or ion-neutral collisional mean free path, the current of the $j-$species on the dust particle can be calculated using the orbital motion limited (OML) theory [84, 85]. The two major assumptions of this model are [86]:

- Any plasma particle initially far from the dust particle can reach the surface of the dust particle and stick to its surface if it is allowed by the conservation laws. Moreover, this process is independent from the structure of the electrostatic potential near the particle.
- For a spherical dust particle, the limiting impact parameter of the plasma particle corresponds to a trajectory which is tangential to the dust particle.

Let's consider a plasma particle j approaching a dust particle from infinity (fig.2.1). When this particle enters the Debye sphere of the dust grain, it experiences a force due to the electrostatic field of the grain and is deflected. Taking v_j as the speed of the particle j before interaction, v_{gj} its speed afterward and b_j the impact parameter, it is obvious that for fixed v_j, if b_j reduces, the particle j collides with the dust grain. The cross section for a j particle-dust grain collision σ_j^d is:

$$\sigma_j^d = \pi b_j^2 \tag{2.5}$$

As dust grains are massive compared to ions and electrons (typically $m_d \gg m_i \gg m_e$), momentum and energy conservation give:

$$m_j b_j v_j = m_j v_{gj} r_d \tag{2.6}$$

$$\frac{1}{2} m_j v_j^2 = \frac{1}{2} m_j v_{gj}^2 + \frac{q_j Q_d}{4\pi\epsilon_0 r_d} \tag{2.7}$$

where m_j is the mass of the j particle and q_j its charge. The dust charge Q_d is directly linked to the potential difference $\phi_d = \phi_g - V_p$ where V_p is the plasma potential. One can

write $Q_d = C \cdot \phi_d$ where C is the capacitance of the dust grain. For a spherical dust grain, $C = 4\pi\epsilon_0 r_d \exp(-r_d/\lambda_D) \approx 4\pi\epsilon_0 r_d$ with $\lambda_D \gg r_d$. With Eqs.2.5, 2.6 and 2.7, one can obtain:

$$\sigma_j^d = \pi r_d^2 \Big(1 - \frac{2q_j\phi_d}{m_j v_j^2}\Big) \tag{2.8}$$

If $f_j(v_j)$ is the $j-$species velocity distribution function, the current I_j on dust grains is:

$$I_j = q_j \int_{v_{j_{min}}}^{\infty} v_j \sigma_j^d f_j(v_j) d^3 v_j \tag{2.9}$$

Two cases must then be considered:

- if $q_j\phi_d < 0$, the interaction force between the j particle and the dust grain is attractive and $v_{j_{min}} = 0$
- if $q_j\phi_d > 0$, the force is repulsive and $(1/2)m_j v_{j_{min}}^2 = q_j\phi_d \Rightarrow v_{j_{min}} = \sqrt{2q_j\phi_d/m_j}$

For a Maxwellian plasma, the velocity distribution function is:

$$f_j(v_j) = n_j \Big(\frac{m_j}{2\pi k_B T_j}\Big)^{3/2} \exp\Big(-\frac{m_j v_j^2}{2k_B T_j}\Big) \tag{2.10}$$

with n_j the density of the plasma $j-$species. Thus, in the attractive case, one can obtain:

$$I_j = 4\pi r_d^2 n_j q_j \Big(\frac{k_B T_j}{2\pi m_j}\Big)^{1/2} \Big(1 - \frac{q_j\phi_d}{k_B T_j}\Big) \tag{2.11}$$

and in the repulsive case, one can obtain:

$$I_j = 4\pi r_d^2 n_j q_j \Big(\frac{k_B T_j}{2\pi m_j}\Big)^{1/2} \exp\Big(-\frac{q_j\phi_d}{k_B T_j}\Big) \tag{2.12}$$

When the dust particle charge reaches steady state, ion and electron currents, I_i and I_e respectively, compensate each other:

$$I_e = I_i \tag{2.13}$$

thus, for negatively charged dust particles (which is generally the case in most laboratory plasma where $T_e > T_i$), the dust potential upper limit is thus [5, 83, 86]:

$$\phi_d = \frac{k_B T_e}{e} \ln\left(\frac{ni}{n_e}\Big(\frac{m_e T_e}{m_i T_i}\Big)^{1/2}\right) \tag{2.14}$$

and the dust particle charge is:

$$Q_d = \frac{4\pi\epsilon_0 r_d k_B T_e}{e} \ln\left(\frac{ni}{n_e}\Big(\frac{m_e T_e}{m_i T_i}\Big)^{1/2}\right) \tag{2.15}$$

Eq.2.15 gives the maximum charge on an isolated dust particle. Matsoukas and Russel [79] showed that this expression must be corrected by a factor C_c depending on plasma parameters giving:

$$Q_d = C_c \cdot \frac{4\pi\epsilon_0 r_d k_B T_e}{e} \ln\left(\frac{ni}{n_e}\left(\frac{m_e T_e}{m_i T_i}\right)^{1/2}\right) \tag{2.16}$$

For typical argon plasmas ($m_e/m_i \approx 1.4 \cdot 10^{-5}$ and $1 < T_e/T_i < 100$, this factor is $C_c \sim 0.73$. For $T_e/T_i > 1000$, Eq.2.16 is a very poor approximation and completely breaks down when $T_e/T_i \gtrsim m_i/m_e$ which are not cases of practical interest.

Influence of trapped ions

In the previous section, the effect of the collisions of the electrons and ions on the dust charging process and the electrostatic shielding have been neglected. However, under some conditions, a significant amount of trapped ions due to charge exchange collisions with the neutral gas background can surround the dust particle. Hence the positive ion current can be significantly increased and the shielding properties of the grain are changed. It has been shown that when $T_i \ll T_e$ (nearly all newly created ions are trapped in the potential well of the dust particle) and when $r_d^2/\lambda_D^2 \ll T_i/T_e$ (few newly created ions fall immediately on the dust particle), the density of trapped ions can be large and the dust particle potential magnitude significantly reduced (as much as 50 %) [87, 88].

Dust charge distribution

The formalism developed above gives the charge of a dust particle in a steady state plasma. It is obvious that, when the dust particle has its equilibrium charge, the average number of collected electrons is equal to the average number of collected ions but since the charging of a dust particle is a discrete process, electrons and ions are captured at random times. The number of charges on a dust particle $Z_d = |Q_d/e|$ fluctuates around its equilibrium value given by the condition that the total current to the particle is zero. Charge fluctuations and dust charge distributions (DCDs) have been the subject of many theoretical studies ([79, 89, 90] and references therein). In the most fundamental process, the charge fluctuation is of magnitude $\pm e$, each time an electron or an ion is captured by the dust particle. A Fokker-Planck description of the charging process in weakly ionised gases and fluctuations arising from the nature of this process have been presented by Matsoukas and Russel [91]. It gives time for charge fluctuations τ_Q, the mean time for collisions of a dust particle with a charge species τ_c as well as the variance σ of the mean charge Q_{mean} on a dust particle.
We consider $W = W(Q_d, t)$ to be the probability for a dust particle to carry the charge Q_d at time t. If it is assumed that the charging currents depend on the instantaneous charge on the dust particle and not on any prior history, the particle charge constitutes a Markov process

whose master equation can be deduced from Eq. 2.4:

$$\frac{\partial W}{\partial t}\Big|_{Q_d} = [I_i W|_{Q_d-e} - I_e W|_{Q_d+e} - (I_i - I_e)W|_{Q_d}]/e \tag{2.17}$$

Assuming that the dust particle charge is a continuous variable and linearising the currents in the vicinity of the steady-state charge Q_{mean} which is defined by Eq.2.13, Eq.2.17 can be rewritten as [91]:

$$\frac{\partial W}{\partial (t/\tau_Q)} = \frac{\partial (Q_d - Q_{mean})W}{\partial Q_d} + \sigma^2 \frac{\partial^2 W}{\partial Q_d^2} \tag{2.18}$$

where τ_Q and σ^2 are defined as:

$$\tau_Q = 1/(-\bar{I_e}' - \bar{I_i}') \tag{2.19}$$

$$\sigma^2 = \frac{e}{2}\Big(\frac{\bar{I_i} - \bar{I_e}}{-\bar{I_e}' - \bar{I_i}'}\Big) \tag{2.20}$$

The primes indicate the first derivative with respect to Q_d and the bars indicate calculation at $Q_d = Q_{mean}$. Eq.2.18 is mathematically identical to the Fokker-Planck equation for the diffusion of a particle in a harmonic potential and views the charge as a stochastic variable diffusing in the charge space and opposed by a force produced by the deterministic charging current. The solution of this equation is (see Ref.[91] and App.A):

$$W(Q_{mean} + x, t) = \frac{1}{\sigma\sqrt{2\pi(1 - e^{-2t/\tau_Q})}} \exp\Big(-\frac{(x - x_0 e^{-t/\tau_Q})^2}{2\sigma^2(1 - e^{-2t/\tau_Q})}\Big) \tag{2.21}$$

where $x = Q_d - Q_{mean}$. From Eq.2.21, it is clear that the charge distribution is Gaussian at all the times and approaches a steady state with a time constant τ_Q, with a mean dust particle charge Q_{mean} and a variance σ which depends on the charging currents. The variance σ can be written as:

$$\Big(\frac{\sigma}{e}\Big)^2 = \frac{\tau_Q}{2\tau_c} \tag{2.22}$$

where $\tau_c = e/(\bar{I_i} - \bar{I_e})$. It has been shown that τ_Q represents the time for charge fluctuations and τ_c represents the mean time for collisions between a dust particles and a charge species [91]. In the case of Maxwellian current, the time for charge fluctuations τ_Q is [91, 92]:

$$\tau_Q = \Big(\frac{4\lambda_i^2}{v_{Ti} r_d}\Big)\frac{1}{1 + T_i/T_e - eQ/4\pi\epsilon_0 r_d k_B T_e} \tag{2.23}$$

Fokker-Planck simulations [93] were performed for 190 nm radius particles (experimental dust radius obtained during dust particle residual charge measurements; see Chap.6) with $T_e = 3$ eV, $T_i = 0.03$ eV and $n = n_e = n_i = 5 \cdot 10^9$ cm^{-3} (see Fig.2.2). It shows that the dust particle charge evolves to an equilibrium charge in a time $\tau_Q \sim 4$ μs which is in agreement with Eq.2.23, and that the charge distribution at equilibrium is a Gaussian. Moreover, the mean charge at equilibrium Q_{mean} is in agreement with the theoretical prediction of Eq.2.16 (which predicts an

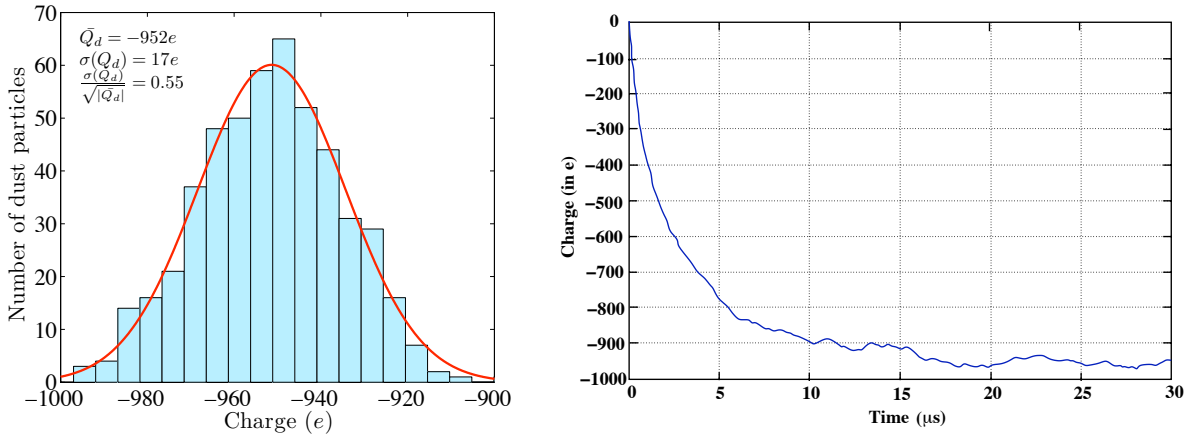

Figure 2.2: Calculation of dust particle charges using a Fokker-Planck algorithm [93] for 190 nm radius particles in a plasma with $T_e = 3\ eV$, $T_i = 0.03\ eV$ and $n = n_e = n_i = 5 \cdot 10^9\ cm^{-3}$. Left: Dust particle charge distribution for 500 iterations. Right: Dust particle charge evolution when immersed in the plasma

equilibrium charge $Q_{mean} = -951.9e$).

Similar results were obtained by Tsytovich et al [89] by assuming the discreteness of the electron and ion distributions. Khrapak et al [94] obtained the magnitude of fluctuation in terms of the temporal autocorrelation function and reported dependence of the dust charge distribution (DCD) on plasma parameters. All proposed models confirm that the DCD is Gaussian and that the standard deviation of the stochastic charge fluctuation varies as $\sigma(Q_d) \simeq \delta\sqrt{|\bar{Q}_d|}$, where Q_d is the dust particle charge, $\bar{Q}_d$ is the mean dust particle charge and δ is a parameter depending on plasma conditions and is close to 0.5. Computer simulations of the charging process also report the same result [56, 93, 95].

Nevertheless, no direct measurement of the DCD has been performed due to the shortness of the charging and characteristic charge fluctuation time scales (in the μs range). So at any particular moment an ensemble of monosized dust particles is characterized by their DCD. However, on the dust time scale (in the ms range) the behaviour of a dust particle is determined by its mean equilibrium charge. Existing experimental techniques for dust charge measurement based on the analysis of dust dynamic response [96–98] can only determine the mean charge which is equal for all monosized particles. However, charge fluctuations may have some impact in dusty afterglow plasma and DCD may be measured in the late discharge afterglow (see Chap.6).

2.1.3 Cloud of dust particles

When the dust particle density in the plasma is high, the global charge carried by the dust particles can be a significant fraction of the global charge carried by the ions and the electrons. In this case, the neutrality condition has to be rewritten in order to take into account the dust

particles:

$$n_i = n_e + Z_d n_d \tag{2.24}$$

where $Z_d = |Q_d/e|$ is the dust particle charge number and n_d the dust particle density. As can be seen, it is possible that the electron density differs significantly from the ion density and it must be taken into account in the charging equation. At steady state ion and electron currents compensate each other. Consequently, combining Eqs.2.11, 2.12 and 2.24, the dust particle charge can be obtained solving:

$$\Big(\frac{T_i}{T_e}\frac{m_e}{m_i}\Big)^{1/2}(1+\frac{T_e}{T_i}\varphi)\exp(\varphi) = 1 - P_H \tag{2.25}$$

where $P_H = Z_d n_d/n_i$ is the Havnes parameter and φ is the dimensionless dust particle surface potential. The latter can be linked do the dust charge number Z_d by:

$$\varphi = \frac{Z_d e^2}{4\pi\epsilon_0 r_d k_B T_e} \tag{2.26}$$

Eqs.2.25 and 2.26 must be solved numerically.

2.2 Forces acting on dust particles

The dust particles are subjected to many forces when immersed in a plasma. In laboratory discharges, the main forces are the gravitational force, the electric force, the neutral drag force, the ion drag force and the thermophoretic force. In most laboratory cases, the radiation pressure force can be neglected.

2.2.1 The electric force

As dust particles acquire an electric charge when immersed in a plasma, they are subject to an electric force $\mathbf{F}_e$ induced by the electric field $\mathbf{E}$ that may exist in the plasma. In capacitively coupled RF discharge, due to higher mobility of electrons, electric fields are greater in the sheath region above the electrodes. A small electric field due to ambipolar diffusion of charged particles toward the wall can also exist. Generally, in a plasma, the electric force F_e acting on dust particles can be written as:

$$\mathbf{F}_e = Q_d\mathbf{E} \tag{2.27}$$

2.2.2 The neutral drag force

This force results from collisions with neutral gas atoms/molecules. It is therefore proportional to the gas pressure. It is the rate of momentum transfer between the neutral atoms/molecules and the dust particles during their collisions. Assuming that the interactions between the dust particles and the neutral gas atoms/molecules are hard sphere, elastic collisions, the neutral

drag force F_{dn} can be approximated by [99]:

$$\mathbf{F}_{dn} \simeq n_n m_n \sigma_{nd} (\mathbf{v_d} - \mathbf{v_n})^2 \tag{2.28}$$

where n_n is the density of neutral atoms/molecules, m_n their mass, σ_{nd} the cross section of the dust neutral interaction, $\mathbf{v_d}$ the average velocity of the dust particle and $\mathbf{v_n}$ the average velocity of the neutral atoms.
More accurate expressions of the neutral drag force have been developed. When the relative speed $|\mathbf{v_d} - \mathbf{v_n}|$ is very small in comparison with the neutral thermal speed $v_{Tn} << 1$ (Epstein limit), the neutral drag force $\boldsymbol{F_{dn}}$ can be approximate as [83]:

$$\boldsymbol{F_{dn}} = -\frac{8}{3}\sqrt{2\pi} r_d^2 m_n n_n v_{Tn} (1 + \alpha_{ac}\frac{\pi}{8})(\mathbf{v_d} - \mathbf{v_n}) \tag{2.29}$$

where $v_{Tn} = \sqrt{8k_B T/\pi m_n}$ is the thermal speed with T the neutral gas temperature, and α_{ac} is the accommodation coefficient. This coefficient would be zero for specular reflection and unity for perfect diffuse reflection.

2.2.3 The ion drag force

The ion drag force describes how momentum is transferred from ions to the dust particles. This force consists mainly of two components [42, 100, 101]: the force due to direct impact of ions, i.e. the collection force $\mathbf{F_{di}^{coll}}$ and the force due to electrostatic Coulomb collision $\mathbf{F_{di}^{coul}}$:

$$\mathbf{F_{di}} = \mathbf{F_{di}^{coll}} + \mathbf{F_{di}^{coul}} \tag{2.30}$$

If $v_i >> v_d$ where v_i is the ion drift velocity, the relative dust-ion velocity can thus be approximated by v_i. In the usual derivation of ion drag force [42], it is supposed that there are no interactions between the ions and the dust particle outside the Debye sphere. Moreover, it is supposed that the ion mean free path is larger than the Debye radius (valid for low gas pressure). The collection force is therefore:

$$F_{di}^{coll} = \pi n_i m_i v_i v_s b_c^2 \tag{2.31}$$

where

$$v_s = \Big(\frac{8k_B T_i}{\pi m_i} + v_i^2\Big)^{1/2} \tag{2.32}$$

is the mean velocity of the ions approaching the dust particles and

$$b_c = r_d\Big(1 - \frac{2q_i\phi_d}{m_i v_s^2}\Big)^{1/2} \tag{2.33}$$

is the maximum impact parameter given by the OML theory.
The Coulomb force is:

$$F_{di}^{coul} = 4\pi n_i m_i v_i v_s b_{\pi/2}^2 \Gamma_c \tag{2.34}$$

where

$$b_{\pi/2} = \frac{eQ_d}{4\pi\epsilon_0 m_i v_s^2} \tag{2.35}$$

is the impact parameter for 90° deflection and

$$\Gamma_c = \frac{1}{2}\ln\left(\frac{\lambda_D^2 + b_{\pi/2}^2}{b_c^2 + b_{\pi/2}^2}\right) \tag{2.36}$$

is the Coulomb logarithm integrated over the interval $[b_c, \lambda_D]$.
It has been shown experimentally that this expression for the ion drag force is a good approximation [102]. However, better expressions for the ion drag force can be found in the literature [103, 104]. In Ref.[103] , the fact that the ion-dust particle interactions can have a length range larger than the Debye length is taken into account and shows that the ion drag force is increased in comparison with the analytical results of Eqs.2.31 and 2.34. In Ref.[104], the effect of the ion-neutral collisions, the distortion of the potential around the grain, the effects of the finite size of the dust particles and the charging collisions are taken into account by combining the binary collision approach with the linear kinetic formalism. Calculations for typical RF discharge parameters have shown that the ion drag force has a complex dependance on the ion flow velocity. The dependence of the ratio of the ion drag-to-electric force on the electric field strength (or the ion flow velocity) decreases rapidly with the electric field. Thus the ion drag force can only be important for subthermal and slightly suprathermal ion flows (when the flow is due to the global electric field).

2.2.4 The gravitational force

In ground based experiments, dust particles are subjected to the gravitational force. This force is proportional to the mass of the dust particle, hence to its mass density ρ and to its volume:

$$\mathbf{F_g} = m_d\mathbf{g} = \frac{4}{3}\pi\rho r_d^3\mathbf{g} \tag{2.37}$$

This force can be neglected for very small dust particles immersed in a plasma ($r_d < 1\ \mu m$) but not for particles that are micrometer size or larger. Furthermore, this force can not be ignored in afterglow plasmas (when the discharge is switched off) whatever the size of the particles since the electrostatic and the ion drag force quickly disappear.

2.2.5 The thermophoretic force

A small dust particle suspended in a gas with a temperature gradient is subjected to a force which will induce motion of the dust particle, in the absence of gas flow, from the hot region to the cold region. This force called the thermophoretic force results from the difference in momentum transfer to the dust particle by the gas molecules colliding with it from the cold and hot side (see Fig.2.3). The expression for the thermophoretic force must be chosen carefully. Indeed, it depends strongly on the Knudsen number $Kn = l_g/r_d$ [105] where l_g is the mean free

path of buffer gas species. In our experiment, we worked at an operating pressure around 1 mbar. In a previous paper [61], the size of grown dust particles was reported between 200 nm and 800 nm. It gives, using results from Varney [106] for an atom-atom cross section, a Knudsen number of $250 < Kn < 1000$. Consequently we operate in the free molecular regime where a dust particle is similar to a very large molecule. Many theories have been developed [105, 107–111] and used [78, 105, 112] for thermophoresis in the free molecular regime. The most commonly used equation is the Waldmann equation [107] which has been verified experimentally [113, 114]:

$$\boldsymbol{F_T} = -\frac{32}{15} r_d^2 \frac{k_{tr}}{v_{Tn}} \boldsymbol{\nabla} T_n \tag{2.38}$$

where $\boldsymbol{\nabla} T_n$ is the temperature gradient in the gas, and k_{tr} is the translational part of the thermal conductivity given by, for a monoatomic gas [115]:

$$k_{tr} = \frac{15 k_B}{4 m_n} \mu_{ref} \left(\frac{T}{T_{ref}} \right)^{\nu} \tag{2.39}$$

where μ_{ref} is the reference viscosity at reference temperature $T_{ref} = 273$ K and the exponent ν results from a best fit of experimental viscosity near the reference temperature. For argon, $\mu_{ref} = 2.117 \cdot 10^{-5}$ Pa·s and $\nu = 0.81$ [115].

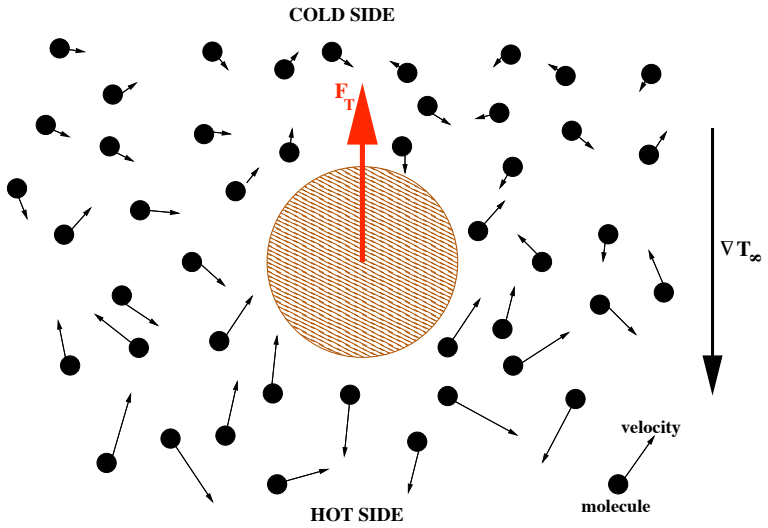

Figure 2.3: A dust particle immersed in a gas with a temperature gradient

2.2.6 Order of magnitude of the different forces

The strength of the different forces acting on the dust particles depends on different power laws of the dust particle radius. The electric force $\mathbf{F_e}$ is proportional to the radius r_d (because the charge Q_d is proportional to the dust radius (Eq.2.16)). The ion drag force, the neutral drag force and the thermophoretic force are proportional to r_d^2. The gravitational force is proportional to r_d^3. Consequently it is clear that for small particles, the electric force will be dominant while

for big particles the gravitational force will become more important.
In Ref.[5], the orders of magnitude of the different forces in a RF argon plasma, with $n = 5 \cdot 10^9$ cm^{-3}, $T_n = T_i = 500$ K, $T_e = 3$ eV, the local electric field at the sheath boundary is 30 V/cm and the gas temperature gradient is 10K/cm, have been calculated for 100 nm and 1 μm dust particles with a density ρ =2g/cm^{-3}. The results are summarised in Tab.2.1.

Table 2.1: Order of magnitude of different forces acting on dust particles for different dust radius (from Ref.[5]).

	$r_d = 100$ nm	$rd = 1$ μm
Electric force	$\sim 2 \cdot 10^{-13}$ N	$\sim 2 \cdot 10^{-12}$ N
Neutral drag force	$\sim 10^{-15}$ N	$\sim 10^{-13}$ N
Ion drag force	$\sim 5 \cdot 10^{-14}$ N	$\sim 10^{-12}$ N
Thermophoretic force	$\sim 10^{-15}$ N	$\sim 10^{-13}$ N
Gravitational force	$\sim 10^{-16}$ N	$\sim 10^{-13}$ N

2.3 Instabilities and waves in complex plasmas

2.3.1 Characteristic frequencies of complex plasmas

An important property of a plasma is its natural oscillations. When the plasma deviates from equilibrium, i.e. the neutrality condition $n_e + Z_d n_d = n_i$ is not satisfied (from a macroscopic point of view), an electric field is created due to the space charge and tends to reestablish equilibrium. Due to their different masses, charged species in the plasma do not respond equivalently.

Electron frequency

The electrons are accelerated by the electric field in order to reestablish quasi neutrality. Due to their inertia, they pass the equilibrium point and a new electric field is created in the opposite direction accelerating electrons the other way. Electrons oscillate around their equilibrium position with electron angular frequency ω_{pe}:

$$\omega_{pe}^2 = \frac{n_e e^2}{m_e \epsilon_0} \tag{2.40}$$

For an argon plasma with $n_e \simeq 10^{10}$ cm^{-3}, the angular frequency is $\omega_{pe} \simeq 6$ GHz.

Ion frequency

Ions are heavier than electrons and so their response to an electric field is much slower. The ion angular frequency ω_{pi} is:

$$\omega_{pi}^2 = \frac{n_i Z_i^2 e^2}{m_i \epsilon_0} \tag{2.41}$$

For an argon plasma with $n_i \simeq 10^{10}$ cm^{-3}, the angular frequency is $\omega_{pi} \simeq 20$ MHz.

Dust frequency

As a charged species, the dust particles also respond to electric field. The plasma dust angular frequency ω_{pd} is:

$$\omega_{pd}^2 = \frac{n_d Z_d^2 e^2}{m_d \epsilon_0} \tag{2.42}$$

For dust particles with mass $m_d \simeq 10^{-16}$ kg, $Z_d \simeq 1000$ and $n_d \simeq 2 \cdot 10^5$ cm^{-3}, the plasma dust angular frequency is $\omega_{pd} \simeq 2$ kHz.

2.3.2 Examples of waves and instabilities observed in complex plasmas

In plasmas, a wide variety of waves exists due to coherent motion of the different plasma species (Langmuir waves and ion acoustic waves for example). In complex plasmas, the charged dust grains change the wave propagation due to inhomogeneities in the dust distribution, the modified quasi-neutrality condition (Eq.2.24) and some considerations about dust particle dynamics. Two major subclasses of waves exist in a complex plasma:

1. Waves and oscillations arising from the collective motion of the plasma particles (ions or electrons) and affected by the dust particles
2. Waves and oscillations due to the collective motion of the dust particles in various dust structures (dust cloud, liquids or crystals)

Dust Acoustic (DA) waves

The DA waves come from the collective motion of the dust grains. The DA wave velocity is much smaller than the ion and electron thermal speeds and consequently ion and electron inertia can be neglected and the DA wave potential can be considered to be in equilibrium. The pressure gradient can be assumed as balanced by the electric force and thus the ion and electron distributions are Boltzmann distributions. The restoration force in the DA waves comes from the ion and electron (considered without inertia) pressure while the dust particle mass provides the wave inertial support.
DA waves have been observed in the laboratory [52, 116]. The reported frequencies are around 10-20 Hz.

Dust-ion acoustic (DIA) waves

The DIA waves come from the collective motion of the ions affected by the presence of the dust particles. For negatively charged dust particles ($n_{i0} > n_{e0}$), the DIA wave phase velocity ω/k is greater than the ion acoustic speed. It can be explained by an increase of the electron Debye length due to electron losses on dust particles. Consequently, the electric fileld $\mathbf{E} = -\nabla\Phi$ is

larger. As $kv_{Ti} \ll \omega \ll kv_{Te}$, Landau damping of DIA waves is negligible. DIA waves have been observed in the laboratory and the typical frequencies are tens of kilohertz [117, 118].

Other waves and instabilities

Other varieties of waves can be found in complex plasma (from individual oscillations of dust particles in sheaths of gas discharge to compressional waves in dust crystals) and their properties (instabilities, damping, etc.) depend on the plasma parameters (see Ref.[62] and references therein). Instabilities can also be self excited in complex plasmas. Thus, it has been reported that the growth of dust particles in a plasma can trigger some instabilities [59, 66, 119] . Instabilities of the void region (centimetre-sized region completely free of dust observed in the centre of dusty discharges) have also been reported [60]. The frequencies of these instabilities are generally in the range 0-1 kHz and can thus be associated with the dust particles.

2.4 Conclusion

In this chapter, the basis of the physics of complex plasmas has been reviewed. The charging processes of dust particles in a running discharge have been described as well as the main forces acting on the dust particles. New phenomena that may occur in a plasma due to the presence of the dust particles have been briefly discussed. This background will be used in the analysis of the results of the following chapters. In chapter 4, the effect of dust particle growth and related instabilities on the discharge and plasma parameters are related to the charging of the dust particles and the dust particle kinetics. In chapter 5, void instabilities are directly related to the dust particle kinetics. In chapter 6, residual dust charge and residual charge distribution in the afterglow plasma are studied in details and hence the dust charging process is at the centre of this research.

2.5 Résumé du chapitre en français

Dans ce chapitre, les bases de la physique des plasmas poussiéreux sont rappelées :

- *Les plasmas poussiéreux sont des gaz partiellement ionisés contenant des poudres chargées. Ces dernières se chargent aux travers des interactions avec les ions et les électrons du plasma environnant. En laboratoire, les courants directs d'ions et d'électrons à la surface des poudres sont le principal mécanisme de chargement. A l'équilibre, les courants d'ions et d'électrons se compensent exactement. Dans les plasmas de laboratoire, la température électronique étant généralement plus élevée que la température des ions, les poudres sont chargées négativement. Suivant les conditions, les collisions des ions et des électrons avec les atomes neutres peuvent modifier le potentiel électrostatique autour des poudres. En particulier, les collisions ion-atome avec échange de charge peuvent aboutir au piégage d'ions autour des poussières et accroître le courant positif d'ions et ainsi réduire la charge des poudres. Enfin, le processus de chargement des poudres est un processus stochastique se faisant par pas de $\pm e$. Par conséquent, la charge des poudres varie constamment autour de la valeur d'équilibre et la distribution de charge est une gaussienne centrée autour de la charge moyenne dont la variance dépend des courants incidents d'ions et d'électrons.*
- *Les poussières sont soumises à différentes forces dans les plasmas complexes. Les principales sont la force électrostatique, la force de friction avec les atomes neutres, la force de friction avec les ions, la gravité et la force de thermophorèse.*
- *Les poudres étant une nouvelle composante chargée du plasma, elles répondent à des perturbations dont la fréquence est bien plus faible que celles des électrons ou des ions en raison d'une masse très importante. De plus, de nouvelles ondes et instabilités peuvent être créées grâce à la présence des poussières. Ces ondes se divisent en deux sous-catégories : les mouvements collectifs des électrons ou des ions modifiés par la présence de poudres chargées, et les mouvements collectifs des poussières.*

Chapter 3

Experimental Setups

3.1 Plasma chambers

3.1.1 The PKE-Nefedov Reactor

The PKE-Nefedov experiment was one of the first scientific experiments on board the ISS. The chamber has been originally designed to study complex plasmas and plasma crystals under microgravity conditions.

Plasma Chamber and pumping system

The PKE-Nefedov reactor is a capacitively-coupled RF reactor operating in push-pull mode. It is a $10 \times 10 \times 5$ cm^3 glass vacuum chamber (Fig.3.1). The RF electrodes are stainless steel flat circular plates with 4.2 cm diameter. A grounded dust dispenser is integrated in the centre of the top electrode. The interelectrode spacing is 3 cm.
The RF source is a Dressler MPI-1 SPACE RF generator operating at 13.56 MHz which is driven by two DC power supplies: a DC power supply (ISO-TECH Dual Tracking Model IPS230300) delivering a 28 V DC voltage and 0.5 A DC current and, a DC Power Supply (AGILENT E3610A) delivering DC voltage in the range $0 - 2.40$ V. The output RF power can be varied from 0 W to 4 W . The RF generator is linked to the electrodes through an integrated matching box. It has been especially developed for low RF powers, which are required to create stable and large complex plasma structures and plasma crystals.
The pumping system consists of a turbomolecular vacuum pump (PFEIFFER, 80 L.s^{-1}) associated with a mechanical vacuum pump (ALCATEL, 8 m^3.h^{-1}). The base pressure is about $2 \cdot 10^{-6}$ mbar. The pressure is measured using two gauges: a full range gauge (Pfeiffer PKR 251) from 10^{-9} mbar up to atmospheric pressure and a capacitive gauge (MKS Baratron with PR 4000S control unit) in the range $10^{-4} - 2$ mbar.
The gas is injected into the chamber through a port at the top. When the desired pressure is reached, the valve controlling the gas flow is closed. The experiments are performed without gas flow.

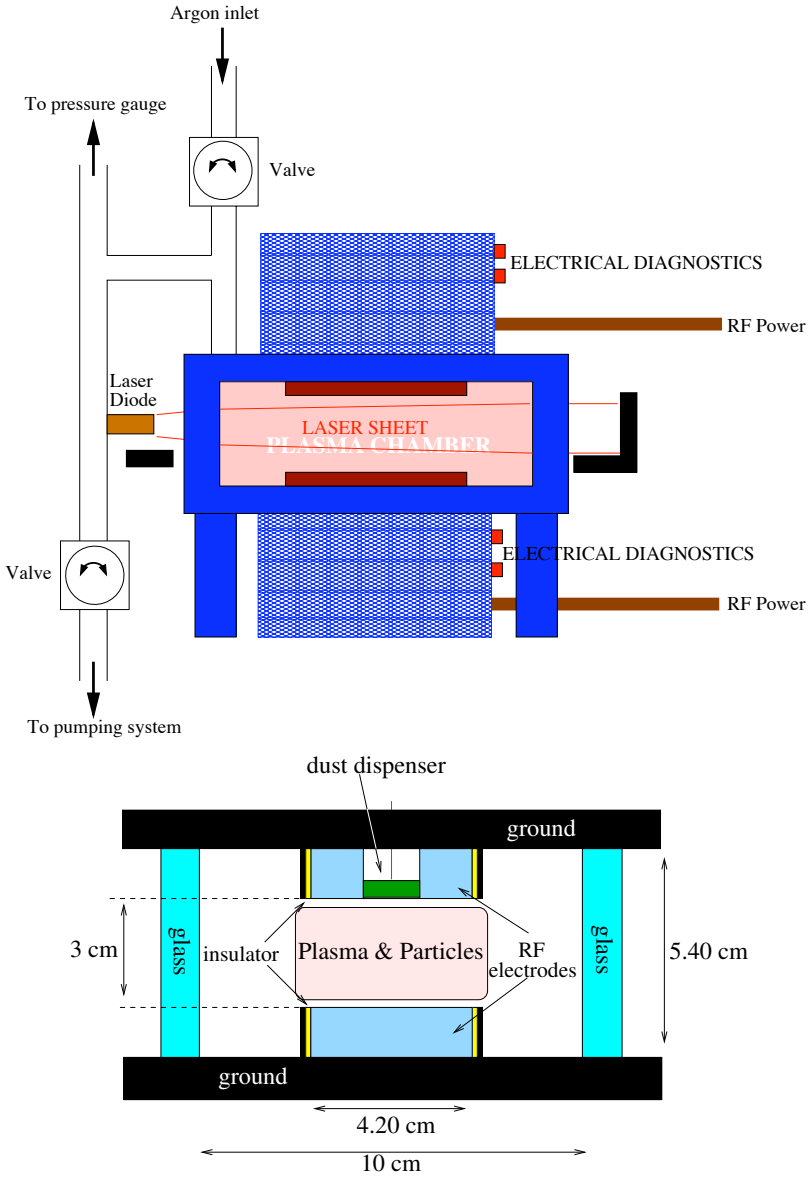

Figure 3.1: Schematic of the PKE-Nefedov reactor

The dust dispenser

In the PKE-Nefedov chamber, the dust particles can be either grown or injected directly in the plasma. Dust particle injection is achieved by means of a dust dispenser in the middle of the upper electrode. It consists of a kind of salt shaker filled with dust particles and stainless steel marbles. A grid closes the shaker. Dust particles are injected into the discharge region between the electrodes by an up and down oscillating motion of the dispenser. The particles are accelerated inside the reservoir and released through a sieve with a mesh size adapted to the particle diameter. Four sizes of dust particles can be injected in the plasma, all made of melamine formaldehyde: 3.4 μm, 1.02 μm, 500 nm and 200 nm diameter dust particles. A 10 μm step sieve was used and, several grid layers were used for the smallest dust particles.

3.1.2 The methane and silane reactor

The PKE-Nefedov reactor was developed originally to perform microgravity experiments and thus its design is very compact. Hence, it is very difficult to add in situ diagnostics. For the studies of dusty afterglow plasmas (see Chap.6), it was necessary to measure directly the electron density decay during the post-discharge phase. Spectroscopic measurement are not sufficiently sensitive during the post-discharge due to the fast decrease of the signal. Consequently, only diagnostics such as the microwave resonant cavity could be used to measure the decrease of electron density during the post-discharge phase with good time resolution. However, this diagnostic could not be adapted to the PKE-Nefedov reactor and thus two other identical RF reactors were used, where dust particles are grown using reactive gases such as methane (CH_4, carbon based particles) or silane (SiH_4, silicon based particles) which has been intensively used to study dust growth mechanism and kinetics[34–36, 119, 120]. These reactors allowed us to use in-situ diagnostics such as the microwave resonant cavity, and furthermore, as the growth mechanisms are well-known (especially for argon-silane plasma), the size and density of the dust particles could be chosen.

Experimental apparatus

The reactor is a capacitively coupled RF discharge box inside a vacuum vessel (Fig.3.2). The discharge box is a grounded stainless steel hollow cylinder. Its inner diameter is 13 cm. A 20% transparency grid with 1 mm diameter holes closes the base and allows a laminar and uniform gas flow. On the lateral surface, four 2×4 mm^2 vertical slits give optical accesses to the plasma in perpendicular directions.

The RF electrode is stainless-steel and shower head style. It provides the gas supply and constitutes the upper surface of the discharge box. The latter is a cylinder 12.8 cm in diameter and 1 cm in height closed with a grid which is similar to that of the anode. A stainless steel tube provides the RF bias and gas supply. A diffuser composed of 3 parallel grids is placed inside the RF electrode in order to provide a uniform gas supply. A ceramic sleeve surrounding the tube, isolates the RF electrode from the grounded discharge box. The interelectrode space is 3.3 cm.

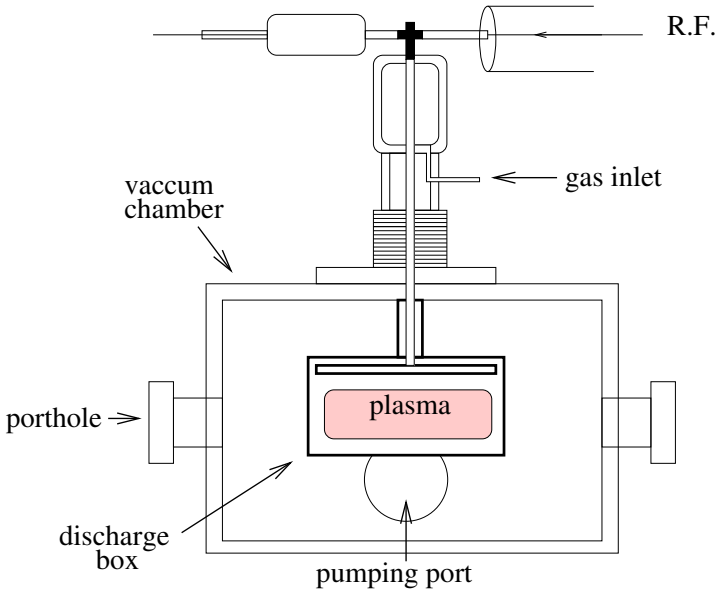

Figure 3.2: Schematic of the Methane/Nitrogen(Argon) reactor

Two pressure gauges are connected to the reactor:

- A Baratron type capacitive gauge measuring the absolute pressure in the range 10^{-4}-2 mbar independently of the gas nature. This gauge is placed near the pumping port of the chamber and allows us to monitor the operating pressure during the experiments.
- A Penning gauge measuring the base pressure down to 10^{-6} mbar.

The pumping system consists of two complementary subsystems. A chemical mechanical vacuum pump (ALCATEL 2033 CP PLUS, 35 $m^3 \cdot h^{-1}$) maintains the operating pressure during the experiments (in the range 0.1-1.5 mbar) and does the primary pump down to 10^{-3} mbar. When silane is used, a continuous flux of nitrogen (N_2) is injected in the pump in order to dilute the SiH_4 to less than 1% and avoid inflammation or explosion due to contact with ambient air. This pump can be isolated with an electric floodgate and a manual floodgate. The base pressure is achieved by a turbomolecular pump (PFEIFFER Vacuum TMH 260, 210 L/s) coupled to a mechanical vacuum pump (ALCATEL, 20 m^3/h) which can be isolated from the vacuum chamber with floodgates.
The gas is supplied by two independent lines. One for the methane (or silane), the other for the dilution gas (Ar, N_2). The gas mixing is made at the entrance of the reactor. Fluxes are controlled by mass flow controllers and measured in sccm (standard cubic centimeter per minute). For our experimental conditions, the gas flow did not exceed 10 sccm for methane or silane and 45 sccm for nitrogen or argon.
The RF excitation (13.56 MHz) is provided by a RF generator (GERAL ARF 101) with an output power varying in the range 0-100 W. This generator is controlled by a PC acquisition board furnishing a digital signal (TTL, Voltage $0 - 5$ V) and can hence be pulsed. A matching

box ensures a good coupling of the RF power between the generator and the discharge box minimizing the reflected power and optimizing the power coupled to the plasma.

3.1.3 The ComPLExS (Complex PLasma Experiment in Sydney) reactor

Plasma Chamber and pumping system

The ComPLExS reactor is a capacitively coupled RF discharge consisting of two parallel electrodes enclosed in a grounded stainless steel cylindrical vacuum vessel (30 cm diameter and 30 cm high; see Fig.3.3). The bottom electrode is powered through a matching network and the top electrode is grounded. The top electrode sits on three ceramic stands which are located at the edge of the bottom electrode. The bottom electrode is 10 cm in diameter and the top electrode is 11.5 cm in diameter. The gap between the two electrodes is 2 cm. The electrode system stands in the centre of the vacuum vessel.

The pumping system consists of two parts. The first part consists of a mechanical vacuum pump

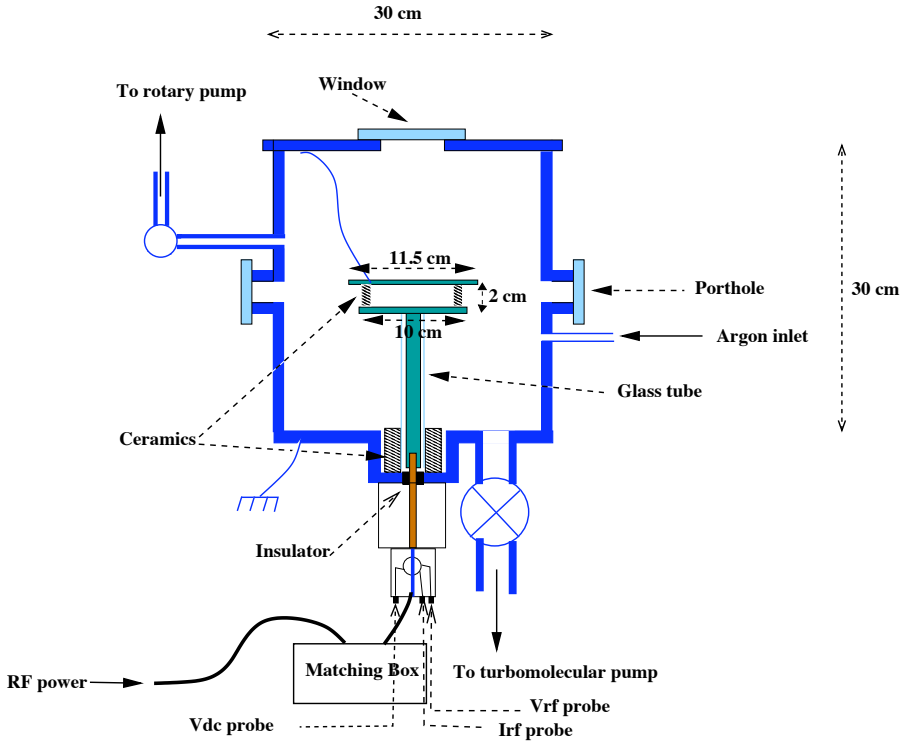

Figure 3.3: ComPLExS reactor schematic

(PFEIFFER DUO 016, 16 m^3/h) directly linked to the vacuum vessel. The pumping speed can be regulated by means of a remotely controlled electronic vacuum valve (MKS Control Valve 001-1575 and associated MKS 600 pressure controller). It maintains the operating pressure during experiments and ensures the preliminary pump down of the chamber to 10^{-3} Torr. The base pressure ($\sim 5 \cdot 10^{-6}$ Torr) is achieved by a turbomolecular pump (BALZERS TPU-510, 510 L/s) coupled with the mechanical vacuum pump. This system can be isolated from the

vacuum chamber with floodgates.
The gas supply is ensured by an independent line. The gas flux is controlled by a mass flow controller and measured in sccm. In our experimental conditions, the argon flow does not exceed 20 sccm. The pressure is monitored by two pressure gauge: a full range gauge (PFEIFFER Full range gauge) and a MKS Barathron gauge (range $10^{-4} - 2$ Torr).
The RF excitation (13.56 MHz) is provided by a RF generator (LEADER Standard signal generator 3215) coupled to an RF amplifier (EIN Model 3100L RF Power amplifier). A matching box ensured good coupling of the RF power between the generator and the discharge minimising the reflected power and optimising the power coupled to the plasma. The RF peak to peak voltage on the powered electrode can be up to V_{pp}=350 V.

3.2 Diagnostics

3.2.1 Electrical diagnostics

Self-bias voltage

When the powered electrode (the cathode) in a discharge is connected to an RF generator through a blocking capacitor (as is the case for capacitively coupled RF discharges), there is some irreversible escape of negative electric charges into the electrode, and hence the gap gas becomes positively charged [121]. In a symmetric discharge, the two electrodes operate in identical regimes and so collect the same amount of charges. Consequently, they have equal mean potentials with or without a blocking capacitor. However, for an asymmetric configuration the amount of charges collected by the electrodes is different and if the circuit does not allow direct current as is the case when there is a blocking capacitor, a different amount of charges is accumulated by each electrode and a difference of potential results between the electrodes: the self bias voltage. In a low pressure discharge, the asymmetry occurs naturally because there is always more grounded surfaces than powered surfaces. In the usual case, the self-bias voltage of the powered electrode is negative with respect to the ground and depends on a power law of the electrode area ratio [20, 122].
The cathode voltage is thus the sum of the RF voltage V_{RF} and the self-bias voltage V_{dc}:

$$V_C(t) = V_{RF}(t) + V_{dc} \tag{3.1}$$

The self bias voltage is explained as follows. During the part of the RF cycle when the cathode is positive compared to the plasma, there is an electron flux to the electrode and the capacitor is charged to a negative potential. During the other part of the RF cycle, there is an ion flux that tends to charge the capacitor to a positive potential. Because the ions are less mobile than the electrons ($m_e \ll m_i$), the electron flux will be greater than the ion flux until the average potential of the powered electrode reaches a negative value for which the ion flux balances exactly the electron flux. Then, for most of the RF cycle the powered electrode is negative with respect to the plasma and there is an ion flux to the electrode. For a small fraction of the cycle the

electrode is positive with respect to the plasma allowing sufficient electrons to flow so that there is no net charge flux to the electrode over the RF cycle.
It has been observed that the self-bias voltage changes as a result of the effect of particle growth in the discharge, and that this variation correlates with particle growth [119]. Hence, this diagnostic has been used on the three different reactors. On the PKE-Nefedov reactor and the Methane reactor, the self bias voltage signal was digitised with a numerical oscilloscope with a minimal sampling rate of 5 kS/s. Due to device limitations, the sampling rate on the ComPLExS reactor was around 25 S/s.

Amplitude of the fundamental harmonic of the RF current

The current in a RF capacitive discharge is the sum of the conduction current and the displacement current. When there is no plasma, there is only the displacement current which corresponds to the reactive current through the vacuum capacitor formed by the parallel electrodes (In reactors in which the RF electrode is surrounded by a counter-electrode, the displacement current is mainly due to the stray capacitance between the cathode and the counter-electrode because the capacitance between the two electrodes is negligible due to the large distance between them). When the discharge is turned on, the conduction current is to a first approximation proportional to the plasma density n_0 [121]. Consequently the evolution of the amplitude of the RF current can give a good idea of the evolution of the plasma density during the life of the discharge.
Moreover, in asymmetric discharges, for a sinusoidal voltage applied across the electrodes, the current waveform exhibits anharmonicity due to the different displacement current densities at the electrodes caused by the asymmetry and the non-uniformity of the sheath (the ion density decreases from the plasma towards the electrodes) [121]. Consequently, the current waveform exhibits harmonics which depend on the discharge conditions. It has been shown that the evolution of the 2^{nd} or 3^{rd} harmonics of the RF current is a good diagnostic to monitor the growth of dust particles in a RF capacitive discharge [119, 123]. In the PKE-Nefedov, previous studies have shown that the fundamental harmonic of the RF current is also sensitive to the dust particle growth [61]. Consequently, the amplitude of the fundamental harmonic of the RF current has been monitored during experiments on the PKE-Nefedov reactor. The signal was digitised with a numerical oscilloscope with a minimal sampling rate of 5 kS/s.

3.2.2 Optical and video diagnostics

These diagnostics have been used on the PKE-Nefedov reactor.

Optical fibres

Five optical fibres were focussed on a defined region of the plasma chamber using cylindrical lenses, each collecting the light emitted by the plasma (integrated over all frequencies) in a precise region of the discharge with a spatial resolution of ~ 3 mm..
The fibres were coupled to a photmultiplier tube (PMT) array which allowed us to resolve fast

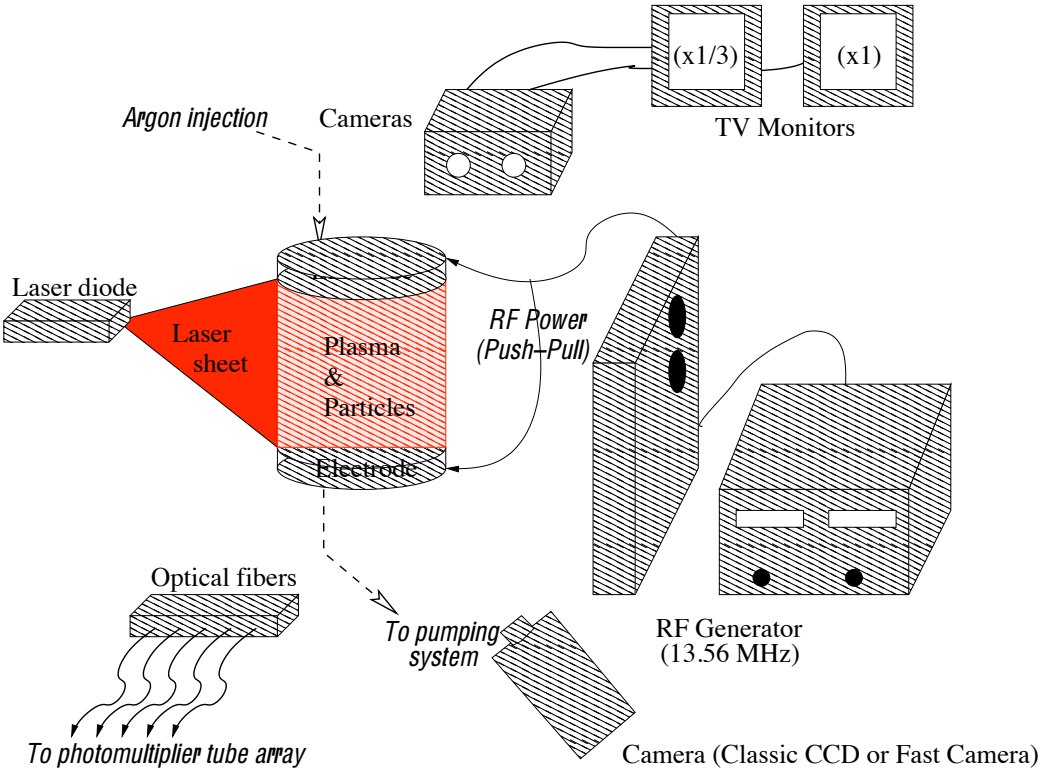

Figure 3.4: Principle schematic of optical diagnostics

variation of the collected light intensity (one photomultiplier per fibre). The signal from each PMT of the array was digitised with a digital oscilloscope with a minimal sampling rate of 5 kS/s.

CCD Cameras

A thin laser sheet perpendicular to the electrodes illuminated the dust particles. It was created by a 685 nm wavelength laser diode and a cylindrical lens. This laser sheet could be widened by adding a mirror on the other side of the reactor.
Two CCD cameras recorded the light scattered by the dust particles at right angles to the laser sheet. Interference filter were placed in front of the camera lenses in order to reduce the plasma glow light. Video signals were transferred to a computer via a frame-grabber card with 8 bit grey scale and 560×700 pixel resolution. The first camera had a field of view over 8.53×5.50 mm^2 confined to the centre of the chamber (approximately a third of the chamber) while the other one had a field of view covering a larger part of the interelectrode space.
A third camera (SONY DXC-1850P Colour) recorded the scattered light at a small angle ($\sim 30°$) from the laser sheet. It allowed observations of the dust particles at an early stage of growth because scattering is more efficient in the forward direction for small particles. An interference filter was placed in front of the camera lens in order to reduce the light emitted by the plasma.

Fast Camera

Fast CCD cameras (Mikrotron MC 1310 and SciTech SpeedCAM MiniVis ECO-1) were used to record the plasma glow light or the scattered laser light. In order to record the laser scattered light, the camera was placed at the position of the SONY camera. An interference filter was placed in front of the lens when only the dust cloud motion was recorded. The plasma glow light could also be recorded from this position by removing the filter. When the laser sheet was turned on, it was possible to resolve the plasma glow and the dust particle cloud at the same time.

3.2.3 Laser extinction measurement

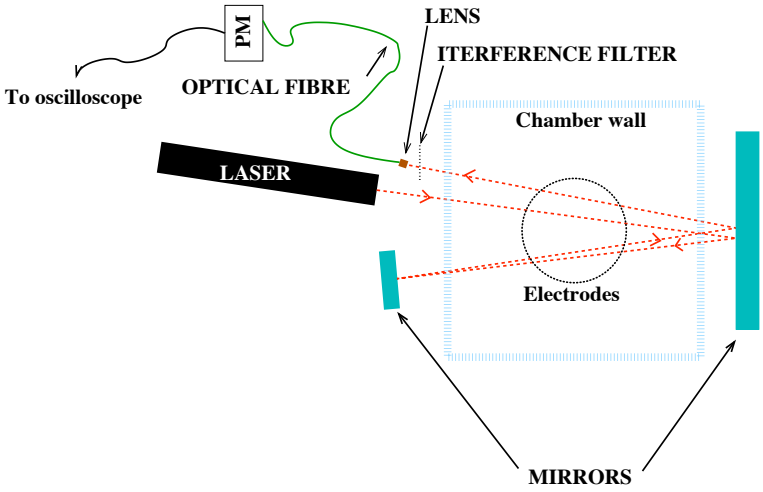

Figure 3.5: Laser extinction measurement schematic

When a laser beam travels through a dust cloud, the incident light intensity is attenuated. The corresponding extinction parameter C_{ext} is defined by the relation:

$$\frac{\mathrm{d}}{\mathrm{d}x} I_t(x) = -C_{ext} n_d(x) I(x) \tag{3.2}$$

where $I_t(x)$ is the intensity of the incoming laser beam and $n_d(x)$ is the local concentration of dust particles. The extinction parameter is linked to absorption and scattering phenomena:

$$C_{ext} = C_{abs} + C_{sca} \tag{3.3}$$

The intensity at a given point x in the particle cloud can be obtained by integrating Eq.3.2:

$$I_t(x) = I_t(x_0) \exp\Big[- \int_{x_0}^{x} n_d(x) C_{ext}(x) \mathrm{d}x \Big] \tag{3.4}$$

where x_0 is the entrance edge of the dust particle cloud. If the cloud is homogeneous in term of extinction coefficient, the intensity of the light passing through the dust particle cloud is related

to the number of dust particles N_d along the light path:

$$I_t(l) = I_{t0} \exp(-N_d C_{ext}) \tag{3.5}$$

where l is the path length through the dust cloud. If the dust particle density is homogeneous, the attenuation will give useful information about the dust particle density along the light path as long as the extinction coefficient is known.
The extinction parameter is a function of the properties of dust particles (size, material, etc.). For spherical particles, this coefficient is independent of the light polarisation. When the radius of the dust particles is much smaller than the radiation wavelength ($r_d \ll \lambda_{rad}$), the absorption and scattering coefficient are within the Rayleigh approximation:

$$C_{sca} = \frac{128\pi^5}{3\lambda_{rad}^4} \left| \frac{m^2-1}{m^2+2} \right| r_d^6 \tag{3.6}$$

$$C_{abs} = \frac{8\pi^2}{\lambda_{rad}} \mathrm{Im}\left(\frac{m^2-1}{m^2+2} \right) r_d^3 \tag{3.7}$$

where m is the complex refractive index which depends on the properties of the dust particles (material, structure, etc.).
Laser light extinction measurements have been performed in the PKE-Nefedov reactor with an HeNe laser ($\lambda_{rad} = 632.8$ nm). The laser light passed through the dust particles cloud four times to improve the extinction signal. A schematic of the experiment is presented in Fig.3.5.

3.2.4 Emission spectroscopy

Optical spectroscopy of plasma emission has been used in many experiments to deduce important parameters of the plasma such as the electron temperature and the electron density (see for example [124, 125]). The main advantage of plasma emission spectroscopy is that it is a non-intrusive method. However, in order to extract the electron temperature and/or density in the plasma, the kinetic processes that populate and depopulate the excited states of the species in the plasma need to be carefully analysed.
In order to monitor the evolution of the electron temperature in the RF argon plasma of the ComPLExS reactor, the intensity of several argon lines have been measured. Then using a simplified steady-state collisional radiative model, referred to as corona equilibrium, the electron temperature is deduced.
In the following section, the experimental setup will be described. Then, the corona equilibrium model is described and the results that can be obtained from it are discussed.

Experimental setup

The simultaneous measurement of the intensity of argon lines while the discharge is running has been done using two monochromators coupled to photomultiplier tubes (Newport Oriel 77348 and PR-1400RF 9902B/1034/1034; see Fig.3.6). The light coming from the centre of the

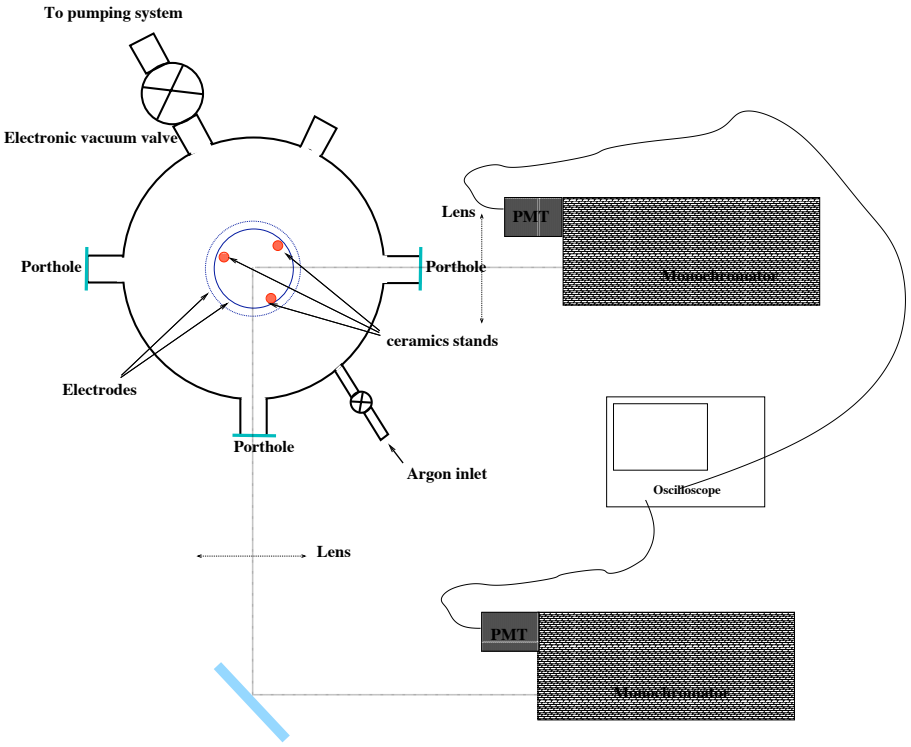

Figure 3.6: Emission spectroscopy measurement schematic

discharge was focused on the monochromator using converging lenses. Slits of defined width were used in front of monochromator's aperture. The intensities of three argon lines were measured: 750.38 nm, 415.86 nm and 518.77 nm. The slit width was 300 μm for the first line and 130 μm for the two other lines[1]. The optical systems have been calibrated using a tungsten ribbon lamp in order to be able to compare the relative intensities of the different lines.

Estimation of T_e: corona equilibrium

If the electron density is sufficiently low, the balance between excitation from the ground state by electron collisions and radiative de-excitation determines the population of excited states of atoms and ions of the plasma. Using this simplified model (steady-state collisional radiative referred to as corona equilibrium[2].), the density of excited state n_k is given by [124]:

$$n_e n_1 k_{1k} = n_k \sum_{j>k} A_{kj} \tag{3.8}$$

where n_1 is the ground state density, k_{1k} is the electron impact excitation rate coefficient from the ground state (level 1) to level k, and A_{kj} is the transition probability for the radiative transition

[1]The slit was wider for the measurement of the intensity of the 750.38 nm line due to the lower sensitivity of the PMTs at this wavelength.

[2]For levels of interest corona equilibrium requires $n_e << 10^{11}$ cm^{-3} [126]. In our experiments, $n_e \sim 10^8 - 10^9$ cm^{-3}

$k \rightarrow j$ where $j < k$. The power radiated per unit of volume for the radiative transition from level k to a lower level j is:

$$I_{kj} = h\nu_{kj} A_{kj} n_k \tag{3.9}$$

where $h\nu_{kj}$ is the energy gap between levels k and j with h the Planck constant and ν_{kj} the frequency of the radiation. The substitution of n_k using Eq.3.8 gives:

$$I_{kj} = h\nu_{kj} A_{kj} \frac{n_e n_1 k_{1k}}{\sum_{j>k} A_{kj}} \tag{3.10}$$

An analytic approximation commonly used for k_{1k} (when the free electron EEDF is assumed Maxwellian) is [124, 127]:

$$k_{1k} = 8.69 \times 10^{-8} \times \alpha_{1k} \times Z_{eff}^{-3} f_{1k} \times \frac{u_a^{3/2}}{u_{1k}} \times \psi_a(u_{1k}, \beta_{1k}) \text{ cm}^3\text{s}^{-1} \tag{3.11}$$

where $u_a = 13.6 k_B T_e$, $u_{1k} = (E_1 - E_k)/k_B T_e$ with E_1 the energy of the ground level and E_k the energy of the k level, α_{1k} is a constant with a value approximately equal to 1, $Z_{eff} = Z - N + 1$, where Z is the atomic number and N is the number of bounded electrons, is the effective atomic number and f_{1k} is the absorption oscillator strength of the transition from the ground state 1 to excited state k. The function $\psi_a(u_{1k}, \beta_{1k})$ is given by:

$$\psi_a(u_{1k}, \beta_{1k}) = \frac{\exp(-u_{1k})}{1 + u_{1k}} \times \left[\frac{1}{20 + u_{1k}} + \ln\left(1.25 \times \left(1 + \frac{1}{u_{1k}} \right) \right) \right] \tag{3.12}$$

where $\beta_{1k} \cong 1$.
Grouping together all the constants (as we are only interested in dependence on T_e):

$$k_{1k} \propto \frac{u_a^{3/2}}{u_{1k}} \times \frac{\exp(-u_{1k})}{1 + u_{1k}} \times \left[\frac{1}{20 + u_{1k}} + \ln\left(1.25 \times \left(1 + \frac{1}{u_{1k}} \right) \right) \right] \tag{3.13}$$

This function will differ for each excited state owing to the dependence via u_{1k} on the excited state energy E_k. Using Eqs.3.10, it is possible to deduce the electron temperature from argon line ratio $I_{k_2 j_2}/I_{k_1 j_1}$. Indeed, the ratio depends only on the electron temperature T_e:

$$\frac{I_{k_2 j_2}}{I_{k_1 j_1}} = \frac{\lambda_{k_1 j_1} A_{k_2 j_2} \sum_{k_1 > j_1} A_{k_1 j_1}}{\lambda_{k_2 j_2} A_{k_1 j_1} \sum_{k_2 > j_2} A_{k_2 j_2}} \cdot \frac{k_{1k_2}(T_e)}{k_{1k_1}(T_e)} \tag{3.14}$$

where λ_{ij} is the wavelength of the radiative transition. The spectroscopic data for the selected argon lines used in this thesis are presented in Tab.3.1. The dependence of the different line ratios[3] and the intensity of the selected lines compared to the intensity at a reference electron temperature $T_{e_{ref}} = 3$ eV and constant electron density n_e are presented in Fig.3.7. As can be

[3]It should be noted that the computed value of the ratio is not the absolute ratio as we do not take into account the value of some constants such as the absorption oscillator strength in our calculation of electron impact excitation rate coefficient as we only want the dependence on T_e.

λ_{kj} (nm)	E_j (eV)	E_k (eV)	configurations	A_{kj} ($10^8 s^{-1}$)	$\sum_{k>j} A_{kj}$ ($10^8 s^{-1}$)	g_k	Number of radiative transitions
415.86	11.54	14.52	$3s^2 3p^5(^2P^\circ_{3/2})4s - 3s^2 3p^5(^2P^\circ_{3/2})5p$	0.014	0.017	5	3
518.77	12.91	15.30	$3s^2 3p^5(^2P^\circ_{3/2})4p - 3s^2 3p^5(^2P^\circ_{1/2})5d$	0.014	0.035	5	6
750.38	11.83	13.48	$3s^2 3p^5(^2P^\circ_{1/2})4s - 3s^2 3p^5(^2P^\circ_{1/2})4p$	0.445	0.448	1	2

Table 3.1: Spectroscopic data and number of radiative transitions from the k^{the} level corresponding to the selected Ar lines emitted by the plasma

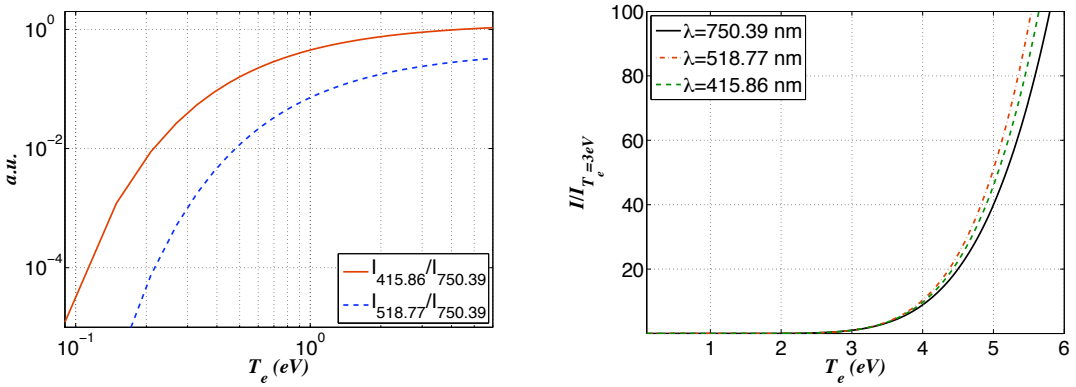

(a) (b)

Figure 3.7: a) Line intensity ratio as a function of T_e. b) Evolution of line relative intensity as a function of T_e

seen, when the electron temperature increases, the considered line ratios are increasing. Also note that the intensity of each line increases when the electron temperature increases.

3.2.5 Electron density measurement by microwave resonant cavity

This diagnostic was used on the methane and silane reactors.

Theory

The propagation of an electromagnetic (EM) wave through a dielectric medium is governed by the dielectric constant of this medium which is related to the density of free charges interacting with the EM fields. In the microwave frequency range, only electrons are able to follow the fast variations of the EM fields.

The microwave resonant cavity method is based on the theory of standing waves in cavities and has been used for a long time for various discharges [128–131] and especially in dusty plasmas [5, 132]. This method requires a metal box which serves simultaneously as reactor electrodes and microwave cavity. When a highly symmetric configuration is chosen for experiments (i.e. cylindrical or rectangular cavity), well-known EM modes can be excited (otherwise, the EM field space shape has to be determined experimentally).

In a cylindrically symmetric cavity, the electric field vector $\overrightarrow{E}(\overrightarrow{x},t)$ can be written as:

$$\overrightarrow{E}(\overrightarrow{x},t) = \overrightarrow{E}_0(x,y)\exp(\pm\imath kz - \imath\Omega t) \tag{3.15}$$

where both k and $\overrightarrow{E}_0(x,y)$ are determined by the cavity geometry. Generally, Ω is complex, thus the imaginary part of $\imath\Omega t$ represents the oscillations and the real part of $\imath\Omega t$ represents the

damping of the mode. The dispersion relation is:

$$\Omega^2 = k^2 \frac{c^2}{n^2} = k^2 \frac{c^2}{\mu_r \epsilon_r} \tag{3.16}$$

where c is the vacuum light velocity and n is the cavity medium refraction index. The relative permeability of the medium μ_r is taken as $\mu_r = 1$. The dielectric constant ϵ_r of the cavity containing the plasma is EM field oscillation frequency dependant and is given by [5]:

$$\epsilon_r = 1 + \imath \frac{1}{Q_0} + \imath \frac{\omega_{pe}^2}{\omega(\nu_e - \imath\omega)} = 1 + \imath \frac{1}{Q_0} - \frac{\omega_{pe}^2}{\omega^2 + \nu_e^2} + \imath \frac{\omega_{pe}^2}{\omega^2 + \nu_e^2} \frac{\nu_e}{\omega} \tag{3.17}$$

where ω is the excitation frequency, ω_{pe} the electron plasma angular frequency and ν_e the electron collision frequency. The second term $\imath/Q_0$ accounts for the non-ideality of the cavity (finite conductivity of the walls, etc.). The third and fourth terms appear in the presence of the discharge. The third term represents the frequency shift of the plasma compared to the resonance frequency of the empty box and the fourth term represents the losses due to electron collisions with other particles. It is obvious that the cavity method can be used as a diagnostic since the electron frequency ω_{pe} is directly related to the electron density n_e (see Chap. 2.3.1). If it is assumed that the deviations of ϵ_r from an ideal case are small (i.e. $Q_0 \gg 1$, $\omega_{pe}/(\omega^2 + \nu_e^2)^{1/2} \ll 1$, etc.), Eq.3.17 can be substituted in the dispersion relation (Eq.3.16) and the result can be linearised yielding for Ω the following:

$$\Omega = \omega_0 + \Delta\omega - \imath \frac{\omega_0}{2Q} \tag{3.18}$$

where ω_0 is the resonance frequency without the plasma and $\Delta\omega$ is the frequency shift caused by the plasma. This frequency shift is:

$$\Delta\omega = \frac{1}{2} \omega_0 \frac{\omega_{pe}^2}{\omega^2 + \nu_e^2} \tag{3.19}$$

Q is a quality factor of the cavity that accounts for the total dissipation:

$$\frac{1}{Q} = \frac{1}{Q_0} + \frac{\omega_{pe}^2}{\omega^2 + \nu_e^2} \frac{\nu}{\omega_0} \tag{3.20}$$

All experiments performed in this thesis were done at low pressure ($P \lesssim 1\ mbar$). The electron collisions are mainly with the neutrals and the electron collision frequency $\nu_e \simeq \nu_{en}$ between electrons and neutrals is $\nu_{en} = n_n v_{Te} \sigma_{en} \simeq 800$ MHz where $\sigma_{en} \simeq 5 \cdot 10^{-20}$ m^2 is the electron-neutral collision cross section. As we operated with microwave frequencies around $f = \omega/2\pi \simeq$ 2700 MHz, the collision frequency ν can be neglected and using Eq.3.19, we obtain:

$$n_e^0 = \frac{2 m_e \epsilon_0 \omega^2 \Delta\omega}{e^2 \omega_0} \tag{3.21}$$

where n_e^0 is the electric field average electron density. Indeed, electrons in the plasma are generally not homogeneously distributed over the cavity and have a certain spatial profile $n_e(\overrightarrow{x})$ giving:

$$n_e^0 = \frac{\int_{cavity} n_e(\overrightarrow{x}) E^2(\overrightarrow{x}) d(\overrightarrow{x})}{\int_{cavity} E^2(\overrightarrow{x}) d(\overrightarrow{x})} \tag{3.22}$$

If the spatial distribution of the electrons is needed, other diagnostics have to be used. However, the density n_e^0 obtained with Eq.3.21 has to be multiplied by a corrective factor A, accounting for the spatial variation of the microwave field, which depends on the discharge geometry and conditions. In dusty plasmas, the electron density is greatly influenced by the dust particles. Hence, the corrective factor evolves with time. This factor is always close to unity [133] and for this reason is taken as 1 in all our calculations .

Experimental procedure

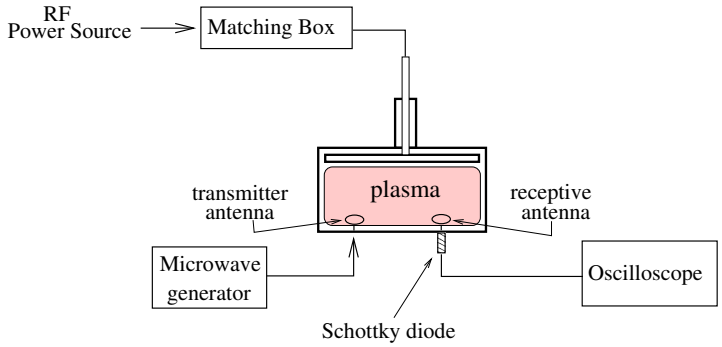

Figure 3.8: Principle schematic of microwave resonant cavity technique

Two antennas are fixed in the plasma box. One is powered by a microwave generator (Rhode & Scharz signal generator with a 100 kHz-4320 MHz bandwidth) and the other is the receptor. This last antenna is linked to a Schottky diode (Agilent Technologies) which converted the amplitude of the microwave signal into a voltage measurable by an oscilloscope (Fig.3.8). By scanning the plasma with frequency around the TM110 mode resonant frequency (2723 MHz in the methane chamber), it is possible to reconstruct the resonance curve and to deduce the resonance frequency and thus the electron density.
In order to be able to reconstruct a resonance curve, many experiments with the same parameters were done with a different frequency applied to the emissive antenna by the microwave generator for each plasma run. The repeatability of the experiments was checked by following the evolution of the self bias voltage of the powered electrode. As the temporal resolution of the cavity is about $\sim$ 100 ns, the output voltage was measured every 500 ns. Resonance curves can then be reconstructed for both running discharge (Fig.3.9) and the plasma afterglow.

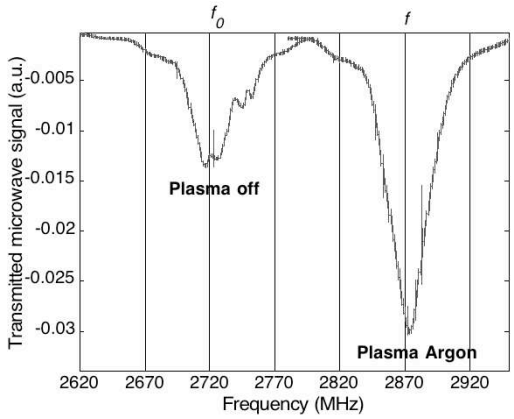

Figure 3.9: Resonance curves of the microwave cavity with or without plasma

3.2.6 Langmuir probe measurement

When a metal probe is inserted into a plasma, it will collect ion and electron currents. Depending on the voltage applied on the probe tip, the drag current will be different as the ions and electrons need to overcome different potential barriers. These probes, called Langmuir probes, have been extensively studied by Mott-Smith and Langmuir [134].
For an applied probe potential equal to the floating potential V_f, there is no net current on the probe as the electron and ion fluxes balance each other. For potentials below the floating potential, the probe collects more ions than electrons and thus the current is, by convention, negative and when the probe potential is highly negative all ions are able to reach the probe surface and the current saturates to the ion saturation current. For probe potential above the floating potential, the probe collects more electrons than ions and the current is, by convention, positive. When the probe potential reaches the plasma potential V_p, ions and electrons are collected with fluxes unaffected by the probe potential. By increasing the probe voltage beyond V_p, all electrons are able to reach the probe and the current saturates to the electron saturation current I_{esat}. Due to a higher mobility of the electrons, the electron current is much larger than the absolute value of the ion saturation current I_{isat}. A typical current-voltage (I-V) characteristic of a Langmuir probe is drawn in Fig.3.10.

Experimental procedure

In order to determine the evolution of the electron temperature of the plasma in the ComPLExS reactor, Langmuir probe measurements were carried out. The Langmuir probe was a HIDEN ESPion RF compensated probe with a 10 mm tungsten cylindrical tip with a diameter of 0.15 mm. The tip of the probe was placed near the edge of the electrodes (about 1 cm inside the interelectrode volume) in the middle of the gap in between the electrodes (Fig.3.11). This configuration was chosen in order to prevent large disturbances of the discharge due to the presence of the probe (such as modifications of the self bias voltage behaviour or arcing to the

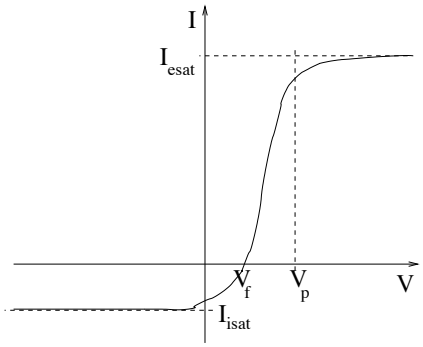

Figure 3.10: Typical I-V characteristic of a Langmuir probe

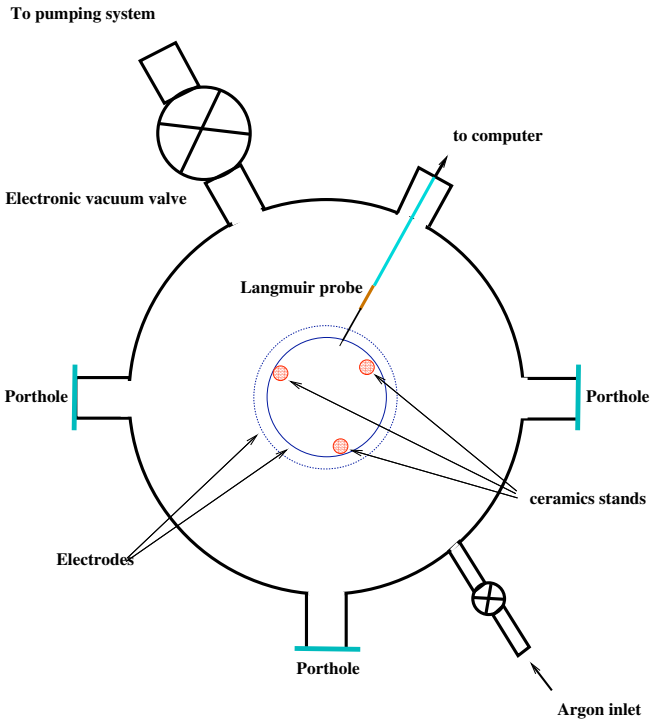

Figure 3.11: Langmuir probe measurement schematic

probe tip).

First estimation

The first estimation that can be made from the probe measurement is the floating potential with respect to the plasma potential and thus the electron temperature. Indeed it is known that a potential drop across the presheath region is necessary to accelerate the ions to the Bohm velocity. This potential drop is [20]:

$$V_p - V_s = \frac{k_B T_e}{2e} \tag{3.23}$$

where V_p is the plasma potential and V_s is the potential at the sheath-presheath edge. The potential drop within the sheath between a plasma and a floating wall can be determined by equating the electron flux and the ion flux at the wall. One can obtain [20]:

$$V_f - V_s = -\frac{k_B T_e}{e} \ln\left(\frac{m_i}{2\pi m_e}\right) \tag{3.24}$$

where V_f is the floating wall potential. Combining Eqs. 3.23 and 3.24, the relation between the electron temperature T_e and the floating potential can be found:

$$V_f - V_p \simeq -\frac{k_B T_e}{2e} \ln\left(\frac{m_i}{2.31 \cdot m_e}\right) \tag{3.25}$$

This method gives a first approximation of the electron temperature. However, it is not always easy to obtain the plasma potential directly from the shape of the probe characteristic.

The EEDF procedure

When the gas pressure is around $P = 1$ Torr, it has been shown that the electron energy distribution function (EEDF) is not Maxwellian [135]. It is still possible to determine the electron temperature using the second derivative of the probe current. Indeed, for non-maxwellian electrons, the electron current is [20]:

$$I_e = eA \int_{-\infty}^{\infty} dv_x \int_{-\infty}^{\infty} dv_y \int_{v_{min}}^{\infty} dv_z v_z f_e(\mathbf{v}) \tag{3.26}$$

where A is the probe area, $f_e(\mathbf{v})$ is the electron velocity distribution function and:

$$v_{min} = \left(\frac{2e(V_p - V)}{m_e}\right)^{1/2} \tag{3.27}$$

where V is the probe voltage. Consequently the second derivative is [20]:

$$\frac{d^2 I_e}{dV^2} = \frac{2\pi e^3}{m^2} A f_e[v(V)] \tag{3.28}$$

The EEDF is:

$$g_e(\epsilon)d\epsilon = 4\pi v^2 f_e(v)dv \tag{3.29}$$

where ϵ is the electron energy. Thus using Eqs.3.28 and 3.29, the EEDF can be derived from the probe current second derivative:

$$g_e(V) = \frac{2m_e}{e^2 A}\Big(\frac{2eV}{m_e}\Big)^{1/2}\frac{d^2 I_e}{dV^2} \tag{3.30}$$

Integrating the EEDF, the electron density n_e can be found:

$$n_e = \int_0^\infty g_e(\epsilon)d\epsilon \tag{3.31}$$

as well as an effective electron temperature:

$$T_{eff} = \frac{2}{3n_e}\int_0^\infty \epsilon g_e(\epsilon)d\epsilon \tag{3.32}$$

This method is often used to study non-Maxwellian plasmas as it enables n_e and T_e to be obtained without an assumption about the EEDF.

The Langmuir procedure

It is not always possible to derive properly the second derivative of the probe signal. Indeed, the probe signal can be noisy and the noise is amplified by the differentiation procedure which leads to non-usable second derivative characteristics.
It is known that for an ideal Maxwellian plasma, the electron temperature can be deduced directly from the electron part of the probe voltage-current characteristic. Indeed, for Maxwellian plasmas, the logarithm of the electron probe current is [20]:

$$\ln\Big(\frac{I_e}{I_{esat}}\Big) = \frac{e\cdot(V-V_p)}{k_B T_e} \tag{3.33}$$

In laboratory RF plasmas, the plasma is rarely Maxwellian and the EEDF varies with the pressure from bi-Maxwellian at low pressure to Druyvesteyn-like for pressures around 1 Torr [135] which was the pressure region of our experiments. It is nevertheless possible to obtain a good approximation of the electron temperature and electron density using the Langmuir procedure. Using the semilog plot of the probe characteristic, one can extract two linear parts of the function $ln(I_e(V))$ where I_e is the electron current. The first one near the floating potential (zero current crossing of the probe characteristic) and one for the highest voltage applied. By extrapolating those two lines, the crossing occurs at the plasma potential V_p and the slope of the first one gives a good approximation of the electron temperature. The plasma density is then obtained from the Langmuir formula [135]:

$$I(V_p) = eAn_e\Big(\frac{k_b T_e}{2\pi m_e}\Big)^{1/2} \tag{3.34}$$

It has been shown that the results given by the Langmuir procedure on Druyvesteyn-like plasmas underestimate the effective electron temperature by about 60 % and the plasma density is overestimated by approximatively 55 % [135]. The order of magnitude are however in good agreement and the Langmuir procedure may be used to obtain the relative changes in parameters.

Using the ion part of the I-V probe characteristic

The ion part of the Langmuir probe characteristic is commonly used in plasma diagnostics.
For example, the calculation of the plasma density from the ion current can be done in various way. The OML approach is the most popular one as it does not require the knowledge of the electron temperature and plasma potential, and in many experiments, the square of the ion current I_i^2 is found to be a linear function of the probe voltage as is expected by the theory. However, the ion-ion and ion-atom collisions as well as the finite length of the probe affect the orbital motion of the ions and tend to destroy it. The ion current under such conditions is due to radial motion rather than orbital motion. The OML theory is already not valid for very low pressure ($P \gtrsim 0.02$ Torr). Radial motion theory of Allen, Boyd and Reynolds (ABR) can be also used to determine the plasma density but are difficult to use as it requires the knowledge of the probe sheath voltage and an inference on the plasma density must done from the ion current and the floating potential which requires a heavy iteration procedure. Consequently, this method is mostly used in a confirmatory mode rather than a predictive mode. For pressure around 1 Torr, the OML theory tends to overestimate the ion density while the ABR theory tends to underestimate it (see Ref.[135] and references therein for more details).
In our experiments, the ion density was deduced from the ion part of the probe current using the software furnished by HIDEN analytical which enables analysis using both the OML and ABR theory.

3.2.7 Electron microscopy analysis

The direct observation of the dust particles is, when possible, the best way to obtain their size and shape. Hence, dust particles grown in the Methane and ComPLExS RF discharges have been collected and analysed ex-situ by electron microscopy. The dust particles grown in the methane reactor have been analysed using both scanning electron microscopy (SEM) and transmission electron microscopy (TEM) while the dust particle grown in the ComPLExS reactor have been analysed using only SEM.

Scanning electron microscopy

For SEM, the sample is scanned with a high energy electron beam (several keV). The electrons interact with the atoms of the sample that produce signals containing information about the surface topography, composition, electrical conductivity, etc. The most common technique for imaging with SEM is the collection of secondary electrons emitted by the sample. Because the mean free path of these electrons through matter is very short, only those emitted close to the

surface of the sample can be collected and thus, high resolution images of the sample surface can be reconstructed (down to 1 nm).

Transmission electron microscopy

For TEM, a beam of electrons focused with electromagnetic lenses is transmitted through an ultrathin specimen and interacts with it. Depending on the density of the material, some electrons are scattered and disappear from the beam. The unscattered electrons hit a fluorescent screen at the bottom of the microscope. A"shadow" image of the specimen is created with the darkness of its different parts related to the opacity of the corresponding regions in the specimen. The most used methods to display the image of the sample are the "dark field mode" and the "bright filed mode". For the dark field mode, the image is creating from a diffracted electron beam. It is particularly useful for studying the crystalline structure of the sample as, depending on the crystal orientation, the electrons pass through the sample in a straight line and one obtain a bright contrast or are deviated and one obtains a dark contrast. For the bright field mode, the screen is placed in the image plane and only the unscattered transmitted electrons are collected. A magnified image of the sample is then observed.

3.3 Conclusion

In this chapter, the different plasma reactors used for this thesis were described. The PKE-Nefedov reactor was used for the studies of all the different phases of a RF discharge life. The Methane reactor was used as a reference for stutying dust particle growth and for the studies of the electron density decay in afterglow plasmas due to the limitation of the PKE-Nefedov chamber. The ComPLExS reactor was used to investigate the dust particle growth by RF sputtering and its effect to the discharge and plasma parameters. The ComPLExS results were then compared to the PKE-Nefedov results to extract essential features of the influence of dust growth by RF sputtering.
The wide range of diagnostics presented in this chapter were used in order to correlate as far as possible the different data and extract important physical information.

3.4 Résumé du chapitre en français

Dans ce chapitre, les différents dispositifs expérimentaux utilisés durant cette thèse sont présentés.

- *Le premier réacteur présenté est le réacteur PKE-Nefedov (Fig.3.1). C'est une décharge RF capacitive développée pour des expériences en microgravité. La chambre à vide est un parallélépipède de verre de 10×10×5 cm^3 de volume. Les électrodes sont des disques d'acier inoxydable de 4.2 cm de diamètre polarisées en mode "push-pull". L'espace interélectrode est de 3 cm. La pression d'argon de travail est entre 0.1 et 2 mbar et la puissance maximale injectée dans le plasma est de 4 W. Ce réacteur a été utilisé pour tous les thèmes abordés dans cette thèse.*
- *Le second réacteur est le réacteur à dilution de méthane. C'est une boîte à décharge en acier inoxydable enfermée dans une chambre à vide (Fig.3.2). La boîte à décharge est un cylindre creux de 13 cm de diamètre intérieur relié à la masse (l'anode). Le base est fermée par une grille percée de trous de 1 mm de diamètre et ayant une transparence de 20 % afin de travailler avec un écoulement de gaz laminaire et uniforme. L'électrode RF est en forme de pomme de douche en acier inoxydable qui vient fermer le haut de la boîte à décharge. Elle a un diamètre de 12.8 cm et une épaisseur de 1 cm et est fermée par une grille similaire à celle de l'anode. Un tube en acier inoxydable assure l'alimentation RF et l'injection du gaz. La puissance varie entre 0 W et 100 W. Les gaz sont injectés par deux lignes indépendantes : une pour l'argon (ou l'azote) avec un flux maximum de 45 sccm, et une pour le methane (ou le silane) avec un flux maximum de 10 sccm. La pression de travail varie entre 0.1 mbar et 1.5 mbar. Ce réacteur a été utilisé pour les recherches concernant la croissance de poudres et celles concernant la décroissance de la densité électronique durant la phase post-décharge.*
- *Le troisième et dernier réacteur est le réacteur ComPLExS (Fig.3.3). Il est constitué de deux electrodes parallèles enfermés dans une chambre a vide cylindrique en acier inoxydable reliée à la masse de 30 cm de diamètre et de 30 cm de hauteur. L'electrode inférieure est polarisée à la RF. Elle est en aluminium et a un diamètre de 10 cm. L'électrode supérieure est un disque en aluminium de 11.5 cm de diamètre relié à la masse et posé sur 3 plots de céramique. L'espace interélectrode est de 2 cm. La pression de travail varie entre 0.1 Torr et 2 Torr. L'argon est injecté avec un flux maximum de 20 sccm. Le tension RF crête à crête peut atteindre 350 V. Ce réacteur a été utilisé pour étudier la croissance de poudres par pulvérisation.*

Différents diagnostics ont été utilisés pour analyser les différents paramètres des décharges, des plasmas et des poudres :

- *Diagnostics électriques : tension d'autopolarisation (PKE-Nefedov, réacteur méthane, ComPLExS) et amplitude de l'harmonique fondamental du courant RF (PKE-Nefedov).*
- *Diagnostics optiques (PKE-Nefedov) : imagerie video (classique et rapide), luminosité du plasma.*
- *Spectroscopie d'émission (ComPLExS).*
- *Cavité résonnante à microondes (réacteur méthane).*
- *Sonde de Langmuir (ComPLExS).*
- *Analyse par microscopie électronique (réacteur méthane et ComPLExS).*

La corrélation entre les résultats obtenus grâce ces différents diagnostics est utilisée pour extraire un maximum d'informations sur les processus physiques mis en jeu.

Chapter 4

Dust particle growth and related instabilities in argon RF discharges

In the laboratory, dense clouds of submicron particles light enough to fill the gap between the electrodes can be obtained using reactive gases such as silane [34, 119] or using a target sputtered with the ions coming from the plasma [59–61, 73, 74]. During the dust particle growth, plasma instabilities sometimes occur.
In the first part of this chapter, the growth of dust particles in sputtering discharges is discussed and the modification of the plasma parameters due to the presence of the growing dust particles is discussed. In the second part of this chapter, instabilities occuring during dust particle growth are investigated experimentally.

4.1 Dust particle growth in plasmas

In chemically active discharges such as Ar/SiH_4 or Ar/CH_4 plasmas, the growth of dust particles occurs naturally. The growth speed is more or less greater depending on the relative proportions of the gas components [35, 36, 119]. It is known that dust particle growth in a plasma modifies the discharge properties and therefore the dust particle growth kinetic can be monitored looking at the evolution of discharge parameters such as the current amplitude (and its harmonics) or the self bias [119, 123]. The growth of dust particles in chemically active discharges has been actively studied. Growth occurs in four phases:

1. Molecular precursors coming from gas dissociation
2. Formation and accumulation of nanoparticles from these precursors
3. Agglomeration of the nanocrystallites
4. Growth by molecular sticking

In sputtering discharges, dust growth has been studied for different materials [59–61, 73, 74, 136]. These results suggest that the growth mechanism is roughly the same except that the molecular

precursors come from the sputtered materials. The number of studies devoted to dust particle growth by RF sputtering is however smaller than the number of studies devoted to dust particle growth in chemically active discharges.
Consequently, we decided to study the growth of dust particles in sputtering discharges. The sputtered material was melamine-formaldehyde (MF) coming from previously injected dust particles inside the discharge. MF is a carbonaceous polymer and preliminary studies showed that the growing dust particles are mainly composed of carbon [66]. In the next section, the growth of particles by RF sputtering and its effects on the discharge are studied.

4.1.1 Dust particle growth in Ar/CH_4 plasma

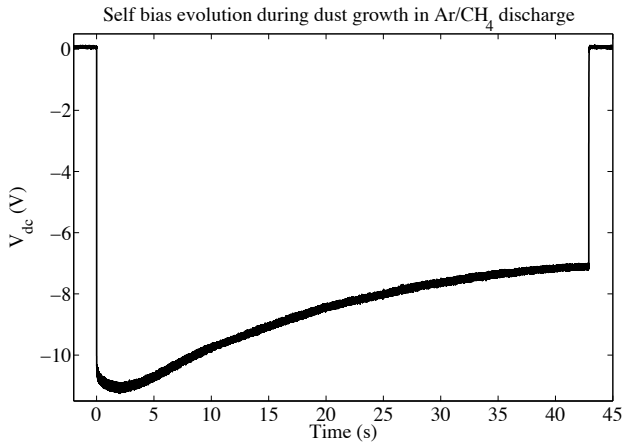

Figure 4.1: Evolution of the self-bias during the growth of dust particles in Ar/CH_4 plasma

In order to have a reference for the studies of the dust particle growth by RF sputtering, the growth of dust particles in an Ar/CH_4 discharge has thus been investigated. The measurement was made in the methane reactor (see Sec.3.1.2). The argon flow was 41.8 sccm and the methane flow was 0.8 sccm (the methane dilution rate was 1.9%). The operating pressure P was 1.1 mbar and the RF power was $P_W = 20$ W. The evolution of the self bias voltage on the driven electrode during the particle growth has been recorded and is presented in Fig.4.1. It shows that during the growth process, the self-bias voltage at the cathode gradually increases. After an initial period of little change a steady increase in self-bias voltage (a decrease in $|V_{dc}|$) was observed with an asymptotic approach to an apparent plateau value. As the plasma changes, the self-bias voltage achieves a value which ensures that no direct current is carried by the powered electrode [20, 137]. Qualitatively, the effect of particle growth on the self-bias can be seen as a consequence of the reduction in electron density due to negative charge accumulating on the particles: a reduced self-bias will reduce the ion flux and allow a longer period of electron flow so that a new equilibrium is established. This result is in agreement with the results obtained in Ar/SiH_4 plasma [119] in which the self-bias voltage evolution was correlated to the dust growth process. After 43 s, the discharge was stopped and the dust particles were collected for

analysis. SEM and TEM measurements show that the grown dust particles are spherical and quasi monosized ($r_d \sim 200$ nm; see Fig.4.2).

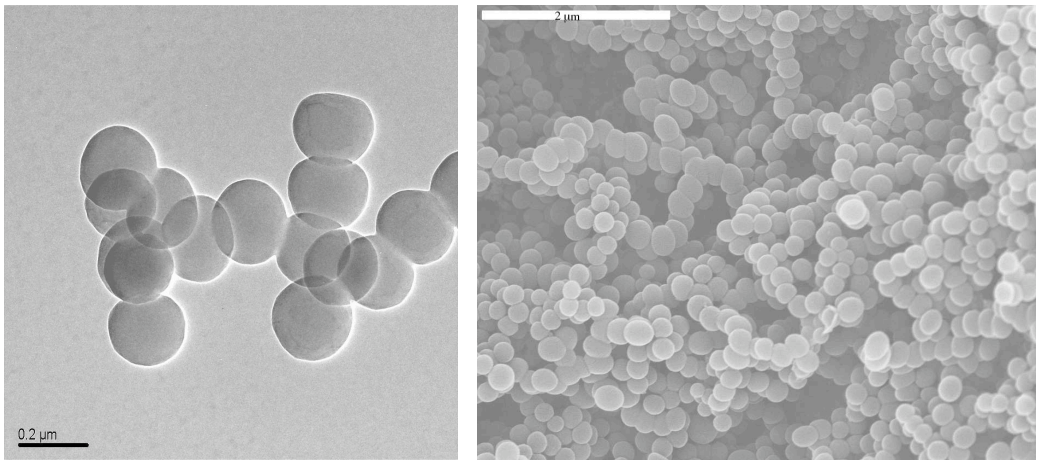

(a) TEM image (b) SEM image

Figure 4.2: Dust particles grown in a Ar/CH_4 plasma

4.1.2 Dust particle growth in the PKE-Nefedov reactor

The dust particles were grown by sputtering of a polymer layer deposited on the electrodes and coming from previously injected dust particles (MF dust particles). They were grown following this routine. First, the plasma chamber was pumped down to the lowest possible pressure (base pressure $\sim 2 \cdot 10^{-6}$ mbar). Then, argon was injected in the reactor up to the working pressure (1.2 mbar$\leq P \leq$ 1.6 mbar static pressure (no gas flow)) and the discharge is ignited. The input power was 3 W $< P_W <$ 4 W. After few tens of seconds, a dust particle cloud appeared in the plasma and was visible by naked eye due to the scattered laser light from the dust particles.
Various situations can be obtained after the dust particle growth (several layers, domelike shaped cloud, 3D dense cloud). This is due to the fact that the sizes and densities of the grown dust particles can not be controlled precisely. Indeed, it has been shown that the growth process in the PKE-Nefedov reactor is extremely sensitive to gas purity [61, 66]. The purity of the gas was also reported to be an important requirement for dust particle growth in similar experiments [59]. As our experiments were performed without gas flow, this effect was amplified. It was indeed necessary to pump for at least 1 hour between each experiments in order to be able to grow dust particles again: the species formed during the previous run and/or coming from the outgassing of the walls and/or from the sputtered matter needed to be eliminated. This was confirmed using plasma emission spectroscopy on successive runs [66]. Impurities such as OH or N_2 were observed and their influence is still under investigation. Moreover, possible dust particle precursors like carbon molecules C_2, CN, and CH appeared. The C_2 molecule seems to be a good indicator of dust formation. High dust density was observed only when the base pressure was sufficiently low (less than 10^{-5} mbar).

Electrical measurements

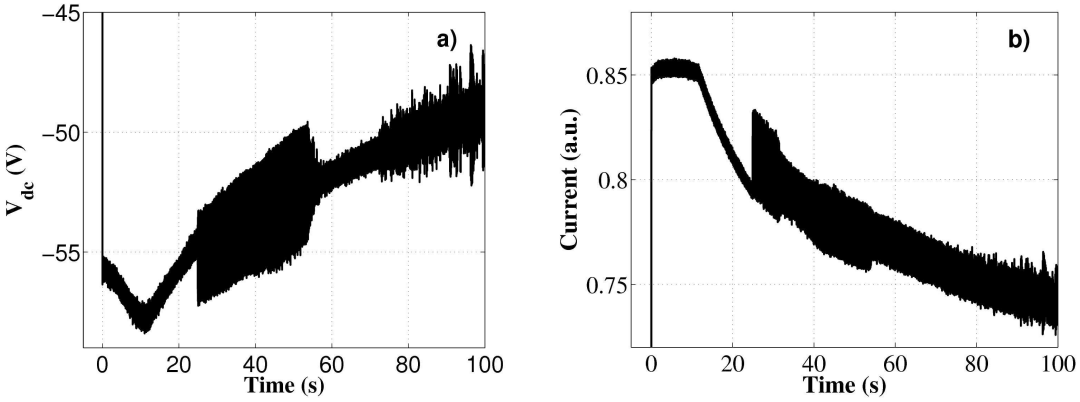

Figure 4.3: a) Self-bias (V_{dc}) of the bottom electrode b)Amplitude of the fundamental harmonics of the RF current (P=1.6 mbar and P_W =3.25 W)

The self-bias voltage of the bottom powered electrode of the PKE-Nefedov chamber has been recorded during the dust particle growth process. As can be seen in Fig.4.3(a), the self bias increases during the dust particle growth (or decreases in absolute value) after a small period of time just after plasma ignition where it decreases slightly. This behaviour is almost equivalent to that observed in chemically active discharges.
The appearance of dust particles in the plasma can also be confirmed by recording the time evolution of the amplitude of the fundamental harmonic of the RF current. Indeed, as dust particles appear and grow in the plasma, they acquire more and more electrons and the amplitude of the current decreases as a consequence. In Fig.4.3(b), this effect is clearly seen: the current amplitude decreases continually after a short period of little change just after plasma ignition. This diagnostic seems to be slightly more sensitive than the self bias voltage.
During dust particle growth, instabilities can appear on the electrical signals (self-bias voltage and amplitude of the first harmonic of the discharge current): the dust particle growth instabilities (DPGI). The DPGI are observed only when the base pressure is below 10^{-6} mbar which confirms that gas purity is an important parameter affecting the dust particle growth process. Instabilities during dust particle growth were also reported in other sputtering discharges [59, 73, 74]. A detailed study of this instability is presented in Sec.4.2.
It is generally believed that the DPGI are directly linked to size and density of the dust particles in the plasma [59, 74]. Therefore, this instability can be used to study the dust particle growth kinetic.
The DPGI typically appear tens of seconds after plasma ignition. The beginning of the DPGI is characterised by strong amplitude oscillations in both the amplitude of the fundamental harmonic of the discharge current and the self-bias voltage of the lower electrode (Fig.4.3). By

looking at the plasma glow with the naked eye, the beginning of the DPGI can also be detected since the light emitted by the plasma is strongly affected.
The DPGI starting time changes slightly from one experiment to another due to differences in the dust particle density which strongly depends on gas purity. Nevertheless, statistics performed on many experiments allow some general behaviour to be extracted. It is shown that the appearance time of the DPGI, and consequently the dust particle growth rate, depends on the gas pressure: the higher the pressure, the shorter the appearance time. Indeed, as can be seen in Fig.4.4, the DPGI appearance time decreases while increasing the pressure. In previous experiments, it was found that a threshold pressure for dust particle growth exists around 1.2 mbar [66]. Thus, for the same input power P_W=3.25 W, nearly 2 minutes are required to initiate the DPGI at 1.4 mbar while only 40 s are necessary at 1.8 mbar. Two hypotheses can explain this behaviour: either a longer time is required to reach the critical dust density necessary to cause the DPGI at low pressure, or the dust density that could be reach at low pressure is lower and bigger dust particles are needed to initiate DPGI (i.e. longer time). However, depending on the initial conditions, two regimes of DPGI exist: a slow one and a fast one. These regimes have different appearance times. Therefore, the dependence on the input power is not so clear even if it seems that the higher the input power, the shorter the appearance time (Fig.4.4).

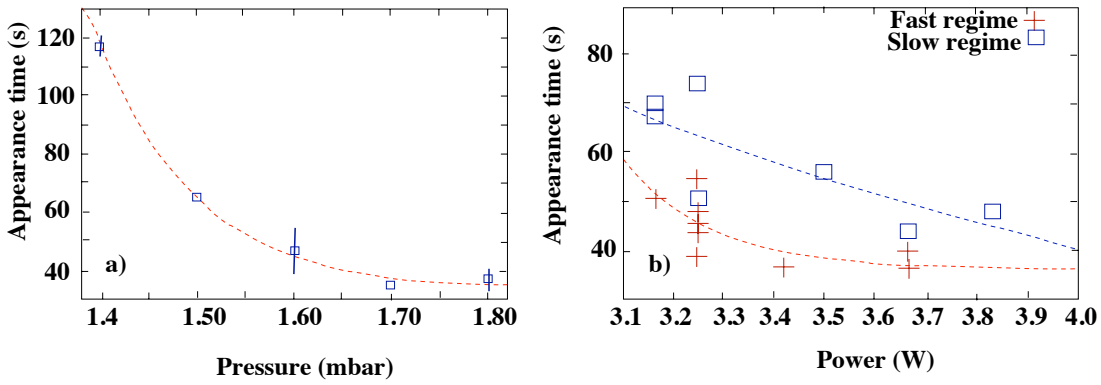

Figure 4.4: Appearance time (a) as a function of pressure (b) as a function of the input power.

Laser extinction measurement

In order to know when the dust particles reach a detectable size and/or density, laser extinction measurement has been performed. The evolution of the transmitted laser light intensity is shown in Fig.4.5. As can be seen the current amplitude has already started to decrease indicating that some dust particles are already formed in the plasma while the transmitted laser light is still at its maximum value. It indicates that either the density or the size of the dust particles is very small. However, in chemically active discharges, the dust density is very high when the dust particles start to grow [36]. It is probably the same in this experiment. Around 50 s, the transmitted laser light starts to decrease indicating that the dust particles are now large

enough to affect the laser light transmission (the scattered light increases as a function of the dust particle radius; Sec.3.2.3). It is worth noting that this decrease occurs before the DPGI start: the plasma is filled with detectable dust particles before the ignition of the DPGI. It may be an indication that the agglomeration phase occurs before the DPGI start. The transmitted laser light steadily decreases showing that dust particles grow continually in the plasma
However, the PKE-Nefedov reactor does not allow us to collect samples of the grown dust particles easily as this reactor was originally designed for microgravity experiments and thus no easy access for sample collection exists. Consequently, it is not possible to deduce the dust sizes and/or the dust density inside the reactor. Moreover, the exact optical index of the dust particles is not known as it is dependent on the material and the exact chemical composition of the dust particles is not known even if it has been proven that the dust particles are mainly composed of carbon [61].

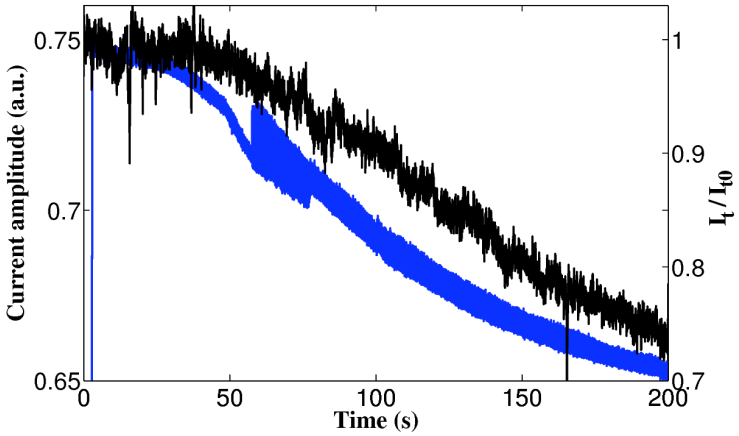

Figure 4.5: Current amplitude (blue curve) and relative laser intensity (black curve) as a function of time during dust particle growth (P =1.6 mbar and P_W =3.25 W).

Plasma emission spectroscopy

Plasma emission spectroscopy was performed during the dust particle growth. The evolution of the intensities of several argon lines was monitored. The evolution of the 750.39 nm argon line is presented in Fig.4.6(a). As can be seen, the line intensity increases during the particle growth process. If we consider that the energy level from which the transition occurs is principally populated by direct excitation from the ground state[1] the line intensity increase should indicate that the electron temperature increases (see Sec.3.2.4). This result would be in agreement with the results obtained by Bouchoule and Boufendi in a Ar/SiH_4 discharge where they reported that the electron temperature increases when dust particles are growing inside the plasma [33].
It has also been shown that the presence of dust particles can increase the metastable density in the plasma [33]. The line intensity ratio $I_{763.5}/I_{800.6}$ of the 763.5 nm and 800.6 nm argon

[1]For levels of interest corona equilibrium requires $n_e << 10^{11}$ cm^{-3} [126]. In our experiments, $n_e \sim 10^8 - 10^9$ cm^{-3}

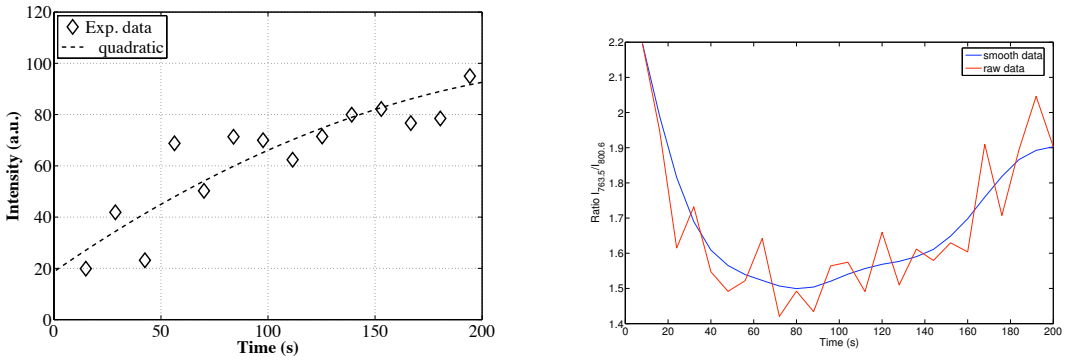

(a) (b)

Figure 4.6: a) Evolution of the intensity of the 750.39 nm argon line during particle growth in the PKE-Nefedov reactor with pressure $P = 1.6$ mbar and input power $P_W = 3.25$ W. b) Evolution of the Intensity ratio $I_{763.5}/I_{800.6}$ of argon lines during particle growth for a pressure of $P = 1.6$ mbar and an input power $P_W = 3.3$ W

lines have been recorded during the dust particle growth (Fig.4.6(b)). As can be seen, the ratio is lower when dust particles are present in the plasma than when the plasma has just been ignited (pristine conditions). It indicates that the $^3P_2$ argon metastable density increases when dust particles are growing in the plasma. Indeed, if the electron density decreases during dust particle growth and the electron temperature (and thus the electron energy) increases, the net rate of excitation of the argon excited levels is increased. The metastable concentration increases because the quenching rate by electron collision decreases and the quenching by collision with dust particles is thought to be neglectable. This effect was already observed by Boufendi in Ar/SiH_4 mixture plasmas [36]. However, as can be seen, the ratio slightly increases after it has reached a minimum a few tens of seconds after plasma ignition indicating that the metastable density tends to diminish. The value of the ratio is still below the value it had just after plasma ignition meaning that the metastable density remains higher than in a dust-free plasma.

4.1.3 Dust particle growth in the ComPLExS reactor

The growth of dust particles by RF sputtering from MF dust particles deposited on the electrodes was also performed in the ComPLExS reactor following the following routine. Firstly, the plasma chamber was pumped down to the lowest possible pressure (base pressure $\sim 5{\cdot}10^{-6}$ Torr). Then, argon was injected into the reactor up to the working pressure (0.6 Torr $< P <$ 1.8 Torr with a flow of 17.9 sccm) and the discharge was turned on. The peak to peak RF voltage was 230 V $< V_{pp} <$ 320 V. After a few tens of seconds, a dust particle cloud appeared in the plasma and was visible to the naked eye as a result of the laser beam light scattered by the dust particles.

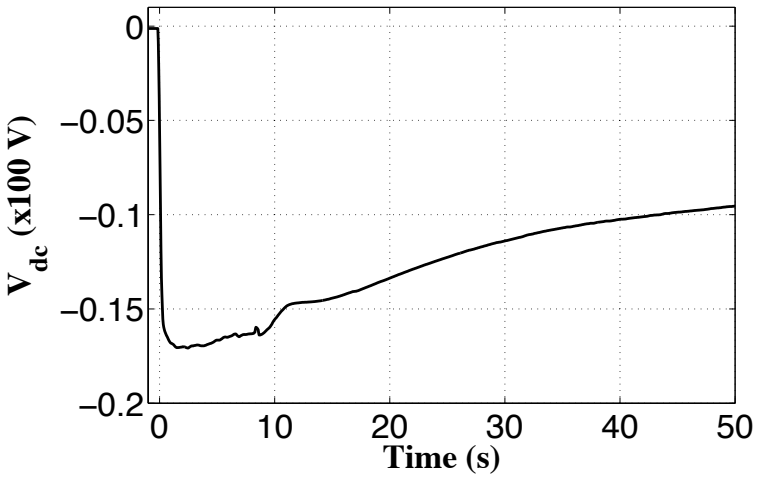

Figure 4.7: Evolution of the self bias voltage of the powered electrode in the ComPLExS reactor during dust particle growth (Pressure P=1.75 Torr and RF voltage V_{pp}=280 V)

Self bias voltage measurement

As in the PKE-Nefedov reactor, the growth of dust particles can be monitored by following some electrical characteristics of the discharge. The evolution of the self-bias voltage of the powered electrode during the dust particle growth is shown in Fig.4.7. As can be seen, an increase of the self-bias V_{dc} (a decrease in absolute value) is observed during the growth cycle after a small period of little change. It is similar to the behaviour observed in the PKE-Nefedov reactor. The total self-bias voltage change is about 50-60 % over a one minute discharge run. A decrease of the RF current amplitude of about 50-60% and a small increase of the RF peak to peak voltage of about 30% are also observed (not presented here). This is due to the modification of the discharge conditions (and therefore the matching conditions) caused by the presence of the dust particles.

Studies of the dependence of the evolution of the self bias voltage (and thus the dust particle

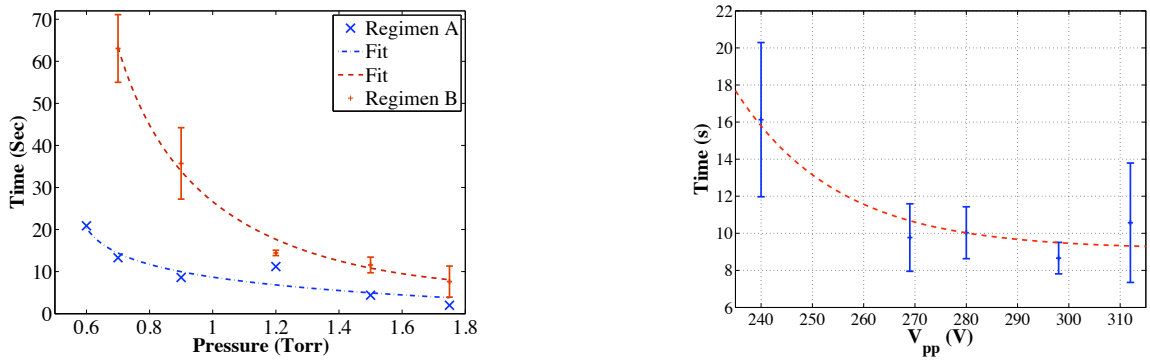

Figure 4.8: Self-bias increase time as a function of: (left) pressure; (right) RF peak to peak voltage at the start of the plasma run (Regimen B)

growth kinetic) on different experimental conditions have been carried out. In Fig.4.8, the results of studies as a function of the argon pressure P and the peak to peak RF voltage V_{pp} are presented. It shows the time needed for the self bias to increase by 5% from its minimum value corresponding to the dust-free plasma condition just after plasma ignition.
An impurity effect was observed in the ComPLExS reactor. Indeed when the pumping time between experiments is one hour (regimen B presented in Fig.4.8) the 5% V_{dc} increase time is much longer than when the pumping time in between the experiments is around 12 hours (regimen A in Fig.4.8). It indicates that the dust particle growth is delayed when the pumping time is shorter. This may be due to the presence of impurities such as residual nitrogen or OH compounds in the plasma chamber. As previously mentioned, a similar impurity effect was reported in the PKE-Nefedov chamber [66].
In Fig.4.8, it can be clearly seen that the argon pressure plays a major role in the dust particle growth process. Indeed, the time needed for the 5% V_{dc} increase is reduced by increasing the pressure. Below a threshold pressure (around 0.5 Torr in the ComPLExS reactor operating in regimen B) no dust growth is observed over plasma runs of duration of a few minutes (typically up to 10 minutes). The dependence on the RF voltage is not as clear: as for the lowest V_{pp}, it seems that the 5% V_{dc} increase takes longer than for higher values, but no clear trend can be extracted from the data in Fig.4.8.

Correlation of the dust size with the self bias measurement

Different dust samples have been collected on silicon wafers for different discharge durations. The wafers were placed on the powered electrode. The argon pressure was P =1.75 Torr and the peak to peak RF voltage was V_{pp} =280 V at plasma ignition. Each sample accumulated the grown dust particles over a minimum of 20 plasma runs. Then, SEM images of these samples have been taken. The sizes of the dust particles have been measured. The results for different discharge durations are:

1. First sample (Fig.4.9(a)): discharge duration of $t \sim 10$ s (the discharge was switched off just before the fast increase of the self bias voltage; see Fig.4.7). The mean radius of the collected particle is 16±5 nm

2. Second sample (Fig.4.9(b)): discharge duration of $t \sim 20$ s (the discharge was switched off at the end of the fast increase of the self bias voltage; see Fig.4.7). The mean radius of the collected particle is 24±6 nm

3. Third sample (Fig.4.9(c)): discharge duration of $t \sim 30$ s. The mean radius of the collected particle is 33±8 nm

4. Fourth sample (Fig.4.9(d)): running time of $t > 120$ s. The mean radius of the collected particle is about 100 nm. However, there is a large dispersion. The possible explanation is the existence of many generations of dust particles.

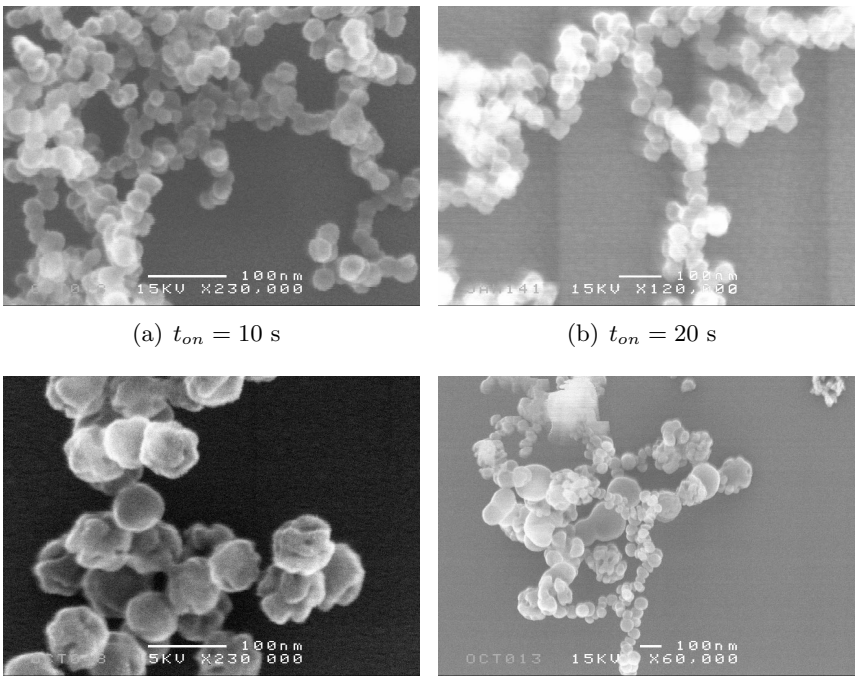

(a) $t_{on} = 10$ s (b) $t_{on} = 20$ s

(c) $t_{on} = 30$ s (d) $t_{on} > 120$ s

Figure 4.9: SEM images of the dust particles collected in the ComPLExS reactor for different discharge times.

The particle were collected over many runs on the powered electrodes. As a result, it may be possible that the real size of the dust particle is slightly larger due to a possible re-sputtering of the grown dust particles of the first runs. However, note that the fast variation of the self bias between 10 s and 20 s is not associated with a sudden variation of the dust particle size. Indeed, the size augmentation between samples 1 and 2 is nearly the same as between samples 2 and 3.

Spectroscopic measurement

Spectroscopic measurements were performed during the dust particle growth process. The argon pressure was P =1.75 Torr and the peak to peak RF voltage was 280 V. The evolution of the intensities of three argon lines has been monitored (415.86 nm, 518.77 nm, 750.38 nm) and different line ratios have been calculated (Fig.4.10). As can be seen the intensity of each line increases with time as in the PKE-Nefedov reactor. However, the ratios I_{415}/I_{750} and I_{518}/I_{750} firstly decrease before slightly increasing again. The interpretation of spectral measurements in terms of plasma parameters presents some complications. The most general approach is to use a collisional-radiative model which takes account of all collisional and radiative processes that influence the populations of excited states, and hence the intensities of spectral emission lines (as a function of the pressure, electron density and electron temperature) (see Sec.3.2.4). In order to simplify the problem the electron distribution is invariably assumed to be Maxwellian. Low pressure discharges such as the one used in this work allow a simplified version of the model

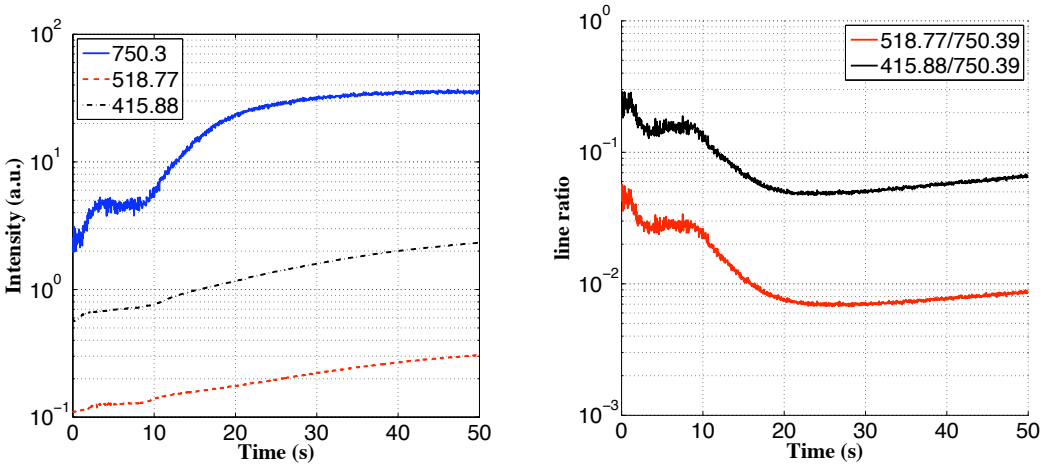

(a) (b)

Figure 4.10: (a) Line intensities and (b) line ratio during dust particle growth at $P = 1.75$ Torr and $V_{pp} = 280$ V

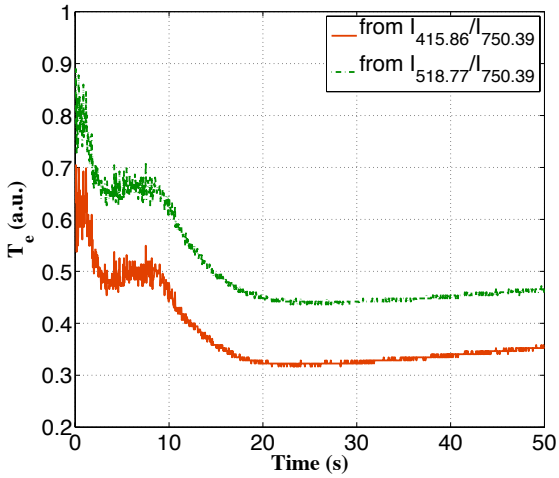

Figure 4.11: Evolution of the electron temperature T_e estimated from the evolution of the line ratio

to be used: the corona approximation, in which the dominant processes are collisional excitation from the ground state and radiative de-excitation.
The rising spectral line intensities during the particle growth process (Fig.4.10(a)) (when electron density is falling) implies an increase in electron temperature. In the latter circumstances the corona model predicts that the intensity ratios of Fig.4.10(b) should rise rather than fall (which implies a decrease of the electron temperature as can be seen in Fig.4.11). The resolution of this discrepancy will need to take account of the well-known fact that such discharges have non-Maxwellian distributions: at sufficiently low pressures the distribution is bi-Maxwellian, becoming Druyvesteyn-like at higher pressures [138, 139]. The present experiment falls within the latter regime. The effect of large dust concentrations on the electron distribution is however problematic. It can be supposed that the fast electrons of the EEDF are the only ones that can overcome the potential barrier of the dust particles at floating potential and are thus collected by them leading to a lack of energetic electrons which might be compatible with a decrease of the line intensity ratios. It might also explained why the metastable density decreases slightly after a few tens of seconds as observed in the PKE-Nefedov reactor. A recent kinetic model suggests that the Druyvesteyn-like distribution is modified by the presence of dust particles in such a way that it becomes nearly Maxwellian [140]. The slow increase in the intensity ratios after 20 s could be interpreted as a providing support for this prediction.

Langmuir probe measurement

Measurement in a pristine plasma:

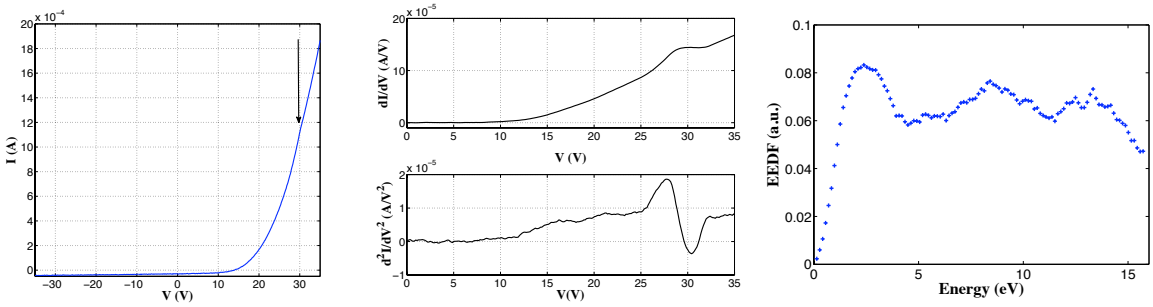

(a) (b) (c)

Figure 4.12: (a) Langmuir probe characteristic. The vertical arrow indicates the position of the plasma potential. (b) First and second derivatives of the probe signal. (c) Estimated EEDF from the second derivative of the probe characteristic (argon plasma with $P = 0.3$ Torr and $V_{pp} = 240$ V).

Langmuir probe measurements have been performed in an argon plasma with parameters which do not favour the dust growth but close to conditions in which dusty plasma experiments were performed. The I-V Langmuir characteristic is presented in Fig.4.12(a) for an argon plasma with $P = 0.3$ Torr and $V_{pp} = 240$ V. The plasma potential V_p corresponds to a change of slope

in the I-V curve and is indicated by a vertical arrow. The position of V_p can be better estimated on the 1^{st} and 2^{nd} derivative curves (Fig.4.12(b)). The derivatives have been computed after a Savitzky-Golay filtering (polynomial filtering) of the probe signal in order to reduce noise. The plasma potential corresponds to the first maximum of the 1^{st} derivative and the zero-crossing of the 2^{nd} derivative. From the second derivative, it is possible to estimate the EEDF (Fig.4.12(c)). As can be seen, the EEDF is far from a Maxwellian distribution and is Druyvesteyn-like. Similar results have been previously reported in other RF argon discharges with similar parameters [135]. However, the energetic tail of the EEDF should decrease faster as electrons with energy close to the ionisation level are lost in excitation and ionisation processes. This is due to the noise in the probe signal. It is still possible to extract some plasma parameters using the second derivative analysis: the electron density is $n_e \simeq 2.9 \cdot 10^9$ cm^{-3} and the effective electron temperature $T_{eff} \simeq 5.2$ eV (this last parameters is slightly overestimated due to the noise-induced increase of the energetic tail of the EEDF).

Measurements in a dusty plasma:

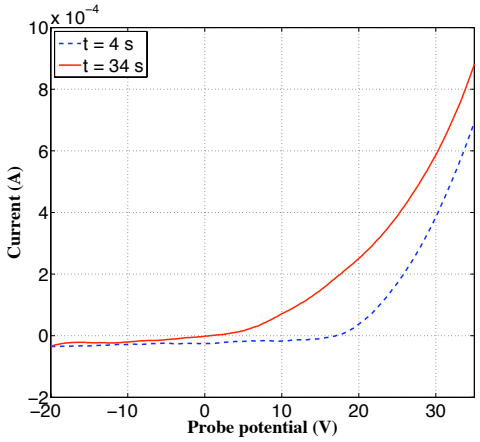

Figure 4.13: I-V Langmuir probe characteristics at different instants of the discharge life (P = 1.75 Torr and V_{pp} = 280 V). The curves have been smoothed.

The Langmuir measurements in a dust-free plasma with parameters close to the parameters of dusty plasma experiments have confirmed that the EEDF is not Maxwellian. However, in order to complement spectroscopic data, Langmuir probe measurements have been performed during the dust particle growth in order to estimate the electron temperature. Some I-V probe characteristics are shown in Fig.4.13 just after plasma ignition and at a discharge time $t >$30 s, after the fast increase of the self bias voltage. Due to very noisy data, the second derivative analysis method could not be applied and classical Langmuir analysis of probe characteristic has been performed.
The ion density was deduced from the ion current part the probe characteristics and is found to be quasi-constant during the whole duration of the discharge ($n_i \simeq (1.3 \pm 0.5) \cdot 10^9$ cm^{-3} using the

Allen-Boyd-Reynolds (ABR) analysis and $n_i \simeq (1.3 \pm 0.4) \cdot 10^{10}$ cm^{-3} using OML analysis[2]). As can be seen in Fig.4.13, the slope of the electron current (positive part of the curves) decreases after plasma ignition (the slope at $t = 4$ s is larger than the slope at $t = 30$ s). This is a strong indication that the effective electron temperature increases during the dust particle growth. As can be seen in Fig.4.14(a), the absolute value of the floating potential ($V_p - V_f$) is increasing with time which supports an increase of the electron temperature. The effective electron temperature elevation is confirmed in Fig.4.14(b): it shows that the effective electron temperature rises from 2.5 eV at plasma ignition to about 3.5 eV after 50 s. As can be seen the effective electron temperature elevation is more pronounced around 10 s after plasma ignition which corresponds to the fast increase of the self bias voltage.

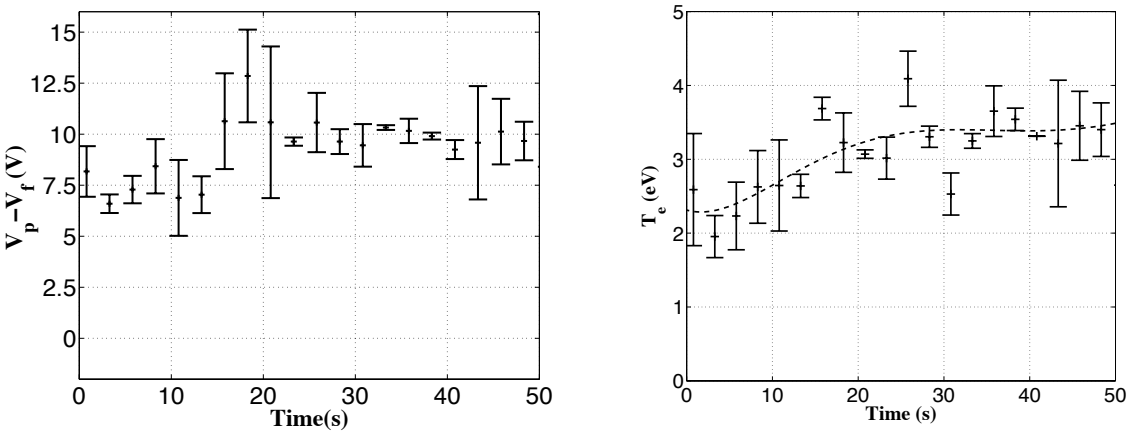

(a) (b)

Figure 4.14: Evolution of plasma parameters obtained with Langmuir probe measurements in an argon plasma with $P = 1.75$ Torr and $V_{pp} = 280$ V. (a) Evolution of the plasma potential and the floating potential extracted from I-V curves. (b) Evolution of the electron temperature deduced from the I-V curves.

Finally, from both spectroscopic and Langmuir probe measurements, it can be deduced that dust particles in the plasma induce an increase of the effective electron temperature. However, as the intensity of selected argon lines increases with time while the line ratio decreases, it tends to show that the energetic electrons of the EEDF tail may be lost on dust particles.

4.1.4 Comparison of results

The growth of dust particles has been investigated in both the PKE-Nefedov reactor and the ComPLExS reactor. Some general behaviour can be extracted. The most interesting features are:

[2]It is known that the first method tends to underestimate the ion density while the second one tends to overestimate it in our range of pressures [135].

- The growth of particles in the plasma modifies the electrical characteristics of the discharge. The current amplitude and the absolute value of the self-bias voltage decrease during the particle growth. This is due to the presence of dust particles which affects the electrons. The electron density decreases due to electron attachment onto the dust particles which is thought to be the main reason for both the decrease of the self bias voltage and current amplitude.

- Spectroscopic measurements in both discharges show a rise in the absolute intensity of some argon lines. As the electron density decreases during the dust growth, it indicates that the electron temperature increases. However, comparison of the evolution of the relative intensity of some argon lines in the ComPLExS reactor suggests that the electron temperature would decrease in the case of a Maxwellian EEDF. This is a strong indication that the EEDF is not Maxwellian and the ratio falls can be due to a depletion of energetic electrons.

- Langmuir probe measurements confirm that the EEDF is not Maxwellian and that the effective electron temperature increases during dust particle growth. Comparison with the spectroscopic measurements supports the idea that there could be a depletion of the energetic electrons.

4.2 Dust particle growth instabilities

In argon-silane RF discharges, instabilities have been observed during the growth of nanoparticles on both the amplitude of the third harmonic (40.68 MHz) of the discharge current and the self-bias voltage (V_{dc}) [119]. A proposed explanation was an attachment induced ionization instability as observed in electronegative plasmas. Instabilities during dust particle growth have also been observed in sputtering discharges [59, 73, 74]. These instabilities were divided into two modes appearing consecutively: the filamentary mode and the great void mode. The triggering of the instabilities was explained by spontaneous local fluctuations of the dust number density leading to a lower depletion of the electrons in the regions of reduced dust particle density inducing a higher local ionisation rate. It creates two forces on the negatively charged dust particles: an inward electric force induced by the positive space charge (and thus electric field) and an outward ion drag force. The threshold for the instability is determined by particle size (charge) and the electric field strength.

4.2.1 Instabilities in the PKE-Nefedov chamber

Similar instabilities have also been observed during the dust particle growth in the PKE-Nefedov reactor [141] but the separation in modes was more complicated. In this section, we focus on the studies of the dust particle growth instabilities at an argon pressure $P = 1.6$ mbar and an input power $P_W = 3.25\ W$. Dust particle growth instabilities (DPGI) typically appear tens of seconds after plasma ignition and can be well observed on both electrical and optical signals

[68, 75, 141]. It is found that the DPGI have two different regimes: a fast regime and a slow regime. These two regimes are characterized by their frequencies and evolution kinetic.

Phases and regimes of the instability

Phases of the DPGI

As mentioned previously, DPGI are evidenced by strong modulations of current amplitude and self bias voltage (see Fig.4.3). As can be seen in Fig.4.15, the DPGI are characterised by different phases which can be better observed looking at the current amplitude evolution in AC mode in order to improve the vertical resolution of the oscilloscope.
In Fig.4.15, the measurement of the AC component of the fundamental harmonic of the RF current is presented with its corresponding Fourier spectrogram for the total duration of a plasma run. The beginning of DPGI occurs approximatively 40 s after plasma ignition and is

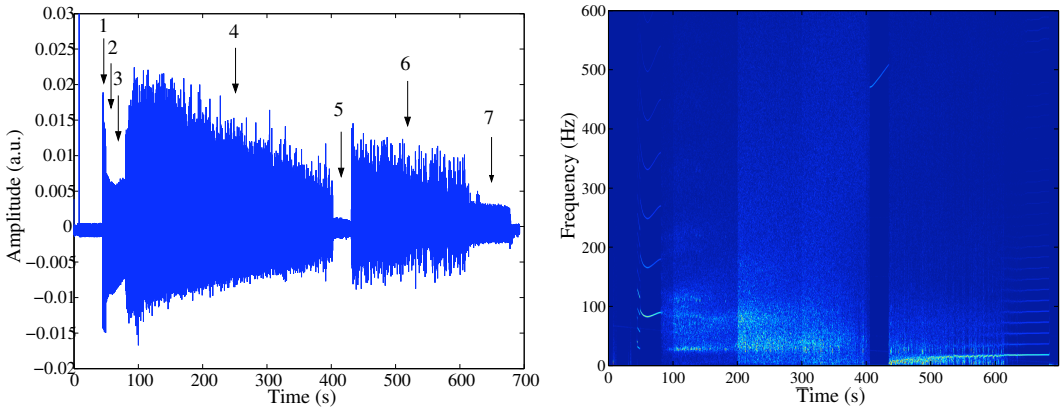

Figure 4.15: Left: Current fundamental harmonic amplitude (AC component). Successive phases are numbered from 1 to 7. Right: Corresponding spectrogram

detected through a strong variation of the AC component of the current amplitude. Clear phases can be identified and are numbered from 1 to 7 in Fig.4.15. These phases are better evidenced by looking at the Fourier spectrogram of the signal. In order to highlight small ordered domains, the spectrogram intensity has been normalised inside each 100 s range. These phases can also be identified on spatially resolved optical measurements (focussed optical fibres) and show roughly the same pattern. From Fig.4.15, the different phases are identified.

1. Three ordered phases P1, P2 and P3 from $\sim$ 40 s to $\sim$ 80 s.
2. Chaotic phase P4 from $\sim$ 80 s to $\sim$ 405 s.
3. High frequency phase P5 from $\sim$ 405 s to $\sim$ 435 s. This phase does not occur in each experiments and is highly dependent on initial conditions.
4. Chaotic phase P6 from $\sim$ 435 s to $\sim$ 600 s. This phase tends to stabilise.

5. Regular oscillation phase P7 from $\sim$ 600 s to $\sim$ 680 s. This phase can have different patterns and is related to the void instabilities (see Chap.5).

These phases are observed on both electrical and optical measurements as well as on high speed video imaging confirming the correlation between an unstable plasma and the dust particle growth. The described pattern of DPGI is robust except for the P5 high frequency phase which is highly dependant on initial conditions such as gas purity. These phases are nevertheless quite different from the instability modes observed by Goree's group [59, 73] where a filamentary mode (which could be related to our chaotic phase) is followed by a regular phase (great void mode).

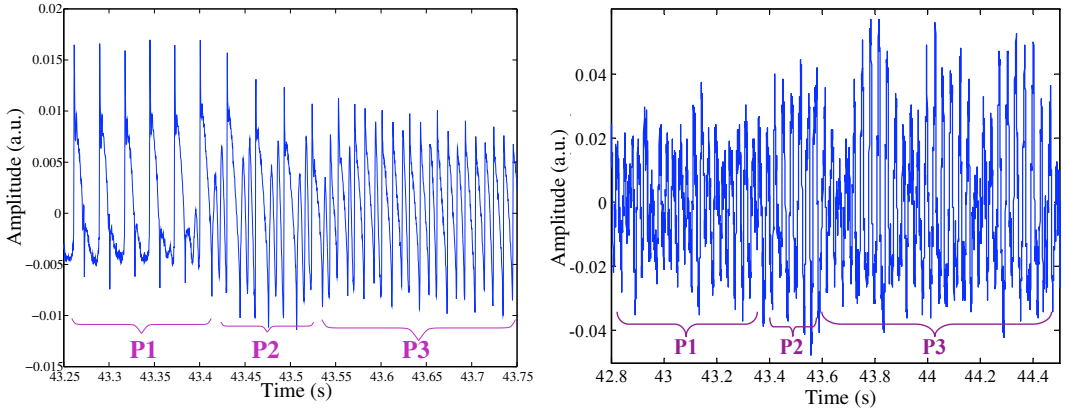

Figure 4.16: Transition between the first 3 ordered phases. Left: Current fundamental harmonic amplitude. Right: Optical signal near the plasma edge

1) DPGI begin with a succession of three ordered phases separated by clear transitions (Fig.4.16). The phases P1 and P2 are short and are not detected in every experiments. On the contrary, the phase P3 can last for a long period of time (few tens of seconds) and is regularly observed. The three phases are well separated and evolve as a function of time. The transition between the different phases can be well observed on the time series of the current amplitude. In Fig.4.16, an example of transitions with a very short P2 phase is presented in order to illustrate the P1-P2 transition and the P2-P3 transition. The P1 phase is characterised by well separated current peaks. The transition from P1 to P2 corresponds to the growth of two small peaks between the higher amplitude pattern. During the P2 phase, the small peaks continue to grow while the higher ones decrease. Finally all peaks reach the same amplitude characterising the P3 phase.

The different phases can also be seen on the frequency spectrum of the instabilities. In Fig.4.17, the Fourier spectrogram and the Hilbert-Huang (HH) spectrum (see App.B) of the three first phases of the DPGI are presented. These spectra do not correspond to the time series presented in Fig.4.16 (In this figure $t = 0$ does not correspond to the plasma ignition but corresponds to a time close to the DPGI beginning). As can be seen the P1 phase (from 0.5 s to 2.5 s in Fig.4.17) has a mean frequency around 40 Hz but the frequency decreases slightly with time.

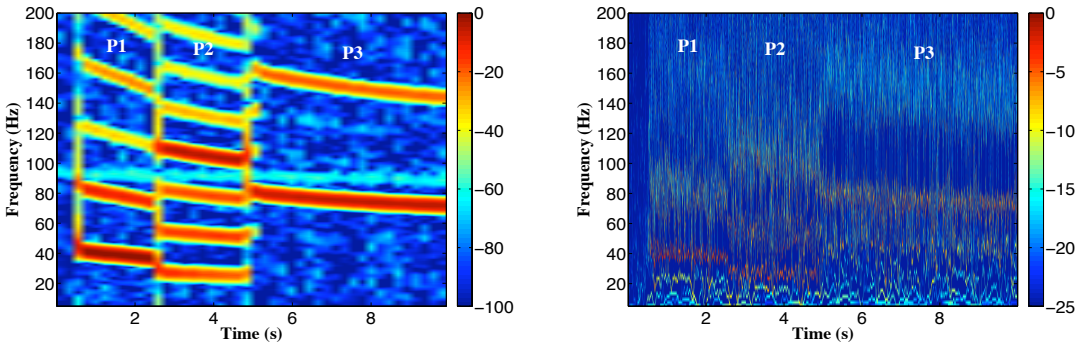

(a) Fourier spectrogram

(b) Hilbert-Huang spectrum

Figure 4.17: Fourier spectrogram and Hilbert-Huang spectrum during the three first phases of DPGI. In this figure $t = 0$ does not correspond to the plasma ignition but corresponds to a time close to the DPGI beginning.

In the Fourier spectrogram (Fig.4.17(a)), the signal is composed of many harmonics. In the Hilbert-Huang spectrum (Fig.4.17(b)), only the main frequencies of the signal are extracted (see App.B). Thus two components are visible during the P1 phase, the main one with a frequency around 40 Hz and another one of little intensity with a frequency around 80 Hz which was also visible on the Fourier spectrum but could be interpreted as a harmonic of the fundamental frequency. The transition from P1 to P2 occurs around 2.5s in Fig.4.17. In the Fourier spectrogram it results in a decrease of the main frequency from around 40 Hz to 30 Hz. However, the time resolution of the Fourier spectrogram is very bad and the position of the transition can only be approximate. In the Hilbert-Huang spectrum, it can be seen that the main frequency of the signal rapidly decreases during the transition and as well as its intensity which becomes a little bit weaker (from -2 to -4 on a logarithmic scale). The transition is also visible for higher frequency components with the decrease of the frequency of the second component from around 80 Hz to 58 Hz and a small increase in its intensity and the appearance of a third component around 100 Hz. The transition from P2 to P3 (around 5 s in Fig.4.17) is characterised by a strong increase of the main frequency of the signal that can be related to the transition from two small peaks and one big peak to three equal peaks. This is visible on both the Fourier spectrogram and the Hilbert-Huang spectrum. In the Hilbert-Huang spectrum, the intensity of the two smallest frequencies rapidly decrease during the transition while the third component observed in the Hilbert-Huang spectrum of the P2 phase gains in intensity but decreases in frequency. In the Hilbert-Huang spectrum it also seems that there is a small intensity component with a frequency around 45 Hz. Another advantage of the Hilbert-Huang spectrum is that that transition are precisely identified in both the time and frequency domains.
The P3 phase is very robust (nearly always observed in our experiments) and lasts a sufficiently long time to evolve significantly during the dust particle growth. The time evolution of its main frequency is always the same: it decreases, reaches a minimum and then slightly increases again until the DPGI enter in the chaotic regime. Furthermore, the mean frequency of the P3 phase

is linearly dependent on the phase duration (see Fig.4.18): the higher the frequency, the shorter

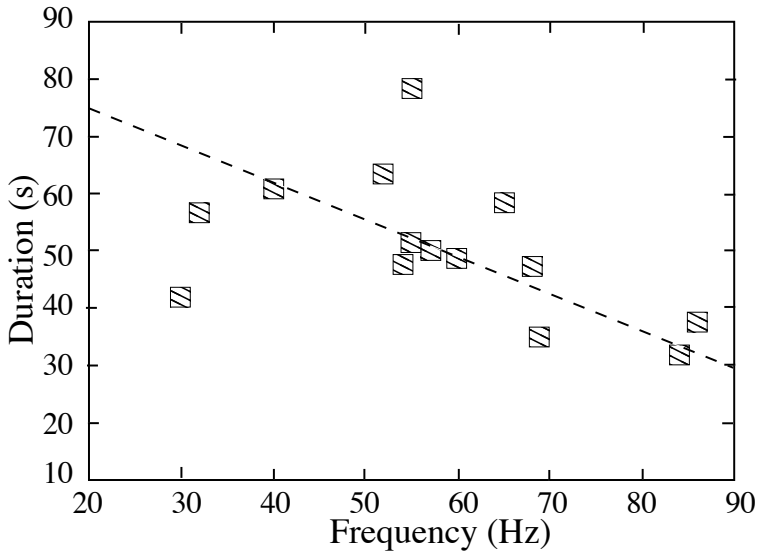

Figure 4.18: Duration of the P3 phase as a function of its frequency

the time duration.

Optical measurements recording the plasma light (integrated over all wavelengths) at different positions also show three ordered phases (Fig.4.16). Nevertheless, the phases P1, P2 and P3 have different characteristics to those observed in the current amplitude measurement. The transition from P1 to P2 is characterised by an increase in the oscillation amplitudes. The P3 phase is characterised by a strong amplitude modulation which is more prominent near the plasma edge than in the plasma centre. There are also some discrepancies in frequency between the optical signal and the current signal especially during the P3 phase. As can be seen in Fig.4.19, the P1 and P2 phases are similar but when the DPGI enter the P3 phase, the current signal frequency nearly triple while, on the optical signal, the main component frequency remains in the continuity with that of the P2 phase. Furthermore, the P3 phase optical measurements are slightly different from one region of the plasma to another. The Fourier transform of the signal recorded by the fibre focussed on the plasma centre (Figs.4.19(c) and 4.19(d)) is not exactly the same as the one recorded near the plasma edge (Figs.4.19(e) and 4.19(f)). Indeed, in the central fibre signal, a main component with frequency around 26 Hz can be extracted as well as a smaller amplitude component around 31Hz (Fig.4.19(d)). In the near plasma edge optical signal the same components can be extracted but additional ones are also seen: one between 26 Hz and 31 Hz and another one around 3 Hz (Fig.4.19(f)). The last one corresponds to the strong modulation observed in Fig.4.16.

These observations underline the fact that spatial considerations must be considered in order to interpret the P3 phase. For this reason, high speed video imaging of the plasma glow during the P3 phase has been performed. The camera was focussed on the plasma centre with a frame rate of 646 fps (frames par second). In Fig.4.20, the evolution of the central line of the video (i.e. the line passing through the discharge centre between the electrodes) is presented. The image

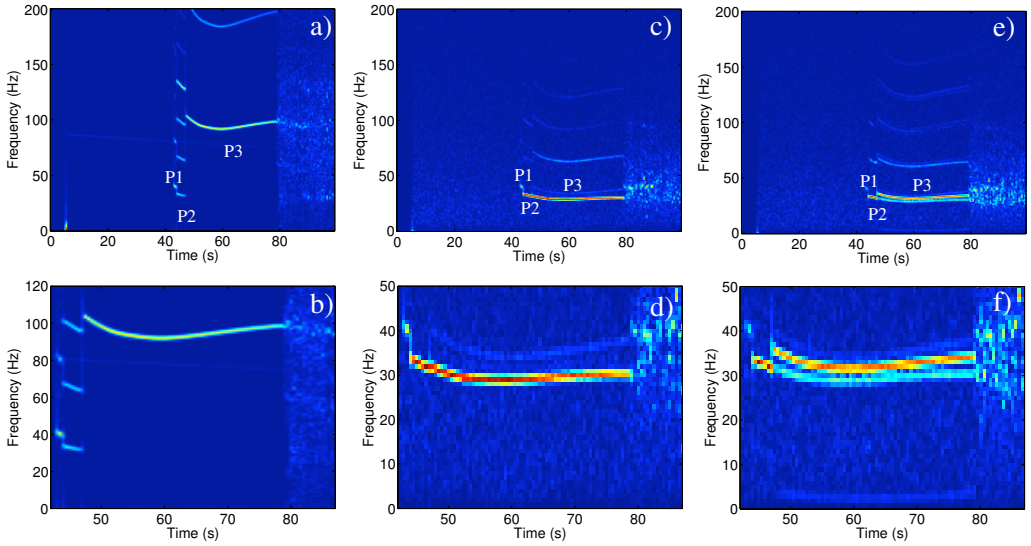

Figure 4.19: Fourier spectrograms of (a) electrical measurements (current fundamental harmonic) and optical measurements (c) in the central fibre, (e) near the plasma edge. (b) Zoom of (a), (d) zoom of (c), (f) zoom of (e)

number is on the x-axis and the pixel number of the line is on the y-axis. Fig.4.20(a) presents the evolution of the raw luminosity of the central line directly extracted from the video images. As can be seen, bursts of luminosity appear regularly and their positions are changing through time. Nevertheless, if the frequency between the maximum luminosity peaks is calculated independently of the position, a frequency of around 96 Hz is found and corresponds to the frequency of the current signal recorded at the same time of the video (not presented here). Consequently a peak in the current signal is associated to the appearance of a region of enhanced luminosity in the plasma and thus enhanced ionisation. In order to give a better view of the spatial evolution of the glow luminosity, the time mean value of each of the line pixels has been subtracted to the corresponding pixel value. The results are presented in Fig.4.20(b). As can be seen, when the glow reaches its maximum luminosity in a certain region of the plasma, the other regions become darker. Furthermore, the position of the maxima changes with time but follows a defined pattern. It seems that the luminosity maxima move from one side of the reactor to the other. The luminosity bursts reappear on the same side of the reactor every three luminosity bursts. This explains why the frequency observed on the optical fibre signal is three times less than the one observed in the current signal (Fig.4.19). A closer look shows that the maximal values of the luminosity bursts are not the same for each burst while in the current signal each peak has more or less the same amplitude. This can be explained if the luminosity burst are not in the plan where the camera is focussed. Moreover it seems that there is a rotation of the burst of luminosity with time. Indeed, when a burst reappears on a reactor side, its position has slightly changed compared to the previous one in the same plasma region. Overall Fig.4.20(b) clearly indicates this rotation with a frequency around 4 Hz. Consequently, the modulation observed by the op-

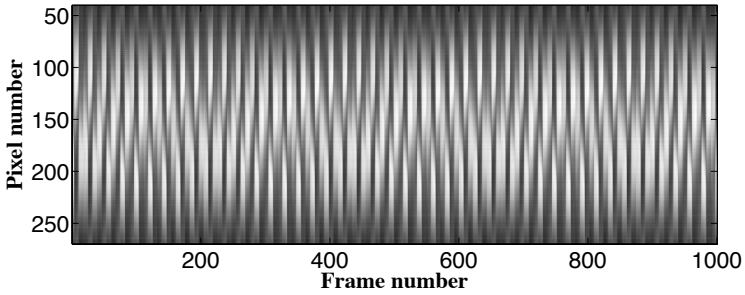

(a)

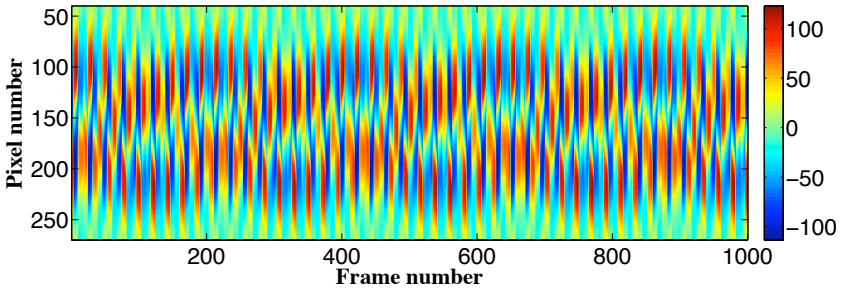

(b)

Figure 4.20: Evolution of the central line: (a) raw data extracts from the video (grey scale) (b) Same as (a) but the mean time values of each pixel of the line have been subtracted (in false colour from dark blue to dark red)

tical fibre is due to the slow rotation around the chamber axis of these three luminosity bursts. A possible explanation for this rotation pattern can come from the PKE-Nefedov geometry. Indeed, in the middle of the upper electrode, there is a grounded dust shaker (used to inject dust particles into the plasma) which must modify the potential and can be the origin of the rotation.

2) After the three ordered phases, the DPGI enter a "chaotic" regime (called P4) (Figs.4.15 and 4.19 after 80 s) characterised amongst other things by a strong increase of the DPGI amplitude. Then the amplitude slowly decreases during the whole duration of the phase. During the P4 phase, structured oscillations appear in a transient manner. These structured oscillations can be identified by some bright spots on the current and optical spectrograms. On the time series, they appeared like bursts of order. In Fig.4.21(a), the transition between the P3 phase and the P4 phase is clearly seen and is indicated by an arrow. A burst of order during the chaotic regime has been encircled. A zoom of this burst of order is shown in Fig.4.21(b). In order to understand the nature of these bursts of order, high speed video imaging has been performed on the plasma glow. The camera was focussed on the centre of the discharge and the frame rate was 646 fps. In Fig.4.22(a), the raw evolution of the luminosity of the central line of the video images passing through the discharge centre is presented. As can be seen, it exhibits luminosity maxima that vary with time and position. Each luminosity maximum probably corresponds to a peak in the current measurement. However, from image 2265 to image 2425, it

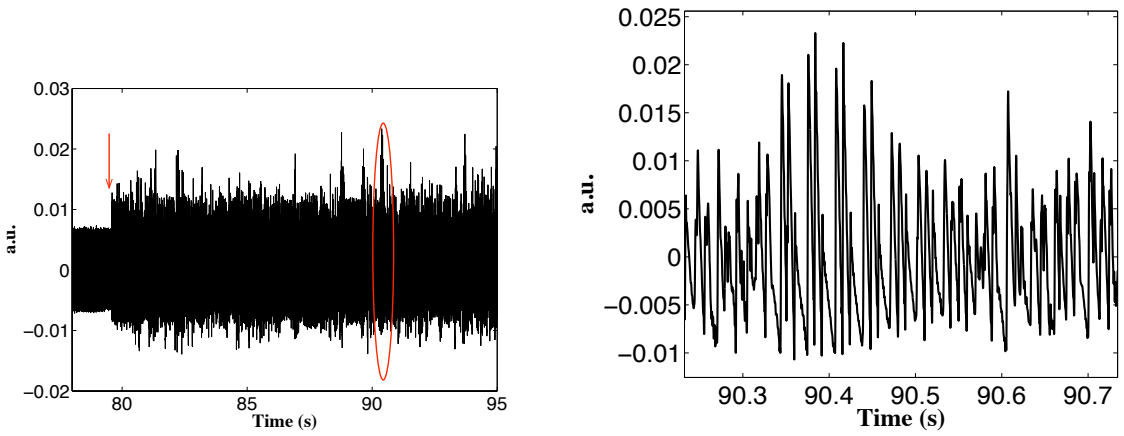

(a) (b)

Figure 4.21: Current signal measurements: (a) transition between P3 and P4 phases and encircles burst of order. (b) zoom of the encircled part of (a).

seems that the luminosity evolution follows a regular pattern. In order to further investigate this observation, the evolution of the luminosity of the line pixels relative to their mean values is shown in Fig.4.22(b). As can be seen, the ordered domain corresponds to the following pattern: appearance of a high luminosity central glow, then fast decrease of the central luminosity and appearance of two bright regions on the edge of the plasma while the centre of the discharge is dark and finally a fast decrease of these luminous regions and the appearance of two new luminous regions (one close to the discharge centre and the other one very decentred toward the edge of the plasma) with a darker region in between. The glow can serve as an indicator of the energetic electrons that cause electron-impact ionisation. Consequently, the fact that the glow is modulated suggests that we are observing a type of ionisation wave or striation. Thus, this three step pattern should correspond to the three peaks pattern observed during the burst of order in the current signal due to these localised high ionisation regions. To compare our observation with the filamentary mode reported by Goree's group [59], a Fourier spectrum of a 4 seconds span over the chaotic regime (from 94.5 s to 98.5 s) has been performed (Fig.4.23). In Fig.4.23(a), a noisy main frequency around 30 Hz is observed. This frequency corresponds to the frequency of the three peak structure of the bursts of order emerging regularly during the chaotic regime. However the spectrum extends over a wide band of frequencies. In Fig.4.23(b), the corresponding spectrum of the central optical fibre signal exhibits the same main frequency. However it extends over a narrower band than the current signal. It confirms the spatial aspect of the instabilities observed clearly on high speed video imaging as the fibres are localised on a defined region of the plasma. These Fourier spectra are very similar to the ones obtained for the filamentary mode [59]; even so in our experiments ordered domains have been observed. Thus we can surmise that the chaotic regime we observe could be similar to the filamentary mode.

3) In some experiments, the chaotic regime is suddenly interrupted by strong frequency and

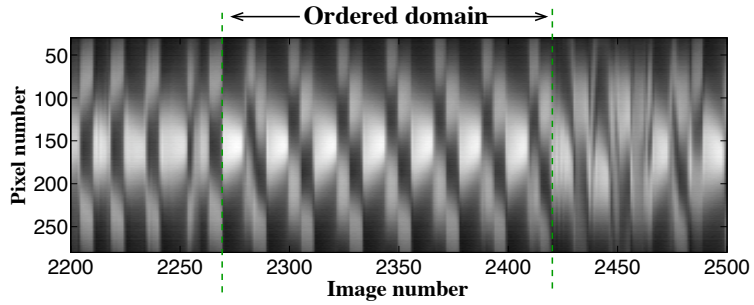

(a)

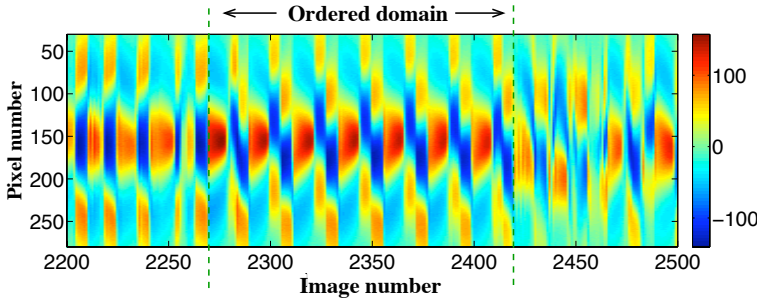

(b)

Figure 4.22: Ordered domain during P4 phase: (a) raw line evolution from the video images. (b) line evolution from the video images where the mean time values of each pixel have been subtracted

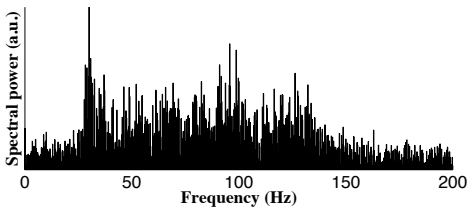

(a)

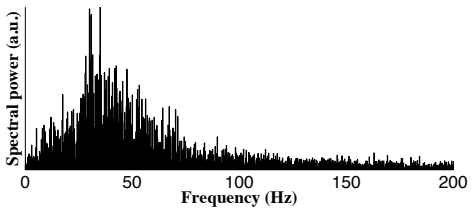

(b)

Figure 4.23: Fourier spectrum of the first chaotic regime. (a) on current signal (b) on central optical fibre signal

amplitude changes (Fig.4.15 around 405 s). This P5 phase is not always observed but when it is present, its characteristics are nearly always the same. This new phase appears after a continuous decrease of the P4 phase amplitude and is defined by a radical change in the DPGI frequency and amplitude which turns into high frequency (around 500 Hz) and low amplitude oscillations. These changes happen when no fast modifications in dust particle density and size are expected. Furthermore, the frequency increases with time. This increase is most of the time nearly linear but non-linear increases are sometimes observed. As already mentioned, this phase does not always appears in the DPGI which means relatively precise conditions must be fulfilled for its existence. Small modifications of the discharge parameters can easily turn the high frequency phase into a chaotic one or regular oscillations.

4) After the high frequency regime a second chaotic phase (P6) is usually observed. It is similar to P4 but exhibits more and more ordered regions.

5) The DPGI ends when the P6 phase tends to stabilise into regular oscillations. Two different behaviours can occur. The first and most common one is that the the transition appears as a small and continuous increase of the DPGI main frequency. At the end of the transition, the signal exhibits regular oscillations. They are related to are self-excited oscillations of the dust void (region in the centre of the discharge completely free of dust particles). The second behaviour occurs in some experiments and is slightly different. Instead of a frequency increase, the frequency decreases and the DPGI enter a regular oscillation phase. Video imaging of the dust cloud shows that this behaviour can correspond to large oscillations of the void or can correspond to rotation of the void in the horizontal plane around the axis of symmetry of the chamber. They are due to the growth of a new generation of dust particles inside the dust void. In both cases, these instabilities have typical signatures in current and optical signals, and high speed video imaging. They are studied in detail in Chap.5.

Regimes of the DPGI

Two regimes of DPGI have been observed: a slow regime and a fast regime. Typical frequencies of the fast regime are generally 2-3 times higher than the slow ones (Fig.4.24). Nevertheless, these regimes are not strictly separated and DPGI frequencies can spread over a wide range.
It has also been found that DPGI phase duration times are much longer for the slow regimes than for the fast regimes. Fig.4.18 shows that the higher the frequency of the P3 phase, the shorter its duration. The frequencies of the first phases of the DPGI can also be linked to the appearance time of the DPGI. As the first phase P1 can be very short (less than 0.1 s), it cannot be used to build statistics. For this reason, the appearance time of the P2 phase as a function of its frequency (around 48 s in the left diagrams of figure 4.24 or around 60 s in the right diagrams of figure 4.24) has been plotted in Fig.4.25. It shows that the high frequency P2 phase appears faster than the low frequency P2 phase.

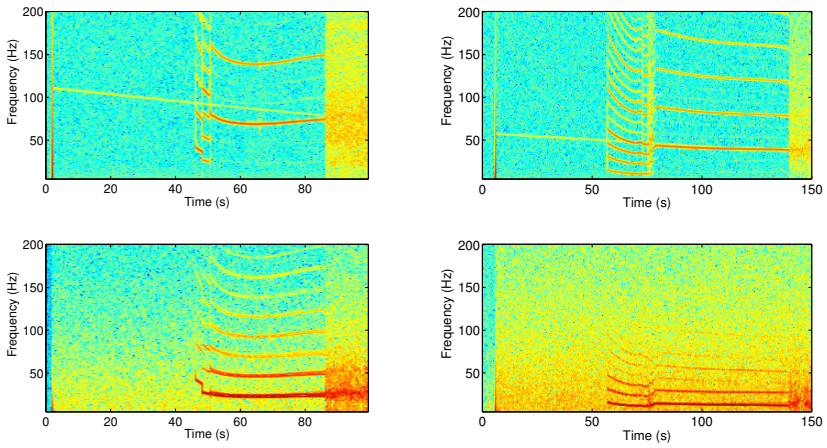

Figure 4.24: Left: Electrical signal Fourier spectrum of the current amplitude (Top) and Optical signal Fourier spectrum (Bottom) for fast regime DPGI. Right: Electrical signal Fourier spectrum of the current amplitude (Top) and Optical signal Fourier spectrum (Bottom) for slow regime DPGI.

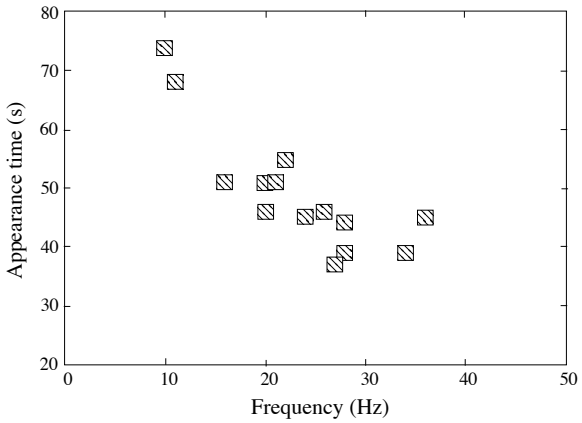

Figure 4.25: Growth instability appearance time as a function of P2 mean frequency

The behaviour of the DPGI can also be predicted by looking at the evolution of the current before the DPGI appears. Indeed, looking at the evolution of the current over first the 30 seconds after the discharge ignition (before the DPGI start), different patterns can be seen (Fig.4.26). In the case of a discharge exhibiting the fast regime DPGI, the current amplitude firstly decreases during $\sim$ 5 s then stabilizes for $\sim$ 10 s and finally decreases again. In the case of a discharge exhibiting the slow regime DPGI, the current amplitude does not decrease immediately after plasma ignition. It starts to decrease after $\sim$ 1 s but very slowly compared to the fast regime DPGI and after $\sim$ 5 s even starts to increase again. Finally after $\sim$ 15 s, the current amplitude slowly decreases.

A possible explanation for the differences between the two regimes is a different dust particle

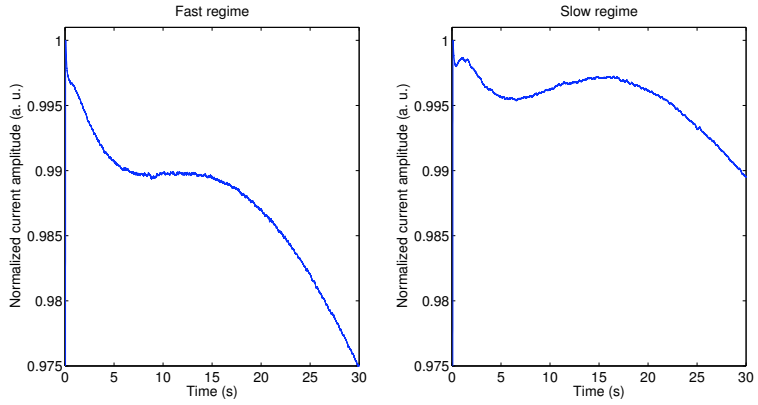

Figure 4.26: Left: Normalized fast regime current amplitude. Right: Normalized slow regime current amplitude

growth rate and thus a variation of the dust density (n_d)/dust size (r_d) ratio in the plasma from the first instants after the discharge ignition. Indeed, it has been shown that dust particle growth is very sensitive to gas purity. Thus slight differences in gas purity from one plasma run to another can induce important deviations in dust density and size. In the case of the slow regime DPGI, a reduced dust growth rate can be assumed. Thus, electron attachment onto dust particles is lesser (smaller dust particles density and/or smaller particles) and the decrease of current amplitude is not as significant as in the case of the fast regime DPGI for which the growth rate is supposed to be larger. Low frequencies of the DPGI phases indicate that the dust density for the slow regime should be lower. As these frequencies are less than 100 Hz, they should be related to the dust plasma frequency which is proportional to $\sqrt{n_d/r_d}$. Thus if this ratio is small, the dust frequency is also small. Ref.[59] proposed that the instabilities related to dust particle growth begin when the dust particle radius r_d reaches a critical value. Thus, for reduced growth rates it takes a longer time to reach this critical dust radius. It has been shown in previous sections that the particle growth slows down for low argon pressure. This result was derived from the DPGI appearance time in the case of the PKE-Nefedov reactor but was confirmed by the results of the ComPLExS reactor. This observation tends to confirm the correlation between the dust growth rate and the DPGI regimes as slow growth kinetics have

already been associated with long DPGI appearance times.

Finally, our observations show that void formation is not a consequence of the DPGI as proposed in Ref.[59]. Indeed, the void can sometimes be observed before the DPGI start. It tends to happen when dust particle growth is very slow and in this case, the DPGI evolution scheme does not exhibit all the phases described previously.

4.2.2 Instabilities in ComPLExS

DPGI were also observed in the ComPLExS reactor. They appear typically a few tens of seconds after the discharge ignition. As can be seen in Fig.4.27, DPGI can be identified by strong oscillations of the self bias voltage of the powered electrode. By looking at the plasma glow, they can also be linked to a strong spatiotemporal modulation of the plasma luminosity (not presented here). It is worth mentioning that DPGI were mainly observed when the pumping time between experiments exceeded 12 hours (Regimen A) confirming the importance of the gas purity. However, due to the the limit of resolution of the digital oscilloscope available in the Complex Plasma Laboratory, a complete study of this DPGI was not possible.

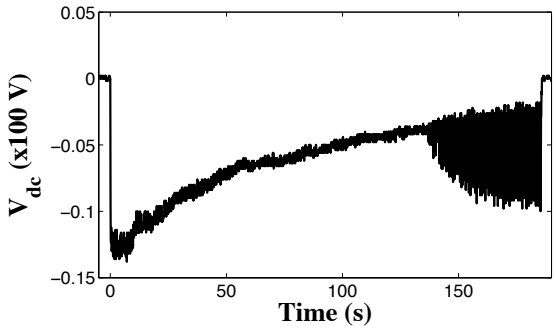

Figure 4.27: Evolution of the self-bias voltage in the ComPLExS reactor for P=1.2 Torr and V_{pp} =240 V. Instabilities during the growth appear as strong oscillations in the self-bias voltage

4.3 Conclusion

In this chapter, the growth of dust particles by RF sputtering in two different RF discharges have been investigated experimentally. It has been shown that the presence of dust particles changes drastically the discharge properties and the plasma parameters. The dust growth kinetics can be monitored by following the discharge characteristics (self-bias voltage, current amplitude, glow modification (focussed optical fibre and high speed video imaging)) and the plasma parameters deduced from Langmuir probe and spectroscopy measurements. It has been thus shown that the growth of the dust particles modify consequently the electron energy distribution function (EEDF). The presence of growing dust particles increases the effective electron temperature of the plasma while the high energy tail of the distribution is thought to be depleted due to

charging of the dust particles.
The influence of plasma conditions have also been studied. It has been shown that high pressures are favourable to the dust particle growth in flowing and static gas. The gas purity plays also an essential role in the dust particle growth process. It has indeed been reported that very low base pressure and long pumping time between experiments are necessary to achieve high dust density and fast dust growth kinetics. The influence of the input power or RF peak to peak voltage have also been investigated. It has been found that high power or large RF peak to peak voltage tend to favour dust particle growth.
Finally, it has been shown that the growth of dust particles can lead to the development of instabilities (DPGI), the evolution of which are directly linked to the dust particle growth rate. The DPGI can be composed of a succession of ordered and disordered phases which were observed in the different studied discharges. However, a complete description of the DPGI evolution pattern has been done only for the PKE-Nefedov chamber due to time and equipment restrictions.

4.4 Résumé du chapitre en français

Dans ce chapitre, la croissance de poudres par pulvérisation dans des décharges RF capacitives a été étudiée expérimentalement. Il est démontré que la présence de poussières modifie grandement les paramètres du plasma et de la décharge. La croissance des poudres peut être suivie en mesurant certains paramètres. Ainsi, la tension d'autopolarisation décroît (en valeur absolue) durant la croissance des poudres à cause de la capture des électrons du plasma par les poudres qui se chargent négativement. La réduction de la tension d'autopolarisation allonge la période de temps autorisant un flux d'électrons sur la cathode et entraîne une diminution du flux d'ions nécessaire au nouvel équilibre. L'amplitude du courant RF diminue aussi lors de la formation des poussières confirmant la diminution de la densité électronique. La collecte des poudres et leur mesure par microscopie électronique ont confirmé que les poudres grossissaient avec le temps dans le plasma mais la variation rapide de la tension d'autopolaristion n'est pas associée à une augmentation rapide de la taille des poussières. Des mesures de sondes de Langmuir associées à de la spectrocopie d'émission ont mis en évidence que la fonction de distribution en énergie des électrons (FDEE) n'est pas maxwellienne et que la température électronique effective augmente durant la croissance des poudres. Les mesures spectroscopiques confirment l'augmentation de la température électronique mais suggèrent la perte des électrons énergétiques de la queue de la FDEE.

L'influence de différents paramètres de la décharge sur la croissance des poudres a aussi été étudiée. Ainsi, les pressions élevées sont favorables à la formation de poussières que ce soit avec ou sans flux de gaz. De plus, des pressions de base très basses ainsi que de longues périodes de pompage avant chaque expérience sont nécessaires pour obtenir des densités de poudres élevées et des cinétiques de croissance rapides. On peut donc en déduire que la pureté du gaz joue aussi un rôle essentiel dans le processus de croissance. L'influence de la puissance injectée ou de la tension de polarisation RF a aussi été étudiée. Il semblerait que de fortes puissances ou des tensions RF élevées favorisent la formation des poussières.

Enfin, la croissance de poudres peut déclencher des instabilités du plasma : les instabilités de croissance des poudres. Ces instabilités suivent un schéma dévolution précis constitué de différentes phases d'amplitudes et de fréquences définies. La valeur des fréquences associées aux instabilités indique que les poudres jouent un rôle majeur dans leur apparition et leur développement. Certaines de ces phases peuvent être comparées aux modex filamentaire et "great void" précédemment observés durant des expériences où les poudres étaient formées par pulvérisation RF [74]. Deux régimes d'instabilités sont observés : un régime lent caractérisé par des basses fréquences et une évolution lente, et un régime rapide caractérisé par des hautes fréquences et une évolution rapide. Ces régimes peuvent être reliés à la cinétique de croissance des poudres, une cinétiques lente induisant le régime lent (les fréquences faibles impliquant des densités faibles et/ou des poudres de grandes tailles).

Chapter 5

Dust cloud instabilities in a complex plasma

After the growth of the dust particles, the gap between the electrodes is filled with a dense cloud of dust particles. The discharge therefore behaves in a completely different manner than a pristine discharge. As the dust particles are charged, the plasma can exhibit many new phenomena directly linked to the dust particles. As the dust particles are massive compared to the other species of the plasma, the phenomena involving dust particle dynamics are relatively slow allowing experimental observation at the fundamental level.
In a complex plasma, a region free of dust particles in the centre of the discharge called a "void" is very often observed [59, 61, 73]. The void is characterised experimentally by a sharp boundary where the dust density changes abruptly (Fig.5.1). Much theoretical work has been devoted to

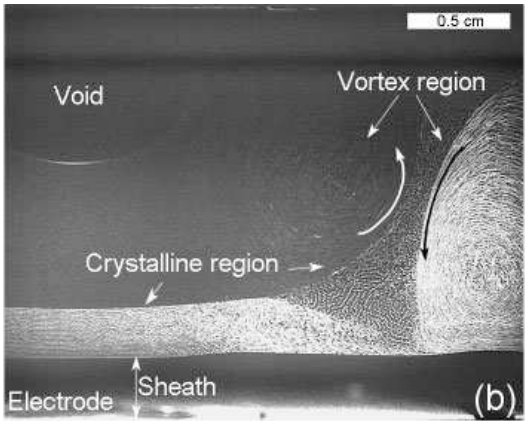

Figure 5.1: Void region in typical dust particle clouds with various sizes of grown particles with crystalline regions and vortex motions (Image from Ref. [61]).

the formation and behaviour of dust voids in complex plasmas [8, 58, 76, 142–147]. The current theory can be summarised as follows: the void is thought to be triggered by an ionisation instability. The ion drag force due to ions flowing from the plasma is thought to maintain the void by balancing the electrostatic forces on the charged dust particles, pressure gradient forces and

other forces on the dust particles at the sharp boundary of the void. It has also been suggested that convective effects can have a significant influence on void formation, size and evolution [146, 148]. However there is no unified theory for the dust void formation.
Under some conditions, the stable void can be disturbed and exhibits oscillations. This instability is named the heartbeat instability due to the contraction-expansion sequence of void size which resembles the heartbeat motion of living bodies [58, 60, 76]. It was first reported during microgravity experiments with injected micrometre dust particles [58] and has since been studied in laboratory experiments with grown sub-micrometer dust particles [60, 66–68]. In these experiments, the investigations have been performed using both electrical measurements and spatially resolved optical diagnostics and have revealed the complex behaviour in the heartbeat instability and roughly described the dust particle motion. Furthermore, it has been found that the self-excited heartbeat instability exhibits threshold behaviour [67, 68]: it was shown that the instability can be triggered by increasing the power or decreasing the pressure. However, the existence of the heartbeat instability is not fully understood theoretically and some experimental data are still not well understood (the sharp peak in RF current signal for example).
In a discharge where the dust particles are grown by RF sputtering, continuous growth of dust particles inside the plasma bulk can occur if the discharge parameters are suitable. Thus, even if a dense cloud of dust particles is already present new dust particles can grow in the discharge. In chemically active plasmas, it has been reported that the dust particles growth follows a generation scheme, i.e. dust particles are grown in a homogeneous group (small dispersion in size and shape) called a dust particle generation which appears regularly during the life of the discharge [37, 149]. It has been shown that a new generation of dust particles grows in the void region of the old dust particle cloud [149, 150]. Successive generations of dust particles have also been reported in discharges where the particles were grown by RF sputtering and the new generations also appeared in the the void of the older dust particle cloud [61].

In this chapter, instabilities of the so-called "void" region of a dusty plasma are reported. The next two sections are devoted to the experimental studies of two types of void instability.

- The first type of instability is a self-excited instability of the dust void (the heartbeat instability). It was first reported in microgravity with injected dust particles (Ref. [58] and references therein) and has been observed on ground experiments with dust particles directly grown in the plasma [60]. Here, different regimes of the heartbeat instability are reported.

- Sometimes the appearance of a new generation of dust particles triggers an instability of the older dust void. Here, two classes of instability due to the growth of a new generation of dust particle inside the void (the delivery instability and the rotating void) are reported.

5.1 The heartbeat instability

The equilibrium between the inward electrostatic force and the outward ion drag force maintaining a stable void can in some conditions be disturbed and the void size exhibits oscillations. This self-excited instability is called the heartbeat instability and has been observed during microgravity experiments, studied in the laboratory and investigated theoretically [58, 60, 76, 151, 152]. Typical unstable voids have a size of about a few millimetres. Beyond a certain size (> 1 cm), voids are usually stable and no instability has been observed in the parameter range explored: their stability cannot be disturbed by decreasing the pressure or increasing the power (such changes are known to be able to initiate the heartbeat instability [60]).
The heartbeat instability has different signatures, and measurements (electrical and optical) show a wide range of signal shapes and frequencies. Nevertheless, two extreme cases exist:

- A high repetition rate (HRR) which consists of a continuous motion of the void and surrounding dust particles. It occurs when the heartbeat instability is well-established and the power delivered by the RF generator is high.
- A low repetition rate (LRR) which consists of contraction-expansion sequence (CES) of the void size well separated in time. In between each sequence, the original conditions (i.e. stable void) are nearly restored. It occurs when the instability tends to slow down before stopping when the power delivered by the RF generator is low.

In between these two extreme cases (which we name "classical heartbeats"), the heartbeat instability can exhibit failed contractions between full sequences.
The extreme cases are studied in Sec.5.1.1 and failed contractions are studied in Sec.5.1.2. The experiments have been performed in the PKE-Nefedov chamber where the heartbeat instability is easily observable through large windows. The heartbeat instability was characterised by its discharge current amplitude signature and was also studied by a direct visualization of the void and its surrounding dust cloud as well as visualization of the plasma glow in the whole interelectrode volume.

5.1.1 Classical heartbeats

Isolated contraction (or low repetition rate (LRR))

Images extracted from a LRR heartbeat video and showing the different steps of a contraction-expansion sequence (CES) are presented in Fig.5.2(a). The video was taken at an angle of $\sim 30^\circ$ with respect to the laser sheet that was illuminating the dust cloud in the PKE-Nefedov chamber and consequently, the aspect ratio is distorted due to the angle of view compressing the horizontal direction. The image numbers appear on the top left hand side of each image. The frame rate of the video was 1,789 fps.
The stable void position is determined from image 30 and an ellipse was drawn on each image in order to be able to compare the void shape and size to its stable configuration. The CES starts

at image 40 where a small but detectable motion of the void boundaries is observed. In image 42, the motion appears clearly and the void boundaries are now inside the drawn ellipse. The contraction lasts up to image 55 where the void reaches its minimum size (the contraction time is ~ 9 ms). From this instant, the dust-free inner part slowly increases in size while a light grey corona region (detectable from image 80) slowly reduces in size. These two regions meet and a stable open void is regained in image 265 (the "reopening" time is ~ 120 ms)

In order to better depict a CES, the time evolution of a column profile is shown in Fig.5.2(b).

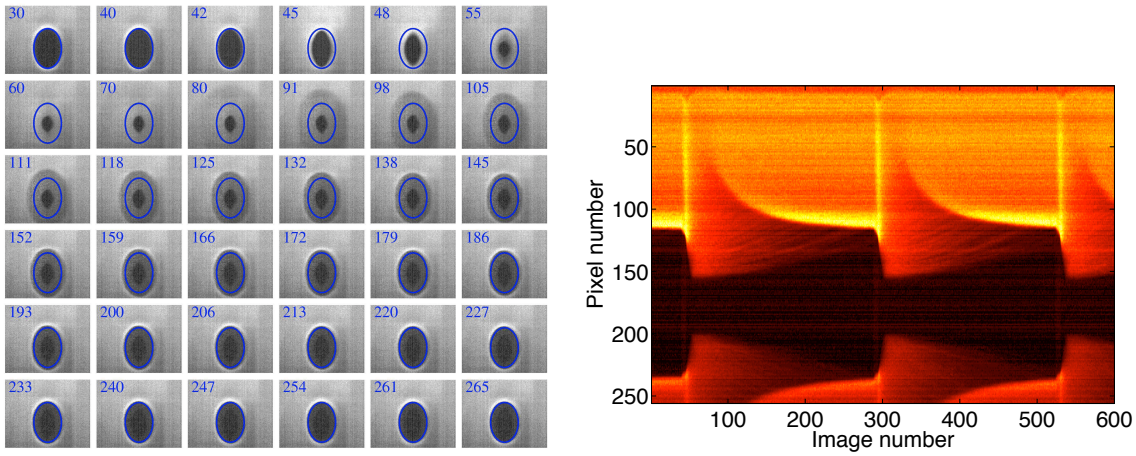

(a) (b)

Figure 5.2: LRR heartbeat instability observed on the dust cloud. (a) Some images of the void region during a CES. The blue ellipse delineates position of the stable open void. (b) Time evolution of the central column profile (vertical line passing through the void centre) constructed from the entire video (False colours from dark red to bright yellow)

This false colour image was constructed by extracting the vertical line going through the centre of the void from each frame of the video. Time is represented by the image number on the x-axis (1 frame is ~ 0.56 ms) and the column profile is given on the y-axis. This representation gives in one single image a clear characterisation of the instability in both space and time. The low dust density region appears dark while the high dust density region are bright. Three CES can be clearly seen and the corresponding frequency is about 7 Hz. Before the first CES (images 1 to 40), high dust density regions are observed at the void boundaries. Then, the CES starts: the contraction takes place and the void reaches its minimum size approximately 2.5 times smaller than the stable void region. From this moment, the size increase of the dark dust-free inner part and the size decrease of the intermediate corona region are well resolved: the regular size increase of the dust-free inner part can be correlated with void size increase (i.e. a void "reopening") assuming that the term "void" refers only to the zero dust density region. From Fig.5.2, the corona region seems to correspond to the motion of dust particles attracted to the plasma centre during the contraction and returning to their original position: this motion is characterised by a moving boundary between a region of high dust density and a region of low dust density. The speed of the moving boundary decreases when it approaches

the original position. The dust particles which come closest to the centre during the contraction react last with the smallest speed. As can be seen, the corona region at its maximum extension is much larger than the stable void. It clearly indicates that the dust particle cloud is affected over a long distance and not only in the vicinity of the void boundary. Collective motions can take place over long distances due to the strong interactions between the dust particles and their strong coupling with plasma parameter changes. Finally, Fig.5.2(b) shows that the inner and corona regions meet (around image 280) and high dust density boundaries are restored just before another CES occurs.

To complete these observations, the interference filter was removed from the high speed camera

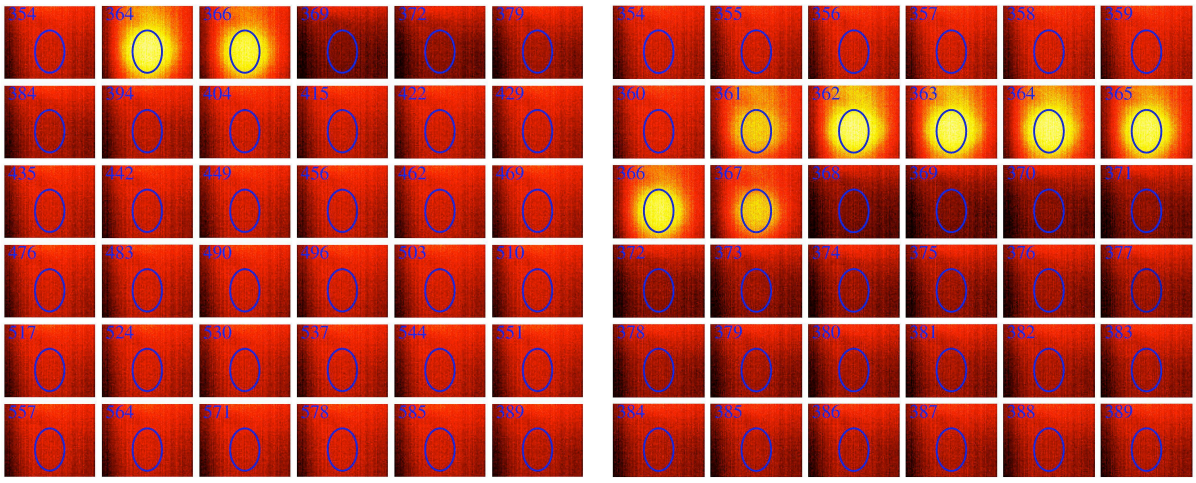

(a) (b)

Figure 5.3: LRR heartbeat instability observed on the plasma glow (in false colour from dark red to bright yellow). (a) Some images of the void region during a CES (image 354 is equivalent to image 30 in Fig.5.2). The blue ellipse delineates position of the stable open void. (b) Intermediate images of (a) during fast plasma glow modifications

in order to record the plasma glow evolution without changing the camera position. The acquired video was obtained ∼2 s after the first one. The electrical measurements were used to check that the instability characteristics (frequency and shape) remained unchanged. In order to synchronise the dust cloud images with the plasma glow images, the small residual plasma glow signal passing through the interference filter was used (slightly visible in Fig.5.2(b) at the beginning of each contraction). Typical images are presented in Fig.5.3(a). In order to bring out changes, a reference image corresponding to a stable void configuration is subtracted from each image and false colours are used. The plasma glow images presented in Fig.5.3(a) correspond to the dust cloud images presented in Fig.5.2(a) (image 30 in Fig.5.2(a) corresponds to image 354 in Fig.5.3(a)and so on). The ellipse corresponding to the stable void that was used on the dust cloud images is also superimposed onto the glow images to facilitate the comparison.

From Figs.5.2(a) and 5.3(a) it clearly appears that the void contraction corresponds to a glow enhancement in the plasma centre. Intermediate images of the fast glow variation occurring

during the contraction are shown in Fig.5.3(b). It appears that the glow is enhanced in a region bigger than the original void even though the larger values are inside the void region. This phenomenon can explain why the corona region observed in Fig.5.2 has a maximum extension bigger than the original void since the plasma is affected over a large volume. The first image showing a glow increase is image 361 in Fig.5.3(b). At this time, the enhanced glow region is already bigger than the drawn ellipse. Due to camera speed limitations (0.56 ms per image) some data are missing between images 360 and 361. Consequently, it cannot be concluded, whether at the very beginning the glow enhancement is bounded by the void and then propagates, or it affects directly a large volume of the plasma bigger than the void region. After reaching its maximum luminosity (around image 364) the plasma glow decreases and reaches a minimum below the mean glow value (darker image 369 in Fig.5.3(a)). Due to dust inertia, the void continues to shrink (Fig.5.2(a)) but when the central glow (i.e. ionisation and consequently ion drag force) starts to increase slowly, the contraction stops and the void starts to reopen (image 55 in Fig.5.2(a) and image 379 in Fig.5.3(a)). The column profiles of these different

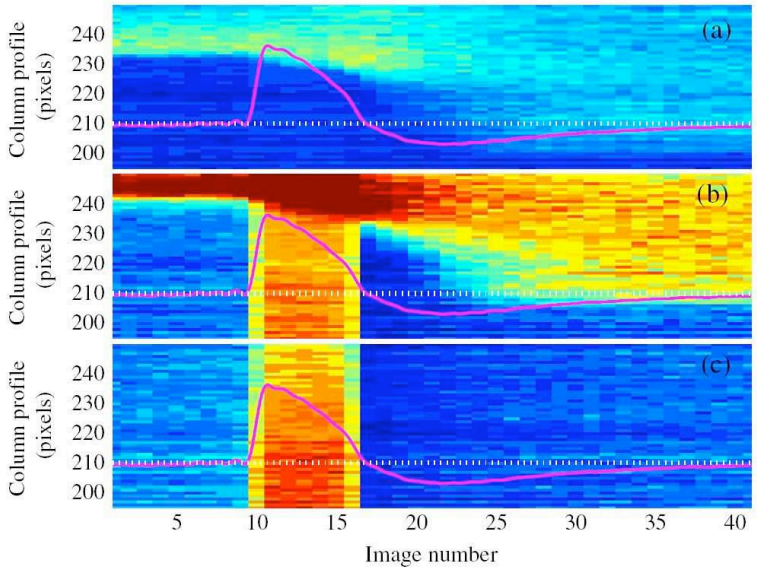

Figure 5.4: LRR heartbeat instability: current amplitude superimposed on column profile for (a) only dust cloud; (b) dust cloud and plasma glow; (c) plasma glow only. Parts (a), (b) and (c) are in false colours from dark blue to red

series are compared in Fig.5.4. This figure shows synchronised profiles obtained from videos showing (a), the dust cloud (obtained using the laser and the interference filter), (b) the dust cloud and the plasma glow (using the laser and the camera without the interference filter) and (c) the plasma glow only (neither laser nor interference filter). The amplitude of the discharge current is superimposed with its mean value (dotted line) corresponding to the stable open void. There is a particularly good correlation between the current and the plasma glow as the main variations are related (Fig.5.4(c)):

- The fast current increase ($\sim$ 0.5 ms) corresponds to the glow enhancement; it is followed by a decrease in both sets of data.
- A small slope change appearing in the current amplitude is related to a faster decrease of the central plasma glow.
- Both parameters values reach their minimum at almost the same time
- Finally, the plasma glow increases to its mean value and the current amplitude slowly tends towards its mean value

The void contraction is therefore related to glow and current amplitude increase (Figs.5.4(a) and 5.4(b)), implying that it is correlated to an increase of the ionisation in the plasma centre. As mentioned, global variations of the glow and the current amplitude are similar but some discrepancies exists due to the fact that the current integrates all the plasma and thus contains information about plasma variations occurring outside the plasma centre.

Consequently, in order to see the global evolution of the plasma glow and to be able to identify some side effects already suggested (relation between a sharp peak in the current amplitude and glow enhancement in the horizontal direction near plasma boundaries [60]), the plasma glow has been recorded over the whole inter-electrode space. The camera was facing the PKE-Nefedov reactor and focussed on the centre of the chamber.
The total plasma glow recorded by fast video imaging (1,789 fps) during CES is presented in Fig.5.5(a). The CES was not exactly the same as the one described previously but was very similar (the frequency was lower). The presheath region above the upper and the lower

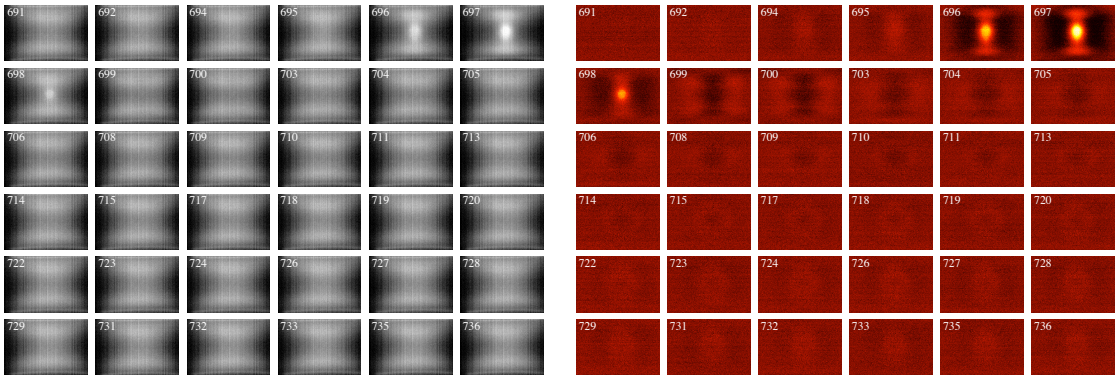

(a) (b)

Figure 5.5: Total plasma glow during a CES of LRR heartbeat instability: (a) some raw images in grey scale directly extracted from the video; (b) same image as (a) with post-processing and false colours (from dark red to bright yellow)

electrodes can clearly be seen in the images in Fig.5.5(a). They correspond to bright regions at the top and the bottom (the electrodes cannot be seen). Before the CES, the central plasma region is uniform with moderate brightness (image 691). Then the glow increases quickly and

concentrates in the discharge centre before disappearing and leaving a darker region in the centre as described previously. In order to emphasise the changes in the plasma luminosity, the glow of a stable configuration has been chosen as a reference image and has been subtracted from every other images. The results are presented in false colour in Fig.5.5(b). As can be seen, the relatively homogeneous glow (image 691) changes into a bright central region (i.e. with higher ionisation) and dark edges (i.e. with lower ionisation) during the contraction. A reverse situation (dark centre and bright edges) starts just before the reopening (image 699). Finally the plasma glow slowly returns to a uniform configuration.

The time evolution of a line profile is presented in Fig.5.6(a) and magnified in Figs.5.6(b) and

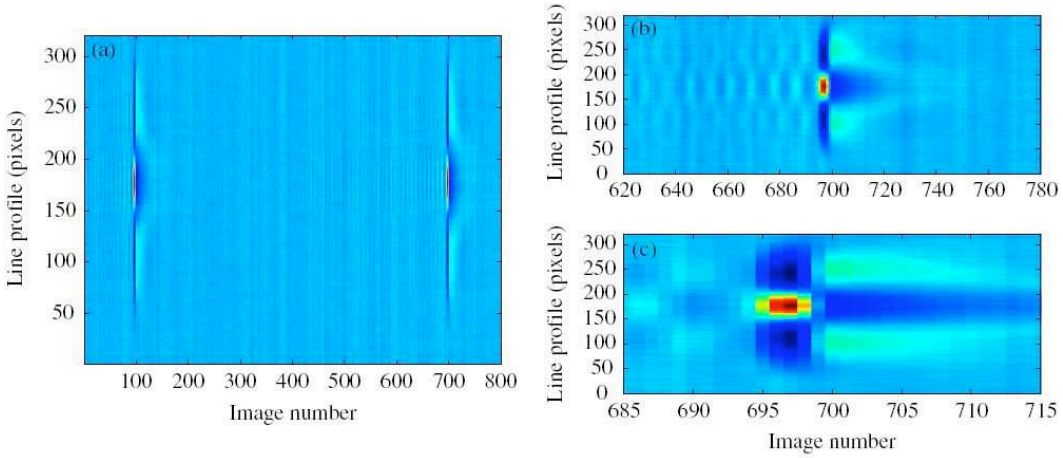

Figure 5.6: LRR heartbeat instability: (a) Line profile (in false colours from dark blue to red) extracted from the image series presented in Fig.5.5; (b) and (c) are different magnifications of (a)

5.6(c). This image was constructed by extracting the line passing through the middle of the discharge from each video frame. This line was chosen because it passes trough the region with the biggest luminosity variations. In order to emphasise the glow variation, the temporal average value of the pixels of the line was subtracted from each corresponding pixel. A smoothing filter was also applied for noise reduction and a better delineation of the changing regions. Column profiles were also extracted for the plasma glow analysis but are not presented here since no original information could be obtained partly due to limitations imposed by the electrodes.

Nearly isolated CES often have very short time duration. In Fig.5.6, the frequency of the instability is around 3 Hz. In between each CES, the original conditions have time to be restored. The complete analysis of the evolution of the plasma glow is easily performed from Figs .5.6(b) and 5.6(c). First some small oscillations are observed before the real CES and correspond to failed contractions appearing near the instability threshold. This behaviour does not change the following analysis and is described in details in Sec.5.1.2. Fig.5.6 confirms that when the void contracts, the glow suddenly concentrates leaving dark edges. The void reopening occurs during the reverse situation with two symmetrical bright regions surrounding the plasma centre. Then these regions diffuse slowly toward the centre until a homogeneous glow is obtained once again.

The correlation with the current amplitude is shown if Figs.5.7(a) and 5.7(b) with non-smoothed

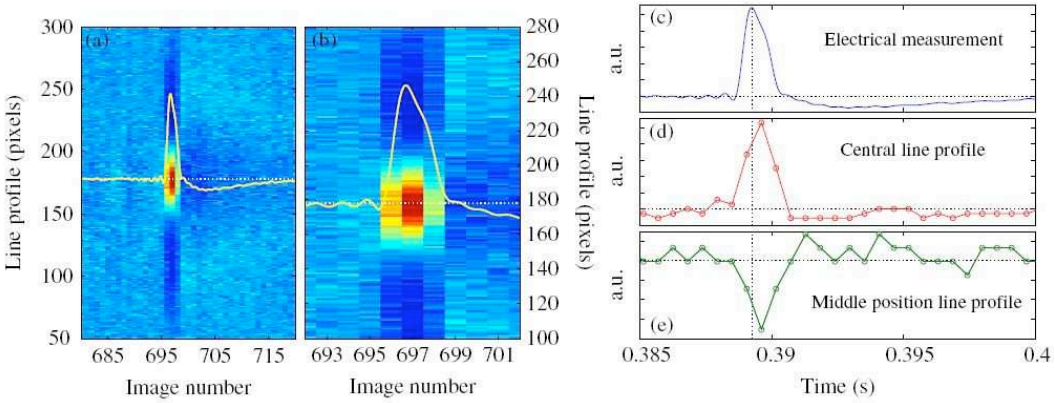

Figure 5.7: LRR heartbeat instability: (a) Line profile (in false colours from dark blue to red) calculated from the image series presented in Fig.5.5 with the current amplitude superimposed; (b) zoom of a; (c) current amplitude; (d) central line (line 178) profile of (a)); (e) middle position line (line 105) profile of (a)

images in order to get pixel precision. The dotted line represents the direct component of the current amplitude. As can be seen, the void contraction corresponds to an increase of the current and thus an increase of the global ionisation. Indeed an increase of the central plasma glow corresponds to an increase of the current amplitude meaning that the central increase is not compensated by the glow decrease at the plasma edge. Then, when the reverse situation occurs, the ionisation appears to be below the stable situation value (current amplitude is below its mean value): the dark central region is not balanced by the larger but slightly brighter near edge regions. Finally these regions tend to rejoin in the centre following the slow increase in the current amplitude. These behaviours are also visible by comparing the evolution of the current amplitude with line profiles (Figs.5.7(c)-(e)) extracted from Fig.5.7(a) (not to be confused with the temporal evolution of the line profile extracted from the video images) and physically corresponding to the time evolution of individual pixels taken in (d) the plasma centre and (e) the near edge.

Successive contractions (or high repetition rate (HRR))

The analysis of a HHR heartbeat sequence is more difficult as the dust cloud is moving fast and constantly. Consequently, the dust cloud has no clear stable position. In Fig.5.8, images and column profile (i.e. vertical line passing through the void) have been extract from a high speed video of a HRR heartbeat. The frame rate was 1,789 fps. In order to increase the contrast, false colours have been used to plot the extracted images. The frequency of the instability was in this case 31 Hz. As can be seen, it clearly appears that the dust cloud has a constant motion. Indeed, horizontal bright regions , corresponding to high dust density void boundaries, are not observed in Fig.5.8. Furthermore, an inner part of the void region which is always free of dust can be identified. This region exhibits only small variations of its size. Dust motion takes place

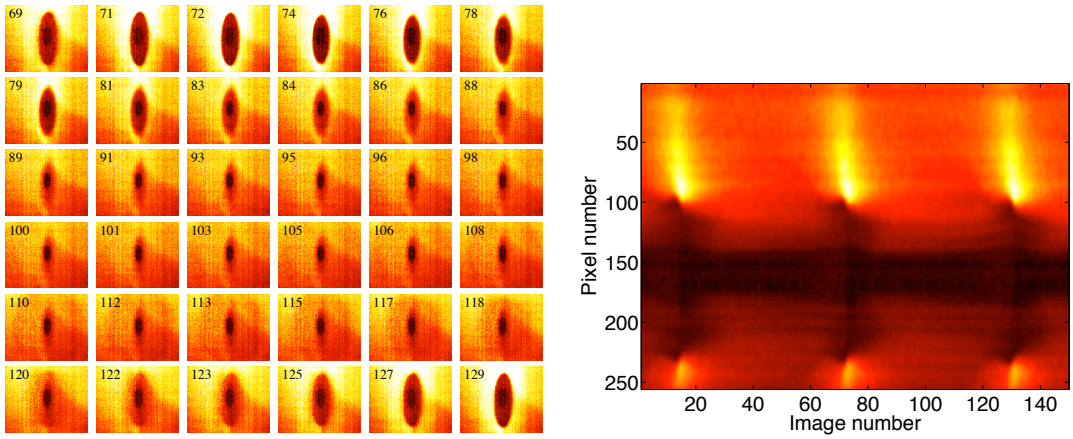

(a) (b)

Figure 5.8: HRR heartbeat instability observed on the dust cloud: (a) some images of the void region (in false colours from dark red to bright yellow; (b) time evolution of the central column profile constructed from the entire video.

in a low dust density region between the dense dust cloud and the dust-free inner part of the void. In the LRR heartbeat sequence, this region has been identified as dust particles going back to their original position. In the HRR heartbeat, a new contraction of the void occurs while the dust particles that entered the void during the previous contraction are still inside and try to reach their original position. As can be seen in Fig.5.8(a), a new contraction starts around image 69 (complex motion does not allow precise determination) while dust particles are still inside the void region. At this time the plasma glow is close to its maximum value in the centre (determined from the video of the plasma glow correlated to the present one). This complex behaviour leads to the relatively constant regions observed in Fig.5.8(b): a dust free black inner region and a low dust density grey intermediate region as the constant motion of the dust cloud maintains more or less constant spatial dust density.

The analysis of the entire plasma glow between the electrodes was also performed for a HRR heartbeat. The experimental procedure was the same as the one described previously for a LRR heartbeat. The frame rate was 1,789 fps. The images extracted from the video are presented in Figs.5.9(a). Fig.5.9(b) was constructed with the same post-processing procedure as Fig.5.5(b) (subtraction of a reference image).

In a HRR heartbeat, the frequency of the CES is such that no exact return to the original stable conditions is achieved and the next CES occurs while the void has not reached its stable state. However the sequences last longer (i.e. there are more CES cycles but the different parts of each CES are not as abrupt as in a LRR heartbeat where the sequence are almost isolated cycles), a better time resolution is obtained and the variation of the plasma glow is well in evidence (Figs.5.9(a) and 5.9(b)). Indeed, for example, the central glow increase lasts for 3 images ($\sim$ 1.5 ms) in the LRR case while it lasts for 17 images ($\sim$ 9 ms) in the HRR case. In comparison with the LRR case, the change from bright centre and dark edges to the reverse situation is more

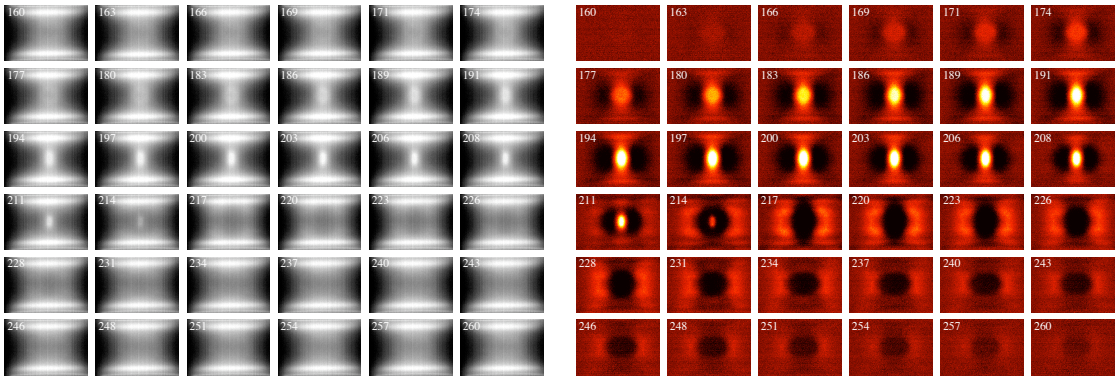

(a) (b)

Figure 5.9: HRR heartbeat instability observed on the total plasma glow: (a) some raw images directly extracted from the video during a CES; (b) same images as (a) with post processing and false colour (from dark red to bright yellow)

strongly marked. The different phases of the CES are the same as previously described for the LRR case but are more distinguishable in the present case.
The extracted line profile is very significant and summarises nearly all results concerning the plasma glow evolution during the heartbeat instability (Fig.5.10). Starting from a void expansion (dark inner part and bright plasma edges), the glow slowly concentrates from the plasma edge towards the centre. This motion can be correlated to the grey corona region observed in the dust cloud and described previously. Furthermore, it clearly appears that the brighter edge regions do not meet completely and no homogeneous plasma is restored as can be seen for a LRR heartbeat (Fig.5.6). The central glow increases at the expense of the plasma edges before the

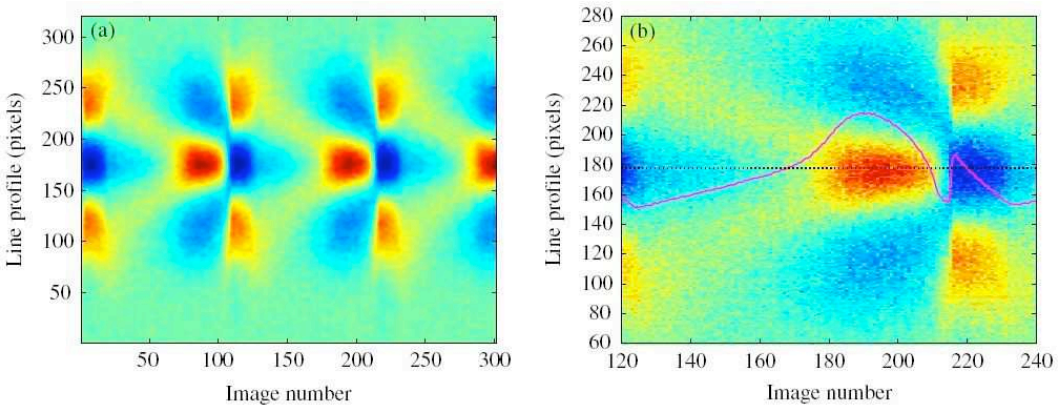

Figure 5.10: (a) Line profile (in false colour from dark blue to red) calculated from the image series presented in Fig.5.9. (b) Zoom of (a) with electrical measurement superimposed.

brighter glow regions have fully converged toward the discharge centre. This central enhancement is then followed by a strong and fast reversal. The amplitude of the discharge current during the instability is superimposed on the line profile in Fig.5.10(b). The bright regions moving from the plasma edge towards the plasma centre correspond to a continuous increase of the

current. Then it appears that the strong reversal of the brightness is related to the presence of a sharp peak in the current. Measurements without this peak certainly correspond to cases where the brightness reversal between the plasma centre and the edge exists but is not as strongly marked (see Fig.5.7 for example). This sharp peak is an interesting feature already observed but not fully explained. In Ref.[60], Mikikian preliminary results suggested that this peak could be correlated with a strong glow decrease in the centre and an increase at the plasma edge. The measurements were performed thanks to a spatially resolved analysis of the argon line emission at 750.39 nm (four different positions). Further results with five optical fibres (also used for the characterisation of the dust particle growth instability (Sec.4.2) and integrating all plasma wavelengths gave similar results [68] but no complete description was available. The present results greatly enhance spatiotemporal resolution of this phenomenon and clearly correlate the sharp peak with an enhancement of the plasma glow outside the central region. Variations of the current amplitude are representative of global change in the plasma. Consequently, from the present analysis, it appears that the discharge current is not dominated by the plasma core only.

These effect are also seen in Fig.5.11 by direct comparison of (a) the evolution of the current am-

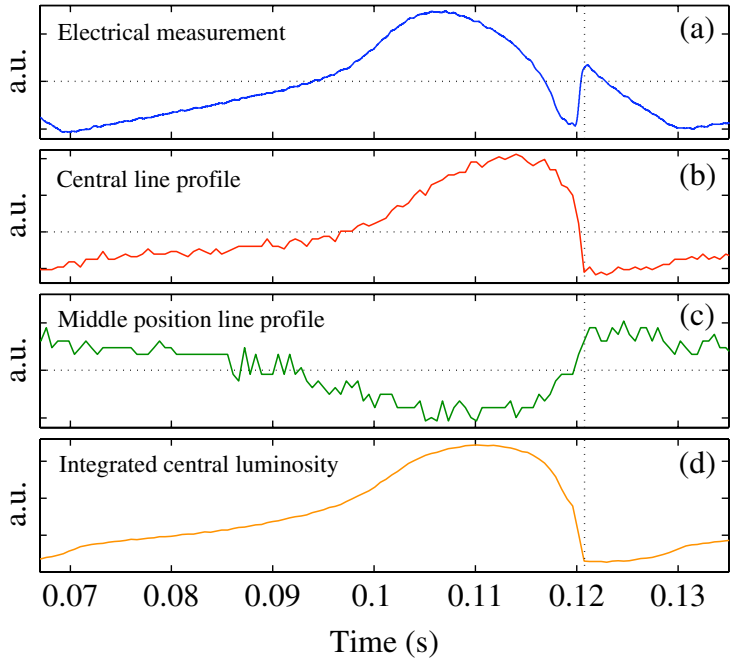

Figure 5.11: Extracted data from Fig.5.10: (a) amplitude of the current; (b) central line profile; (c) line profile in the plasma edge (glow reversal region); (d) Plasma glow integrated over a small central volume from complete image series of Fig.5.9

plitude with data extracted from Fig.5.10: (b) central line profile (i.e. physically corresponding to the evolution of the signal of the central pixel), (c) middle position line profile (i.e. variation of the signal of a pixel in the glow reversal region) and directly from the video: (d) integrated central luminosity (i.e variation integrated over a small centred area assumed to represent the

core of the plasma). As can be seen, the main plasma centre changes are observed in the current amplitude evolution. Nevertheless, it appears that the maximum value of the central glow occurs while the current has already started to decrease. In fact, at this time, electrical measurements are affected by the edge plasma glow decrease as observed in Fig.5.11(c). Finally, the sharp peak in current amplitude is directly related to the strong and fast enhancement of the plasma edges while the centre become the less luminous part. This result confirms the preliminary results obtained by Mikikian and Boufendi (Fig. 7 of Ref.[60]).
In order to have a good temporal resolution of the glow reversal, very high speed video imaging (10,000 fps) of the plasma luminosity has been performed. The evolution of the luminosity of the central line (line going through the plasma centre) is presented in Fig.5.12. In order to highlight the glow variation, the temporal average value of each pixels of the line was subtracted from the corresponding pixel. As can be seen in Fig.5.12, the glow reversal does not seem to

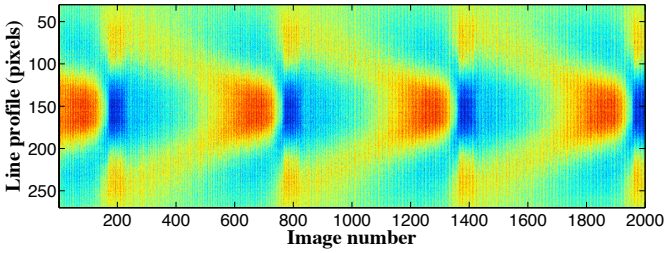

(a)

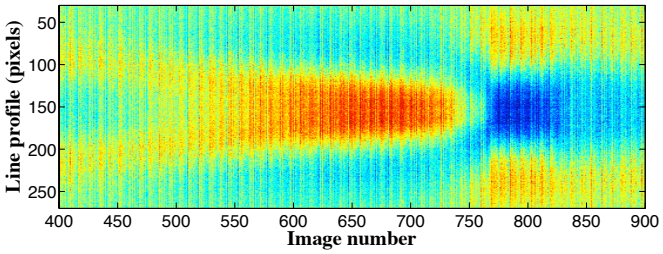

(b)

Figure 5.12: (a) Evolution of the central line luminosity of the images extract from very high speed video (10,000 fps) during a HRR heartbeat (in false colour from blue to red). (b) zoom of (a)

correspond to a fast propagation from the centre to the edge of the plasma. Indeed the plasma edge luminosity increases at the same time the plasma centre luminosity decreases while, in the intermediate region, the luminosity does not vary significantly. Following the hypothesis that a strong glow luminosity corresponds to a high ionisation rate, it indicates that the ionisation is favoured at the plasma edges but no ionisation waves seems to propagate from the centre toward the edge.

Asymmetry in the void contraction during the heartbeat instability

An interesting phenomenon concerning the dust cloud motion during the heartbeat instability is the observable delay appearing in the response of the horizontal and vertical directions. Indeed in some conditions (currently not clearly defined) the dust cloud shrinks horizontally before shrinking vertically [67, 68]. As an example, a record containing both the dust cloud and the plasma glow when a stable open void suddenly became unstable and started size oscillations is shown in Fig.5.13. The frame rate of the video was 1,789 fps and the two first CES are shown. In Fig.5.13, image 135 clearly shows the stable open void with the corresponding drawn ellipse.

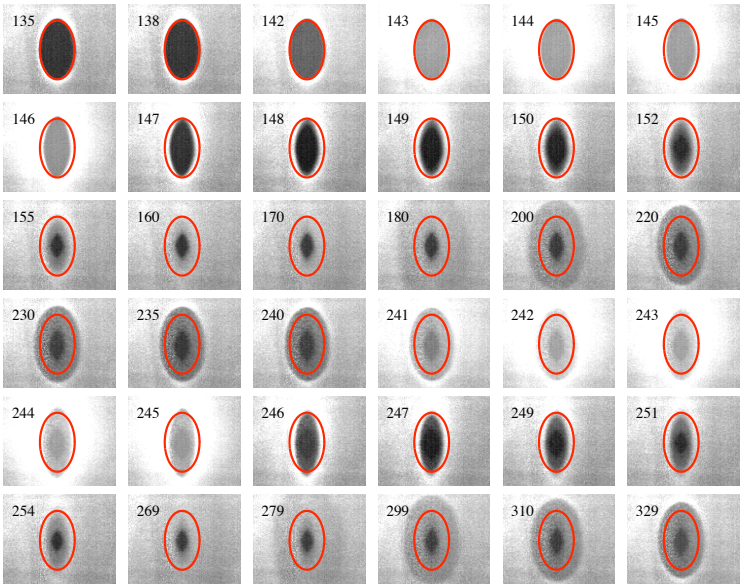

Figure 5.13: Simultaneous record of the plasma glow and the dust cloud in the void region during the setting up of the heartbeat instability. From image 135: stable open void (delineated by a red ellipse) followed by a first contraction. A new contraction starts at image 241 before the original conditions have been restored

In image 142 the plasma glow starts increasing and reaches its maximum value at image 144. In this last image, it appears that the plasma glow enhancement affects a region larger than the void size and a correlation with the corona region previously mentioned can be suggested again. This hypothesis is correct assuming that the intensity increase in the surrounding dust cloud is entirely due to plasma glow changes and not due to any dust density changes. The drawn ellipse allows us to see that the void first collapses in the horizontal direction (image 143) followed by a contraction in the vertical direction (image 147). As the images are compressed in the horizontal direction due to the angle of view of the camera, a detectable motion on the horizontal axis clearly indicates a motion of the dust cloud and cannot be an artefact. The plasma glow reaches its minimum around image 148 and, as already observed, the void continues to shrink to its minimum size around image 155. From this point, the inner part of the void slowly increases in size and the grey intermediate region, consisting of dust particles going back to their original position, becomes gradually visible. The next CES occurs before the initial

conditions have been completely restored (image 241).

These various steps are well observed on the column profile shown in Fig.5.14(a). For a better

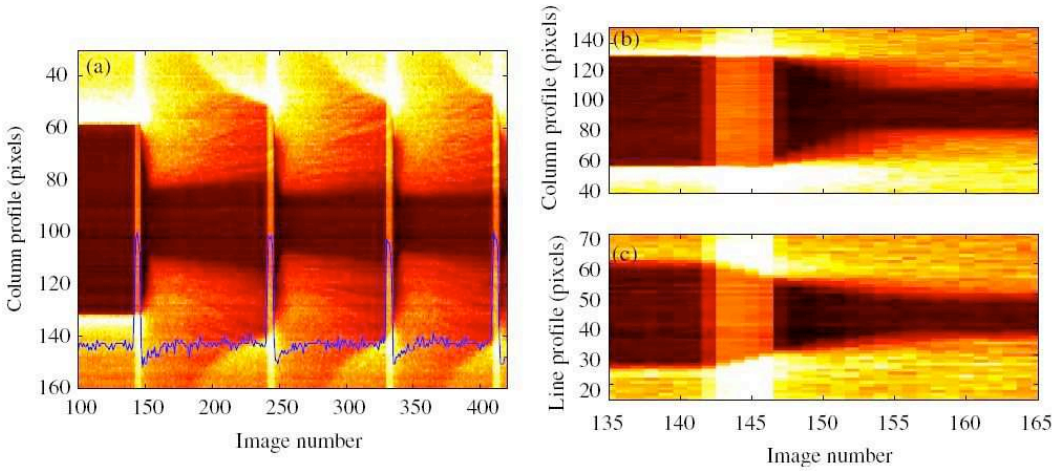

Figure 5.14: (a) Column profile (in false colour from dark red to bright yellow) extracted from image series presented in Fig.5.13 with central plasma glow evolution superimposed (blue curve corresponding to line 95 of Fig.5.14(a)) (b) zoom of (a), (c) corresponding line profile.

understanding, the temporal evolution of the glow (central pixel of the void) is superimposed at the bottom of the image. The stable void is accurately defined with its constant size and its high dust density boundaries (between image 100 and 142). When the plasma glow increases, the void shrinks. Its minimum size is reached while the plasma glow in the plasma centre has already reached its minimum value and has started to slowly increase again. Then the glow stays relatively constant in the void centre while dust particles are expelled to their original position. It clearly appears that the void did not reach its original size when a new glow increase occurs. This effect is characterised first by a dark inner region which does not rejoin the position of the stable void and second by the intermediate corona region which is bigger than the original void size. This last point means that the "wave front" formed by the returning dust particles is still moving towards the original void boundaries. The speed of this wave front slows down when approaching the original conditions. Furthermore, it is clear that the instability is in a setting up phase: starting from a stable open void, the characteristics of the first and the second CES are slightly different in terms of minimum void size and reopening time duration. Concerning the time delay appearing in the vertical direction (see Fig.5.13) it can also be seen by comparing column and line profiles extracted from the video. These two profiles are shown respectively in Figs.5.14(b) and 5.14(c). Mikikian *et al.* suggested that the different collapse times can be correlated with the different slopes in the current signal [67]. The reason for this asymmetry is still unclear due to the lack of statistics and the spatiotemporal limitations of the video acquisition. Nevertheless, one possible hypothesis is the geometry of the PKE-Nefedov reactor and the different confining conditions in the horizontal and vertical directions. Indeed the electrode are ~ 4 cm in diameter and glass boundaries are ~ 3 cm away from the electrode edges. Consequently, the plasma usually diffuses beyond the electrodes towards the lateral sides.

The plasma width is then nearly twice as large as the height and it is nearly the same for the trapped dust cloud and the void. No strong electrostatic barrier exists due to the distance to the glass boundaries and the plasma and the void changes in the horizontal direction are relatively unconstrained. On the contrary, the electrodes impose a strong electrostatic barrier in the vertical direction and thus changes and motion in this direction are drastically controlled by the sheaths.

5.1.2 Failed or aborted heartbeat

It has been observed previously that sometimes the CES during an heartbeat instability are not complete and terminate before a void contraction has occurred [68, 75]. It results in failed or aborted peaks easily observable on the discharge current amplitude.
In Fig.5.15, the AC component of the amplitude of the discharge current has been recorded for no failed peak in a HRR heartbeat, 1 failed peak, 2 failed peaks and 3 failed peaks. The presented signals come from the same experiment, where the heartbeat instability exhibits more and more failed contractions. On the time axis the 0 has been chosen at the minimum value of the current amplitude of a complete CES in order to be able to compare its evolution during a full CES for the different cases. As can be seen, the evolution of the current just after the

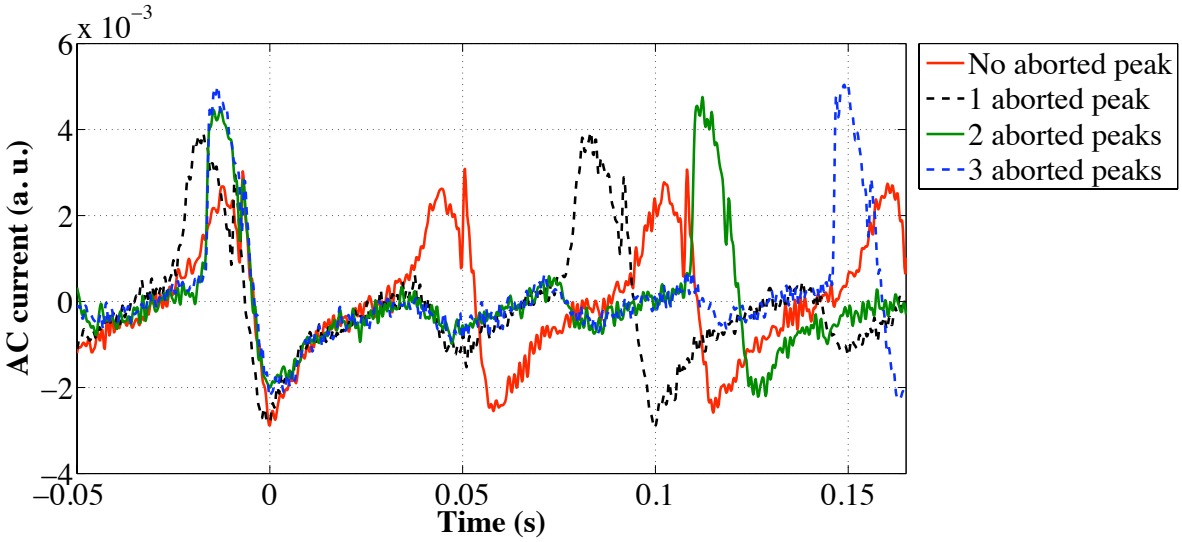

Figure 5.15: Current during the heartbeat instability for different number of aborted peaks

sharp current decrease corresponding to the void contraction is very similar in all cases: the current increases until it is a little above its mean value (0 in Fig.5.15 as it does not show the DC component of the current). Then, as the signal corresponding to a heartbeat without failed peak continues to increase and follow the same behaviour as describes previously for a HRR heartbeat, the other signals decrease. All signals with at least one failed peak reach a minimum at the same instant and the current starts to increase again. The signal with only 1 failed peak exhibits then a complete sequence while the two other ones decrease again. The same difference

is then observed between a signal with two failed peaks and 3 failed peaks. It has to be noted that a failed peak occurs exactly at the instant a full CES is expected. This behaviour tends to confirm that the heartbeat instability is a threshold phenomenon. Another feature that can be observed in Fig.5.15 is the increase of the sharpness of the major peak when the number of failed peaks increases. Indeed, as can be seen, the duration of the fast increase followed by the fast decrease in the current amplitude is shorter when the number of failed peaks is larger.
The transition from one aborted peak to two aborted peaks on the current signal is analysed in details in Fig.5.16. In Fig.5.16(a), the evolution of the amplitude of the current (blue curve) is shown. The instantaneous energy (red curve) calculated from Hilbert-Huang analysis (see App.B) is superimposed on the current. In Fig.5.16(b) the Fourier spectrogram of the current is plotted and in Fig.5.16(c) the Hilbert-Huang spectrum is shown. As can be seen, the transition occurs at time $t \sim 1.5$ s. In the Fourier spectrogram (Fig.5.16(b)), the transition results in a decrease of the main frequency from 12 Hz to 8.5 Hz and the appearance of more harmonics in the signal. In the Hilbert-Huang spectrum (HHS) (Fig.5.16(b)), the transition is also accompanied by a decrease of the main frequency from 11.5 Hz to 8 Hz. It worth mentioning that in the Hilbert-Huang analysis, the intensity of a frequency at a time instant represents the probability of a wave with such frequency to develop (see App.B). The main advantage of the HHS is that the transition can be precisely identified in the frequency domain as it records the instantaneous frequency (see App.B). Thus, it can be seen that the red line around 11.5 Hz at $t = 1$ s decreases at $t = 1.5$ s which is exactly when the transition occurs on the current signal (Fig.5.16(a)). The other advantage of the HHS spectrum is that it permits identification of the main frequency components of the signal without their harmonics. Thus, before the transition, the signal exhibits two main components (around 12 Hz and around 22 Hz) and after the transition it exhibits three main components (8 Hz, 16 Hz and 23.5 Hz) which are visible on both spectra but accompanied by a lot of harmonics in the Fourier spectrum. Finally, the HHS allows us to see that the main frequency seems to be slightly modulated. The instant energy carried by the signal (i.e. the sum over all frequencies of the intensity of each frequency) can be extracted from the HHS (Fig.5.16(a)). It can be seen that the main peak of the heartbeat carries the most energy: a closer look to the HHS shows that, during the main peak, the probability of local high frequency waves appearing is high (temporally localised red lines in regions above 50 Hz in the HHS particularly visible around $t = 2$ s and below the arrows in Fig.5.16(d)). It seems that for two aborted peaks the instantaneous energy is more important than for one aborted peak. This two last observation can be understood by the fact that the main peak is characterised by sharp increase and decrease of the current and in the case of two aborted peaks, the main peak is even sharper. This sharpness is then accompanied by the high probability of existence of local high frequency components in the signal.

The evolution of the total plasma glow between the electrodes has been recorded. The frame rate was 894 fps. Some images extracted from the video are presented in Fig.5.17. Fig.5.17(a) shows raw images of the plasma glow during a heartbeat sequence with two failed

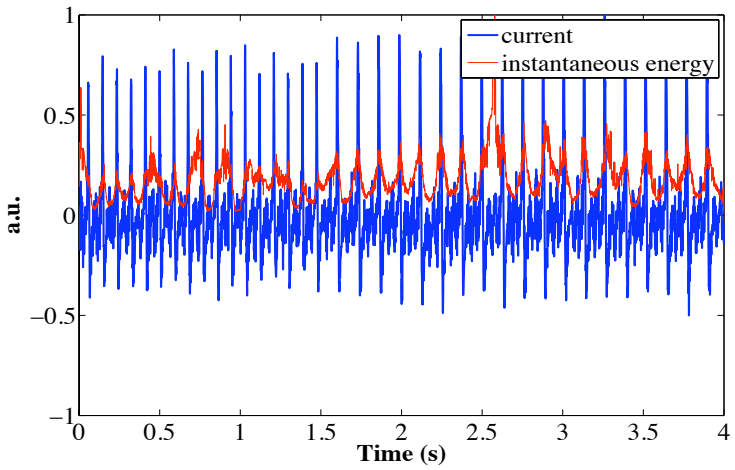

(a) Current and instant energy

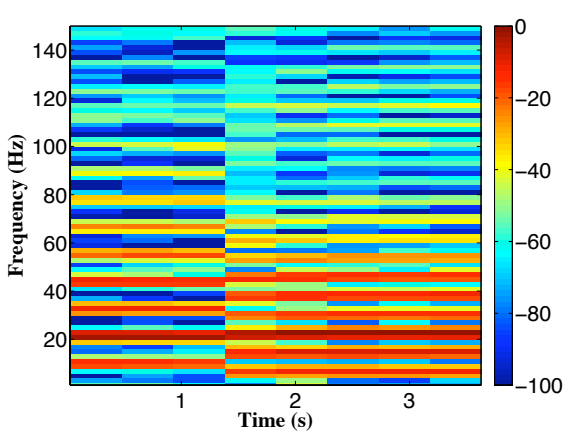

(b) Fourier spectrogram (the intensity varies from dark blue to red (logarithmic scale))

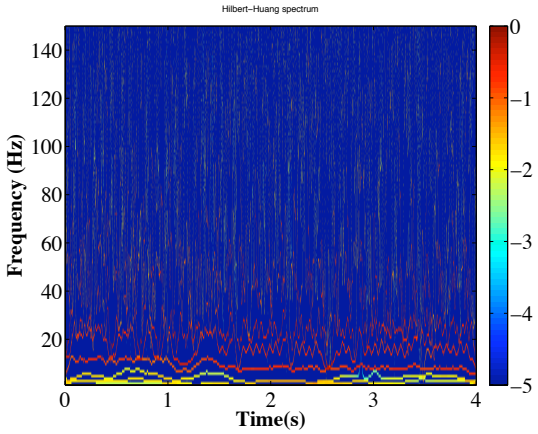

(c) Hilbert-Huang spectrum (the intensity varies from dark blue to red (logarithmic scale))

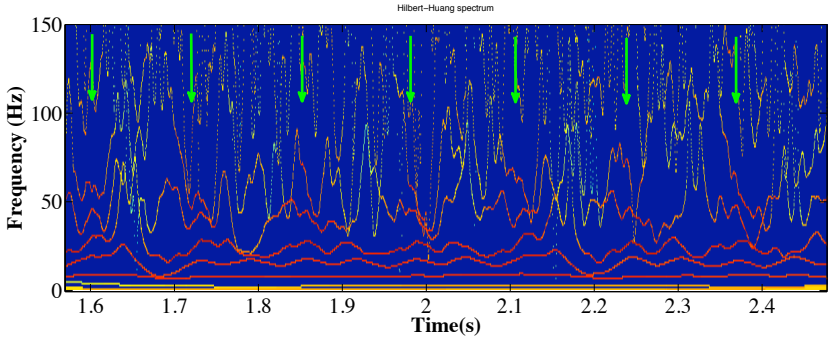

(d) zoom of c). The green arrows indicate the position of a main peak in the current signal

Figure 5.16: Transition from one aborted peak to two aborted peaks

peaks. Fig.5.17(b) shows the same images with the image of the plasma glow before the first failed peak chosen as a reference image and subtracted from every other images.

In Fig.5.17(a) the bright presheath region of the plasma are clearly visible at the top and the

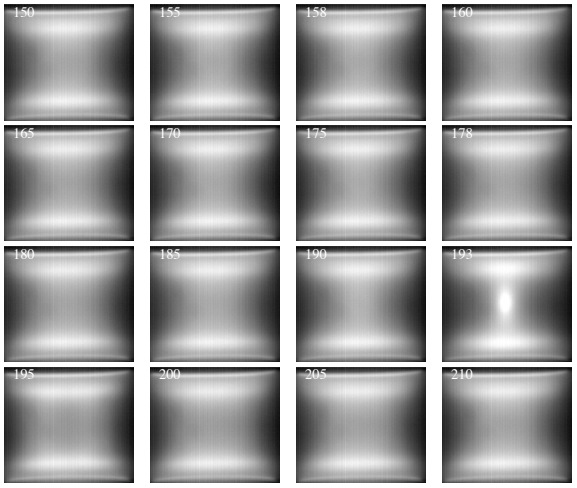

(a) Raw images extract from the video

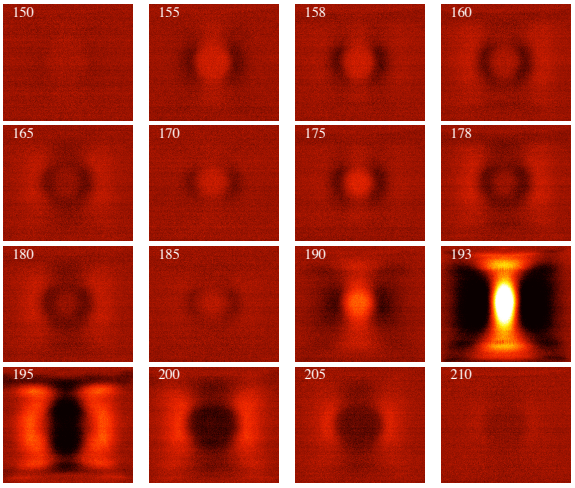

(b) Images from the video after postprocessing and false colour (dark red to bright yellow)

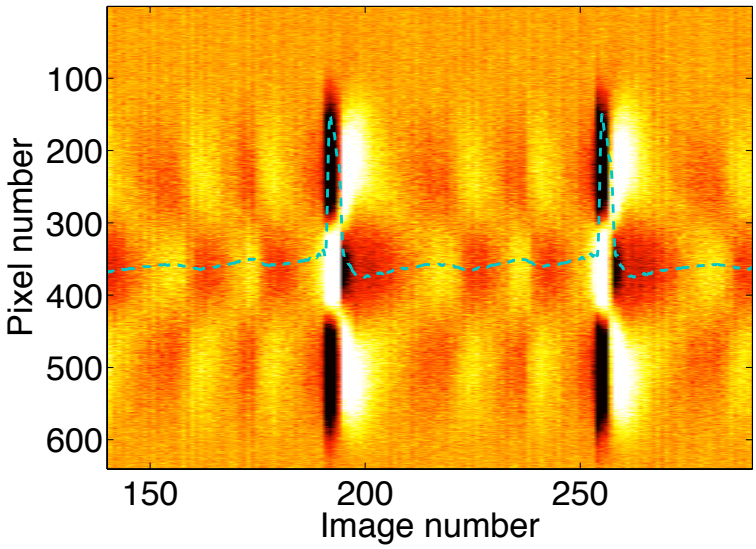

(c) line profile extract from the image series of (a). The blue dash line represent the evolution of the current amplitude.

Figure 5.17: Evolution of glow during a heartbeat with two failed peaks

bottom of the images. However as can be seen, the change in the central glow is barely visible and only the glow increase due to the main CES is clearly identified (image 193). In Fig.5.17(b), the relative changes are easily identified. It can be seen that for the first failed contraction, the central glow tends to increase (image 155 and 158) while the plasma edges are less luminous. Then the plasma edges become brighter while the central glow decreases (images 160 -165). The main difference with the complete CES of HRR and LRR heartbeat is that, in the present case,

the luminosity changes both at the plasma centre and the plasma edges are smaller. Then a new failed contraction with the same glow pattern occurs (images 170-185). However, the maximum value of the central luminosity has slightly increased. From image 190, the main CES occurs: a strong increase of the central glow while the edges become darker is followed by an abrupt change to bright edges and dark centre (image 195). The glow then returns slowly to its original configuration.

This pattern can be clearly identified on the line profile presented in Fig.5.17(c). This figure shows the evolution of the line passing trough the plasma centre (y-axis) as a function of time (x-axis). The time average value of each pixel in the line has been subtracted from the corresponding pixel in order to emphasise the relative changes of the glow. Two main contractions are visible in this figure. As can be seen, after a main CES, the glow converges towards the centre (but it cannot reach the same high value as for a main contraction) before the situation is reversed and the edges are brighter than the centre. It is worth noting that the luminosity of plasma centre does not decrease as much as for the case of a main CES. These observations can also be correlated with the evolution of the current amplitude. As can be seen in Fig.5.17(c), the current increase during failed peaks is quite low and the current decrease is not very abrupt. This may explain why the plasma centre luminosity changes are smaller. On the other hand during a main peak the current increase is much more important and the decrease is very sharp and the current goes well below its mean value as was already observed for LRR and HRR heartbeats.

The motion of the dust cloud has been recorded for heartbeat sequences with two failed peaks. The frame rate was 1,789 fps and the camera was at an angle $\sim 30^{\circ}$ with respect to the laser sheet. An interference filter was used in order to cut out most of the plasma light. Raw frames from the video are not presented as they do not bring forward much information compared to those which were presented for the HRR heartbeat. However, the evolution of the central column profile (i.e. the column passing through the centre of the void) is presented in Fig.5.18(a) as it allows small changes in the dust cloud configuration to be seen. In order to emphasise those changes, the time average value of each pixel in a line has been subtracted from the corresponding pixel (Fig.5.18(b)). The evolution of the current amplitude has been superimposed on both figures.

As can be seen in Fig.5.18, the dust cloud is in constant motion as for a HRR heartbeat where only a central region (between pixels 130 and 140) is always dust free (the darker region in Fig.5.18(a)). An intermediate region filled with moving dust particles is observed between each main contraction. As observed previously, the void starts to contract when the current and the central glow increase strongly. The central glow increase can be seen clearly in Fig.5.18(b) where the changes in the residual light passing through the interference filter are magnified. Nevertheless, the most interesting feature in Fig.5.18 is the behaviour of the corona region. Indeed as can be seen, it does not exhibit the same smooth movement as observed for the LRR and HRR heartbeats. Indeed, the failed peaks observed on the current amplitude signal correspond to small contractions of the dust cloud which are accompanied by sudden acceleration of the

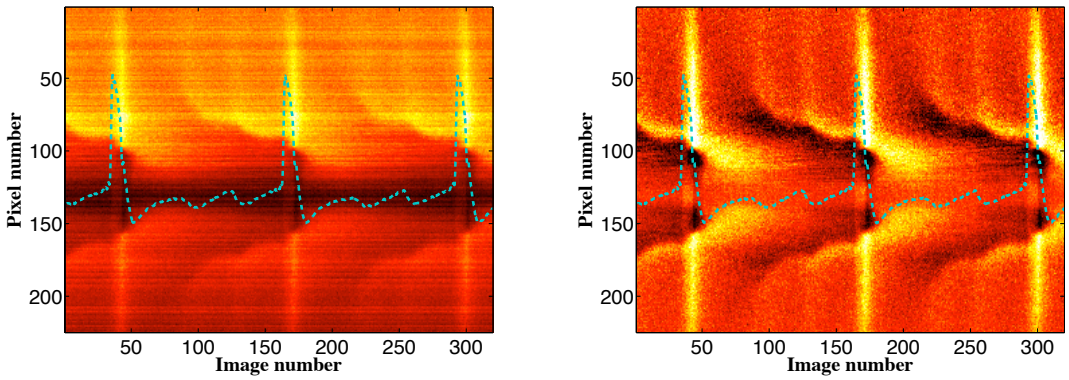

(a) Line profile extracted from dust cloud video (in false colour from dark red to bright yellow)

(b) Same as (a) except that the time mean value of each pixels have been subtracted (in false colour from dark red to bright yellow)

Figure 5.18: Evolution of the central column extracted from the dust cloud video during a heartbeat instability with two failed peaks. The dashed blue line superimposed to the images represents the evolution of the current amplitude.

corona region towards the centre. This is particularly clear in Fig.5.18(b).

It has been recently shown that the evolution pattern of the transition followed a mixed-mode oscillation (MMO) scheme (alternation of small amplitude oscillations between two large ones) and that the frequency of the heartbeat slightly decreases during a sequence with n failed peaks [153]. In this article, it is shown that when the heartbeat instability is stopping, the number of failed oscillations increases steadily and the progressive occurrence of the failed contractions follows an incomplete devil's staircase scheme.

5.1.3 Physical interpretation of the heartbeat instability

From the different analyses reported in the previous sections, several features of the heartbeat instability can be brought to the fore.

- The void contraction corresponds to an increase of the central plasma glow. It suggests that a sudden enhanced ionisation in the plasma centre changes the ratio between the inward electrostatic force and the outward ion drag force: this enhanced ionisation may increase the positive space charge inside the void region due the higher mobility of the electrons that diffuse away much faster. Consequently the electric field in the plasma is enhanced as is the ion flux. However, it has been theoretically shown that the ratio of the ion drag-to-electric forces decreases rapidly with the electric field [104]. Hence, the electrostatic inward force become predominant and the dust particles enter the void region. The void centre becomes darker but the dust particles continue to move inward due to their inertia with a more or less constant speed and stop suddenly (see for example 5.2). The void is however not completely filled indicating that a force is preventing a further

motion towards the centre. As the gravitational force is acting over all dust particles and, among others, those constituting the upper part of the dust cloud, the force preventing the void closure has to be stronger than the gravitational force. A that time, the central glow is weak and nearly homogeneous, a property usually associated with weak electric field. In Ref.[104], it is shown that for weak electric field the ion drag force exceeds the electrostatic force and it is reasonable to assume that the force stopping the dust particles is the ion drag force.

- The dust particles situated near the plasma centre are then nearly immobile while a dust particle "wave front" coming from the plasma edge is detected. At the same time, a corona region of brighter plasma glow and thus higher ionisation is observed at the plasma edges. This region surrounds the plasma centre and moves slowly towards it. The correlation with the dust cloud motion indicates that this region may correspond to the corona region. An enhanced ionisation at the plasma edges can create an outward electrostatic force in the vicinity of the corona region if it is assumed that in analogy with the contraction phase, a plasma region with an enhanced glow attracts the dust particles. Thus, the central dust particles are immobile (far from the interface) while the particles close to the corona region are attracted to it. As the dust particles move, the local conditions change and the corona region moves inwards attracting the inner dust particles one after the other. While the plasma homogeneity is restored, the wave front speed decreases and the last particles to move outward are the closest to the void centre. In the LRR case, a stable void is restored between each CES which can be considered as isolated and independent while the HRR case leads to a continuous motion of the dust cloud as the central dust particles are unable to reach their initial positions.

- Asymmetry of the void contraction has been observed under some conditions. This asymmetry can find its origin in the discharge geometry. Indeed, the plasma is confined by the electrodes in the vertical direction and can almost freely diffuse in the horizontal direction. The corona region confirmed this hypothesis when observed on the plasma glow images: in the vertical direction it is merged with the bright presheath region.

- The sharp peak in the current signal can be associated with the glow reversal from bright centre and dark edges to bright edges and dark centre when this phenomena is strongly marked. It is replaced by a change in the slope in weaker cases. This reversal is very fast but imaging at very high speed shows that the edge glow increase starts at the same time as the centre glow decreases. The hypothesis of the propagation of an ionisation wave seems thus very unlikely. It is more reasonable to assume that ionisation is favoured at the plasma edge when the dust particles enter the void region.

Failed or aborted heartbeats have been identified from the discharge current, the plasma glow and the dust cloud motion. It has been shown that the appearance of failed contraction reduce the frequency of the main peaks and that the sharpness of the main peaks is increased when

the number of failed peaks increases. The transition from n to $n+1$ failed peaks is sharp in both temporal and frequency domains. However, it has been recently shown that the evolution pattern of the transition followed a mixed-mode oscillation (MMO) scheme (alternation of small amplitude oscillations between two large one) and that the frequency of the heartbeat slightly decreases during a phase with n failed peaks [153].
It has been discussed previously that for a LRR heartbeat the CES is very short. In Fig.5.6, some oscillations are observed in the central glow of a LRR heartbeat before the main CES. We have also mentioned that LRR heartbeats are observed when the instability is about to stop. Consequently, when the heartbeat instability slows down before it stops, it may be possible that a heartbeat instability evolves form HRR to LRR with a continuous increase of the number of failed peaks following a mixed-mode oscillation scheme. Our hypothesis is, since the heartbeat instability is a threshold phenomenon [67, 68], energy needs to be accumulated by the system and is relaxed during a CES. Then, two possibilities can explain the stopping of the instability in a more or less similar way: energy from the plasma is dissipated and not fully balanced by the input power or, the plasma parameters are evolving and the instability threshold changes. In both cases, it may be more difficult for the plasma to accumulate enough energy to trigger a full CES and a failed peak occurs instead. It has been shown theoretically that the heartbeat instability involves many parameters (ionisation level, ion flux, ion density, electron density, electric fields, dust particle charge, etc) [76]. All these parameters have different time scales. It has been demonstrated that MMO occurs in systems with multiple time scales and that varying a control parameter (not defined yet for the heartbeat instability) can change the MMO pattern (i.e. the number of small oscillations; see Ref.[154] and references therein). Theoretical investigations are thus needed to fully understand the physical processes involved in the heartbeat instability and its evolution.

5.2 Instabilities related to the growth of a new generation of dust particles

In a discharge where the dust particles are grown by RF sputtering, continuous growth of dust particles inside the plasma bulk can occur if the discharge parameters are suitable. Thus it has been reported that new generations of dust particles grow in the void region in sputtering discharges [61] or reactive plasmas [149, 150]. Under some conditions, the new generation can trigger an instability of the old dust void.

5.2.1 The delivery instability

After dust particle growth in the PKE-Nefedov chamber, the dust particle cloud is often in the following state (Fig. 5.19): a void in the centre of the chamber is surrounded by a cloud of dust particles. The dust particle cloud can be composed of different dust particle generations which

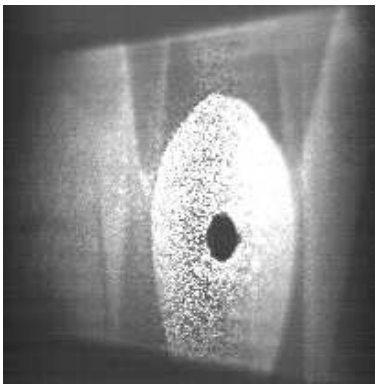

Figure 5.19: Dust cloud used for the study of the "delivery" instability.

are clearly separated. When the discharge parameters are suitable to dust particle growth, new generations of dust particle can regularly grow and appear in the void region. Under some conditions (not defined yet), the growth of a new generation of dust particle can trigger an instability of the void region: the "delivery" instability.

The "delivery" instability starts with a sudden expansion of the void size followed by a contraction to its original size. An expansion-contraction sequence (ECS) of the delivery instability is shown in Fig.5.20. It presents images extracted from high speed video imaging of the dust cloud during a delivery instability. The camera was placed at an angle of $\sim 30^{\circ}$ with respect to the laser sheet that was illuminating the dust cloud in the PKE-Nefedov chamber and the frame rate was 500 fps. One of the main differences with the heartbeat instability is that, during a delivery instability, the minimum size of the void corresponds to its size before the instability starts while during the heartbeat instability the maximum size of the void is its stable configuration. As can be seen, the expansion in the vertical direction is more pronounced than in the horizontal direction. Fig.5.21 presents the time evolution of the video image central column going through the void extracted from the same video images presented in Fig.5.20. Time is represented by the frame number in the x-axis (1 frame is 2 ms) and the column profile is given in the y-axis. It is clear that the amplitude of the void oscillation increases with time during the delivery instability. It is also worth noting that the expansion time is longer than the contraction time. This is also the case during the heartbeat instability but the characteristic times of the heartbeat instability are much shorter than those of the delivery instability (see Ref.[151] and Sec.5.1) . For example, a full ECS of the delivery instability lasts for $\sim$ 300 ms while a full CES of the heartbeat instability lasts for at most a few tens of milliseconds. As can be seen in Fig.5.22, both frequency and amplitude of the instability evolve with time. These changes must be linked to the evolution of the plasma (and/or dust) parameters during the instability. The delivery instability ends when the new generation of dust particles reaches critical dimensions (size and/or density of dust particles). Indeed, soon after the void stops oscillating, the new cloud becomes visible to the naked eye. A new delivery instability can eventually start again when a new generation of dust begins to grow. Consequently, the evolution of the plasma pa-

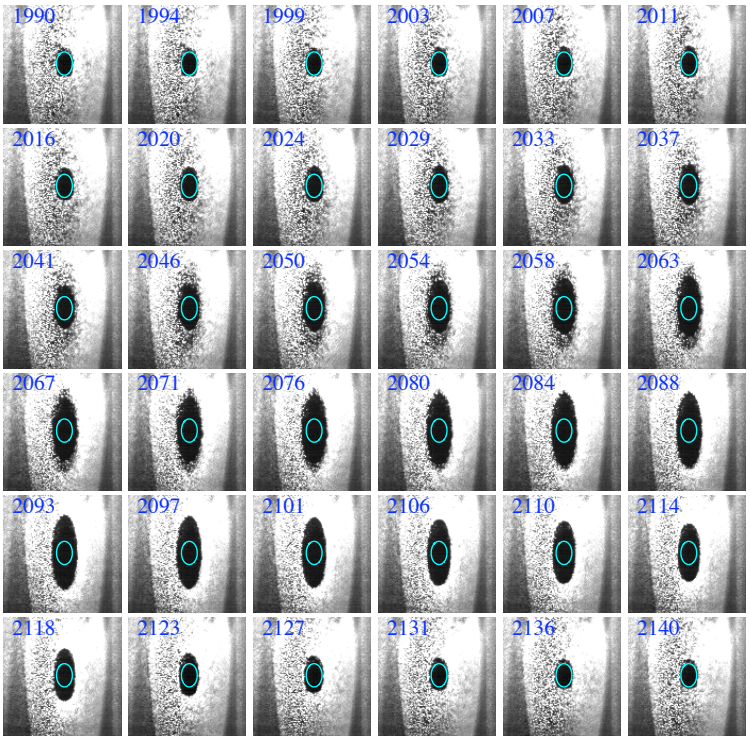

Figure 5.20: Evolution of the void during one expansion-contraction sequence of the delivery instability. The blue ellipse delineates position of the stable open void.

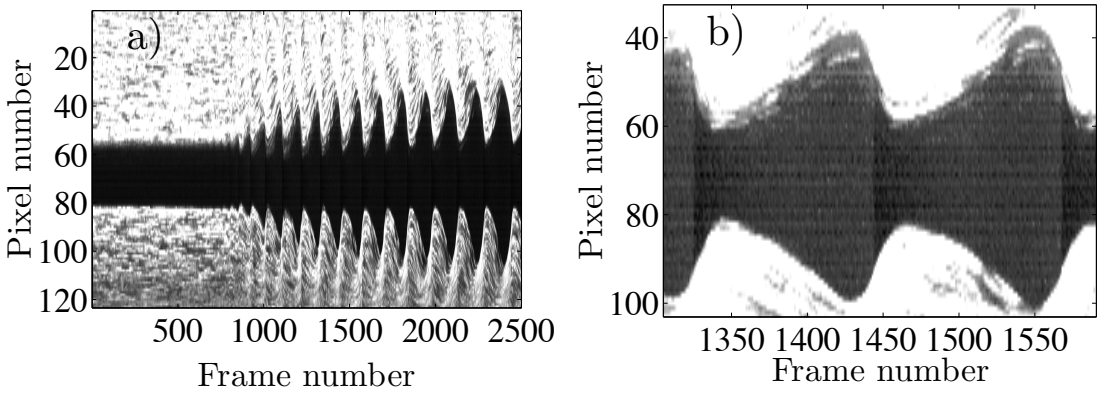

Figure 5.21: a) Evolution of the central column going through the void (frame rate: 500 fps). b) Zoom of a) with enhance contrast. The plasma glow luminosity was not totally stopped by the interference filter allow us to visualize major glow luminosity fluctuation at the same time as the dust cloud.

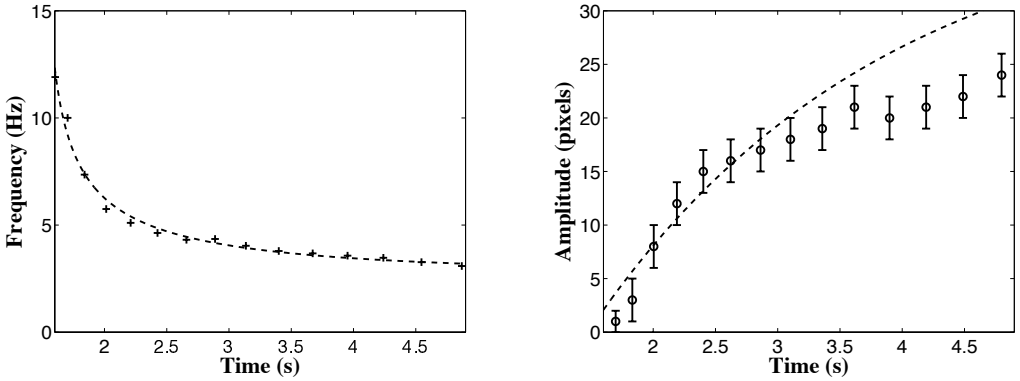

(a) (b)

Figure 5.22: (a) Evolution of the delivery instability frequency. The dashed curves represent the theoretical fit. (b) Evolution of the delivery instability amplitude (1 pixel $\sim$ 100 μm). The dashed curves represent the theoretical fit.

rameters during the instability have to be correlated with the growth kinetic of the new dust particle generation.

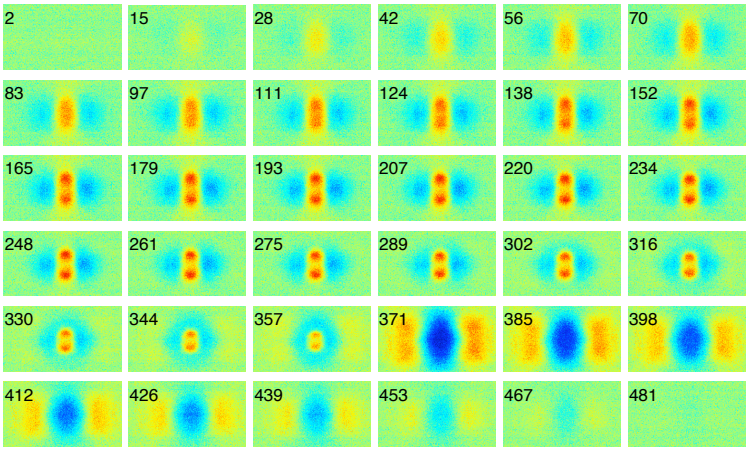

Figure 5.23: Evolution of the glow during one expansion-contraction sequence of a "delivery" instability (in false colour from blue to red). In order to improve the visibility of the luminosity variations, the image 1 is taken as the reference image and subtract to every other images.

In order to see the global evolution of the plasma glow, the plasma glow has been recorded over the whole inter-electrode space. The camera was facing the PKE-Nefedov reactor and focussed on the centre of the chamber. In Fig.5.23, images extracted from a video (1,789 fps) of the plasma during a delivery instability are presented. It shows the evolution of the plasma glow luminosity during one expansion-contraction sequence of the delivery instability (not during the same experiment as in Figs.5.20 and 5.21). The plasma glow starts to contract toward the centre before it splits in two luminous vertically aligned glow bubbles. These bubbles tend to come

closer to each other before they suddenly disappear and the outer part of the plasma becomes brighter. The luminosity of the plasma returns then to its original configuration. These effects are clearly seen in Fig.5.24. In Fig.5.21, it can also be seen that that the void contraction starts before the central glow faints. The discharge current (Fig.5.24) during the instability also exhibits interesting features: the first increase corresponds to an increase of luminosity in the plasma centre. Then the current decreases slowly while the two plasma bubbles are formed and converge toward each other. The abrupt decrease corresponds to a fast luminosity decrease in the centre while the plasma edges become brighter. The current decrease indicates that the total ionisation in the plasma decreases although localized regions of high ionisation exist.
The fact that the enhanced central glow luminosity (suggesting a higher ionisation rate) splits into two distinctive regions during the delivery instability (Fig.5.23) tends to indicate that there might be a cloud of very small dust particles in the centre of the void which prevents a high ionisation rate due to the loss of charge carriers on dust particle surfaces. The complex shapes of the enhanced ionisation area as well as the presence of this inner dust particle cloud must result in complex ion drag force and electrostatic force directions and magnitudes. It can however be deduced that the confining force increases on both dust clouds when the luminous central glow regions becomes brighter as the void starts to contract before the central high luminosity regions vanish (Fig.5.21(b)). In the case of the inner growing dust cloud, it is difficult to conclude which of the ion drag force or the electrostatic force is the dominant force due to the complexities exhibited by the system. When the situation reverses to dark centre and brighter edges, the void continues to shrink until it reaches its equilibrium dimension and then a new expansion-contraction starts again.

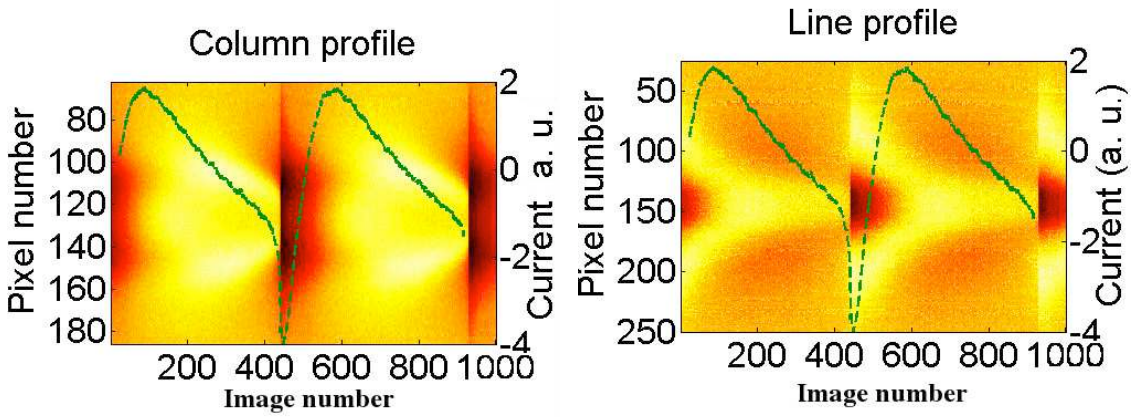

(a) (b)

Figure 5.24: Evolution of glow luminosity extracted from the video images presented in Fig.5.23 (in false colour from dark red to bright yellow). (a) Evolution of the central column luminosity. (b)Evolution of the central line luminosity (frame rate: 1789 fps). In both cases, the time average value of each pixels has been subtracted in order to enhance luminosity variations. The dashed green line superimposed on each picture represents the discharge current (AC component) during the delivery instability.

As previously discussed, the instability ends with the appearance of a new generation of dust particles inside the void. Consequently, it can be assumed that some dust particles are growing inside the void and are modifying the plasma parameters. The evolution rate of the latter must so be linked to the growth rate of the dust particles. It has been shown in chemically active plasmas that during the growth of dust particles, the dust particle density n_{d_g} decreases at the beginning when dust particles are growing by agglomeration and then the dust density stays almost constant when the dust particles are growing by surface molecular deposition [34]. As the first stage is very short compared to the second one, let's assume that the density of the growing dust particles is constant inside the void and that the dust particle radius r_{d_g}evolves as:

$$r_{d_g}(t) = r_{d_{max}} \cdot (1 - \exp(-(t - t_0)/\tau_G)) \tag{5.1}$$

where τ_G is some growth time constant, $r_{d_{max}}$ is the maximum radius a dust particle can reach and t_0 the time when the dust particles begin to grow in the discharge. Let's assume that, as a first approximation, the void contraction frequency ω_d during the delivery instability is a function of the dust plasma frequency of the growing dust particles ω_{pd_g} and the dust plasma frequency of the old dust particles ω_{pd_o} :

$$\omega_d = f(\omega_{pd_g}, \omega_{pd_o}) \tag{5.2}$$

If we assume that the properties of the old dust particle cloud remain constant during the delivery instability, the simplest assumption that can be made is a linear dependence of ω_d with ω_{pd_g} and the delivery instability frequency ω_d is thus proportional to the dust plasma frequency of the growing dust particles $\omega_{pd_g} = \sqrt{n_{d_g} Q_{d_g}^2 / m_{d_g} \epsilon_0}$ where Q_{d_g} is the electric charge on the growing dust particles and $m_{d_g} = (4/3)\pi\rho r_{d_g}^3$ their mass and ρ their mass density. According to the OML theory, the dust particle charge is (see Chap.2):

$$Q_{d_g} = C_c \cdot (4\pi\epsilon_0 r_{d_g} k_B T_e / e) \ln((ni/n_e) \cdot (m_e T_e / m_i T_i)^{1/2}) \tag{5.3}$$

So it can be considered that in first approximation:

$$Q_{d_g}(t) \propto r_{d_g}(t) \tag{5.4}$$

Thus it can be deduced that the delivery instability frequency evolves as:

$$\omega_d(t) \propto \omega_{pd_g}(t) \propto \sqrt{r_{d_g}^{-1}(t)} \tag{5.5}$$

The delivery instability frequency has been fitted by such a function and the results is presented in Fig.5.22. As can be seen, there is good agreement and a growth time constant $\tau_g = 2.35s$ has been found. This value is in good agreement with the dust particle appearance time measured in other sputtering experiments [59].
A strong electrostatic repulsion force between the two clouds of dust particles as the major

process seems to be, as a first approximation, a good assumption. Consequently, if we assume that in the "void" $n_e \sim n_i$ (assuming that the density and/or size of the growing dust particles is not large enough to significantly affect the electron density), by applying Gauss theorem it can be found that the force exerted on the old dust particle cloud by the growing one F_{og} evolves as:

$$F_{og}(t) \propto r_{dg}(t) \tag{5.6}$$

Thus the amplitude of the void oscillation during the delivery instability has the same evolution. In Fig.5.22, the delivery instability amplitude has been fitted by a function proportional to the function $r_{d_g}(t)$ obtained by fitting the delivery instability frequency. As can be seen, it matches well for small amplitude oscillations but some discrepancies appear for larger oscillations. This was expected as the model neglected other forces such as ion drag force and furthermore, for big amplitudes non-linear effects have to be taken into account.
Nevertheless, the delivery instability frequency evolution as well as its amplitude evolution confirm that the delivery instability is associated with the growth of dust particles inside the void. These new dust particles cannot be seen by laser light scattering from the beginning of the instability because they are too small.

5.2.2 The rotating void

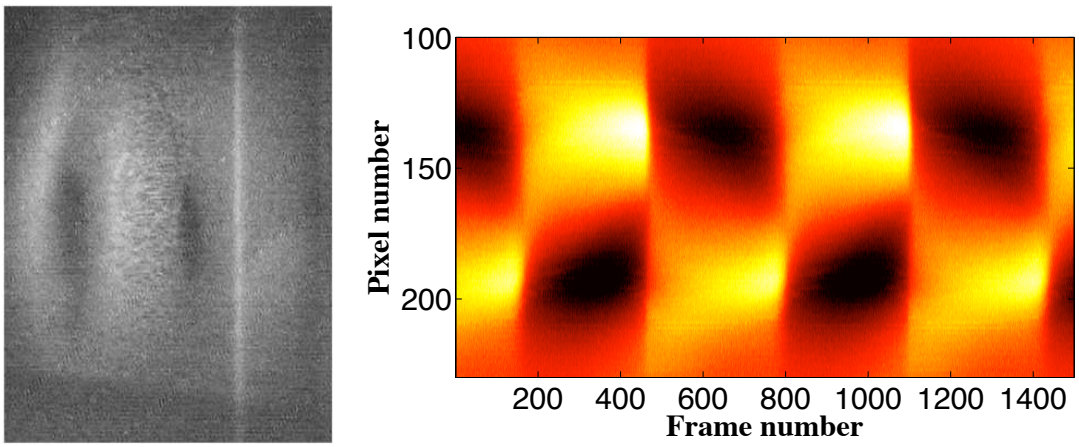

(a) (b)

Figure 5.25: (a) Rotating void: the void is not in the centre of the discharge and can be observed on the right or on the left of the laser sheet alternatively. (b) Line profile during a rotating void instability (in false colour from dark red to bright yellow).

In some cases (not well defined yet), the delivery instability evolves into another instability. The void starts to rotate around the axis of symmetry of the chamber. A typical image of this situation is presented in Fig.5.25(a). As can be seen, the dust free region is not located in the centre of the discharge anymore but it is slightly decentred. This behaviour can also be

observed on the time evolution of the the plasma glow luminosity. Indeed, in Fig.5.25(b), the central line profile evolution (i.e. line going through the centre of the discharge) is presented. The camera was focussed on the centre of the discharge and the frame rate was 1,789 fps. As can be seen, the bright glow goes from one side of the reactor to the other side. This rotating glow is associated with the dust void also rotating around the axis of symmetry of the chamber as the plasma luminosity is most of the time increased inside the void (except for very short time during heartbeat and delivery instability when the plasma edges are brighter then the void plasma centre).

5.3 Conclusion

In this chapter, instabilities that can occur when a dense cloud of dust particles is present in the plasma have been described experimentally. All these instabilities are linked to the presence of a dust-free void in the centre of the discharge. They can be observed via the discharge current evolution, the plasma glow evolution and the dust cloud motion. Two types of void instabilities have been presented:

1. Self-excited instability of the void: the heartbeat instability which can been divided in two distinct cases: the high-repetition rate heartbeat and the low repetition rate heartbeat. The last one is characterised by isolated contraction-expansion sequences and the dust-void has time to reach its equilibrium size before a new contraction occurs while the first one is characterised by a constant motion of the dust cloud and a constant evolution of the plasma glow. Intermediate heartbeat cases characterised by the presence of failed or aborted contractions have also been presented. The asymmetry in the void contraction that can sometimes occurs was also presented

2. Instability of the void due to the growth of a new generation of dust particles: when dust particles are growing inside the old dust particle void, it can trigger large amplitude and low frequency oscillation of the dust void. The amplitude and the frequency of the void oscillation have been linked to the new generation of dust particles. This instability can sometimes evolve to a rotation of the dust void around the axis of symmetry of the discharge.

Thus, the presence of dust particles inside a plasma can lead to unusual instabilities. Theoretical investigations are needed to fully understand the physical processes involved in the appearance of these instabilities and the parameters driving their evolution with time.

5.4 Résumé du chapitre en français

Dans ce chapitre, nous nous sommes intéressé aux instabilités d'un nuage dense de poudres piégé dans le plasma. Une région sans poudre, appelée « void »d'environ 1 cm de diamètre et aux contours clairement délimités, est souvent présente au centre du plasma. Les théories actuelles décrivent communément ce « void »comme découlant d'un équilibre entre une force électrostatique confinante et une force de friction des ions ayant tendance à expulser les poudres du plasma. Sous certaines conditions, ce « void »devient instable. Ces instabilités peuvent alors être repérées sur les paramètres électriques de la décharge, sur la luminosité du plasma et sur la dynamique du nuage du poudres. Deux types d'instabilités ont été observée :

- *Le premier type est une instabilité auto-excitée du « void »appelée l'instabilité « heartbeat ». Elle correspond à des battements, c'est à dire des séquences de contraction-expansion (SCE) des dimensions du « void ». Ce type d'instabilité a également été observé lors d'expériences en microgravité avec des poudres micrométriques injectées. Le « heartbeat » présente deux cas extrêmes : un cas avec un taux de répétition faible qui se compose de SCE très rapides séparées par de longues périodes durant lesquelles le système a le temps de retourner à l'équilibre (ce cas est observé lorsque l'instabilité est sur le point de s'arrêter), et un cas avec un fort taux de répétition composé de SCE plus lentes mais qui se succèdent rapidement sans retour à l'équilibre. Dans les deux cas la contraction s'accompagne d'une forte augmentation de la luminosité du plasma à l'intérieur du « void »(aussi associée à une forte augmentation du courant) suggérant un accroissement de l'ionisation induisant une rupture de l'équilibre entre la force électrostatique et la force de friction des ions. Quelques millisecondes après le début de la contraction du « void », la luminosité au centre du plasma diminue fortement alors que la périphérie devient brillante. Cela suggère que les régions de forte ionisation se sont déplacées à cause de l'entrée des poudres dans le void. Lorsque l'instabilité ralentie avant de s'arrêter, elle présente des SCE avortées entre les SCE complètes. Plus le nombre de SCE avortées est grand entre chaque SCE complète, plus ces dernières sont rapides. Il a été montré que ces SCE avortées suivies de SCE complètes sont des « mixed-mode oscillations »[153]. Ces derniers sont connus pour apparaître dans les systèmes où différentes échelles de temps coexistent [154].*
- *Le second type d'instabilité est amorcée par la croissance d'une nouvelle génération de poudres dans le « void ». Il est en effet possibe d'avoir une formation continue de poussières dans le plasma lorsque les paramètres de la décharge sont favorables, et de nombreuses générations de poudres peuvent ainsi se succéder. Lorsqu'une nouvelle génération de poudres croît dans le « void »de l'ancienne génération, elle peut, sous certaines conditions (non-déterminées pour l'instant), déclencher une instabilité du « void »qui ne s'arrête que lorsque les poudres de la nouvelle génération ont atteint un taille et/ou une densité critiques. Cette instabilité est marquée par des séquences d'expansion-contraction des dimensions du « void »à basse fréquence et grande amplitude. La différence la plus notoire avec le « heartbeat »est que dans le cas cette instabilité, les dimensions minimales du « void »correspondent à la situation stable. De plus, l'augmentation de la luminosité au centre du plasma n'est pas homogène : deux régions distinctes de forte luminosité (suggérant une ionisation plus importante) apparaissent dans les parties supérieures et inférieures du « void »suggérant ainsi la présence d'un nuage interne de poudres en formation. L'évolution temporelle de la fréquence et de l'amplitude des oscillations est directement reliée à la croissance de la nouvelle génération de poudres. Cette instabilité se transforme parfois en une rotation du void autour de l'axe de symétrie de la décharge.*

Chapter 6

Complex plasma afterglow and residual charge

After the studies of the effect of dust particle growth on discharge parameters and the related instabilities, and the studies of the instabilities of a well established dust particle cloud filling the interelectrode gap, it is time to investigated the last stage of the life of a complex plasma: the discharge afterglow. When the power input to the discharge is turned off, the RF field rapidly disappears and the ionisation processes become negligible compared to the plasma loss processes. In low pressure monatomic plasmas, plasma losses are essentially diffusion losses and the charge carriers recombine on the reactor wall. However it is known that, in a complex plasma afterglow, the dust particles have a strong effect on the plasma loss processes. It has indeed been shown experimentally that the presence of dust drastically shortens the plasma decay time [21]. Moreover, as the particles are charged in a running discharge, the dust particle charge has to relax during the discharge afterglow. The decharging process of the dust particles must be linked to the diffusion of the charge species. It has also been observed that dust particles can keep a small residual electric charge in the late afterglow of a dusty plasma [77].
Consequently, in this chapter the influence of dust particles on plasma decay, the dust particle decharging process and dust particle residual charge have been investigated both theoretically and experimentally.

6.1 Afterglow in dust free plasma

When a discharge is switched off, the electrons and the ions diffuse to the walls of the reactor. In a monatomic gas such as argon, the plasma losses are mainly due to diffusion-recombination at the walls while in molecular gases such as nitrogen, volume recombination must also be considered. This last process can be neglected in low pressure monatomic gases because it needs three body collisions which are very unlikely due to small cross sections.
In the following sections, we consider the diffusion of charged species in the dust-free plasma afterglow of a monatomic gas. Experimental measurements of electron density decay in both

nitrogen and argon plasma are presented and compared.

6.1.1 Diffusion in dust free plasma

In most low temperature laboratory discharges, the electron temperature is not in equilibrium with the ion and neutral atom temperature. Consequently when the discharge is switched off, the electron temperature relaxes to room temperature following [77, 137]:

$$\frac{d\tilde{T}_e}{dt} = -\frac{\tilde{T}_e - 1}{\tau_T} \tag{6.1}$$

where $\tilde{T}_e = T_e/T_i$, $\tau_T^{-1} = \sqrt{\pi/2}\sqrt{m_e/m_i}v_{Ti}/l_{en}\sqrt{\tilde{T}_e} = \sqrt{\tilde{T}_e}/\tau_T^{\infty}$, l_{en} is the mean free path of electron-neutral collision, and τ_T is the electron temperature relaxation time. The ∞ exponent stands for the limiting value at very long time.
In the discharge afterglow, ions and electrons diffuse to the wall of the reactor. The ion and electron density evolution $n_{i(e)}(t)$ are linked to the fluxes of ions and electrons $\Gamma_{i(e)}$:

$$\frac{\partial n_e}{\partial t} + \Delta\Gamma_e = S_e \tag{6.2}$$

$$\frac{\partial n_i}{\partial t} + \Delta\Gamma_i = S_i \tag{6.3}$$

where $S_{i(e)}$ is the ion (electron) source term. In the plasma afterglow, $S_{i(e)} = 0$ because the ionization rate is null and there is no sink term. The fluxes of electrons and ions are strongly linked to the ion and electron densities and the electric field. When there are no external field, diffusion flux and space charge electric field E are given by::

$$\Gamma_e = -D_e\nabla n_e - \mu_e n_e\mathbf{E} \tag{6.4}$$

$$\Gamma_i = -D_i\nabla n_i + \mu_i n_i\mathbf{E} \tag{6.5}$$

where $\mu_{e(i)} = e/m_{e(i)}\nu_{e(i)n}$ is the mobility of electrons (ions) where $\nu_{e(i)n}$ is the electron (ion)-neutral collision frequency, and $D_{e(i)}/\mu_{e(i)} = k_b T_{e(i)}/e$ is the diffusion coefficient of electrons (ions).
The electric field E is determined using the Gauss equation:

$$\nabla\mathbf{E} = \frac{e}{\epsilon_0}(n_i - n_e) \tag{6.6}$$

At the very beginning of the afterglow, the ion and electron densities are high enough to couple the diffusion process of the ions and the electrons. Indeed, as the electrons have a diffusion coefficient which is larger than the ion one, they tend to diffuse faster to the wall of the reactor. This induces a break in the neutrality condition and creates a space electric field E. This electric field will slow down the electrons and accelerate the ions. When the plasma density is high (typically $> 10^8\ cm^{-3}$ [155]), the electric forces are important and space charge separation,

and thus the electric field, will adjust in order that the ions and the electrons diffuse together: this is the ambipolar diffusion regime. During this regime, ion and electron fluxes are equal ($\Gamma_e = \Gamma_i = \Gamma$) and have the same ambipolar diffusion coefficient D_a. During this regime, we have $n_e = n_i = n$. As $\Gamma_e = \Gamma_i = \Gamma$, Eq.6.4 and Eq.6.5 can be combined giving:

$$(\mu_i n_i + \mu_e n_e)\Gamma = -D_e \mu_i n_i \nabla n_e - \mu_e \mu_i n_e n_i E - D_i \mu_e n_e \nabla n_i + \mu_e \mu_i n_e n_i E \tag{6.7}$$

Thus,

$$\Gamma = -\frac{(D_e \mu_i + D_i \mu_e)\nabla n}{\mu_i + \mu_e} \tag{6.8}$$

So, in laboratory plasma where $\mu_e \gg \mu_i$ the ambipolar diffusion coefficient is (using the definition of μ_α and D_α [20]):

$$D_a \equiv \frac{D_e \mu_i + D_i \mu_e}{\mu_i + \mu_e} \simeq D_i(1 + \frac{T_e}{T_i}) \tag{6.9}$$

The solution of Eqs.6.2 and 6.3 can be solved easily for 1D ambipolar diffusion. The density n of the plasma follows:

$$\frac{\partial n}{\partial t} - D_a \nabla^2 n = 0 \tag{6.10}$$

The variables can be separated, giving:

$$n(x,t) = X(x)T(t) \tag{6.11}$$

which when substituted into Eq.6.10 gives:

$$X\frac{\mathrm{d}T}{\mathrm{d}t} = D_a T \frac{\mathrm{d}^2 X}{\mathrm{d}x^2} \tag{6.12}$$

If Eq.6.12 is divided by XT, the left hand side becomes time dependant only and the right hand side becomes space dependant only. Consequently both must be equal to a constant we call $-1/\tau_D$. It can then be deduced:

$$T = T_0 \exp(-t/\tau_D) \tag{6.13}$$

and for the spatial part:

$$\frac{\mathrm{d}^2 X}{\mathrm{d}t^2} = -\frac{X}{D_a \tau_D} \tag{6.14}$$

The solution in 1D has the form [20]:

$$X = A\cos\frac{x}{\Lambda} + B\sin\frac{x}{\Lambda} \tag{6.15}$$

where $\Lambda = (D_a\tau_D)^{1/2}$ is the diffusion length. Solving Eq.6.14 for a slab geometry of length l and taking the symmetric lowest-order solution, X and T can be combined to give:

$$n(x,t) = n_0 \exp(-t/\tau_D)\cos(\pi x/l) = n_0 \exp(-t/\tau_D)\cos(x/\Lambda) \tag{6.16}$$

This equation can be generalized to 3D. The diffusion length Λ depends on the geometry of the reactor. Integrating Eq.6.16 over space, it can be found that in the afterglow the density will decrease exponentially in time with a time constant τ_D.

$$n(t) = n_0 \exp(-t/\tau_D) \tag{6.17}$$

When the plasma density is low enough the electrons and the ions start to diffuse with different speeds and finally diffuse freely. This process is the transition from ambipolar to free diffusion. Let's consider that during the transition, the electron flux and ion flux are equal ($\Gamma_e = \Gamma_i = \Gamma$) but $n_e \neq n_i$ and $v_e \neq v_i$. The hypothesis of proportionality that allows to treat the transition from ambipolar to free diffusion is [155]:

$$\frac{n_i(r)}{n_e(r)} = C_t \tag{6.18}$$

where C_t is a constant. Eq.6.18 can be rewritten as:

$$n_i \nabla n_e = n_e \nabla n_i \tag{6.19}$$

From Eq.6.7, it is possible to derive Γ:

$$\Gamma = -\left[\frac{(D_e\mu_i + D_i\mu_e)n_i}{\mu_i n_i + \mu_e n_e}\right]\nabla n_e = -D_{eff}\nabla n_e \tag{6.20}$$

The electric conductivity is:

$$\sigma = (\mu_i n_i + \mu_e n_e)e \tag{6.21}$$

and the charge density is:

$$\rho = (n_i - n_e)e \tag{6.22}$$

Using Eqs. 6.9, 6.20, 6.21 and 6.22, the effective electron diffusion coefficient can be written as:

$$D_{eff} = D_a\Big(1 + \frac{\mu_e \rho}{\sigma}\Big) \tag{6.23}$$

As can be seen the effective electron diffusion coefficient is directly linked to the conductivity and the space charge. As $\Gamma_e = -D_e\nabla n_e - \mu_e n_e \mathbf{E} = -D_{eff}\nabla n_e$, the electric field is:

$$E = -\frac{(D_e - D_{eff})}{\mu_e}\frac{\nabla n_e}{n_e} \tag{6.24}$$

with the Poisson equation:

$$\nabla \cdot E = \frac{\rho}{\epsilon_0} = -\frac{(D_e - D_{eff})}{\mu_e}\nabla\left(\frac{\nabla n_e}{n_e}\right) \tag{6.25}$$

and thus:

$$\rho = -\frac{\epsilon_0(D_{eff} - D_e)}{\mu_e}\left[\left(\frac{\nabla n_e}{n_e}\right)^2 - \frac{\nabla^2 n_e}{n_e}\right] \tag{6.26}$$

For free diffusion $D_{eff} = D_e$ and consequently $\rho = 0$, i.e. the space charge is negligible.
Let's consider that the plasma is symmetric and derive D_{eff} as a function of the conductivity σ_0 on the axis of symmetry. On this axis, $\nabla n_e = 0$ and $\nabla^2 n_e / n_e = -1/\Lambda^2$ [155]. Consequently with Eqs.6.23 and 6.26:

$$\begin{aligned} D_{eff} &= D_a\left(1 + \frac{\epsilon_0(D_{eff} - D_e)}{\Lambda^2 \sigma_0}\right) \\ &= D_a\left(\frac{1 + \frac{\Lambda^2\sigma_0}{D_e\epsilon_0}}{\frac{D_a}{D_e} + \frac{\Lambda^2\sigma_0}{D_e\epsilon_0}}\right) \end{aligned} \tag{6.27}$$

If we suppose that the conductivity is mainly electronic ($\sigma_0 \approx \mu_e n_e e$), then:

$$D_{eff} \approx D_a\left(\frac{1 + \frac{\Lambda^2}{\lambda_{De}^2}}{\frac{D_a}{D_e} + \frac{\Lambda^2}{\lambda_{De}^2}}\right) \tag{6.28}$$

The evolution of the electron diffusion coefficient derived from Eq.6.28 is presented in Fig.6.1. As

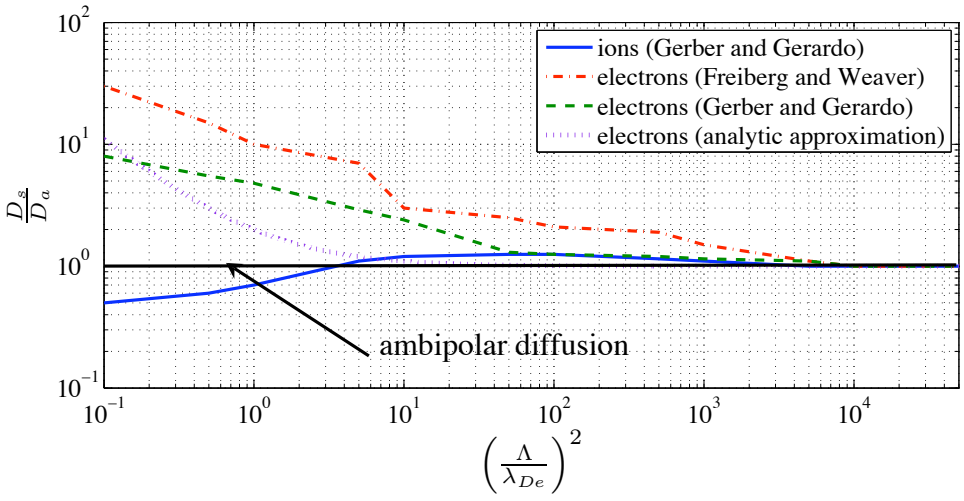

Figure 6.1: Evolution of the electron and ion diffusion coefficient (D_s; $s = i, e$) as a function of $(\Lambda/\lambda_{De})^2$

can bee seen in Fig.6.1, the deviation from ambipolar diffusion using the analytic approximation starts to be important when $(\Lambda/\lambda_{De})^2 \sim 1$. A common approximation for the transition from ambipolar to free diffusion is to consider that ambipolar diffusion takes place until $(\Lambda/\lambda_{De})^2 = 1$ and then electrons and ions diffuse freely.
However, experimental measurements in helium discharge have shown that the deviation from ambipolar diffusion starts when $(\Lambda/\lambda_{De}) \sim 100$ [128, 156]. The experimental results extracted from Refs.[128, 156] are presented in Fig.6.1.

6.1.2 Measurement of plasma decay in dust-free plasma

Measurements of the electron density decay in afterglow plasma have been performed in two kinds of dust-free plasma: a molecular gas plasma (nitrogen N_2) and a monatomic gas plasma (argon Ar). The microwave cavity resonance technique (see Sec.3.2.5) was used to measure the electron density.

In the case of the argon plasma, the Ar flow was 41.8 sccm. The operating pressure was $P = 1.1$ mbar and the RF power was $P_W = 20$ W. In order to reconstruct the resonance curves, the plasma was pulsed with times $t_{on} = 10$ s and $t_{off} = 30$ s. These times were necessary to obtain the same conditions for each run and construct accurate resonance curves.

In the case of the pure nitrogen plasma, the N_2 flow was 43.5 sccm. The operating pressure was $P = 0.9$ mbar and the RF power was $P_W = 40$ W. In order to reconstruct the resonance curves, the plasma was pulsed with times $t_{on} = 10$ s and $t_{off} = 30$ s.

As can be seen on Fig. 6.2 , the electron density decay is slightly different for nitrogen afterglow

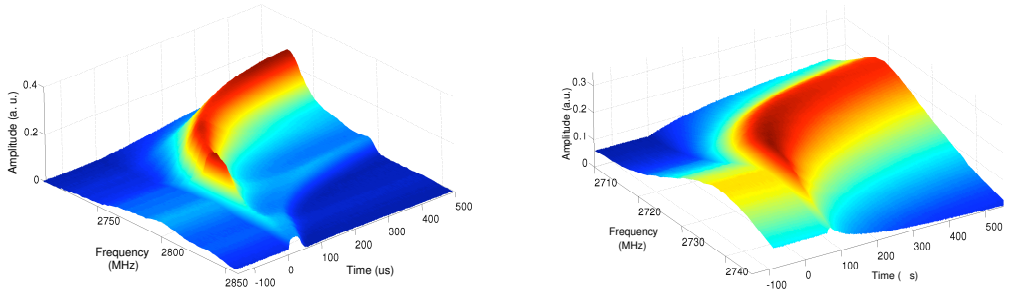

(a) (b)

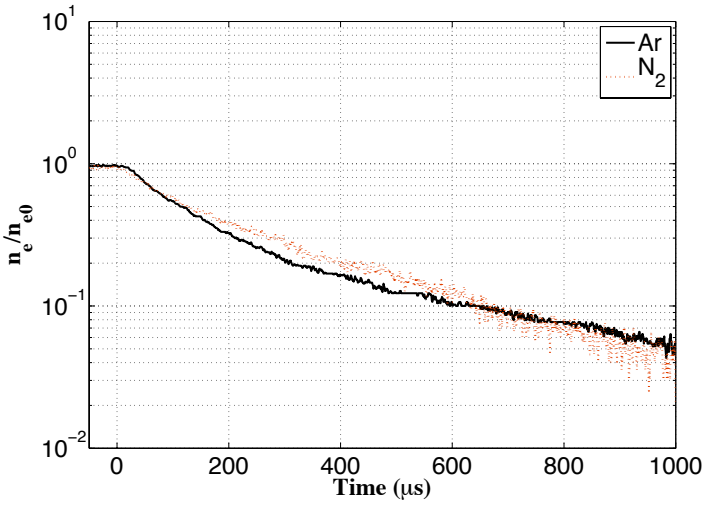

(c)

Figure 6.2: (a) Evolution of the microwave cavity resonant frequency in an Ar afterglow plasma. (b) Evolution of the microwave cavity resonant frequency in an N_2 afterglow plasma. (c) Evolution of the relative electron densities in Ar and N_2 afterglow plasmas

plasma and argon afterglow plasma. The plasma decay time of the nitrogen afterglow plasma is found to be $\tau^0_{L_{N_2}} \sim 200$ μs at the beginning of the afterglow and evolves to $\tau_{L_{N_2}} \sim 350$ μs at the end of the data span. The plasma decay time of the argon afterglow plasma is found to be $\tau^0_{L_{Ar}} \sim 150$ μs at the beginning of the afterglow and evolves to $\tau_{L_{Ar}} \sim 550$ μs at the end of the data span. The differences between the decay time are partially due to the difference in pressures. Moreover for a molecular gas plasma, volume losses of charges species are the most important process while in a monatomic gas plasma, losses are mainly by diffusion (i.e. diffusion and recombination on to the walls of the reactor). In an argon plasma, the diffusion time is inversely proportional to the electron temperature (Eq.6.9), whereas in a nitrogen plasma the recombination coefficient is $\alpha(N_2^+) \propto T_e^{-0.4}$ [157], and so the evolution of the decay time is more pronounced in the case of the argon plasma than the nitrogen plasma.

6.2 Afterglow in complex plasma

In a complex plasma afterglow, the dust particles interact with the ions and the electrons and thus surface recombinations of the charge carriers occur at the dust particle surfaces. Consequently, the dust particles act as a sink for charge species and sink terms must be added in Eqs.6.2 and 6.3:

$$S_e = -\nu_{ed} n_e \tag{6.29}$$

$$S_i = -\nu_{id} n_i \tag{6.30}$$

where $\nu_{e(i)d}$ is the dust-electron (ion) collection frequency. The plasma losses are, in complex plasmas, a combination of diffusion losses and losses by absorption-recombination on dust particle surfaces.

In the first part of this section, the plasma losses due to the presence of dust particles are investigated theoretically. Then electron density decay measurement in the afterglow of chemically active dusty plasmas is presented and compared to dust-free plasma electron density decay. Finally, the possible use of the plasma loss time measurement as a complementary diagnostic for dusty plasma is presented and supported by the comparison with available experimental data.

6.2.1 Diffusion in complex (dusty) plasma

When a discharge is switched off, the ions and electrons of the plasma starts to diffuse and the plasma density decreases as follows:

$$\frac{d\tilde{n}}{dt} = -\frac{\tilde{n}}{\tau_L} \tag{6.31}$$

where $\tilde{n} = n_{i(e)}/n_0$ and τ_L the plasma decay time. In a complex plasma, plasma losses are due to the diffusion of the ions and the electrons toward the wall of the reactor and by recombination

onto the dust particle surfaces. Consequently, the plasma decay time τ_L is:

$$\tau_L^{-1} = \tau_D^{-1} + \tau_A^{-1} \tag{6.32}$$

where τ_D is the plasma diffusion time and τ_A the dust particle absorption time. As the dust particles are charged due to the fluxes of ions and electrons flowing to their surfaces, the dust particle absorption time will depend on the charge (and surface potential) of the dust particle. Using the orbital motion limited approach the charge on a dust particle is given by [86]:

$$\frac{dQ_d}{dt} = J_i - J_e = -\pi e r_d^2 [n_e v_{T_e} e^{-\varphi} - n_i v_{T_i}(1 + \frac{T_e}{T_i}\varphi)] \tag{6.33}$$

where Q_d is the dust particle charge, $J_{i(e)}$ is the ion (electron) flux, r_d is the dust particle radius, $n_{i(e)}$ is the ion (electron) density, $v_{T_{i(e)}}$ the ion (electron) thermal speed, $T_{i(e)}$ is the ion (electron) temperature and φ is the dimensionless dust surface potential. The latter can be linked to the dust charge number Z_d by:

$$\varphi = \frac{Z_d e^2}{4\pi\epsilon_0 r_d k_B T_e} \tag{6.34}$$

It has been shown that when $T_i \ll T_e$ and $(r_d/\lambda_D)^2 \ll T_i/T_e$ where λ_D is the Debye length, the trapped ions play a significant role in the charging process of dust particles [87, 88] and Eq.6.33 has to be modified appropriately. However, for the conditions we are interested in, $(r_d/\lambda_D)^2 \sim T_i/T_e$.

In a complex plasma afterglow, the recombination on dust particle surfaces is directly linked to the flux of ions onto the dust particles as the dust particles are negatively charged in a laboratory plasma. Consequently, the dust particle absorption time τ_A can be written as :

$$\tau_A^{-1} = \pi r_d^2 n_d v_{Ti}(1 + \frac{T_e}{T_i}\varphi) \tag{6.35}$$

In a dust-free plasma ($n_e = n_i$), the equilibrium surface potential of an isolated dust particle can be found by solving $dQ_d/dt = 0$ and thus by solving:

$$\Big(\frac{T_i}{T_e}\frac{m_e}{m_i}\Big)^{1/2}(1 + \frac{T_e}{T_i}\varphi_0)\exp(\varphi_0) = 1 \tag{6.36}$$

Nevertheless, in a complex plasma, the ion density n_i and the electron density n_e are different due to the charging of the dust particles. However, as the plasma is quasi-neutral, the electron density can be deduced using the neutrality equation:

$$n_e = n_i - Z_d \cdot n_d \tag{6.37}$$

The ratio of the electron density to the ion density can be thus written as:

$$\frac{n_e}{n_i} = 1 - \frac{Z_d n_d}{n_i} = 1 - P_H \tag{6.38}$$

where $P_H = Z_d n_d / n_i$ is the Havnes parameter. As can be seen from Eq.6.37 and Eq.6.38, for very low dust density, the electron density is very close to the ion density ($n_e \simeq n_i$ and $P_H \sim 0$). Consequently, the surface potential of the dust particle will be the same as for isolated dust particles and the dust particle absorption time τ_{A_0} is inversely proportional to the dust density:

$$\tau_{A_0}^{-1} = \pi r_d^2 n_d v_{Ti} (1 + \frac{T_e}{T_i}\varphi_0) \tag{6.39}$$

However, when the dust density increases, the electron and ion densities start to deviate from each other and the Havnes parameter increases. Consequently, as already mentioned in Sec.2.1.3, solving $dQ_d/dt = 0$, the dust surface potential follows:

$$\Big(\frac{T_i}{T_e}\frac{m_e}{m_i}\Big)^{1/2}(1 + \frac{T_e}{T_i}\varphi)\exp(\varphi) = 1 - P_H \tag{6.40}$$

This equation has to be solved numerically and the value of the surface potential explicitly depends on the dust particle density. This will directly affect the dust particle absorption time. However,if the dust density is not to high, the deviation of the dimensionless dust surface potential from the isolated dust particle surface potential will be small so one can write $\varphi = \varphi_0 + \Delta\varphi$. Using a first order approximation, Eq.6.40 can be rewritten as:

$$\begin{aligned}\Big(\frac{T_i}{T_e}\frac{m_e}{m_i}\Big)^{1/2}\Big(1 + \frac{T_e}{T_i}(\varphi_0 + \Delta\varphi)\Big)\exp(\varphi_0)(1 + \Delta\varphi) \\ = 1 - \frac{Z_d n_d}{n_i}\end{aligned} \tag{6.41}$$

From Eq.6.34 and Eq.6.36, it can then be deduced that:

$$\begin{aligned}\Delta\varphi \;=\; & -\Big(1 + \Big(\frac{T_e}{T_i}\frac{m_e}{m_i}\Big)^{1/2}\exp(\varphi_0) + \frac{4\pi\epsilon_0 r_d k_B T_e n_d}{e^2 n_i}\Big)^{-1} \\ & \times \quad \frac{4\pi\epsilon_0 r_d k_B T_e}{e^2}\frac{\varphi_0 n_d}{n_i}\end{aligned} \tag{6.42}$$

In a typical laboratory plasma, $(T_e m_e / T_i m_i)^{1/2}\exp(\varphi_0) \sim 10^{-2}$ and $(4\pi\epsilon_0 r_d k_B T_e n_d)/(e^2 n_i) \sim 10^{-1}$, thus:

$$\Delta\varphi \simeq -\frac{4\pi\epsilon_0 r_d k_B T_e}{e^2}\frac{\varphi_0 n_d}{n_i} \sim -Z_{d0}\frac{n_d}{n_i} \tag{6.43}$$

where $Z_{d0} = |Q_{d0}/e|$ is the charge number of an isolated dust particle. The dust particle absorption time can be rewritten as:

$$\begin{aligned}\tau_A^{-1} \;\simeq\; & \pi r_d^2 n_d v_{Ti}\Big(1 + \frac{T_e}{T_i}\varphi_0\Big) \\ & -\pi r_d^2 n_d^2 v_{Ti}\cdot\frac{T_e}{T_i}\frac{4\pi\epsilon_0 r_d k_B T_e}{e^2}\frac{\varphi_0}{n_i}\end{aligned} \tag{6.44}$$

The dust particle absorption time is no longer inversely proportional to the dust density. There is a term in n_d^{-2} which tends to attenuate the effect of the dust particles on plasma losses. Indeed

when the dust density is high the dust surface potential is lower as is the dust charge number Z_d. Consequently the ion flux is reduced and the dust particle absorption time is increased compared to the value it would have if the dust particles can be considered as isolated.

Numerical results

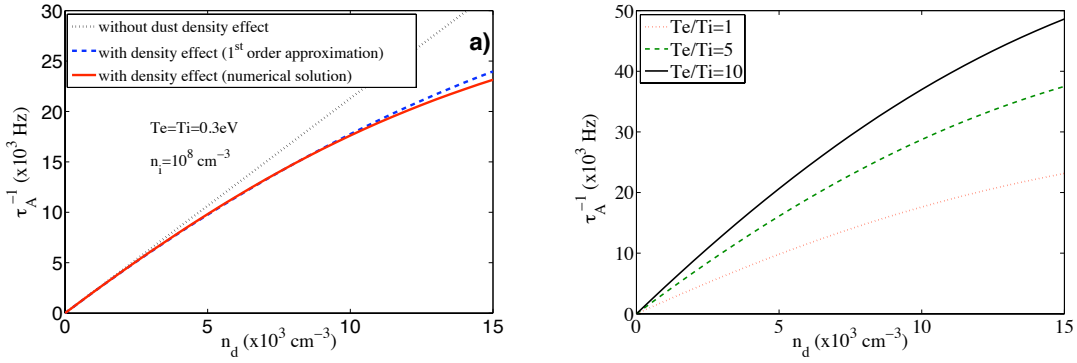

Figure 6.3: Particle absorption time as a function of the dust density. a) With or without taking into account the dust density effect. b) For different T_e/T_i

In this section, exact numerical solutions of Eq.6.40 are presented and compared to the approximate solution of Eq.6.44.
In Fig.6.3, the absorption frequency τ_A^{-1} has been computed for $n_i = 10^8\ cm^{-3}$, $T_e = 0.3$ eV (close to the experimental value of Ref.[21]) and the dust particle radius is $r_d = 10\ \mu m$. As can be seen in Fig.6.3(a), for low dust densities the dust absorption frequency τ_A^{-1} is increasing linearly as expected. On the contrary, for high dust density the absorption frequency τ_A^{-1} deviates from the linear evolution $\tau_{A_0}^{-1}$. The exact solution and the first order approximation are in agreement even though some small discrepancies are observed at high dust density. In Fig.6.3(b), the exact solution is presented for different ratio T_e/T_i. As can be seen, the absorption frequency τ_A^{-1} increases when this ratio increases. Indeed, when the electron temperature is higher than the ion temperature, ion and electron fluxes are greater at equilibrium (Eq.6.6) resulting in an increased dust particle absorption frequency.
In Fig.6.4, the ratio $\tau_A^{-1}/\tau_{A_0}^{-1}$ as well as the Havnes parameter P_H have been computed for different dust and ion densities. As can be seen in Fig.6.4(a), the deviation from $\tau_{A_0}^{-1}$ is marked at high dust density and low ion density. In Fig.6.4(b) the latter corresponds to a Havnes parameter close to 1. For small Havnes parameters (i.e. small dust density and high ion density), it can be seen that $\tau_A^{-1}/\tau_{A_0}^{-1} \sim 1$. This confirms that when dust particles can be considered as isolated inside the plasma the absorption frequency is directly proportional to the dust density while for high dust density the charge carried by a dust particle is reduced as the dust density increases and consequently the dust absorption frequency does not evolve linearly with the dust density.
In a plasma afterglow, the plasma density decreases with time. Consequently the effect of the

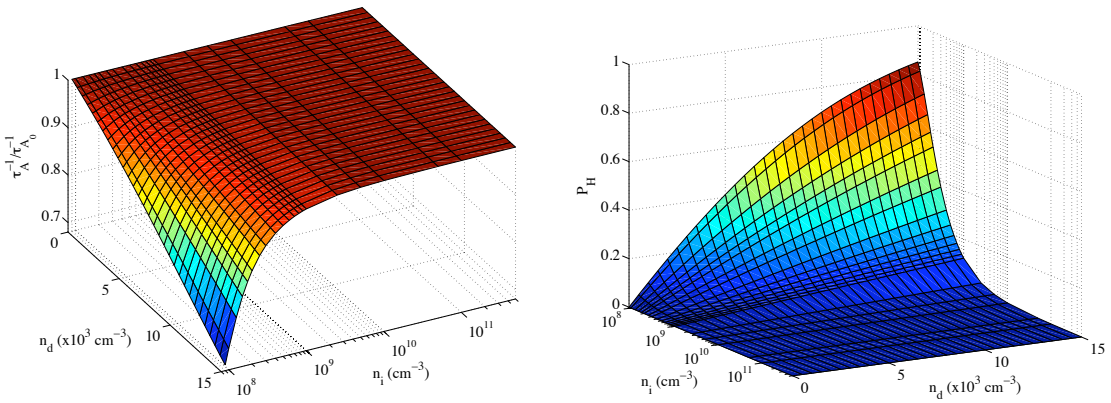

(a) (b)

Figure 6.4: (a) Ratio of the dust particle absorption frequency taking into effect dust density effect τ_A^{-1} relative to the dust particle absorption frequency not taking into effect dust density effect $\tau_{A_0}^{-1}$ for different values of dust and plasma densities. (b) Havnes parameter P_H for different values of dust and plasma densities.

dust particles can become more and more important over time. In order to see this effect, the first instant of the decay of a complex plasma has been computed using Eq.6.31, Eq.6.32, Eq.6.35 and Eq.6.38. The results are presented in Fig.6.5. The plasma diffusion loss is taken into account by choosing a diffusion frequency $\tau_D^{-1} = 500$ Hz (which is a typical value for a laboratory discharge with an argon pressure around 1 Torr and these plasma parameters). As can be seen in

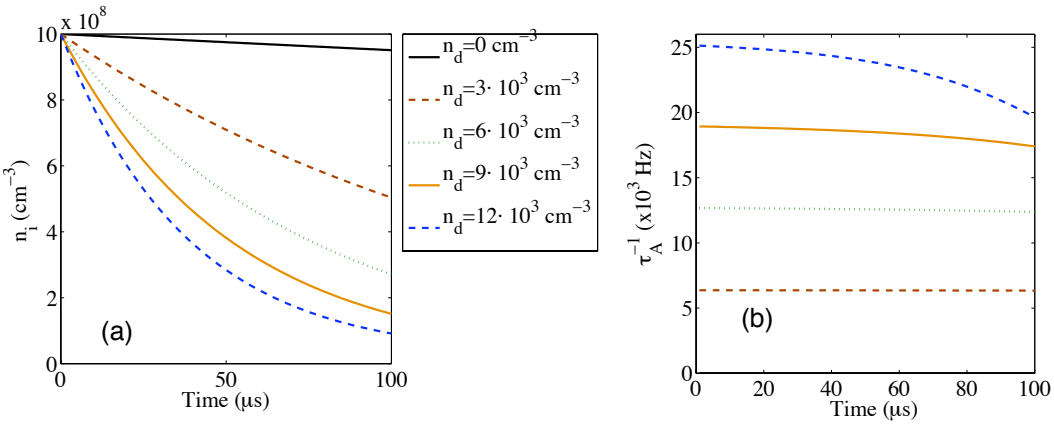

Figure 6.5: (a) Evolution of ion density n_i during the first microsecond of a plasma afterglow for different dust densities. (b) Evolution of the dust particle absorption frequency τ_A^{-1} during the first microseconds of a plasma afterglow for different dust densities. The diffusion frequency is $\tau_D^{-1} = 500\ Hz$

Fig.6.5(a), the dust particles enhance plasma losses and the greater the dust density, the greater the effect on plasma losses. In Fig.6.5(b), it can be seen that at the very beginning of the plasma afterglow, the absorption frequency is roughly proportional to the dust density. This is due to the high value of the plasma density at this time which allows a small Havnes parameter and

thus dust particles can be considered as isolated. However, as the density decreases, the effect of the dust particles become more and more important and the particle absorption frequency decreases. Indeed the Havnes parameter increases with time as the plasma density decreases. Consequently the dust particles are more and more affected by the presence of the other dust particles. The ion flux as well as the dust particle charge number decrease leading to a decrease of the dust absorption frequency. This effect is clearly visible in Fig.6.5(b) for high dust density.

6.2.2 Measurement of plasma decay in complex plasmas

In order, to check the influence of the presence of dust particles in an afterglow plasma, the electron density decay has been measured for different gas mixtures in chemically active plasmas. Dust particles have been grown in Ar/CH_4 plasma, Ar/SiH_4 plasma and N_2/CH_4 plasma. The microwave resonant cavity technique (see Sec.3.2.5) was used to measure the electron density.
In the case of the Ar/CH_4 plasma, an argon flow of 41.8 sccm and a methane flow of 0.8 sccm were used. The dilution rate was thus 1.9%. The operating pressure was P =1.1 mbar and the RF power was $P_W = 20$ W. In order to reconstruct the resonance curves, the plasma was pulsed with $t_{on} = 40$ s and $t_{off} = 80$ s. These times are necessary to obtain the same conditions for each plasma and achieve good resonance curves.
In the case of the N_2/CH_4 plasma, an argon flow of 43.5 sccm and a methane flow of 1.3 sccm were used. The dilution rate was thus 3%. The operating pressure is P =0.9 mbar and the RF power was $P_W = 40$ W. In order to reconstruct the resonance curves, the plasma was pulsed with $t_{on} = 30$ s and $t_{off} = 60$ s.
In the case of the Ar/SiH_4 plasma, an argon flow of 20 sccm and a silane flow of 1.2 sccm were used. The dilution rate was thus 6%. The operating pressure was P =0.12 mbar and the RF power was $P_W = 10$ W. In order to reconstruct the resonance curves, the plasma was pulsed with $t_{on} = 0.8$ s and $t_{off} = 20$ s.
The plasma decay times have been estimated just after the RF power supply has been turned

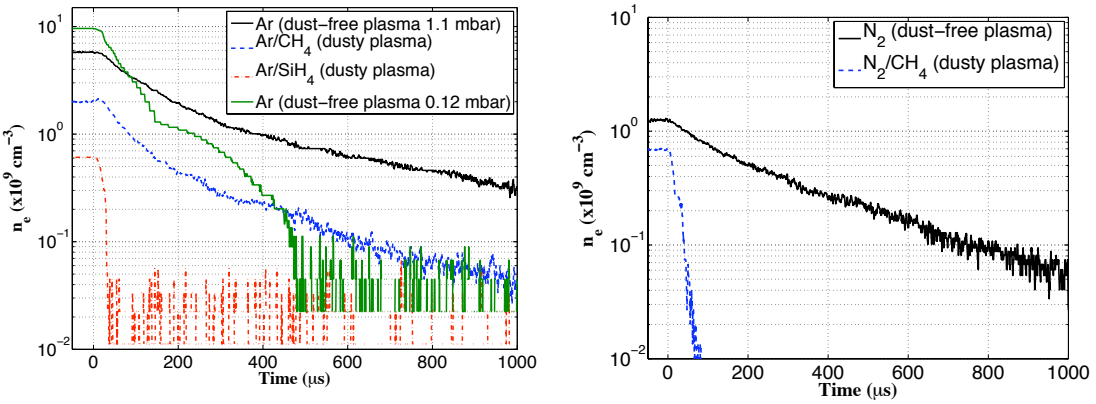

(a) Argon plasmas

(b) Nitrogen plasmas

Figure 6.6: Electron density decay in dusty and dust-free plasmas.

off for the various plasmas (Fig.6.6). It has to be noted that before the discharge is switched off the electron density is always smaller in the dusty plasma than in the dust-free plasma at the same pressure.

For the Ar/CH_4 plasma (in which 200 nm diameter dust particles are grown), the decay time is $\tau^0_{L_{Ar/CH_4}} \sim 83$ μs which is much shorter than the decay time measured for a pristine argon plasma at the same pressure ($\tau^0_{L_{Ar}} \sim 150$ μs). It has also to be noted that in this Ar/CH_4 plasma the electron density does not decrease immediately and a small increase of the electron density is even observed at the very beginning of the afterglow. This effect has also been reported in argon-acetylene discharge [158].

For the Ar/SiH_4 plasma (in which 50 nm diameter dust particles are grown), the decay time is $\tau^0_{L_{Ar/CH_4}} \sim 25$ μs which is much shorter than the decay time measured for a pristine argon plasma at the same pressure ($\tau^0_{L_{Ar}} \sim 60$ μs)[1]. However, no increase of the electron density is observed at the very beginning of the afterglow.

For the N_2/CH_4 plasma (in which 150 nm diameter dust particles are grown), the decay time is $\tau^0_{L_{Ar/CH_4}} \sim 40$ μs which is much shorter than the decay time measured for a pristine argon plasma at the same pressure ($\tau^0_{L_{N_2}} \sim 200$ μs). Again, in this case, no increase is observed at the very beginning of the afterglow.

To conclude, measurements of the electron density decay in various dusty plasmas have shown that the presence of dust particles drastically shorten the plasma decay time as predicted theoretically. However, in one particular gas mixture (Ar/CH_4), the electron density decay does not take place immediately but is preceded by a short and small increase of the electron density. Such an increase has been also reported in a C_2H_4/Ar afterglow plasma (in which the dust density can be very high ($n_d \simeq 4.5 \cdot 10^6$ cm^{-3})) [158, 159]. Berndt *et al.* attributed this increase to an electron release by the dust particle [158, 159]. Such an increase has already been observed in pulsed helium discharges and attributed to a re-ionisation due to metastable-metastable collisions [160, 161], and as the presence of high dust particle density in an argon dilution plasma enhances the metastable density [33]. The fact that this electron density increase is not observed in other mixtures suggests that this release of electrons may be dependant on the dust particles material.

6.2.3 Complex plasma afterglow as a diagnostics

As we demonstrated in Sec.6.2.1, the dust density influences greatly the dust absorption-recombination process in an afterglow plasma. Thus, the dust absorption frequency does not increase linearly with the density, and for high density it is smaller than the absorption frequency that would occur if each dust particle could be considered as isolated in the plasma. Moreover, it was shown in Sec.6.2.1 that if the dust density is not too high, a first order approximation of the absorption frequency matches very well with the exact solution. In Eq.6.44, there are only a few parameters to know (T_e, T_i, r_d, φ_0 and n_i). Consequently, it is possible to use the

[1] A break can be seen in the curve corresponding to the electron density decay in a pristine argon plasma at $P = 0.12$ mbar (Fig.6.6). This break is not physical and is due to an experimental problem.

measurement of the absorption frequency in the afterglow of a complex plasma in parallel with other diagnostics to deduce some important parameters of the plasma.
For example, in Ref.[21], the dust particle absorption frequency has been measured in the afterglow of a linear pulsed discharge. The argon pressure was 1.9 Torr and the density of dust varied from 0 to $10^4\ cm^{-3}$. The dust particles had a mean radius $r_d \simeq 15\mu m$. It is reported that the electron temperature was roughly equal to the ion temperature ($T_e \sim T_i$) [21]. Consequently, the influence of trapped ions on the dust particle charge can be neglected. In Fig.6.7, experimental results from Ref.[21] are fitted using Eq.6.36 and Eq.6.44. The fit gives $T_i \simeq 0.042\ eV$, $(T_e/T_i)\varphi_0 = 4.4$ and thus assuming $T_i \leq T_e \leq 5T_i$ (depending when the measurement has been performed in the plasma afterglow), it gives $10^7 cm^{-3} \leq n_i \leq 5 \cdot 10^7 cm^{-3}$. The range for the ion density and the ion temperature are much lower than those that were supposed in Ref.[21] but it could be due to the fact that their measurements were performed quite late in the plasma afterglow and temperature relaxation needed to be taken into account.

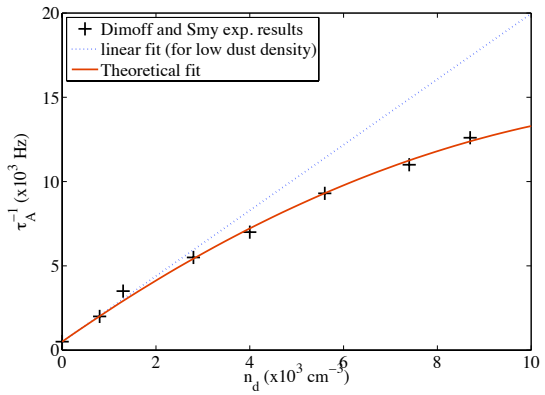

Figure 6.7: Fit of experimental results of Ref.[21] using the first order approximation (Eq.6.44)

6.2.4 Conclusion

The influence of the dust density on plasma losses has been studied. It has been shown that the presence of dust particles can drastically shorten the plasma loss time and that the increase of the dust absorption frequency does not depend linearly on the dust particle density. Finally, by comparing our results with existing experimental data, the possible use of absorption frequency measurement as a diagnostic for complex plasma is mentioned. Comparison with existing experimental data [21] supports this idea.

6.3 Residual dust charge

As the charge carries are lost during the afterglow stage, the charge on dust particles must evolve at the same time. There are many publications reporting on the investigation of dust charging

in discharge plasma [80, 86, 98, 162–167] . However there are only few papers devoted to dust charging, or decharging to be more specific, in the discharge afterglow. In [168] a diffusion of fine dust particles (8-50nm) in the afterglow of a dusty plasma has been studied. From the afterglow decay of dust number density the charged fraction of particle was measured. It was found that some particles carried a very small residual charge and some were neutral. A model has been proposed to explain charges on particles in the late afterglow of a dusty plasma. In microgravity experiments, it was shown that dust particles keep about 2% of the charge acquired in the plasma [77]. Experiments were performed in the PKE-Nefedov reactor [64] under microgravity conditions on board the ISS. The existence of negative residual charges was shown and a simple theoretical model that describes data obtained was proposed. The residual charges were attributed to the presence of an excitation electric field that was used for dust charge measurements. Limitations of the Space Station experiment prevented further investigation of this hypotheses. Theoretical predictions on an effect of RF plasma parameters on residual charges has not been verified.

So any new experimental evidence of residual dust charges in afterglow plasma will lead to a better understanding of the decharging of complex plasma. Indeed the value and nature of residual charges after plasma extinction is of great importance. The dust particle charge in afterglow plasma could induce problem in future single-electron devices where a residual charge attached to deposited nanocrystals would be the origin of dysfunction. It could make easier industrial plasma processing reactor decontamination using a specially designed electric field. The residual charges on dust particles in fusion reactors (such as ITER) could also make the cleaning process much easier.

Furthermore, complex plasma afterglow provides a unique opportunity to perform measurements of the dust charge distribution (DCD). In a decaying complex plasma, the dust particle charges as well as the DCD evolve with the other plasma parameters such as the plasma density and the electron temperature. In the late stages of plasma decay the dust charge is frozen and does not change further and the DCD remains unchanged for a long time.

In this section, laboratory measurements of dust residual charges are reported. These experiments have been performed using dust particles directly grown in the plasma which can be confined in the volume of the reactor after the plasma is turned off by using an upward thermophoretic force which balance the gravity force. The residual electric charge of the dust particle is deduced by inducing oscillations of the dust particle using a well-known sinusoidal electric field. Thus dust residual charge distributions have been measured for different experimental conditions

A model taking into account the transition from ambipolar to free diffusion has been developed to explain the existence of residual charge and the measured dust residual charge distribution.

6.3.1 Evidence and measurement of residual dust charge

Evidence of the existence of residual dust charge

High speed video recording of the laser light scattered by the dust particles during the fall of the dust particles cloud grown in the PKE-Nefedov chamber with $P_{Ar} = 1.6$ mbar and $P_W = 3.6$ W has been done for different bias voltages applied to the bottom electrode. The evolution of the central column intensity is presented in Fig.6.8. The intensity of the light is roughly proportional to the density of dust particles. As can be seen in Fig.6.8, when no bias is applied the dust cloud

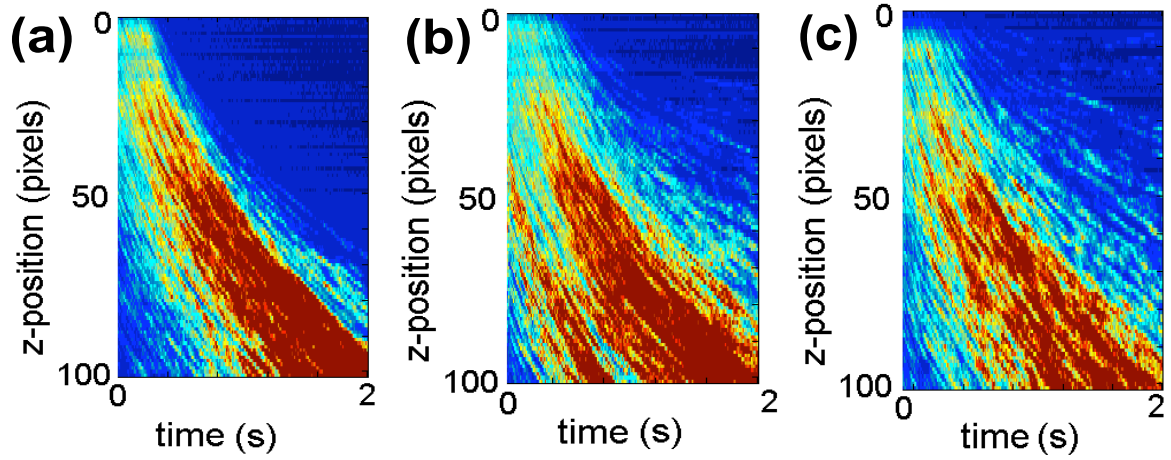

Figure 6.8: Line profile of a high speed video imaging during the fall of the dust particle cloud in discharge afterglow at $P = 1.6$ mbar (in false colour from blue to red). (a) No bias on the lower electrode. (b) -10V bias on the powered electrode. (c) +10 V bias on the power electrode

is less dispersed that when a positive or negative bias is applied. This is a strong indication that the dust particles are charged in the discharge afterglow and are interacting with the applied electric field. Moreover, the observed spread for both positive and negative bias condition is a strong indication that positively and negatively charged dust particles coexist in the discharge afterglow.

Measurement of residual dust charge distribution

For the study concerning residual charges, the top electrode was cooled (Fig. 6.9). An upward thermophoretic force was applied to dust particles in order to counterbalance gravity [78] when the plasma is off. To study particle charges, a sinusoidal voltage produced by a function generator with amplitude $\pm 30\ V$ and frequency of $1\ Hz$ was applied to the bottom electrode. Induced low frequency sinusoidal electric field $\boldsymbol{E}(\boldsymbol{r}, t)$ generated dust oscillations for dust particles that have a residual electric charge.

An important effect that must be considered in the estimation of the thermophoretic force is an influence of the finite volume of gas (Fig.6.10). If the pressure is low enough, the gas mean free path can become comparable to the length scale of experimental apparatus and the gas can no longer be treated as a continuous medium. Under such conditions, an additional Knudsen

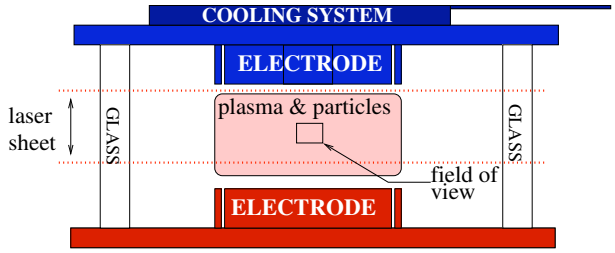

Figure 6.9: Schematic of the experimental apparatus

number must be considered [105] $Kn_L = l_g/L$ where l_g is the mean free path of buffer gas species and L is the length scale of the reactor. In this experiment, the length between electrodes is $L = 3$ cm giving $Kn_L \sim 5 \cdot 10^{-3}$ which means the gas can be considered as a continuous medium.

The temperature gradient between the electrodes was calculated using the FEMLAB© code

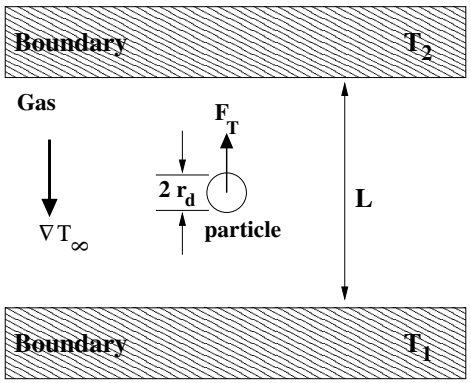

Figure 6.10: Thermophoresis in finite volume of gas

(steady state analysis of heat transfer through convection and conduction with heat flux, convective and temperature boundary conditions using Lagrange-Quadratic element). The temperatures on the electrodes were measured by a thermocouple and used as boundary conditions for the problem. The contour-plot obtained is presented in Fig.6.11. It shows that the vertical component of the temperature gradient is constant near reactor centre. The value of the temperature gradient is about 2 K/cm for our experiment. There is also a small horizontal component of the temperature gradient. This is the reason for the particle drift in horizontal direction. Such drifts allowed us to resolve particle trajectories and made particle charge measurement more convenient.

The residual charge measurements have been performed as follows. First the chamber was pumped down to the lowest possible pressure (base pressure $\sim 2 \cdot 10^{-6}$ mbar) and the cooling system was turned on. After this, argon was injected until the operating pressure was reached, the discharge was started and particles were grown, forming familiar structures such as a void (see for example [60]). Then, the discharge was switched off and a sinusoidal voltage was applied

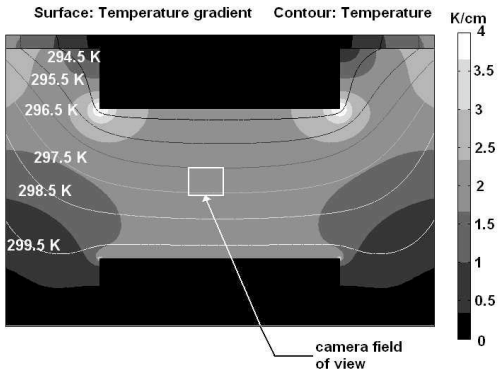

Figure 6.11: Temperature profile and gradient

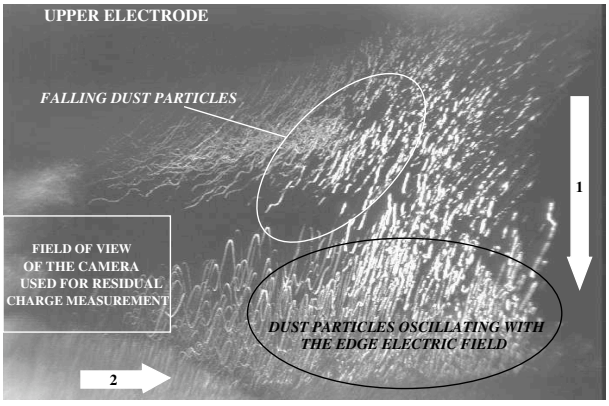

Figure 6.12: Superimposition of video frames taken with a large field of view CCD camera. Arrows 1 and 2 represent respectively the vertical and the horizontal components of the temperature gradient. Edge effects as well as falling dust particles can be seen.

to the bottom electrode.
In the afterglow plasma, the dynamics of dust particles is determined by the temperature gradient and excitation electric field. Fig.6.12 presents a superimposition of images taken after the discharge had been switched off. There are two different types of motion observable. Dust particles drift upwards, downwards and to the side due to existing temperature gradients and they oscillate due to the electrostatic force. It is obvious that the thermophoretic force acts on any dust particle in chamber, while the electrostatic force acts only on particles that have charge in afterglow. Thus the presence of oscillating particles (see Fig.6.12) clearly indicates that dust particles do have residual charges after the discharge has been switched off. Dust particles oscillating in opposite phases as well as non-oscillating dust grains have been observed indicating that negatively charged, positively charged and non-charged dust particles coexist after plasma extinction.
It is worth mentioning that in order to observe dust oscillations the discharge must be switched off abruptly. It was shown that if the power was decreased slowly until the plasma disappears there are no residual charges (no oscillations of dust particles in the sinusoidal electric field were observed). Another interesting fact is that residual charge on dust particles has a long relaxation time and does not depend on time over which the excitation electric field was applied. Dust oscillations were observed for more than one minute after plasma extinction and in both cases when the function generator was switched on during the discharge or few seconds after the discharge is turned off.
As can be seen in Fig.6.12, there are dust particles falling after the discharge is switched off. These particles are too big to be sustained by the thermophoretic force. Other particles drift horizontally at constant height; this means for these particles the gravity force is balanced by the vertical component of the thermophoretic force. These particles have been used to measure residual charges. It is clear from Fig.6.12, that use of a large field of view camera gives us good pictures of the decaying dusty plasma but it is not suitable for residual charge measurement because edge effects cannot be neglected. Thus a camera with the small field of view was used for the charge measurement (see Fig.6.12). The superimposition of images from this camera is shown in Fig.6.13. These images show clear tracks of dust oscillations allowing dust grain trajectories to be reconstructed

Particle size (mass) and residual charge measurements are strongly related in this experiment. Charge, size and mass of the dust particles have to be determined. Considering that dust particles levitating in reactor at a constant height after plasma extinction are the ones for which the gravitational force is exactly balanced by the thermophoretic force, the dust particle radius can be found using Eq.2.37 and Eq.2.38:

$$r_d = -\frac{8}{5\pi\rho g}\frac{k_{tr}}{v_{th}}\nabla T \tag{6.45}$$

The dust particles are assumed to be spherical and mainly made of carbon based on the recent results for dust particles grown in the PKE-Nefedov chamber by sputtering of a polymer material

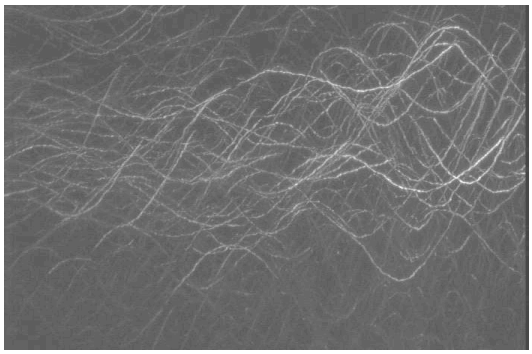

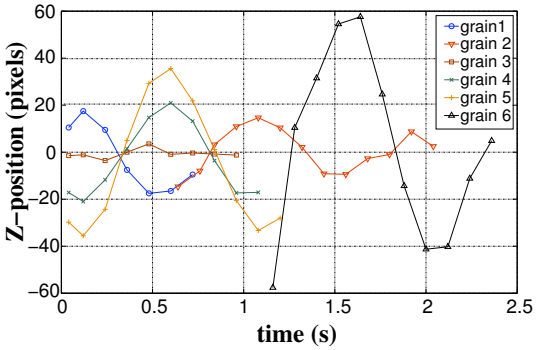

Figure 6.13: Left: Superimposition of video frames 10 seconds after plasma extinction. Dust particle oscillations can clearly be seen. The temperature gradient has a slight horizontal component. Therefore, trajectories are in the 2D laser plane. Right: Oscillation of 6 dust grains 10 seconds after plasma extinction. Non oscillating dust grain and oscillations of opposite phase are also observed.

[61]. It has been also shown in Samsonov and Goree [74] that particles are mainly spherical for carbonized dust particles (such as those in the present study). Bouchoule and Boufendi showed in silane discharges that when dust particles grow, the shape tends to be spherical [34] while for sizes of a few tens of nanometres more complex agglomerated structures are observed. Consequently the mass of the dust particles m_d can be deduced from Eq.6.45:

$$m_d = \frac{4}{3}\pi r_d^3 \cdot \rho \tag{6.46}$$

where ρ is the mass density of graphite. For our experimental conditions, the radius of the levitating dust grains is estimated to be $r_d \simeq 190\ nm$ and their mass is $m_d \simeq 6.5 \cdot 10^{-17}\ kg$. From the measurements of oscillation amplitude, the residual charge on a dust particle can be obtained. As the gravitational force is compensated by the thermophoretic force, the equation of motion for one dust particle, neglecting its interactions with other dust particles, is reduced to:

$$m_d \ddot{z} = F_E(z,t) + F_{nd}(\dot{z}) \tag{6.47}$$

Taking $E(t) = E_0(z_{mean})\cos(\omega t)$ (the amplitude of the electric field E_0 is the one at the mean dust levitation height z_{mean}) and using Eq.2.27, Eq.2.29 and Eq.6.47, the dust particle oscillation amplitude b can be obtained [169]:

$$b(\omega, Q_d, E_0) = \frac{Q_d E_0(z_{mean})}{m_d \omega \sqrt{\omega^2 + 4\gamma^2/m_d^2}} \tag{6.48}$$

where $\gamma = (4/3)\sqrt{2\pi} r_d^2 m_n n_n v_{Tn}(1 + \alpha_{ac}(\pi/8))$ is the damping coefficient and $\omega = 2\pi f$ where f is the frequency imposed by the function generator.

Eq.6.48 can easily be inverted to yield the dust residual charge:

$$Q_{d_{res}} = \frac{m_d b(\omega, Q_d, E_0(z_{mean}))\omega\sqrt{\omega^2 + 4\gamma^2/m_d^2}}{E_0(z_{mean})} \tag{6.49}$$

The sign of the dust particle charge is deduced from the phase of the dust particle oscillation with respect to the excitation electric field. Oscillation amplitudes up to 1.1 mm have been measured (depending on the operating pressure) and charges from $-12e$ to $+6e$ are deduced where e is the elementary charge. By measuring the oscillations of many dust particles, dust oscillation amplitude distributions have been constructed and were converted to DCDs (Fig.6.14). The DCD obtained at P =0.7 mbar is difficult to analyse due to the lack of statistics and it can hardly be compared to the other experimental DCDs because the particle were not of the same size. It has been found that, for dust particles of similar sizes, at high pressures dust particles keep a higher mean residual charge (Fig.6.14 and Tab.6.1). The distributions have been fitted by a Gaussian function (red line). The mean residual charges are negative for every pressures and their values correspond to a few electrons ($\bar{Q}_{d_{res}} \sim -3e$) for P =0.4 mbar, $\bar{Q}_{d_{res}} \sim -3e$) for P =0.7 mbar and ($\bar{Q}_{d_{res}} \sim -5e$) for P =1.2 mbar. Positive residual charges were observed for the every cases. The standard deviation of the DCD is of the same order of magnitude for every pressures ($\sigma \sim 2e$), see Fig.2. The coefficient $\delta = \sigma(Q_{d_{res}})/\sqrt{|\bar{Q}_{d_{res}}|}$ is about unity.
The error on the measurement need to be discussed. The assumption that dust particles in the experiment are almost mono-size is based on the fact that only particles of particular size can be levitated when the discharge is switched off. Taking into account that the temperature on the electrodes is known with a precision of $\pm$0.5 K, dust particles with radius 190 ± 15 nm will be levitated under our conditions. In order to avoid as much as possible uncertainties in relation to dust particle size, measurements have been performed a few seconds after plasma extinction. Just after the plasma extinction, various sizes of dust particles can coexist. At this time, the heaviest dust particles (not sustained by the thermophoretic force) fall down, whereas lightest ones move upwards. Thus, waiting few seconds allows these particles to be eliminated and restricts size dispersion. Furthermore, measurements have been performed on horizontal trajectories, meaning that gravity is closely counterbalanced by thermophoresis.
The uncertainty on the neutral drag force is mainly due to the knowledge of the dust particle radius and the accommodation coefficient α_{ac}. In an argon discharge, the accommodation coefficient is often taken to be $\alpha_{ac} = 1$ (see for example Ref.[170]). However, it has been measured that for carbon particles at room temperature, α_{ac}=0.90 [171]. Consequently, the overall precision on the damping coefficient is about 17%
Taking into account all sources of errors (radius, mass, electric field, neutral drag force), the residual charge on each particle is known with a precision of $\pm$50%.
If we apply the potential error of the experimental procedure to a theoretically predicted Gaussian distribution of residual charges with $\delta = \sigma/\sqrt{Q_{mean}} = 0.5$ and $|Q_{mean}| = 5e$ we will obtain a distribution with the same Q_{mean} but broadened to $\delta = 0.75$. This value of δ is below the measured value of $\delta = 1$ for a comparable DCD (pressure =1.2 mbar). For the measurement at

0.4 mbar (with a different Q_{mean}), the same procedure will lead to an broadened DCD with δ changing from 0.5 to 0.80. In this case we are also below the measured value of 0.91.
By addressing the problem in a reverse way (if we consider that the measured DCDs have been enlarged by the error), we can artificially remove this potential error on the DCDs. For 0.4 mbar we find an estimated error-free width of $\delta = 0.72$ and for 1.2 mbar an estimated error-free width of $\delta = 0.79$.
We can also analyse the error that can arise from the limited statistics. It is known that the relative uncertainty of the variance for m experimental points is $\Delta\sigma = \sqrt{2/(m-1)}$ which leads to $\Delta\sigma_m = 12\%$ for the measurement at 1.2 mbar (and thus an experimental width of $\delta = 1 \pm 0.07$ and an estimated error-free width of $\delta = 0.79 \pm 0.09$), and $\Delta\sigma_m = 17\%$ for 0.4 mbar (and thus an experimental width of $\delta = 0.91 \pm 0.09$ and an estimated error-free width of $\delta = 0.72 \pm 0.11$). In both cases the estimated values of δ is larger than the $\delta = 0.5$ predicted for a running discharge [56, 79, 90, 93, 94].

Table 6.1: Measured maximum, minimum and mean dust particle residual charges for two operating pressures.

	$P = 1.2\ mbar$	$P = 0.4\ mbar$
∇T	$-190\ K \cdot m^{-1}$	$-177\ K \cdot m^{-1}$
r_d	$194\ nm$	$180\ nm$
m_d	$6.9 \cdot 10^{-17}\ kg$	$5.4 \cdot 10^{-17}\ kg$
γ	$1.36 \cdot 10^{-13}\ kg \cdot s^{-1}$	$0.39 \cdot 10^{-13}\ kg \cdot s^{-1}$
$Q_{d_{res}max}$	$+2e$	$+6e$
$Q_{d_{res}min}$	$-12e$	$-13e$
$Q_{d_{res}mean}$	$-5e$	$-3e$

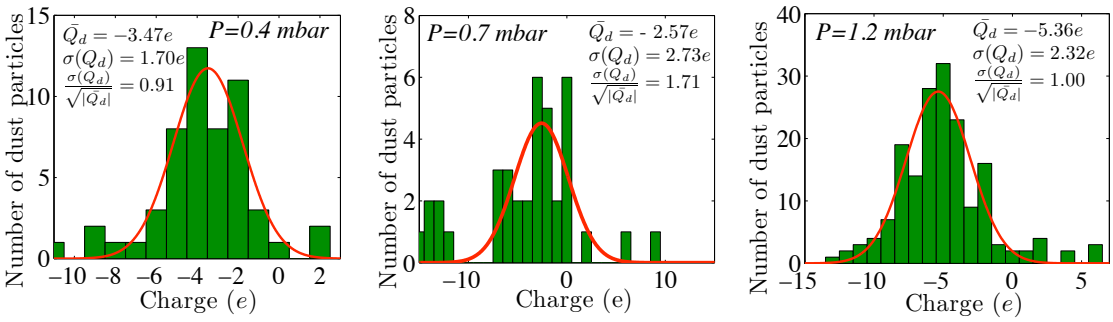

Figure 6.14: Measured residual dust charge distributions. From the left to the right: $P = 1.2$ mbar with grown dust particles; $P = 0.7$ mbar with injected $r_d = 250$ nm dust particles; $P = 0.4$ mbar with grown dust particles.

6.3.2 Modelling of dust particle decharging

The evolution of dust charge in afterglow plasma depends on the evolution of plasma parameters. In a decaying plasma (afterglow plasma), the kinetic of plasma losses is mainly governed by the electron temperature relaxation, plasma diffusion and recombination processes [137].

A four stage model

The charging (decharging) process of dust particle in a plasma is governed by the contributions of all currents entering (or leaving) the dust surface, involving plasma electron and ion currents, photoemission and thermionic emission currents, etc:

$$\frac{dQ_d}{dt} = \sum I_a + \sum I_l \tag{6.50}$$

where I_a and I_l are currents absorbed and emitted by the particle (with appropriate sign). As already mentioned, in most cases for discharge plasmas we can ignore the emission current and kinetics of the particle charge is given by Eq.6.33. According to Eq.6.33, the charge on a dust particle depends on the electron-ion masses, temperatures and density ratios m_e/m_i, n_e/n_i, T_e/T_i. Thus to analyse the decharging of dust particle in afterglow plasma one need to consider the kinetics of plasma decay.

The plasma diffusion loss and electron temperature relaxation determine the kinetics of the discharge plasma decay [137]. In presence of dust particles, plasma loss is due to diffusion to the walls complemented by surface recombination on dust particles. Equations for electron temperature relaxation and plasma density decay are given by Eqs.6.1 and 6.31 [137, 172]. The expressions for the time scales are [137, 172]:

$$\tau_L^{-1} = \tau_D^{-1} + \tau_A^{-1} \tag{6.51}$$

$$\tau_D^{-1} \simeq \frac{l_{in} v_{T_i}}{3\Lambda^2}(1+\tilde{T_e}) \equiv \frac{1}{2}(1+\tilde{T_e})\frac{1}{\tau_D^{\infty}} \tag{6.52}$$

$$\tau_A^{-1} \simeq \pi r_d^2 n_d v_{T_i}(1+\varphi\tilde{T_e}) \equiv \left(\frac{1+\varphi\tilde{T_e}}{1+\varphi}\right)\frac{1}{\tau_A^{\infty}} \tag{6.53}$$

$$\tau_T^{-1} = \sqrt{\frac{\pi}{2}}\sqrt{\frac{m_e}{m_i}}\frac{v_{T_i}}{l_{en}}\sqrt{\tilde{T_e}} \equiv \frac{\sqrt{T_e}}{\tau_T^{\infty}} \tag{6.54}$$

where τ_D is the ambipolar diffusion time scale onto the walls, τ_A is the particle absorption time scale, $l_{i(e)n}$ is the mean free path of ion (electron)-neutral collision, Λ is the characteristic diffusion length ($\Lambda \sim 1\ cm$ in this experiment). The ∞ exponent stands for the limiting value at very long time.

For charging time scales less than the plasma decay or temperature relaxation time scales the charge on dust particle is in equilibrium, i.e. ion and electron fluxes balance each other, $\varphi \simeq \varphi_{eq}$

Table 6.2: Values of the different time scales for two operating pressures.

	$P = 0.4$ mbar	$P = 1.2$ mbar
τ_D^0	90 μs	260 μs
τ_D^∞	4.5 ms	13 ms
τ_A^0	0.4 ms	0.4 ms
τ_A^∞	30 ms	30 ms
τ_L^0	75 μs	160 μs
τ_L^∞	3.9 ms	9 ms
τ_T^0	90 μs	38 μs
τ_T^∞	900 μs	380 μs
τ_Q^0	4 μs	4 μs
t_c	50 ms	110 ms
$\tau_Q(t_c)$	1.4 s	1.4 s

and using Eq.6.33, φ_{eq} is given by:

$$\frac{n_e}{n_i}\sqrt{\tilde{T}_e}e^{-\varphi_{eq}} = \sqrt{\frac{m_e}{m_i}}(1+\tilde{T}_e\varphi_{eq}) \tag{6.55}$$

In this case, expressions for charge fluctuation and charge fluctuation time scale τ_Q are:

$$\frac{dQ_d}{dt} \simeq -\frac{Q_d - Q_{deq}}{\tau_Q} \tag{6.56}$$

$$\tau_Q^{-1} \simeq \frac{v_{T_i} r_d}{4\lambda_{i0}^2}(1+\varphi_{eq})\tilde{n} \equiv \frac{\tilde{n}}{\tau_Q^0} \tag{6.57}$$

where $\lambda_{i0} = \sqrt{\epsilon_0 k_B T_i / n_0 e^2}$ is the initial ion Debye length.

It should be noted that the time scale for dust charge fluctuations strongly depends on plasma density and can vary from microseconds at the initial stages of plasma decay up to seconds for an almost extinguished plasma. Taking into account Eq.6.31 and Eq.6.57, the time dependence of τ_Q can be expressed as [77]:

$$\tau_Q^{-1} = \frac{1}{\tau_Q^0} exp(-t/\tau_L) \tag{6.58}$$

To understand the dusty plasma decharging dynamics we have to compare different time scales. In Tab.6.2, time scales for this experiment are presented. It can be seen that the initial charge fluctuation time scale is the shortest. The temperature relaxation time scale is shorter or becomes comparable (for 0.4 mbar) to the plasma density decay time scale, and plasma losses are mainly determined by diffusion. The latter means that for our experimental conditions dust particles did not affect the initial stages of plasma decay. Fig.6.15 presents the qualitative dependence of the main plasma and dust particle parameters during the afterglow. Four stages of the dust plasma decay can be labelled.

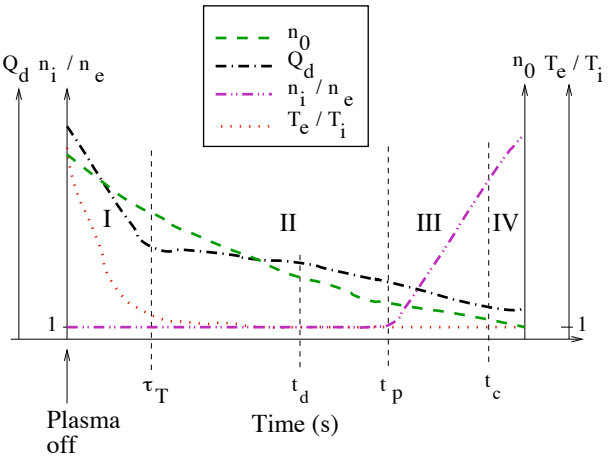

Figure 6.15: Qualitative time evolution of dust charge, plasma density and electron temperature during the afterglow. Four stages of the dust plasma decay can be identified: I - temperature relaxation stage up to t_T II - plasma density decay stage up t_p, III- dust charge volume stage t_c, IV - frozen stage.

1. As we can see the first stage of the plasma decay ($t < \tau_T$) is characterized by the electron temperature T_e falling to room temperature, while the plasma density (especially in case $\tau_T^0 < \tau_L^0$) is only slightly decreased. As the charging time scale is almost independent of $\tilde{T}_e$ (Eq.6.57), the charge is still determined by its equilibrium value (Eq.6.55). During the temperature relaxation stage the particle charge should decrease to the value [77]:

$$Q_{drT} = \frac{1}{\tilde{T}_{e0}} \left(\frac{\varphi_{eq}(1)}{\varphi_{eq}(\tilde{T}_{e0})} \right) Q_{d0} \simeq \frac{Q_{d0}}{62} \simeq -15e \tag{6.59}$$

   where Q_{d0} is the initial dust charge in the plasma and Q_{drT} the value of the residual dust charge at the end of the first decay stage. The dust charge in the plasma Q_{d0} was estimated as $Q_{d0} = -950e$ by solving numerically Eq.6.55, with given parameters $T_i = 300\ K$ and $T_e \simeq 3\ eV$, for argon plasma with $n_i \cong n_e$. It has been shown that when $T_i \ll T_e$ and $(r_d/\lambda_D)^2 \ll T_i/T_e$ where λ_D is the Debye length, the trapped ions play a significant role in the charging process of dust particles [87, 88]. However, as the electron temperature decreases very fast the effect of the trapped ions rapidly becomes negligible and thus is not taken into account in our model.

2. At the next stage of decay, electron temperature is stabilised while the plasma density is still decreasing (see fig 6.15). So τ_Q continues increasing according to Eq.6.33 and Eq.6.57. When τ_Q becomes comparable to τ_L, the particle charge can not be considered to be in equilibrium and to determine particle charge we should use Eq.6.33. The time scale when the particle charge starts sufficiently deviating from the equilibrium value can be estimated

as (Eq.6.51 and Eq.6.57):

$$t_d \sim -\tau_L^{\infty} \ln\left(\frac{8}{3} \cdot \left(\frac{\lambda_{i0}}{\Lambda}\right)^2 \cdot \frac{l_{in}}{r_d}\right) \sim 7\tau_L^{\infty} \tag{6.60}$$

However, according to Eq.6.33, as long as plasma is neutral ($n_e = n_i$) the charge on dust particles does not change. The plasma will maintain quasineutrality until the decay rates for the electrons and ions are the same. This will be the case for ambipolar diffusion. When the nature of the diffusion changes, electrons and ions start to diffuse independently resulting in a changing n_e/n_i ratio and consequently a changing dust charge change.

3. The nature of the plasma diffusion changes when the particle volume charge cannot be ignored or when the plasma screening length becomes comparable to the chamber size. In first case the ion diffusion will be influenced by the negatively charged dust particles, while the electrons will diffuse freely. In second case, large density differences appear over distances less than the screening length and electrons and ions diffuse independently. Lets us estimate the characteristic times for both cases.
The influence of the overall particle charge is determined by the value of the Havnes parameter $P_H = -n_d Q_d / e n_e$. Based on the model discussed, the qualitative evolution of the Havnes parameter P_H in the dusty plasma afterglow can be plotted as shown in Fig.6.16. The initial value of P_H is small (~ 0.06 with an estimated dust density $n_d \sim 2 \cdot 10^5$ cm^{-3} and $n_0 \simeq n_{e0} \sim 5 \cdot 10^9$ cm^{-3}) and there is no influence from dust. At the first stage of decay (temperature relaxation stage) P_H decreases due to a dramatic decrease of dust charge while the plasma density decreases by a factor of 1.1. At $t = \tau_T$, P_H reaches its minimum value of $\sim 10^{-3}$. After this, P_H starts increasing. During this stage the dust particle charge changes slowly while plasma number density decays quickly (see Fig.6.15). The time at which P_H becomes ~ 1 can be estimated as (Eqs.6.31-6.54):

$$t_p \sim \tau_L^{\infty} \ln\left(\left(\frac{T_{e0}}{T_n}\right)\left(\frac{-en_0}{Q_d N}\right)\right) \sim 8\tau_L^{\infty} \tag{6.61}$$

The screening length becomes comparable to the chamber size, i.e. $\lambda_i(\tilde{n}_c) \sim \Lambda$ when the density drops down to $\tilde{n}_c = \lambda_{i0}^2/\Lambda^2$. This occurs at [77]:

$$t_c \sim \tau_L^{\infty} \ln \tilde{n}_c^{-1} \sim 12\tau_L^{\infty} \tag{6.62}$$

At time $t = \min[t_p, t_c]$, electrons start running away faster than ions and the ratio n_i/n_e grows. For our experimental conditions $t_p < t_c$, thus the neutrality violation due to the presence of dust particles happens before the Debye length exceeds the chamber size. So the third stage of dusty plasma decay starts at t_p. During this stage the charge on dust particles changes due to the changing n_e/n_i ratio. At this stage $t_d < t_p$, thus Eq.6.33 should be used for estimating the charge variation. The upper limit of the charge change can be estimated

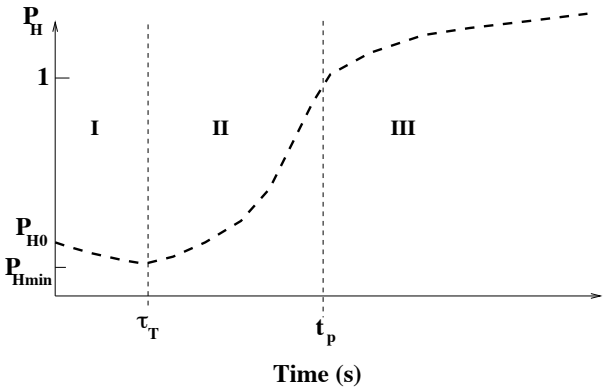

Figure 6.16: Qualitative time evolution of the Havnes parameter after the power is switched off.

by ignoring the electron current and considering the time interval between t_p and t_c,

$$\frac{dQ}{dt} < J_i \Big|_{t_p}^{t_c} \tag{6.63}$$

$$< \pi e r_d^2 n_i(t_p) v_{T_i} \Big(1 - \frac{e}{4\pi\epsilon_0 k_B r_d T_i} Q_d\Big) \Big|_{t_p}^{t_c} \tag{6.64}$$

Solving Eq.6.63, the charge should evolve following:

$$Q_d = \Big(Q_{dT} - \frac{1}{\alpha}\Big) \exp\Big(-K\alpha\Delta t\Big) + \frac{1}{\alpha} \tag{6.65}$$

where $\alpha = e/4\pi\epsilon_0 k_B r_d T_i \sim 0.28/e$, $K = \pi e r_d^2 n_i(t_p) v_{T_i} \sim 190e$, and thus $(K\alpha)^{-1} \sim 20$ ms $\sim \Delta t = (t_c - t_p)$.
Therefore, the charge during the third stage decreases to $-3e$.

4. At the forth stage of plasma decay, $t > t_c$, the plasma density decreases such that any further changes of dust charge become negligible and charge remains constant for a while. Thus the final residual charge for our condition is expected to be about $Q_{d_{res}} \sim -3e$ which is well correlated with the charges measured in the experiment.

This model predicts the existence of a negative residual charge of a few electrons but it is unable to predict a positive residual charge. The limits of the model are the step transition from ambipolar to free diffusion and the failure to properly take account of the influence of dust particles. Indeed the effect of the dust particles is ignored until the dust charge density is the same as the electron density, which leads to an abrupt change from ambipolar to free diffusion of ions and electrons. The assumption of the step transition from ambipolar to free diffusion is quite unphysical and contradicts existing experimental data [128, 156, 173, 174]. As previously mentioned, electrons and ions are diffusing at different rates very early in the decay process. This smooth transition must lead to a change in dust charges as the ratio n_i/n_e will be modified early in the decaying process. Under the conditions of our experiments, the ratio $(\Lambda/\lambda_{De}) \sim 50$ when the discharge is switched off. Consequently, this must result in a different dust particle

charge evolution in the afterglow compared to previous assumptions [77, 92]. For this reason, in the next sections, a modified model taking into account the gradual transition from ambipolar to free diffusion is used to simulation of complex plasma afterglow.

A Fokker-Planck model

In plasma afterglow, the electron temperature relaxes due to energy exchange in collisions with neutrals. At the initial stage of plasma decay the electron temperature T_{e0} is much higher than the neutral temperature T. In our model, the electron temperature T_e decreases during the afterglow period and tends asymptotically to T (Eq.6.1).
In the presence of dust particles in the plasma, the temperature relaxation and diffusion losses may be different from those for a dust-free plasma. However, no experimental data nor theoretical estimations of the transition from ambipolar to free diffusion in dusty plasma exist. Consequently, in our model, we will assume that the electron temperature relaxation and diffusion processes of ions and electrons are not significantly affected by the presence of dust particles, allowing us to treat ion and electron diffusion in a similar way to dust-free plasma. In the model, electron and ion density diffusion losses are thus treated separately and follow:

$$\frac{dn_i}{dt} = -\frac{n_i}{\tau_{Di}} \tag{6.66}$$

$$\frac{dn_e}{dt} = -\frac{n_e}{\tau_{De}} \tag{6.67}$$

where $n_{i(e)}$ is the ion (electron) density and $\tau_{D_{i(e)}} = \Lambda^2/D_{i(e)}$ is the ion (electron) diffusion time. In the simulation, electron and ion densities are studied in a fluid manner solving numerically Eqs.6.66 and 6.67 using the same constant time step $t_f << \tau_{D_{i(e)0}}$ where $\tau_{Di(e)0}$ is the diffusion time for ions (electrons) at the beginning of the simulation (i.e the very beginning of the decaying plasma).
The diffusion times were computed taking into account experimental data on the transition from ambipolar to free diffusion and are a function of the ratio $(\Lambda/\lambda_{D_e})^2$ and are calculated using experimental results from Gerber and Gerardo [156] or Freiberg and Weaver [128] (Fig.6.1). These data give the ratio of ion and electron diffusion coefficients to the ambipolar diffusion coefficient D_a as a function of the ratio $(\Lambda/\lambda_{D_e})^2$ in helium plasma where λ_{D_e} is the electron Debye length. The ambipolar diffusion coefficient is:

$$D_a \propto ((k_B T_i)^{3/2})/(P\sigma_{in} m_i^{1/2}) \tag{6.68}$$

where P is the neutral gas pressure and σ_{in} is the ion-neutral collision cross section. As $\sigma_{in_{Ar^+}} \sim 2.5\sigma_{in_{He^+}}$ [106] and $m_{i_{Ar^+}} \sim 10 m_{i_{He^+}}$, $D_{a_{Ar}} \sim (1/8) \cdot D_{a_{He}}$ for equal pressures. Consequently, it can be assumed that the diffusion of an argon plasma with argon pressure P_{Ar} has the same behaviour as an helium (He) plasma with helium pressure $P_{He} \simeq 8 \cdot P_{Ar}$. The available

experimental data for Helium are in the range of pressure $0.4 - 4\ Torr$ [128] and $9 - 22.8\ Torr$ [156] which correspond to $0.05 - 0.5\ Torr$ and $1.13 - 2.85\ Torr$ respectively in equivalent argon pressure. Our simulations were performed in the range $0.3 - 1\ Torr$ ($0.4 - 1.3\ mbar$) Consequently, the data from Ref.[128] are used to compute the diffusion time of electrons and data from Ref.[156] are used for ions as they are only data available.
As the diffusion is treated as in a dust-free plasma, it restricts the validity of our simulations to the case of low dust particle densities. In this case, the influence of dust particles will be restricted to plasma absorption losses on the particle surface. Indeed, when immersed in a plasma, a dust particle acquires a net electric charge due to ions and electrons "falling" on its surface [5, 83, 86]. In dusty plasmas, ions and electrons captured by dust particles can be considered as "lost" by the plasma and thus the charging process of dust particles is also a loss process.
A dusty afterglow plasma is not a steady case but the OML approach can be used to obtain the charge on dust particles. A Fokker-Planck model of dust charging due to the discreetness of the charge currents (ion and electron) can be used to obtain dust particle charge distributions. Indeed, the plasma particle absorption time interval as well as the sequence in which electrons and ions arrive at the dust particle surface vary randomly but observe probabilities that depend on the dust particle potential ϕ_d. The probability per unit of time for absorbing an electron $p_e(\phi_d)$ or an ion $p_i(\phi_d)$ are calculated from the OML currents [93]:

$$p_e = -I_e/e \tag{6.69}$$

$$p_i = I_i/q_i \tag{6.70}$$

The ion and electron currents can be calculated using Eq.2.11 and Eq.2.12 (the equation used for the selected species depends on the charge of the dust particle). The effect of trapped ions is neglected as the electron temperature decrease very fast during the afterglow.
The contribution of dust particles to plasma losses is taken into account in the following way:
The charges of N_d dust particles are computed. Knowing the dust density n_d in the plasma, an equivalent volume V_{eq} to these N_d dust particles can be calculated.
For a dust particle, a time step t_{p_j} for which the probability of collecting an ion or an electron of the plasma is computed [93]:

$$t_{p_j} = -\frac{\ln(1 - R1)}{p_{tot}} \tag{6.71}$$

where $0 < R1 < 1$ is a random number and $p_{tot} = p_e + p_i$ is the total probability per unit of time to absorb an ion or an electron.
While $\sum_j t_{p_j} \leq t_f$, an electron or an ion is absorbed during the time step t_{p_j} and the nature of the absorbed particle is determined comparing a second random number $0 < R2 < 1$ to the ratio p_e/p_{tot}. If $R2 < p_e/p_{tot}$, then the collected particle is an electron otherwise it is an ion. The probability p_e and p_i are recalculated and a new time step $t_{p_{j+1}}$ is computed.
When $\sum_j t_{p_j} > t_f$, one more iteration is applied to the dust particle. Nevertheless, the probability of collecting an ion or an electron in the time interval $\Delta t = t_f - \sum_{k=1}^{j-1} t_{p_k}$ is

$p(\Delta t) = 1 - \exp(-\Delta t \cdot p_{tot})$ (if $t_{p_1} > t_f$ then $p(t_{p_1})$ is computed). A random number $0 < R3 < 1$ is then generated and if $R3 < p(\Delta t)$ a plasma particle (ion or electron) is absorbed. The choice between ion and electron is decided as previously described.
When all the N_d dust particles have been treated, the number of absorbed ions and electrons N_{iabs} and N_{eabs} respectively by the N_d dust particles during the time step t_f is known and can be transformed using the equivalent volume V_{eq} into absorbed ion and electron densities n_{iabs} and n_{eabs} respectively which are subtracted from the ion density n_i and electron density n_e before the next iteration of time step t_f.
For each iteration, we calculate the mean time $\bar{t_p}$ necessary for one particle to collect a plasma particle (i.e. an ion or an electron) as well as the ratio $r_{loss} = n_{e(i)_{diff}}/n_{e(i)_{abs}}$ where $n_{e(i)_{diff}}$ is the density of electron (ion) lost by diffusion. The program is stopped when $\bar{t_p} >> \tau_{Di}$ ($\bar{t_p} > 10 \cdot \tau_{Di}$ in this simulation) when the charge on dust particles can be considered as frozen due to a plasma loss time becoming less than the particle charging time.

The numerical dust particle charge distributions are reconstructed by simulating the charge of $N_d = 500$ dust particles corresponding to a density $n_d = 5 \cdot 10^4$ cm^{-3}. The initial ion density is $n_{i0} = 5 \cdot 10^9$ cm^{-3} and the initial dust particle charge distribution is computed using a Cui-Goree algorithm [93] and the quasi-neutrality condition:

$$Z_d n_d + n_e = n_i \tag{6.72}$$

The initial electron density n_{e0} is deduced from this calculation. Many iterations of the algorithm are necessary to obtain the initial dust charge distribution and the initial electron density: the first iteration assumes $n_{e0} = n_{i0} = 5 \cdot 10^9$ cm^{-3}, and for the next iteration n_{e0} is calculated using Eq.6.72 and the dust particle charges of the first iteration. A new dust particle charge distribution is then computed. This process is performed again and again until n_{e0} and the dust charge distribution are stabilised. The obtained dust particle charge distribution is presented in Fig.6.17 The mean charge is $Q_{mean} \simeq -952e$ and the standard deviation $\sigma(Q_d) \simeq 17e$. Eq.6.55

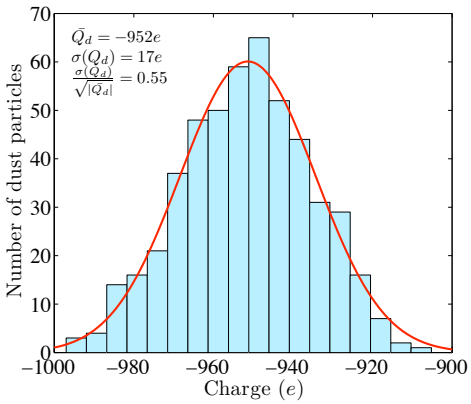

Figure 6.17: Dust charge distribution for 190 nm radius dust particles with $n_{i0} = 5 \cdot 10^9$ cm^{-3} and $n_d = 5 \cdot 10^4$ cm^{-3}

predicts dust particle charges $Q_d = -950e$ which is in very good agreement with our simulation results.

The decay of a dusty argon plasma is then simulated using the algorithm previously described for two gas pressures ($P = 0.4$ mbar and $P = 1.2$ mbar (Fig.6.18)).

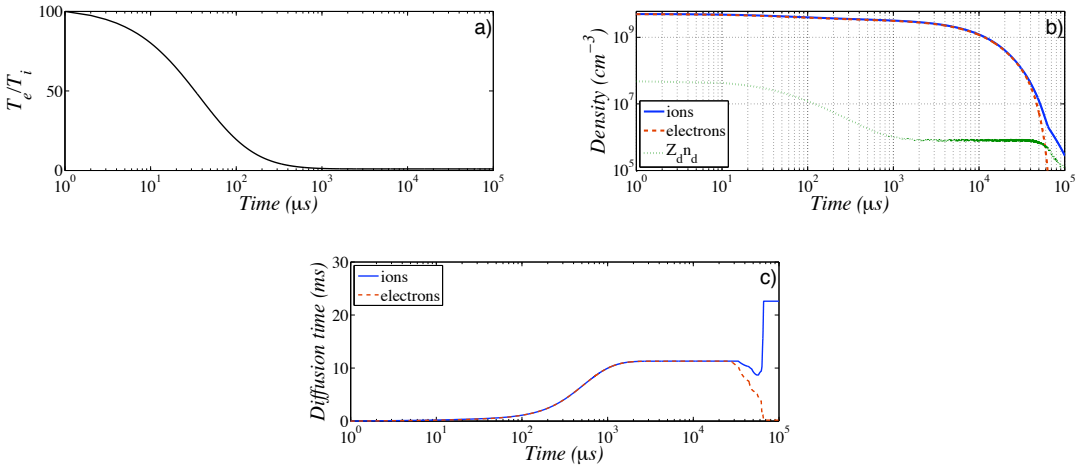

Figure 6.18: Decay of an argon plasma at $P = 1.2$ *mbar* with a fast ambipolar-to-free diffusion transition. a) Electron temperature relaxation; b) density evolution; c) evolution of diffusion time.

The ion-neutral mean free path is calculated using the cross section from Varney [106] and the electron-neutral mean free-path is calculated using the cross section from Kivel [175]. The initial electron temperature is taken as $T_{e0} = 3$ eV and the ion temperature is assumed to be equal to the neutral temperature $T_i = T = 0.03$ eV. The diffusion length is taken $\Lambda = 1$ cm which is approximately the diffusion length of the PKE-Nefedov reactor in which experiments on residual dust charge have been performed [77, 92]. The transition from ambipolar to free diffusion is based on either experimental results from Gerber and Gerardo [156] or experimental results from Freiberg and Weaver [128] (the former suggest a slower transition from ambipolar to free diffusion than the latter, see Fig.6.1).

As can be seen in Fig.6.18, the first decrease of the dust particle charge corresponds to the electron temperature relaxation. Then, while electrons and ions diffuse ambipolarly, the charge remains constant. Finally, when the transition occurs (after tens of ms), electron and ions densities deviate from each other and the dust charge decreases until it freezes.

For a pressure $P = 0.4$ mbar ($P = 0.3$ Torr), the simulated final dust charge distributions (i.e. $\bar{t_p} > 10 \cdot \tau_{Di}$) are presented in Fig.6.19. The residual charge is $Q_{d_{res}} \simeq -16e$ when no transition in the diffusion process is taken into account (Fig.6.19a). When using a model based on an abrupt transition from ambipolar to free diffusion at a Havnes parameter of $P_H = 0.5$, the residual charge is smaller (in absolute value) $Q_{d_{res}} \simeq -13e$ but still far from experimental value (Fig.6.19b). It should be noted that, typically, the Havnes parameter reaches 0.5, after 10 ms; it corresponds to a Λ/λ_{De} ratio close to unity. Using Gerber and Gerardo data (slow transition, lower curve in Fig.6.1) , the mean residual charge $Q_{d_{res}} \simeq -13e$(see Fig.6.19c) whereas it is

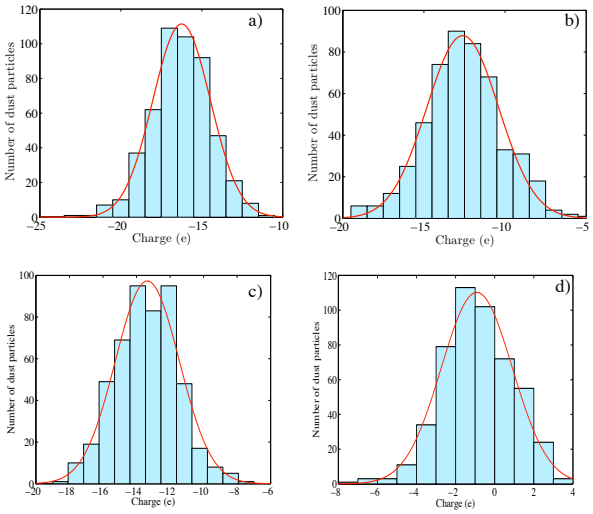

Figure 6.19: Numerical results for 190 nm radius dust particles with argon pressure $P = 0.4$ mbar ($P = 0.3$ Torr) and $n_d = 5 \cdot 10^4$ cm^{-3}. a) Ambipolar diffusion until the end of the decay process. b) Abrupt transition from ambipolar to free diffusion when $P_H = 0.5$. c) Using data from Gerber and Gerardo for transition from ambipolar to free diffusion [156]. d) Using data from Freiberg and Weaver for transition from ambipolar to free diffusion [128]

$Q_{d_{res}} \simeq -1e$ (see Fig.6.19d) using Freiberg and Weaver data (fast transition, higher curve in Fig.6.1). In the slow transition case, there are no positive particles observed in the simulated dust particle charge distribution whereas there are in the case of the fast transition. The residual charge distribution for the fast transition is similar to the experimental results (see Fig.6.14).
For a pressure $P = 1.2$ mbar ($P = 0.9$ Torr), the simulated final dust particle charge distributions are presented in Fig.6.20. The residual charge is $Q_{d_{res}} \simeq -16e$ when no transition in the diffusion process is taken into account (Fig.6.20a). When using a model based on an abrupt transition from ambipolar to free diffusion (at a Havnes parameter of $P_H = 0.5$), the residual charge is smaller (in absolute value) $Q_{d_{res}} \simeq -7e$ but still far from experimental value (Fig.6.20b). A dependence on the ambipolar to free diffusion transition is again seen with $Q_{d_{res}} \simeq -14e$ for the slow transition and $Q_{d_{res}} \simeq -2e$ for the fast transition. The latest charge distribution is the closest to experimentally measured distribution (Fig.6.14). The results for both pressures are summarised in Tab.6.3

In Fig.6.21, the simulated DCDs at different time in the plasma afterglow are presented. The resulting mean dust charge evolution is in agreement with qualitative predictions of the four stage model (Fig.6.15).
During the first stage of the plasma decay, the charging time of dust particles t_{Q_0} is very short compared to the plasma loss time τ_L (typically $t_{Q_0} \sim 1 - 10$ μs $<< \tau_L \sim 1 - 10$ ms) so the charge on dust particles can be considered to be in equilibrium with the surrounding plasma. The electron temperature relaxes to the room temperature leading to a strong decrease of the dust charge. In Fig.6.21, this corresponds to the first milliseconds. Then during the plasma decay

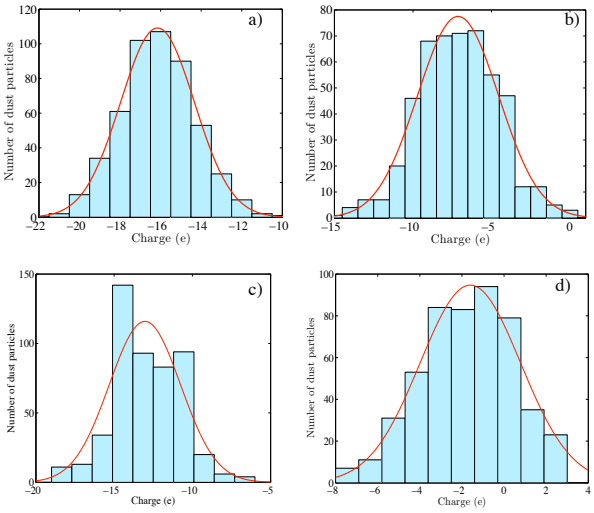

Figure 6.20: Numerical results for 190 nm radius dust particles with argon pressure $P = 1.2$ mbar ($P = 0.9$ Torr) and $n_d = 5 \cdot 10^4$ cm^{-3}.a) Ambipolar diffusion until the end of the decay process. b) Abrupt transition from ambipolar to free diffusion when $P_H = 0.5$. c) Using data from Gerber and Gerardo for transition from ambipolar to free diffusion [156]. d) Using data from Freiberg and Weaver for transition from ambipolar to free diffusion [128]

Table 6.3: Dust particle residual charges for two operating pressures.

	$P = 1.2$ mbar	$P = 0.4$ mbar
Experimental results	$-5e$	$-3e$
Ambipolar diffusion	$-16e$	$-16e$
Havnes transition	$-7e$	$-13e$
Slow transition [156]	$-14e$	$-13e$
Fast transition [128]	$-2e$	$-1e$

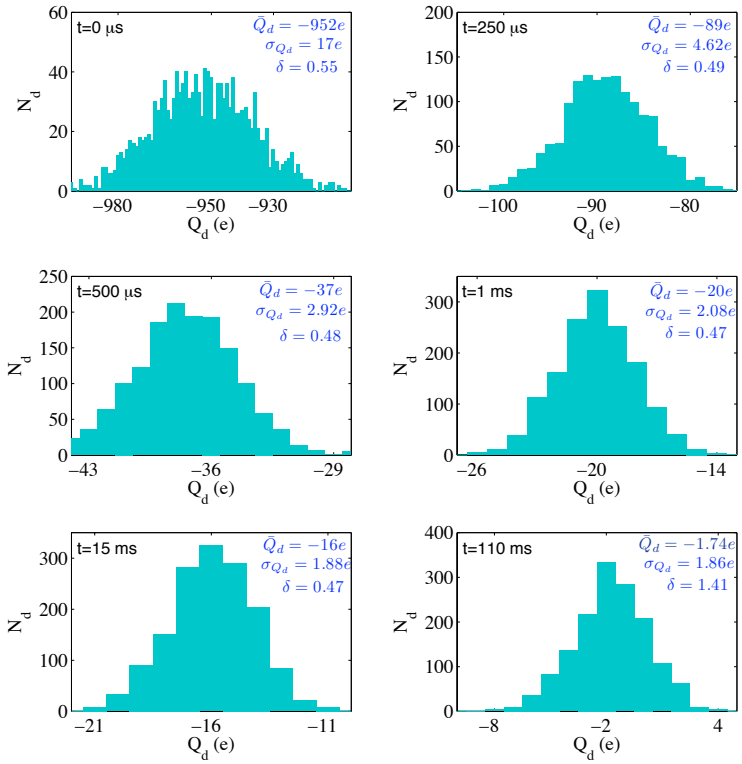

Figure 6.21: Simulated DCDs at different times in the afterglow plasma ($P = 1.2$ mbar and $\sum N_d = 1500$).

stage dust charge stabilizes. During the third stage charge decreases until it becomes frozen. The simulation is stopped during the fourth stage when the charging time becomes much bigger than the diffusion time. Drastic DCD broadening is observed in the third stage when the charge of the particles continues to decrease (from $t = 15$ ms in Fig.6.21) and δ is steeply increasing. The broadening of the distribution was observed until the end of the simulation. As can be seen in Fig.6.21 ($t = 110$ ms), the frozen DCD is very wide with a tail in the positive charge region. The simulated DCD is in good agreement with the experimental one (Fig.6.14).

We now discuss the results and limits of our model. In general, we found that the transition from ambipolar to free diffusion plays a major role in the decharging process of the dust particle. It is instructive to see how the transition affects the residual dust charge, in particular, the width of dust charge distribution. The fact that electrons and ions began to diffuse independently at an early stage of afterglow changes the dust charge distribution function drastically.

As we can see from data in Fig.6.19(a,b,c) for the pressure of 0.4 mbar the distributions for ambipolar diffusion, abrupt and slow transitions do not differ significantly. So any difference in diffusion in the late afterglow (low ratio of Λ/λ_{De}) has little effect on residual charge. In contrast, a slight difference at an early stage has a large influence on the final dust charge distribution and leads to the appearance of positively charge particles (Fig.6.19d). For the higher pressure (1.2 mbar) this effect is not so pronounced, and the diffusion in the late afterglow plays a noteworthy role. In this case an abrupt transition, due to the influence of the dust charge

particle volume effect, tends to decrease the residual dust particle charge (Fig.6.20b). It does not, however, give us the experimentally observed value of residual charge or the positive tail of the charge distribution. So the results obtained let us conclude that the four stage model can be used only for the rough estimation of residual charge. For a more accurate calculation one has to take into account the actual diffusion rates for the electrons and ions.

We now discuss the validity of the model. This model is valid only for low dust particle densities. As the losses by diffusion are treated as in a dust-free plasma, the influence of dust particle has to be very small compared to the total process. Indeed if losses due to dust particles are similar to or greater than those due to diffusion, this last process must be significantly affected. It has thus been shown that the presence of a high density of dust particles significantly reduces the plasma loss time [21]. Moreover, if the total dust charge is not negligible compared to that of ions and electrons, the diffusion process must also be modified as the dust particles will repel the electrons and attract the ions.

Consequently, the influence of dust particles can be treated independently from the other loss processes only if the total charge carried by the dust particles is small compared to the charge carried by electrons or ions during the decay process. Furthermore, losses on dust particle surfaces must not be the main loss process (i.e. $r_{loss} \gg 1$) to allow ion and electron diffusions to be treated in the same way as in dust-free plasma. This condition is definitely satisfied for a discharge plasma but could change during the afterglow so we have to calculate evolution of the ratio $n_{i_{diff}}/n_{i_{abs}}$ in discharge afterglow where $n_{i_{diff}}$ is the ion density lost by diffusion and $n_{i_{abs}}$ the ion density lost by absorption onto the dust particle surfaces. Fig.6.22 shows that this ratio stay more or less above 5 during the whole decay process regardless of the conditions of pressure or data used to take into account the transition from ambipolar to free diffusion (only results using Gerber and Gerardo data are presented in fig.6.22). It means that during the plasma

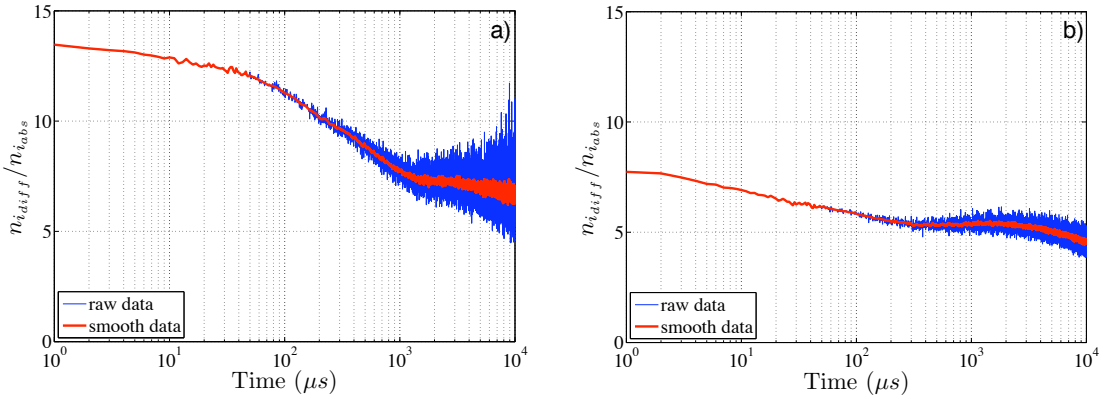

Figure 6.22: Evolution of $n_{i_{diff}}/n_{i_{abs}}$ using data from Gerber and Gerardo for transition from ambipolar to free diffusion [156]. a) $P = 0.4$ mbar. b) $P = 1.2$ mbar

decay, losses to dust particles are very small compared to the losses to the reactor walls and our model for plasma decay is valid to the end of the afterglow. Furthermore, looking at the ratio $|\bar{Q_d} n_d / e n_i|$ presented in Fig.6.23, it can be seen that, except at the very end of the afterglow

(i.e. a few ms before the residual charges freeze), the total dust charge volume is much smaller than the total charge of ions. The charge on the dust particles thus represents a negligible part of the total charge during the major part of the decay process.
The data presented in Figs.6.23(a) and 6.23(b) confirmed that, in our case, the overall influence of dust particles on the plasma decay can be neglected and, consequently, the assumption of dust-free plasma diffusion can be considered as valid for the whole decay process.
It should be noted that the transition from ambipolar to free diffusion is not the only process that influences the dust residual charge. Indeed, it has been shown that in reactive plasmas such as C_2H_4/Ar plasma [158, 159] in which the dust density can be very high ($n_d \simeq 4.5 \cdot 10^6$ cm^{-3}) [159]), the afterglow electron density shows an unexpected increase at the very beginning of the decay process. We obtained a similar result in CH_4/Ar plasma (Fig.6.6). Berndt *et al.* attributed this increase to an electron release by the dust particle [158, 159]. However, as such an increase has already been observed in pulsed helium discharges and attributed to a re-ionisation due to metastable-metastable collisions [160, 161], and as the presence of high dust particle density in an argon dilution plasma enhances the metastable density [33], the reason of the increase of the electron density at the very beginning of the afterglow is still not clear. In all cases, these "extra electrons" must affect the charge on dust particles and consequently the residual charge distributions.
Moreover, it has been shown that the pressure in noble gases such as argon and neon significantly influences the diffusion coefficient [176]. Indeed, at low pressure the electron diffusion cooling process, i.e. the fast loss of energetic electrons to the walls of the reactor which are imperfectly compensated through elastic collisions of the electrons with gas atoms resulting in an electron temperature below that of the gas, causes a reduction of D_aP and thus an enhancement of the ambipolar diffusion time $\tau_D = \Lambda^2/D_a$. As mentioned previously, the dust particle charges are related to ion and electron density. Diffusion cooling can also affect dust particle charge distribution evolution. Nevertheless, the present model does not take into account the phenomena of diffusion cooling (see Eq.6.1) and its importance has to be investigated.

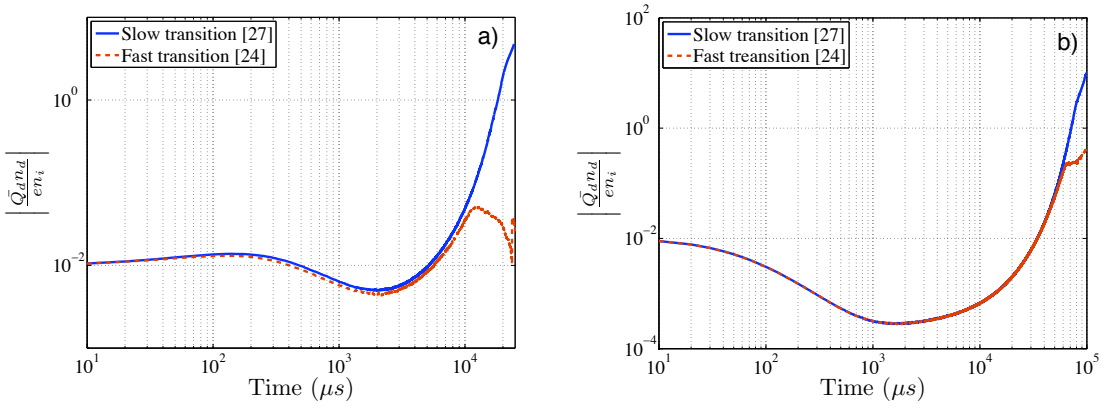

Figure 6.23: Evolution of $|\bar{Q}_d n_d/en_i|$. a) $P = 0.4$ mbar. b) $P = 1.2$ mbar

6.4 Conclusion

In this chapter, the last stage of the life of a complex plasma discharge has been investigated. The influence of the dust particles on the complex plasma decay has been discussed.
It has been shown experimentally and theoretically that the dust particles can drastically shorten the plasma decay time as they act as an absorption-recombination sink for the charge carriers of the plasma. It has been demonstrated that the dust absorption frequency does not increase linearly with the dust density due to the increase in dust particle-dust particle interactions when the dust density rises. Under certain conditions, the decay time measurement can be used as a complementary diagnostics for complex plasmas. This last statement is supported by comparison with available data.
Moreover, It has been found that the dust particles do retain a small residual charge. Complex afterglow plasmas offer therefore the unique opportunity to measure the residual dust charge distribution. The mean residual charge is negative and the dust charge distribution has a tail that extends into the positive charge region. It is found that the width of the residual dust charge distribution is larger than the width of the dust charge distribution predicted theoretically for running discharges. Simulations have shown that the residual dust charge distributions are very sensitive to the transition from ambipolar-to-free diffusion. The experimental dust charge distribution is explained by a transition starting early in the plasma decay stage.

6.5 Résumé du chapitre en français

Ce chapitre est consacré à l'étude de la phase post-décharge des plasmas poussiéreux. Dans un plasma sans poudre, lorsque l'alimentation de la décharge est coupée, le taux d'ionisation diminue fortement et devient rapidement négligeable. Les porteurs de charge du plasma diffusent et se recombinent en gaz neutre sur les parois du réacteur. La diffusion des espèces chargées se fait selon l'un des deux régimes suivant : la diffusion ambipolaire durant laquelle les ions et les électrons diffusent à la même vitesse car la charge déspace est suffisament importante pour maintenir un champ électrique ambipolaire qui accélère les ions et ralentit les électrons, et la diffusion libre durant laquelle les ions et les électrons diffusent indépendament. La transition d'un régime à l'autre se fait de manière progressive et est fonction du rapport entre la longueur de diffusion du réacteur et la longueur de Debye électronique.
Dans un plasma poussiéreux, les poudres, chargées de par les interactions avec les ions et les électrons du plasma, jouent un rôle significatif dans la disparition du plasma. Elles agissent comme des pièges sur lesquels les porteurs de charge se recombinent et ainsi réduisent fortement le temps d'extinction du plasma. Cet effet a été mis en évidence expérimentalement en comparant les temps d'extinction dans des décharges avec ou sans poudres. En revanche, il est démontré que le fréquence d'absorption des porteurs de charge par les poudres n'augmente pas linéairement avec la densité de poussières. Ceci est dû au fait que les interactions poudre-poudre, augmentant avec la densité de poudres, réduisent la charge électrique de ces dernières et donc les flux de porteurs de charge. Il est ainsi proposé d'utiliser la mesure du temps d'extinction du plasma comme un diagnostic complémentaire pour les plasmas poussiéreux. La comparaison avec des données expérimentales existantes [21] soutient cette idée.
Comme les poudres se chargent durant la phase plasma, cette charge électrique doit disparaître durant la phase post-décharge. Cependant, il a été observé que les poudres gardent une faible charge résiduelle et que celle-ci peut être positive ou négative. Le temps de chargement des poudres étant extrêmement long à la fin de la phase post-décharge, des fonctions de distribution de charges ont pu être mesurées pour différentes conditions. Ainsi, la charge moyenne des poudres est négative mais les queues des distributions s'étendent vers les charges positives. L'écart type des distributions est aussi plus grand que celui prédit théoriquement pour les distributions de charge en phase plasma. Les simulations numériques montrent que la diffusion des porteurs de charge et plus particulièrement la transition de la diffusion ambipolaire vers la diffusion libre joue un rôle majeur pour expliquer les distributions de charges résiduelles observées. Ainsi, une transition abrupte lorsque la longueur de Debye électronique atteint la longueur de diffusion du réacteur est incapable d'expliquer l'existence de charges résiduelles positives. En effet, la vitesse de transition est essentielle pour expliquer la charge moyenne et l'écart type des distributions mesurées. Des transitions rapides aboutissent à des charges résiduelles moyennes plus faibles (en valeurs absolues) et des distributions plus larges.

Chapter 7

General conclusion

7.1 General conclusion in English

In this thesis, we focussed on the influence of dust particles on RF discharges from the plasma ignition to the discharge afterglow. Experimental investigations under different discharge conditions have been performed. Different diagnostics have been used in order to understand the different processes involved in plasma-dust particle interactions. These allowed us to carefully analyse the possible effects of dust particles on RF discharges during different times in the life of the discharge:

1. The first stage of the life of dusty RF discharges is the plasma ignition and the growth of dust particles. It has been shown that dust particle growth by RF sputtering can be followed by monitoring plasma and discharge parameters. Therefore, the self bias voltage evolution in discharges where dust particles are grown by RF sputtering is shown to be very similar to its evolution in chemically active dusty discharges. Qualitatively the effect of particle growth on the self-bias can be seen as a consequence of reduction in electron density due to negative charge accumulation on the dust particles. A reduced self-bias voltage reduces the ion flux and allows a longer period of electron flow so that a new equilibrium is established. Collections of dust particles and measurements of their size for different discharge running times, corresponding to different times during the self bias voltage evolution pattern, showed that the dust particles increase in size as a function of time. However strong changes in the self bias voltage do not seem to be correlated to strong modifications of the particles sizes. The effect of the dust particle growth is also clearly shown from the evolution of the RF current amplitude which decreases with time confirming the reduction of electron density due to accumulation of negative charges on the dust particles.
   In order to estimate how much the electrons are affected by growing dust particles, Langmuir probe measurements and spectroscopic measurements were performed. They showed that the EEDF is not Maxwellian and that effective electron temperature increases during dust particle growth process. Spectroscopic measurements suggest a depletion of the

energetic electron tail.

The influence of plasma conditions has also been studied. It has been shown that high pressures are favourable to the dust particle growth in flowing and static gas. The gas purity also plays an essential role in the dust particle growth process. It has indeed been reported that very low base pressure and long pumping time in between experiments are necessary to achieve high dust particle density and fast dust growth kinetics. The influence of the input power or RF peak to peak voltage has also been investigated. It has been found that high power or high RF peak to peak voltage tend to favour dust particle growth.

Finally it has been observed that the dust particle growth can trigger instabilities in the plasma: the dust particle growth instabilities (DPGI). It has been found that these instabilities followed a well defined pattern separated into different phases with characteristic frequencies and amplitudes. Some of these phases have been related to the filamentary mode and the great void mode previously reported in experiments where the dust particles were grown by RF sputtering [74]. It has also been found that the growth kinetics have an influence on the DPGI. Slow growth kinetics lead to DPGI with lower frequencies which evolve over longer periods of time than for fast growth kinetics.

2. The second stage of the dusty RF discharge life corresponds to the existence of a well established dense cloud of dust particles. The dust cloud very often exhibits a centimetre size dust free region with very sharp boundaries in the centre of the plasma called the dust "void". It is generally admitted that the dust void is the result of an equilibrium between an inward electric force that confines the dust particles inside the plasma bulk and an outward ion drag force which tends to repel the dust particles from the plasma. Under specific conditions, the dust void can exhibit some instabilities which can be identified from the electric parameters of the discharge, the plasma glow, and the dust particle cloud motion. Two kinds of instabilities have been reported.

   The first kind of instability is a self excited instability of the dust void consisting of contraction-expansion sequences (CES) of its size, called the "heartbeat instability". This instability was also observed under microgravity conditions with injected dust particles. This instability exhibits two extreme cases: a low repetition rate case which consists of fast CES events separated by long periods of time in which the dust void can reach its equilibrium size, and a high repetition rate case which consists of slower CES events which follow each other without re-establishment of the equilibrium condition. In both cases, the void contraction is accompanied by a strong increase of the plasma glow inside the void region (identified also by a strong increase of the discharge current) which suggests an ionisation increase that can break the equilibrium between the electric force and the ion drag force. Between these two extreme cases, the instability exhibits failed or aborted CES events between the full sequence. It is observed that the more failed CES there are in between full sequences, the faster the complete CES.

   The second kind of instability is due to the growth of a new generation of dust particles

inside the void region. Continuous growth of dust particles inside the plasma bulk can occur if the discharge parameters are suitable, and many generations of dust particles can follow each other. A new generation of dust particles grows inside the void region of an older generation and, under specific conditions not yet well understood, this can trigger an instability of the "void" which stops when the new dust particles are big enough: the "delivery instability". This instability is characterised by low frequency and large amplitude expansion-contraction sequences of the dust void size. The time evolution of the frequency and the amplitude of the instability is directly linked to the growth kinetics of new dust particles. This instability sometimes evolves into another one where the dust void is rotating around the axis of symmetry of the discharge.

3. The last stage is the discharge afterglow. The charge carriers of the plasma diffuse onto the walls of the chamber and recombine into neutral gas. In a complex plasma, the charged dust particles play a significant role in the plasma decay. They act as absorption-recombination sinks and thus drastically shorten the plasma decay time. This has been very well observed by comparison of measurements of electron density decay in dust-free afterglow plasma and dusty afterglow plasma. It has been shown that the dust particle absorption frequency does not depend linearly on the dust particle density. This is due to strong dust-dust interactions which increase with the dust density and reduce their mean charge and thus the fluxes of charge carriers on dust particles. It is proposed to use the plasma decay time measurement as a complementary diagnostic for complex plasma.
   As the dust particles are electrically charged, their charges must also relax during the afterglow phase. However, it has been shown experimentally that the dust particles do keep a small residual electric charge which can be either positive or negative. As the dust particle charge time becomes very long in the late discharge afterglow, it has been possible to measure the residual dust charge distribution. It has thus been shown that the mean residual charge is negative but the tail of the distribution extends in the positive charge region. It has also been found that the standard deviation of the dust charge distribution in the afterglow plasma is larger than the one predicted for a running discharge. Simulations have shown that the diffusion process for charge carriers and especially the transition from ambipolar-to-free diffusion is essential in explaining the experimental dust charge distributions. Indeed an abrupt transition from ambipolar-to-free diffusion, when the electron Debye length reaches the diffusion length, is not able to explain the existence of positively charged dust particles in the late afterglow. It has also been shown that the speed of the transition is essential to explain the mean residual charge and the width of the distribution. A fast transition leads to smaller mean residual charge and larger standard deviation of the dust charge distribution.

To conclude, a detailed analysis of different phenomena that can occur in RF dusty discharges has been performed. The work presented in this thesis has led us to a better understanding of complex plasmas at every stage of the life of the discharge.

7.2 Conclusion générale en français

Dans cette thèse, l'influence de la présence de poudres sur des décharges RF depuis leur allumage jusqu'à leur extinction a été étudiée. Des expériences sous différentes conditions ont été réalisées. Différents diagnostics ont été utilisés afin de comprendre les différents processus impliqués dans les intéractions plasma-poussière. Cela nous a permis d'analyser finement les différents phénomènes pouvant affecter une décharge RF poussiéreuse aux différents instants de son évolution.

- *La première étape dans la vie d'une décharge RF poussiéreuse est l'allumage du plasma et la croissance des poudres. Il a été démontré que la formation des poussières par pulvérisation peut être suivie à l'aide des paramètres de la décharge et du plasma. Ainsi, l'évolution de la tension d'autopolarisation est très similaire à celle des décharges où les poudres sont formées dans des plasmas réactifs : qualitativement, l'effet de croissance des poussières sur la tension d'autopolarisation peut être vu comme une conséquence de la diminution de la densité électronique due à l'accumulation de charges négatives sur les poudres. Une réduction de la tension d'autopolarisation induit une réduction du flux d'ions positifs et un allongement de la durée du flux d'électrons nécessaires au nouvel équilibre. La collecte des poudres et la mesure de leurs tailles pour différentes durées du plasma ont montré que les poudres grossissent avec le temps mais que les fortes modifications de la tension d'autopolarisation ne sont pas accompagnées d'une forte variation de la taille des poussières. La croissance des poudres peut aussi être suivie grâce à l'évolution de l'amplitude de l'harmonique fondamentale du courant RF. En effet, celle-ci diminue durant la formation des poussières confirmant la réduction de la densité électronique due à l'accumulation des charges négatives sur les poudres.*
  Afin d'estimer l'effet des poudres sur la fonction de distribution en énergie des électrons, des mesures de sonde de Langmuir associées à de la spectroscopie d'emission ont été effectuées. Il a ainsi été démontré que la fonction de distribution en énergie des électrons n'est pas maxwellienne et que la température électronique effective croît durant la formation des poudres. La spectroscopie d'emission semble indiquer que la queue énergétique de la fonction de distribution se dépeuple dans le même temps.
  L'influence des différents paramètres de la décharge sur la croissance des poudres a aussi été étudiée. Il a ainsi été montré que les pressions élevées sont favorables à la formation de poussières que ce soit avec ou sans flux de gaz. La pureté du gaz joue aussi un rôle essentiel dans le processus de croissance. En effet, des pressions de base très basses ainsi que de longues périodes de pompage entre chaque expérience sont nécessaires pour obtenir des densités de poudres élevées et des cinétiques de croissance rapides. L'influence de la puissance injectée ou de la tension RF a aussi été étudiée. Il apparaît que de fortes puissances ou des tensions RF élevées favorisent la formation des poussières.
  Enfin, la croissance de poudres peut déclencher des instabilités du plasma : les instabilités de croissance des poudres. Ces instabilités suivent un schéma d'évolution précis constitué de différentes phases de fréquences et d'amplitudes définies. Certaines de ces phases peuvent être comparées aux modes filamentaire et "great void" précédemment observés durant des expériences où les poudres étaient formées par pulvérisation RF [74]. La cinétique de croissance des poudres a une influence sur les instabilités : des cinétiques lentes induisent des instabilités basses fréquences qui évoluent sur des périodes de temps bien plus longues que dans le cas de cinétiques rapides.
- *La seconde étape de la vie d'une décharge RF poussiéreuse coïncide avec l'existence d'un nuage dense de poudres piégé dans le plasma. Une région sans poudre, d'environ 1 cm de diamètre et aux contours clairement délimités, est souvent présente dans le nuage au centre du plasma. Cette région est appelée « void ». Il est communément admis que ce « void » est le résultat d'un équilibre entre une force électrostatique confinante et la force de friction des ions qui a tendance à expulser les poudres du plasma. Sous certaines conditions, ce « void »devient instable. Ces instabilités peuvent être repérées sur les paramètres électriques de la décharge, sur la luminosité du plasma et sur la dynamique du nuage du*

poudres. Deux types d'instabilités ont été observés :

Le premier type est une instabilité auto-excitée du « void » appelée l'instabilité « heartbeat ». Elle se compose de battements, c'est à dire de séquences de contraction-expansion (SCE) des dimensions du « void ». Ce type d'instabilité a également été observé lors d'expériences en microgravité avec des poudres micrométriques injectées. Le « heartbeat » présente deux cas extrêmes : un cas avec un taux de répétition faible qui se compose de SCE très rapides séparées par de longues périodes durant lesquelles le système a le temps de retourner à l'équilibre, et un cas avec un fort taux de répétition composé de SCE plus lentes mais qui se succèdent rapidement sans retour à l'équilibre. Dans les deux cas la contraction s'accompagne d'une forte augmentation de la luminosité du plasma à l'intérieur du « void » (aussi associée à une forte augmentation du courant) suggérant un accroissement de l'ionisation rompant l'équilibre entre la force électrostatique et la force de friction des ions. Entre ces deux cas extrêmes, l'instabilité présente des SCE avortées entre les SCE complètes. Plus le nombre de SCE avortées est grand entre chaque SCE complète, plus ces dernières sont rapides.

Le second type d'instabilité est amorcé par la croissance d'une nouvelle génération de poudres dans le « void ». Lorsque les paramètres de la décharge sont favorables, il peut y avoir une formation continue de poussières dans le plasma et de nombreuses générations peuvent ainsi se succéder. Lorsqu'une nouvelle génération de poudres croît dans le « void » de l'ancienne génération, elle peut, sous certaines conditions (non-déterminées pour l'instant), déclencher une instabilité du « void » qui ne s'arrête que lorsque les poudres de la nouvelle génération ont atteint une taille et/ou une densité critiques. Cette instabilité est marquée par des séquences d'expansion-contraction des dimensions du « void » à basse fréquence et de grande amplitude. L'évolution temporelle de la fréquence et de l'amplitude des oscillations est directement reliée à la croissance de la nouvelle génération de poudres. Cette instabilité se transforme parfois en une rotation du void autour de l'axe de symétrie de la décharge.

– *La dernière étape est la phase post-décharge. Les porteurs de charge du plasma diffusent et se recombinent en gaz neutre. Dans un plasma poussiéreux, les poudres chargées jouent un rôle significatif dans la disparition du plasma. Elles agissent comme des pièges sur lesquels les porteurs de charge se recombinent et ainsi réduisent fortement le temps d'extinction du plasma. Cet effet a été mis en évidence expérimentalement en comparant les temps d'extinction dans des décharges avec ou sans poudres. Il a été démontré que la fréquence d'absorption des porteurs de charge par les poudres n'augmente pas linéairement avec la densité de poussières. Ceci est dû au fait que les interactions poudre-poudre, augmentant avec la densité de poudres, réduisent la charge électrique de ces dernières et donc les flux de porteurs de charge. Il a ainsi été proposé d'utiliser la mesure du temps d'extinction du plasma comme un diagnostic complémentaire pour les plasmas poussiéreux.*
Comme les poudres se chargent durant la phase plasma, cette charge électrique doit donc disparaître durant la phase post-décharge. Cependant, il a été observé que les poudres gardent une faible charge résiduelle et que celle-ci peut être positive ou négative. Le temps de chargement des poudres étant extrêmement long à la fin de la phase post-décharge, des fonctions de distribution de charges ont pu être mesurées pour différentes conditions. Ainsi, la charge moyenne des poudres est négative mais les queues des distributions s'étendent vers les charges positives. L'écart type des distributions est aussi plus grand que celui prédit théoriquement pour les distributions de charge en phase plasma. Les simulations numériques montrent que la diffusion des porteurs de charge et plus particulièrement la transition de la diffusion ambipolaire vers la diffusion libre joue un rôle majeur pour expliquer les distributions de charges résiduelles observées. Ainsi, une transition abrupte lorsque la longueur de Debye électronique atteint la longueur de diffusion du réacteur est incapable d'expliquer l'existence de charges résiduelles positives. En effet, la vitesse de transition est essentielle pour expliquer la charge moyenne et l'écart type des distributions mesurées. Des transitions rapides aboutissent à des charges résiduelles moyennes plus faibles (en valeur absolue) et des distributions plus larges.

En conclusion, une analyse détaillée des différents phénomènes pouvant survenir dans des décharges RF poussiéreuses a été réalisé. Les travaux présentés dans cette thèse nous ont permis de mieux comprendre les différents processus physiques impliqués dans les intéractions plasma-poudre.

Appendix A

Dust charge distribution in running discharges

The Eq.2.18 can be solved this way. Taking $x = Q_d - Q_{mean}$ and $\tau = t/\tau_Q$ and then introducing the dimensionless variable $\xi = x/\sigma$, Eq.2.18 can be rewritten as:

$$\frac{\partial W}{\partial \tau} = \Big(\frac{\partial^2}{\partial \xi^2} + \frac{\partial}{\partial \xi}\xi\Big)W \tag{A.1}$$

In the following, the initial condition is:

$$W(Q_d, 0) = \delta(Q_d - Q_0) \tag{A.2}$$

with Q_0 a value of Q_d within the linear range of the current. This condition can be rewritten as:

$$W(\xi, 0) = \delta(\xi - \xi_0) \tag{A.3}$$

As W is a probability we have:

$$\int_{-\infty}^{+\infty} dQ_d W(Q_d, t) = \int_{-\infty}^{+\infty} d\xi W(\xi, t) = 1 \tag{A.4}$$

We introduce the time dependant position variable $y = \xi e^{\tau}$. We thus have :

$$\frac{\partial}{\partial \xi} = e^{\tau}\frac{\partial}{\partial y} \tag{A.5}$$

and thus

$$\frac{\partial}{\partial \tau}W(y(\tau), \tau) = \frac{\partial}{\partial \tau}W(y(\tau), \tau) + \frac{\partial y}{\partial \tau}\frac{\partial}{\partial y}W(y(\tau), \tau) \tag{A.6}$$

$$\frac{\partial}{\partial \tau}W(y(\tau), \tau) = \frac{\partial}{\partial \tau}W(y(\tau), \tau) + y\frac{\partial}{\partial y}W(y(\tau), \tau) \tag{A.7}$$

Eq.A.1 can be rewritten as

$$\frac{\partial}{\partial\tau}W(y(\tau),\tau) = e^{2\tau}\frac{\partial^2}{\partial y^2}W(y(\tau),\tau) + W(y(\tau),\tau) \tag{A.8}$$

We take $W = e^{\tau}f$, Eq.A.8 becomes

$$\frac{\partial}{\partial\tau}f = e^{2\tau}\frac{\partial^2}{\partial y^2}f \tag{A.9}$$

which is the equation of diffusion with a time-dependant diffusion coefficient $\tilde{D}(\tau) = e^{2\tau}$. The solution is [177]:

$$f(y,\tau) = \Big(4\pi\int_0^{\tau} d\tau'\tilde{D}(\tau')\Big)^{-1/2}\exp\Big(-\frac{(y-y_0)^2}{4\int_0^{\tau}d\tau'\tilde{D}(\tau')}\Big) \tag{A.10}$$

which gives [91]:

$$W(Q_{mean}+x,t) = \frac{1}{\sigma\sqrt{2\pi(1-e^{-2t/\tau_Q})}}\exp\Big(-\frac{(x-x_0e^{-t/\tau_Q})^2}{2\sigma^2(1-e^{-2t/\tau_Q})}\Big) \tag{A.11}$$

From Eq.A.11, it is clear that the charge distribution is Gaussian at all the times and approaches with a time constant τ_Q a steady states with a mean dust particle charge Q_{mean} and a variance σ which depend on the charging currents. From Eq.2.19 and Eq.2.20, the variance σ can be rewritten as:

$$\Big(\frac{\sigma}{e}\Big)^2 = \frac{\tau_Q}{2\tau_c} \tag{A.12}$$

where $\tau_C = e/(\bar{I}_i - \bar{I}_e)$. It has been shown that τ_Q represents the time for charge fluctuations and τ_c represents the mean time for collisions between a dust particles and a charge species [91].

Appendix B

Empirical Mode Decomposition (EMD) and Hilbert-Huang (HH) spectrum

Data analysis is a procedure which allows us to understand the physical processes implicated in observed phenomena. However, problems are often encountered when one tries to analyse data:

- the total data span is too short
- the process which generates the data is non-linear
- the data are non stationary

The most common way to analyse data is Fourier analysis, but this is very limited for analysis of non-linear and/or non-stationary data. Indeed Fourier analysis supposes that the data are stationary and that the signal may be decomposed using trigonometric functions with fixed amplitudes over the whole span of the data. Consequently, local time variations of a signal are very hard to track. Moreover, non-linear data need to be decomposed over a wide range of harmonics and as a result, the energy will be spread over a large frequency range.
The characteristics of the function used to analyse a signal can be misinterpreted and taken as characteristic of the signal itself. Consequently, it is better to choose analysis functions in accordance with the intrinsic structure of the analysed signal. For this purpose, Huang et al. introduced a new method to analyse non-linear and non- stationary time series [178]. It is based on the empirical mode decomposition (EMD) and the Hilbert-Huang transform (HHT). The key aspect of this method is to decompose the signal into a finite number of intrinsic mode functions (IMF) based on local characteristic time scales of the data and then to determine the instantaneous frequency of these IMFs using the HHT.

B.1 The empirical mode decomposition

The main idea in EMD is to consider oscillations in the signal at a very local level. It is needed to identify the time scale that will reveal the physical characteristics of the studied process. Then, these time scales have to be extracted into intrinsic mode functions (IMF). Consequently, the EMD is a data sifting process which eliminates locally riding waves as well as the local asymmetry in the time series profile [179]. For a signal $X(t)$, the effective algorithm for EMD can be summarized as [178]:

1. Identify all extrema of $X(t)$
2. Interpolate between maxima using cubic spline line to obtain the envelope $e_{max}(t)$ and interpolate between minima to obtain the envelope $e_{min}(t)$
3. Calculate the mean $m(t) = (e_{max}(t) - e_{min}(t))/2$
4. Extract the first component $h_1(t) = X(t) - m(t)$
5. Iterate on $m(t)$

The step 1 to 4 may have to be repeated several times until the component $h(t)$ can be considered as zero mean according to some stopping criterion[178]: each $h_i(t)$ is treated as the signal and when it fits the stopping criterion, it is considered as the IMF and $m(t)$ is treated as the signal. At the end of the process, the signal $X(t)$ is decomposed into a finite number n of IMFs $C_j(t)$ and a residue $r_n(t)$. The original signal can be reconstructed by superimposition of the IMFs and the residue as follows:

$$X(t) = r_n(t) + \sum_{j=1}^{n} C_j(t) \tag{B.1}$$

By definition an IMF has to satisfy two conditions [178]:

- The number of extrema must be equal or differ at most by one from the number of zero crossings. It is similar to the narrow band requirements for a stationary Gaussian process
- At any point, the mean value of the envelope defined by the local maxima and the envelope defined by the local minima is zero. It ensures phase function without bias and modifies the classical global requirement to a local one. This is necessary so that the instantaneous frequency will not have unwanted fluctuations induced by asymmetric wave forms.

The stopping criterion is thus very important in order to obtain physically meaningful IMFs. The sifting process is terminated when two conditions are fulfilled:

1. The number of extrema must differ at most by one from the number of zero crossings.
2. The mean between the upper and lower envelope must be close to 0 according to some criterion

The stopping criterion is based on two thresholds θ_1 and θ_2 [180]. It aims at guaranteeing globally small fluctuations while taking into account locally large excursions. It is based on the mode amplitude $a(t) = (e_{max}(t) - e_{min}(t))/2$ and the evaluation function $\sigma(t) = |m(t)/a(t)|$ so that the sifting is iterated until $\sigma(t) < \theta_1$ for some prescribed fraction of the signal $(1-\alpha)$ while $\sigma(t) < \theta_2$ for the remaining fraction. The set of values used in this thesis is $\alpha = 0.01$ $\theta_1 = 0.05$ and $\theta_2 = 0.5$.

B.2 The Hilbert Huang spectrum

After the signal $X(t)$ has been decomposed into IMF, the Hilbert-Huang transform (HHT) can be applied. The HHT on an IMF $C_j(t)$ is defined as:

$$\widehat{C}_j(t) = \frac{1}{\pi} P \int_{-\infty}^{+\infty} \frac{C_j(t')}{t - t'} dt' \tag{B.2}$$

where P indicates the Cauchy principal value. It is then possible to deduce the amplitude a_j, the phase φ_j and the instantaneous frequency ω_j:

$$a_j(t) = \sqrt{C_j^2(t) + \widehat{C}_j^2(t)} \tag{B.3}$$

$$\varphi_j(t) = \arctan\left(\frac{\widehat{C}_j(t)}{C_j(t)}\right) \tag{B.4}$$

$$\omega_j(t) = \frac{d\varphi_j(t)}{dt} \tag{B.5}$$

The original signal can be expressed as:

$$X(t) = Re \sum_{j=1}^{n} a_j(t) \exp\left(\imath \int \omega_j(t) dt\right) \tag{B.6}$$

where Re stands for real part.
By definition IMFs have positive frequencies because they are symmetric with respect to the local mean and consequently admit a well-behaved HHT [1].
As can be seen from Eq.B.6, IMFs represent a generalized Fourier expansion. The main improvement is that the variable amplitude and the instantaneous frequency enable the expansion to accommodate non-stationary data. The frequency and amplitude modulations are also clearly separated.
From Eq.B.6, it is also possible to construct the frequency-time distribution of the amplitude designated as the Hilbert-Huang amplitude spectrum $H(\omega, t)$ (HHS) [178]. The time resolution in the HHS can be as precise as the sampling rate of the data and the frequency resolution is arbitrary. The lowest extractable frequency is $f_{min} = 1/T$ where T is the time duration of the data and the highest frequency extractable is $f_{max} = 1/(k\Delta t)$ where Δt is the sampling rate of

[1] It is shown in Ref.[178] that the Hilbert transform can lead to non-physical negative frequencies if the signal is not locally symmetric with respect to the zero mean level.

the data and k the minimum number of points necessary to define the frequency accurately. For a sine wave, $k = 5$ [178, 179].
From the HHS, it is possible to extract the marginal Hilbert spectrum defined as [178]:

$$h(\omega) = \int_0^T H(\omega, t)dt \tag{B.7}$$

$$h_2(\omega) = \int_0^T H^2(\omega, t)dt \tag{B.8}$$

It represents the cumulative amplitude (or squared amplitude) over the entire data span and offers a measure of the total energy contribution from each frequency. It is different from the Fourier spectrum in a sense that in the Fourier spectrum the existence of energy at a frequency ω means that a sine or cosine wave with this frequency persists during all the data span while for the marginal Hilbert spectrum it only means that during the whole span of the data such a wave with frequency ω has a high probability to appear locally.
It is also possible to define the instantaneous energy density level IE as [178]:

$$IE(t) = \int_\omega H^2(\omega, t)d\omega \tag{B.9}$$

As IE depends on time, it can be used to check the energy fluctuations of the signal.

B.3 Examples

B.3.1 Analysis of an analytic non-linear signal

Let's considered the following signal $X(t)$ [2]:

$$X(t) = \cos\Big(\omega t + \epsilon \sin \omega t\Big) \tag{B.10}$$

where $\omega = 125.6$ Hz (frequency $f = 20$ Hz) and $\epsilon = 0.1$ (Fig.B.1). This is a non-linear wave with a small frequency modulation. The function is solution of the following non-linear equation:

$$\frac{\mathrm{d}^2x}{\mathrm{d}t^2} + (\omega + \epsilon\omega \cos \omega t)^2 x - \epsilon\omega^2 \sin \omega t(1 - x^2)^{1/2} = 0 \tag{B.11}$$

As $X(t)$ is already an IMF, the Fourier spectrogram and the HHS are presented in Fig.B.2. As it can be seen, the Fourier analysis enlightens the main frequency at 20 Hz but also shows harmonics which are necessary to reproduce the non-linear signal. On the other hand, the HHS shows only one frequency around 20 Hz which is modulated at a frequency of 20 Hz.
The harmonic content obtained from the Fourier analysis arises only from the decomposition of

[2] A more detailed description of this example with parameter values is given in Ref.[178]

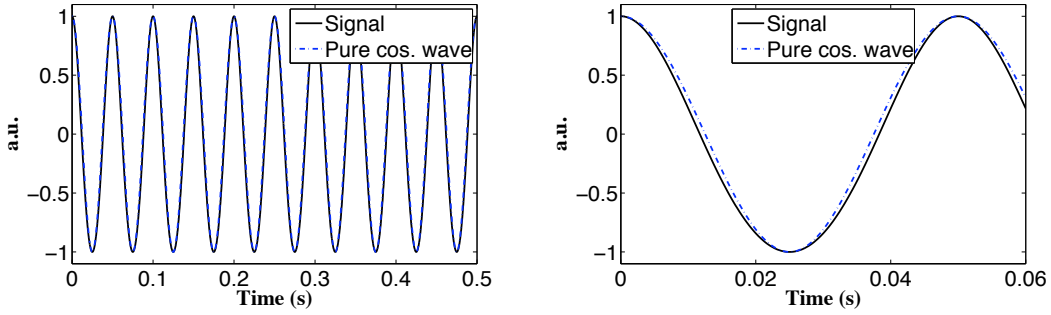

(a) Signal (b) zoom of a)

Figure B.1: Non-linear signal of a wave with small frequency modulation and pure cosine wave with the same mean frequency

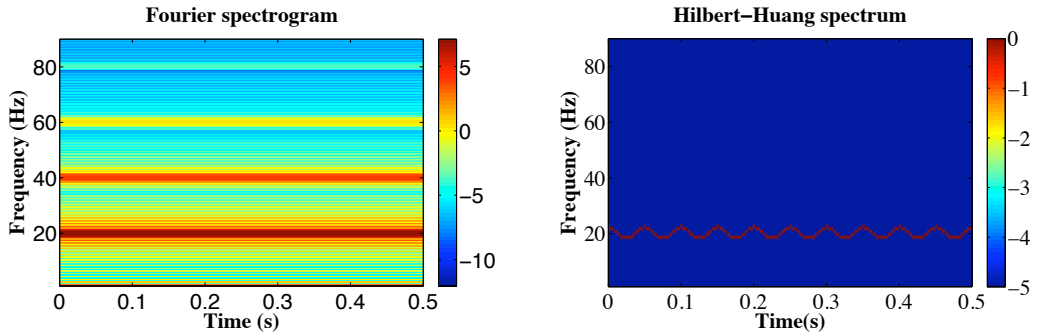

(a) Fourier spectrogram (b) Hilbert-Huang spectrum

Figure B.2: Fourier spectrogram and Hilbert-Huang spectrum of a non-linear wave signal with small frequency modulation

a non-linear wave as a sum of linear waves. Indeed Eq.B.10 can be written as:

$$\begin{aligned} X(t) &= \cos\Big(\omega t + \epsilon \sin \omega t\Big) \\ &= \cos\omega t \cos(\epsilon \sin \omega t) - \sin \omega t \sin(\epsilon \sin \omega t) \\ &\simeq \cos\omega t - \epsilon \sin^2 \omega t \simeq (1 - \frac{1}{2}\epsilon)\cos\omega t + \frac{1}{2}\epsilon \cos 2\omega t \end{aligned} \tag{B.12}$$

Consequently this example shows that the harmonic components of a signal can be the result

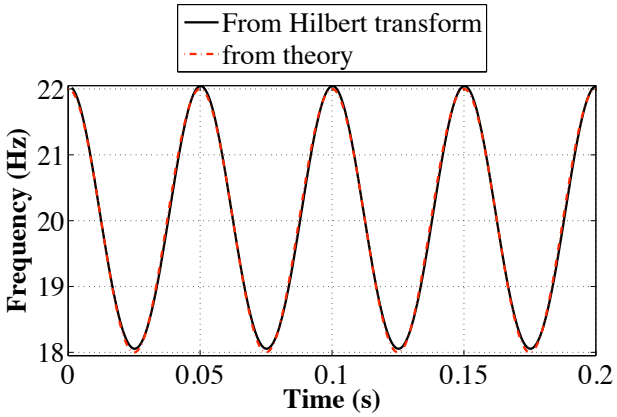

Figure B.3: Evolution of the frequency of the non-linear wave

of using a linear system to simulate a non-linear one.
From Eq.B.10, it is also possible to obtain frequency modulation from classical wave theory:

$$\Omega = \frac{\mathrm{d}\theta}{\mathrm{d}t} = \omega(1 + \epsilon \cos \omega t) \tag{B.13}$$

In Fig.B.3, the frequency obtained from the Hilbert transform is compared to the theoretical one obtained from Eq.B.13. As can be seen, it is in very good agreement. It thus confirms that a deformed sinusoidal wave can be interpreted as an intra-wave frequency modulated wave.

B.3.2 EMD of a heartbeat signal

The empirical mode decomposition has been applied to a heartbeat signal (AC current; see Chap.5). The results are presented in Fig.B.4. As can be seen, the signal is composed of a finite number of modes.

The modes with the highest amplitude (IMF 5 to 7) are the main modes of the signal. Indeed as can be seen in Fig.B.5, the sum of these modes reproduce the main characteristics of the measured signal.

The Hilbert transform has been applied to the IMFs. The HHS and marginal spectrum have been plotted (Fig.B.6). As can be seen in Fig.B.6(a), the signal has a main frequency centred around 20 Hz and exhibits a slightly weaker component with large frequency excursion centred around 40 Hz.

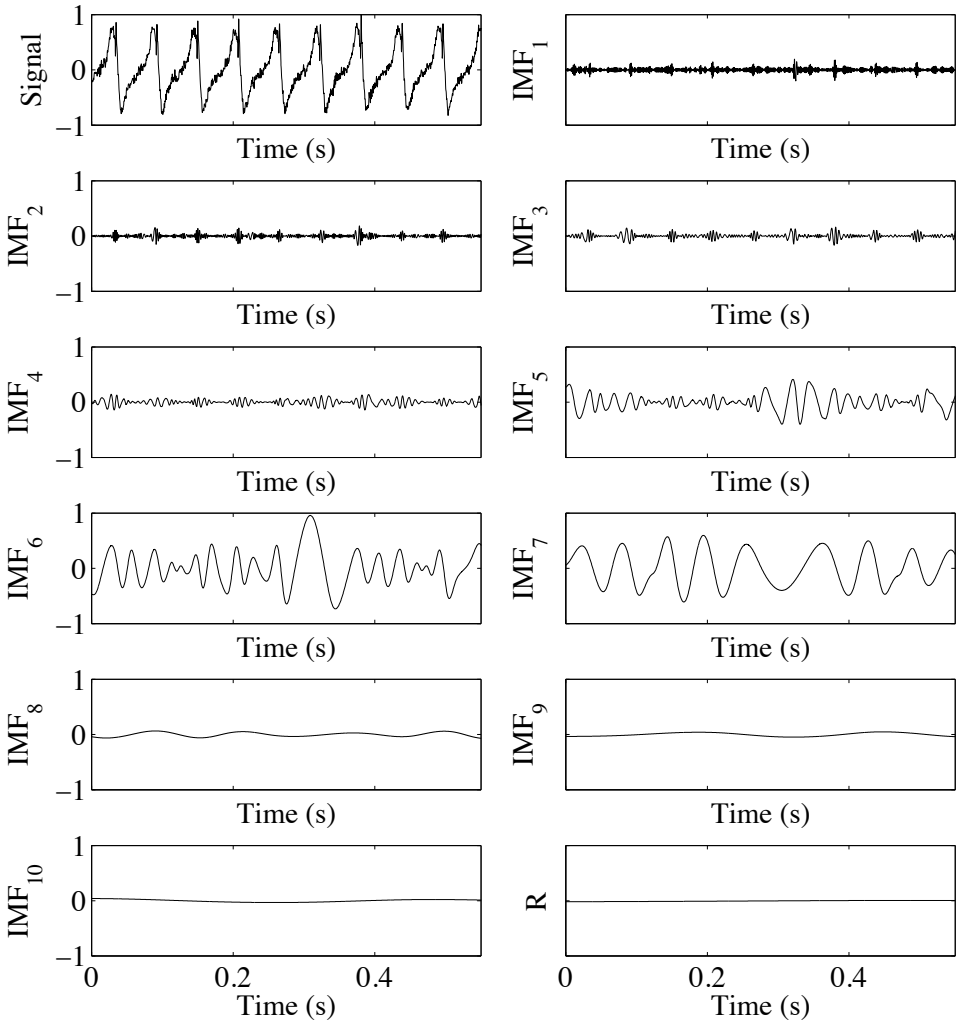

Figure B.4: Heartbeat signal (AC current) and its IMFs from EMD

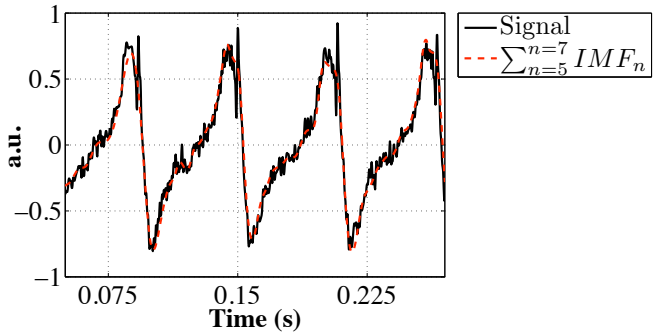

Figure B.5: Heartbeat signal (solid line) and the sum of its largest amplitude IMFs (dashed-line)

The marginal Hilbert spectrum is also compared to the Fourier spectrum of the signal (Fig.B.6(b)). The two frequencies previously observed are present in both spectra. However, in the marginal Hilbert Spectrum they are not represented by sharp peaks indicating that the frequencies are effectively varying around their mean values while in the Fourier spectrum those frequencies are observed with sharp peaks and accompanied by additional harmonics necessary to reconstruct the non-linear data. This suggests the additional harmonics are not characteristic of the physical process leading to the non-linear signal, but merely provide a linear reconstruction.

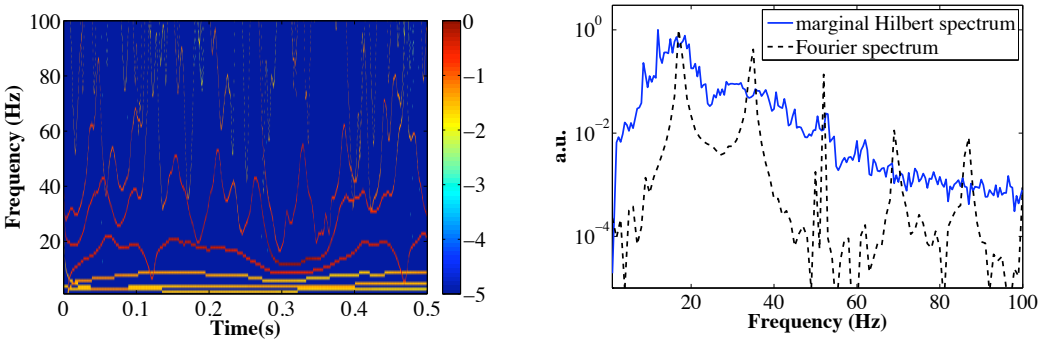

(a) Hilbert-Huang spectrum

(b) marginal Hilbert Spectrum and Fourier spectrum

Figure B.6: HHS and marginal Hilbert spectrum of the heartbeat signal

Appendix C

Matlab program for dust resisual charge simulation

C.1 Main program

```
 %electrons and ions density are computed idependantly
%dust charge computed through a Focker Planck algorithm
function [ni,ne,CR,CRevol,t,tde,tdi,tabs,Te]=ModelResCharge3(ts,nd,n0)

%ts: simulation time
%n0: initial density
%nd: dust density
ttinfty=0.900e-3; %electron temperature relaxation time (to modify as a function of studied conditions)
te0=100; %initial Te/Ti)
tdinfty=3.5e-3; %diffusion time (to modify as a function of studied conditions)
ldi0=18e-6; %initial debye length for ni=5e9 cm-3
lambda=1e-2; %reactor diffusion length
%time step and number of step
dt=1e-6; %time step
N=ts/dt; %numner of step
%Number of dust particles
    Np=500;
    rd=190e-9;%dust radius
    Veq=Np/nd; %equivalent volume of the Nd dust particles

%initialisation of parameters
    t=zeros(1,N);
    Te=zeros(1,N);
    td=zeros(1,N);
    tabs=zeros(1,N);
    tde=zeros(1,N);
    tdi=zeros(1,N);
    ni=zeros(1,N);
    ne=zeros(1,N);
    CRevol=zeros(int16(N/10)+1,Np);

% %initialisation de la charge sur les poudres
    [CR,ne(1),ni(1)]=PlasmaActif(Np,nd,n0,rd,10e-7,te0,-700);
    disp('**************');
    disp('initialisation finished');
    disp('**************');
wx=1; %time step to save charge distribution
for i=1:N
        if (mod(i,100)==0)
```

```
        disp('still running');
        disp(i);
    end
    Te(i)=CalculerTe(dt*(i-1),ttinfty,te0);
    %density of electrons and ions
    if i =1
        nev=ne(i-1);
        niv=ni(i-1);
    else
        nev=ne(1);
        niv=ni(1);
    end
    niabs=0;
    neabs=0;
    tabs(i)=0;
    for j=1:Np
        temps=0;
        tm1=0; %charging time until now for the jth dust particle
        k=0;
        while temps<dt
            %calcul des courants d'ions et d'electrons
            %Calcul du potentiel de surface de la poudre traitee
            PhiS=CR(j)*1.602e-19/(4*pi*8.854e-12*rd);
            if nev<0;
                nev=0;
                disp('ne neg');
                disp(i);
                return;
                %break;
            end
            if niv<0;
                niv=0;
                disp('ni neg')
                disp(i);
                return;
                %break;
            end
            I0i=4*pi*rd*rd*niv*1.602e-19*sqrt(1.38e-23*(1.602e-19*0.03/1.38e-23)
                /(2*pi*6.63e-26))*(1+30e-3*Te(i));
            I0e=-4*pi*rd*rd*nev*1.602e-19*sqrt(1.38e-23*(1.602e-19*0.03/1.38e-23)*Te(i)
                /(2*pi*9.11e-31));
            %ion current
            if PhiS<0
                Ii=I0i*(1-PhiS/(0.03));
            else
                Ii=I0i*exp(-PhiS/(0.03));
            end
            %electron current
            if PhiS>0
                Ie=I0e*(1+PhiS/(Te(i)*0.03));
            else
                Ie=I0e*exp(PhiS/(Te(i)*0.03));
            end
            %proba collection electron
            pre=-Ie/1.602e-19;
            %proba collection ion
            pri=Ii/1.602e-19;
            ptot=pre+pri;
            %charging time step
            R1=rand(1);
            while (R1==1 — R1==0)
                R1=rand(1);
            end
            deltat=-log(1-R1)/ptot;
            if k==0
```

```
            tabs(i)=tabs(i)+deltat;
        end
        tm1=temps;
        temps=temps+deltat;
        if temps<dt
            %choice of the absorbed particles
            R2=rand(1);
            if R2<(pre/ptot)
                CR(j)=CR(j)-1; %electrons
                neabs=neabs+1;
            else
                CR(j)=CR(j)+1;%ions
                niabs=niabs+1;
            end
        end
        if temps>dt
            R3=rand(1);
            P=1-exp(-(dt-tm1)*ptot);
            if R3<P
                R2=rand(1);
                if R2<(pre/ptot)
                    CR(j)=CR(j)-1; %electrons
                    neabs=neabs+1;
                else
                    CR(j)=CR(j)+1;%ions
                    niabs=niabs+1;
                end
            end
        end
        if deltat<0
            disp('crash);
            disp(temps);
            disp(deltat);
            return;
        end
        k=k+1;
        if k>1000000
            disp('crash2');
            disp(i);
            disp(deltat);
            return;
        end
    end
end
t(i)=(i-1)*dt;
tabs(i)=tabs(i)/Np;
if i==1
    td(i)=Calcultd(t,tdinfty,ttinfty,Te(i));
    ldi=sqrt(8.85e-12*0.03/(ni(1)*1.602e-19));
    lde=sqrt(8.85e-12*Te(1)*0.03/(ne(1)*1.602e-19));
else
    ldi=sqrt(8.85e-12*0.03/(ni(i-1)*1.602e-19)); %longuer de debye ionique
    if ne(i-1)>0
        lde=sqrt(8.85e-12*Te(i)*0.03/(ne(i-1)*1.602e-19));
    else
        lde=10000; %artefact for ne=0 w/o numerical pb
    end
    ld=lde*ldi/sqrt(lde^2 +ldi^2);
    [corr_De,corr_Di]=CorrectionDiffusion2(lambda,lde);
    %Correction to ambipolar diffusion
    td(i)=Calcultd(t,tdinfty,ttinfty,Te(i)); %diffusion time
    %
    if td(i)<0
        disp('td neg');
        return;
```

```
            end
            %correction diffusion times
            %Phys Rev A 7,781 (1972)
            tde(i)=td(i)./corr_De;
            tdi(i)=td(i)./corr_Di;
            %evolution of ion and electrondensities
            ne(i)=ne(i-1)-dt*ne(i-1)*(1/(tde(i)*1))-neabs/Veq;
            ni(i)=ni(i-1)-dt*ni(i-1)*(1/(tdi(i)*1))-niabs/Veq;
            if ne(i)<0
                ne(i)=0.;
            end
        end
        if ( i==1 — mod(i,10)==0)
            CRevol(wx,:)=CR(:);
            wx=wx+1;
        end
        %stop when charging time biger than diffusion time
        if (tabs(i)>20.*tdinfty)
            disp('i fin');
            disp(i);
            disp(ldi);
            return;
        end
    end
```

C.2 Subprogram

C.2.1 Initialisation of dust particle charges

```
function [CR,ne,ni]=PlasmaActif(Np,nd,n0,rd,dt,Te,c0)

%charge on dust taking ito account quasi neutrality and dust density
%some parameters such as dt and the starting dust charge must be adjust manually to improve speed
%land stability

Veq=Np/nd; %volume occupe par les 500 poudres
ni=n0;
ne=n0;
neprev=ne+0.5*ne;
Zdmeanprev=5000;
Zdvarprev=5000;
diff=100.*abs(neprev-ne)/ne;
diff2=100;
diff3=100;
%dt=1e-6;
k=1;
%Te=100;
CR=c0*ones(1,Np);
while (diff>0.05 | diff2>0.05 | diff3>0.05 | k<25)
    i=1;
    disp(k);
    Zdmeanprev=mean(CR);
    Zdvarprev=std(CR);      for j=1:Np
        %disp(j);
        temps=0;
        while temps<dt
            %disp(temps);
            %calcul des courants d'ions et d'electrons
            %Calcul du potentiel de surface de la poudre traitee
            PhiS=CR(j)*1.602e-19/(4*pi*8.854e-12*rd);
            I0i=4*pi*rd*rd*ni*1.602e-19*sqrt(1.38e-23*(1.602e-19*0.03/1.38e-23)
                /(2*pi*6.63e-26));
```

```
            I0e=-4*pi*rd*rd*ne*1.602e-19*sqrt(1.38e-23*(1.602e-19*0.03/1.38e-23)*Te
                /(2*pi*9.11e-31));
            %courant d'ion
            if PhiS<0
                Ii=I0i*(1-PhiS/(0.03)); %car Te(j)=Te/Ti en realite
            else
                Ii=I0i*exp(-PhiS/(0.03));
            end
            %courant d'electrons
            if PhiS>0
                Ie=I0e*(1+PhiS/(Te*0.03));
            else
                Ie=I0e*exp(PhiS/(Te*0.03));
            end
            %proba collection electron
            pre=-Ie/1.602e-19;
            %proba collection ion
            pri=Ii/1.602e-19;
            ptot=pre+pri;
            %calcul pas temps
            R1=rand(1);
            if (R1==1 — R1==0)
                R1=rand(1);
            end
            deltat=-log(1-R1)/ptot;
            temps=temps+deltat;
            if temps<dt
                %choix particule absorbee
                R2=rand(1);
                if R2<(pre/ptot)
                    CR(j)=CR(j)-1;
                else
                    CR(j)=CR(j)+1;
                end
            end
            if deltat<0
                disp('crash');
                disp(temps);
                return;
            end
            end
        end
    end
    neprev=ne;
    ne=ni+sum(CR)/Veq;
    diff=100.*abs(neprev-ne)/ne;
    diff2=100.*abs(Zdmeanprev-mean(CR))/mean(CR);
    diff3=100.*abs(Zdvarprev-std(CR))/std(CR);
    k=k+1;
end
figure(5);
clf;
hist(CR,20);
xlabel('Charge (e)','fontsize',16);
ylabel('Number of dust particles','fontsize',16);
```

C.2.2 Characteristic times and coefficients

```
function [Te]=CalculerTe(t,tautinfty,te0)

%fonction pour Calculer la temperature electronique (Te/Ti) dans l'afterglow
%d'un dusty plasma
%On a resolu analitiquement l'equation 3 de
%Phys. Rev. Lett. 90(5), 055003 (2003)
```

```
fte0=abs((sqrt(te0)-1)/(sqrt(te0)+1));
Te=((fte0*exp(-t/tautinfty)+1)/(1-fte0*exp(-t/tautinfty)))^2;


    function [td]= Calcultd(t,tdinfty,ttinfty,Te)

%Calcul pour calculer le temps caracteristique de
%perte du plasma par diffusion
%d'apres Phys. Rev. Lett. 90(5), 055003 (2003)

%Te=CalculerTe(t,ttinfty,te0);
td=1./(0.5*(1+Te)/tdinfty);

    function [corr_De,corr_Di]=CorrectionDiffusion(lambda,lde)

%program pour calculer les corrections a la diffusion ambipolaire suivant
%les donnees tirees de l'article Phys Rev A 7, 781 (1973)

%rapport de la longueur de diffusion sur la longueur de Debye electronique
ratio2=(lambda/lde)^2;
%calcul des coefficeints de correction
if ratio2<= 1e-1
    pente1=(9.-8.)/(7e-2 - 1e-1);
    b1=9-pente1*7e-2;
    corr_De=(pente1*ratio2) + b1;
    if corr_De>100;
        corr_De=100;
    end
    corr_Di=0.5;
end
if ( ratio2>1e-1 & ratio2<=5e-1)
    pente1=(8-5.5)/(1e-1 - 5e-1);
    b1=5.5-pente1*5e-1;
    corr_De=(pente1*ratio2) + b1;
    %
    pente2=(5e-1 - 6e-1)/(1e-1 - 5e-1);
    b2=6e-1 -pente2*5e-1;
    corr_Di=(pente2*ratio2) + b2;
end
if ( ratio2>5e-1 & ratio2<=1)
    pente1=(5.5-4.8)/(5e-1 - 1.);
    b1=4.8-pente1*1;
    corr_De=(pente1*ratio2) + b1;
    %
    pente2=(6e-1 - 7e-1)/(5e-1 - 1.);
    b2=7e-1 -pente2*1;
    corr_Di=(pente2*ratio2) + b2;
end
if ( ratio2>1 & ratio2<=5)
    pente1=(4.8-2.9)/(1 - 5);
    b1=2.9-pente1*5;
    corr_De=(pente1*ratio2) + b1;
    %
    pente2=(7e-1 - 1.1)/(1 - 5);
    b2=1.1-pente2*5;
    corr_Di=(pente2*ratio2) + b2;
end
if ( ratio2>5 & ratio2<=10)
    pente1=(2.9-2.4)/(5-10);
    b1=2.4-pente1*10;
    corr_De=(pente1*ratio2) + b1;
    %
    pente2=(1.1-1.2)/(5-10);
    b2=1.2-pente2*10;
```

```
    corr_Di=(pente2*ratio2) + b2;
end
if ( ratio2>10 & ratio2<=50)
    pente1=(2.4-1.3)/(10 - 50);
    b1=1.3-pente1*50;
    corr_De=(pente1*ratio2) + b1;
    %
    pente2=(1.2-1.25)/(10 - 50);
    b2=1.25-pente2*50;
    corr_Di=(pente2*ratio2) + b2;
end
if ( ratio2>50 & ratio2<=100)
    pente1=(1.3-1.25)/(50 - 100);
    b1=1.25-pente1*100;
    corr_De=(pente1*ratio2) + b1;
    %
    pente2=(1.25-1.25)/(50 - 100);
    b2=1.25-pente2*100;
    corr_Di=(pente2*ratio2) + b2;
end
if ( ratio2>100 & ratio2<=500)
    pente1=(1.25-1.20)/(100 - 500);
    b1=1.20-pente1*500;
    corr_De=(pente1*ratio2) + b1;
    %
    pente2=(1.25-1.15)/(100 - 500);
    b2=1.15-pente2*500;
    corr_Di=(pente2*ratio2) + b2;
end
if ( ratio2>500 & ratio2<=1e3)
    pente1=(1.20-1.15)/(500 - 1e3);
    b1=1.15-pente1*1e3;
    corr_De=(pente1*ratio2) + b1;
    %
    pente2=(1.15-1.1)/(500 - 1e3);
    b2=1.1-pente2*1e3;
    corr_Di=(pente2*ratio2) + b2;
end
if ( ratio2>1e3 & ratio2<=5e3)
    pente1=(1.15-1.1)/(1e3 - 5e3);
    b1=1.1-pente1*5e3;
    corr_De=(pente1*ratio2) + b1;
    %
    pente2=(1.1-1)/(1e3 - 5e3);
    b2=1.-pente2*5e3;
    corr_Di=(pente2*ratio2) + b2;
end
if ( ratio2>5e3 & ratio2<=1e4)
    pente1=(1.1-1)/(5e3 - 1e4);
    b1=1.-pente1*1e4;
    corr_De=(pente1*ratio2) + b1;
    %
    pente2=(1.-1.)/(5e3 - 1e4);
    b2=1.-pente2*1e4;
    corr_Di=(pente2*ratio2) + b2;
end
if ratio2>1e4
    corr_De=1;
    corr_Di=1;
end

    function [corr_De,corr_Di]=CorrectionDiffusion2(lambda,lde)

%program pour calculer les corrections a la diffusion ambipolaire suivant
```

```
%les donnees tirees de l'article Phys Rev A 7, 781 (1973)
%avec resultats de freiberg pour les electrons

%rapport de la longueur de diffusion sur la longueur de Debye electronique
ratio2=(lambda/lde)^2;
%calcul des coefficeints de correction
if ratio2<= 1e-1
    pente1=(40.-30.)/(7e-2 - 1e-1);
    b1=40-pente1*7e-2;
    corr_De=(pente1*ratio2) + b1;
    if corr_De>100;
        corr_De=100;
    end
    corr_Di=0.5;
end
if ( ratio2>1e-1 & ratio2<=5e-1)
    pente1=(30-15)/(1e-1 - 5e-1);
    b1=15-pente1*5e-1;
    corr_De=(pente1*ratio2) + b1;
    %
    pente2=(5e-1 - 6e-1)/(1e-1 - 5e-1);
    b2=6e-1 -pente2*5e-1;
    corr_Di=(pente2*ratio2) + b2;
end
if ( ratio2>5e-1 & ratio2<=1)
    pente1=(15-10)/(5e-1 - 1.);
    b1=10-pente1*1;
    corr_De=(pente1*ratio2) + b1;
    %
    pente2=(6e-1 - 7e-1)/(5e-1 - 1.);
    b2=7e-1 -pente2*1;
    corr_Di=(pente2*ratio2) + b2;
end
if ( ratio2>1 & ratio2<=5)
    pente1=(10-7)/(1 - 5);
    b1=7-pente1*5;
    corr_De=(pente1*ratio2) + b1;
    %
    pente2=(7e-1 - 1.1)/(1 - 5);
    b2=1.1-pente2*5;
    corr_Di=(pente2*ratio2) + b2;
end
if ( ratio2>5 & ratio2<=10)
    pente1=(7-3)/(5-10);
    b1=3-pente1*10;
    corr_De=(pente1*ratio2) + b1;
    %
    pente2=(1.1-1.2)/(5-10);
    b2=1.2-pente2*10;
    corr_Di=(pente2*ratio2) + b2;
end
if ( ratio2>10 & ratio2<=50)
    pente1=(3-2.5)/(10 - 50);
    b1=2.5-pente1*50;
    corr_De=(pente1*ratio2) + b1;
    %
    pente2=(1.2-1.3)/(10 - 50);
    b2=1.3-pente2*50;
    corr_Di=(pente2*ratio2) + b2;
end
if ( ratio2>50 & ratio2<=100)
    pente1=(2.5-2.1)/(50 - 100);
    b1=2.1-pente1*100;
    corr_De=(pente1*ratio2) + b1;
```

```
    %
    pente2=(1.3-1.3)/(50 - 100);
    b2=1.3-pente2*100;
    corr_Di=(pente2*ratio2) + b2;
end
if ( ratio2>100 & ratio2<=500)
    pente1=(2.1-1.9)/(100 - 500);
    b1=1.9-pente1*500;
    corr_De=(pente1*ratio2) + b1;
    %
    pente2=(1.3-1.15)/(100 - 500);
    b2=1.15-pente2*500;
    corr_Di=(pente2*ratio2) + b2;
end
if ( ratio2>500 & ratio2<=1e3)
    pente1=(1.9-1.5)/(500 - 1e3);
    b1=1.5-pente1*1e3;
    corr_De=(pente1*ratio2) + b1;
    %
    pente2=(1.15-1.1)/(500 - 1e3);
    b2=1.1-pente2*1e3;
    corr_Di=(pente2*ratio2) + b2;
end
if ( ratio2>1e3 & ratio2<=5e3)
    pente1=(1.5-1.1)/(1e3 - 5e3);
    b1=1.5-pente1*1e3;
    corr_De=(pente1*ratio2) + b1;
    %
    pente2=(1.1-1)/(1e3 - 5e3);
    b2=1.-pente2*5e3;
    corr_Di=(pente2*ratio2) + b2;
end
if ( ratio2>5e3 & ratio2<=1e4)
    pente1=(1.1-1)/(5e3 - 1e4);
    b1=1.-pente1*1e4;
    corr_De=(pente1*ratio2) + b1;
    %
    pente2=(1.-1.)/(5e3 - 1e4);
    b2=1.-pente2*1e4;
    corr_Di=(pente2*ratio2) + b2;
end
if ratio2>1e4
    corr_De=1;
    corr_Di=1;
end
```

Appendix D

Publications related to this thesis

D.1 Publications related to Chapter 4

- Mikikian, M.; Cavarroc, M.; Couëdel, L. & Boufendi, L., "Low frequency instabilities during dust particle growth in a radio-frequency plasma", Phys. Plasmas, **13**, 092103 (2006)
- Mikikian, M.M.; Couëdel, L.L.; Cavarroc, M.M.; Tessier, Y.Y. & Boufendi, L.L.,"Plasma Emission Modifications and Instabilities Induced by the Presence of Growing Dust Particles", IEEE Trans. Plasma Sci., In press (2008)

Low frequency instabilities during dust particle growth in a radio-frequency plasma

Maxime Mikikian,[a] Marjorie Cavarroc, Lénaïc Couëdel, and Laïfa Boufendi
GREMI, Groupe de Recherches sur l'Energétique des Milieux Ionisés UMR6606, CNRS/Université d'Orléans, 14 rue d'Issoudun, BP6744, 45067 Orléans Cedex 2, France

(Received 1 June 2006; accepted 26 July 2006; published online 6 September 2006)

In this paper, instabilities appearing in a dusty plasma are experimentally investigated. These low frequency self-excited instabilities appear during dust particle growth and are characterized by a frequency spectrum evolving during this process. The onset, the time evolution and the main characteristics of these instabilities are investigated thanks to electrical and optical measurements. Both signals show a clear evolution scheme with a well-defined succession of phases. From the beginning to the end of this scheme, regular oscillations and/or chaotic regimes are observed. Finally, instabilities stop when the dust particle size reaches a few hundreds of nanometers and a stable three-dimensional dust cloud is obtained. A dust-free region called void is then usually observed in the plasma center. © *2006 American Institute of Physics*. [DOI: 10.1063/1.2337793]

I. INTRODUCTION

In a plasma, dust particles can be grown using reactive gases like silane[1–3] or by ion bombardment on materials.[4–9] This formation is actively studied due to strong consequences that can arise from the presence of dust in plasma processing reactors[10,11] for microelectronics where cleanliness is a major requirement.[12] Furthermore, the interest is actually increasing due to the fact that nanometer dust particles can be useful for industrial applications like solar cells[13] or memories.[14] Laboratory dusty plasmas are also a very efficient way to produce and study astrophysical dusty media like planet atmospheres.[15] In capacitively coupled radio-frequency discharges, a dense cloud of submicrometer dust particles filling the whole space between the electrodes can be obtained. During their growth, dust particles acquire a negative charge by attaching more and more electrons.[16–18] Consequently, the growth can be studied through its influence on the plasma characteristics and in particular on the discharge current harmonics. Indeed, the current third harmonic is a robust tool to accurately follow and identify growth steps.[19] Dust particle growth strongly affects plasma properties and can induce plasma instabilities. Self-excited instabilities have been observed in silane plasmas[20] (frequencies of few kHz for dust particles of few nanometers) and also in dusty plasmas produced by sputtering a carbon target[7,8] (frequencies around 100 Hz for dust particles around hundred nanometers). In this last experiment, the authors describe two different instability modes called the filamentary mode and the great void mode. The first one appears approximately 1 min after the plasma ignition and is characterized by a broadband spectrum centered around 100 Hz. It corresponds to a beamlike striation of dust density and plasma glow. As dust particles are still growing, this stage is then followed by the great void mode, which corresponds to the formation of a dust-free region called void[7,9,21–23] and its rotation in a horizontal plane in between the electrodes. The void region is due to the equilibrium between various forces acting on the negatively charged dust particles. These forces are principally due to ion drag, electric fields, thermal gradients, gas flow, and gravity, and they define the cloud shape. The ion drag force is presently actively studied because it is suspected to be the main responsible of the void formation,[8,24–33] pushing the dust particles away from the discharge center. In this paper, observations and analyses of instabilities appearing during dust particle growth are performed. These instabilities look like the filamentary and great void modes in some stage of their evolution. Nevertheless, their time evolution is much more complicated and seven different regimes can be identified. Indeed, well-defined frequencies are observed and the associated spectrum strongly evolves during the growth process. The instability complex shape underlines the coexistence of different phenomena that could interact and give regular or chaotic oscillations. The instability time evolution reveals drastic and sudden changes in shape and frequency that could not be easily correlated to dust particle size and density. A detailed analysis of the instability main characteristics is performed in order to underline and bring to the fore the complex phenomena that could arise in a plasma containing changing dust particles.

II. EXPERIMENTAL BASIS

A. Experimental setup

The work presented here is performed in the PKE-Nefedov (Plasma Kristall Experiment) chamber designed for microgravity experiments.[34] The experimental setup consists of a parallel plate rf discharge where an argon plasma (0.2–2 mbar) is created in a push-pull excitation mode (0–4 W). The electrodes are separated by 3 cm and their diameter is 4 cm. The dust cloud is illuminated by a thin laser sheet perpendicular to the electrodes and the scattered light is recorded at 90° with two standard charge-coupled device (CCD) cameras at 25 images per second. In the first stages of growth, dust particles are very small and the scattered light is maximum in the laser direction. Consequently, a third camera is watching the cloud with an angle lying approximately between 20° and 30° with respect to the incident laser direction. Instabilities are characterized by two different diagnostics. First, the time evolution of the amplitude of the discharge current fundamental harmonic is recorded. This electrical measurement is representative of global changes in plasma properties, especially concerning the electron density. The second diagnostic is based on spatially resolved optical measurements. Five optical fibers are horizontally aligned (5 mm in between each fiber) and record the total plasma light with a spatial resolution of about 3 mm. This diagnostic gives local measurements that are of interest to detect any plasma motion or localized changes in order to better understand the integrated electrical measurements.

[a]Electronic mail: maxime.mikikian@univ-orleans.fr

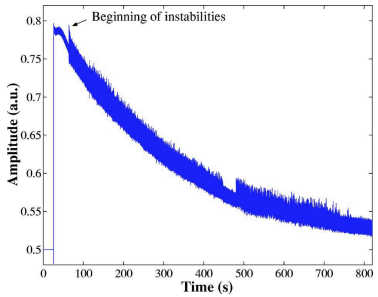

FIG. 1. (Color online) Time evolution of the amplitude of the discharge current fundamental harmonic during dust particle growth. Instabilities appear around 40 s after plasma ignition.

B. Dust particle growth

Dust particles are grown by sputtering a polymer layer deposited on the electrodes and coming from previously injected dust particles (3.4 μm, melamine formaldehyde). A typical working pressure is around 1.6 mbar and rf power is about 2.8 W. With these parameters dust particles start to be detected by the cameras approximately 1 min after the plasma ignition. A more complete description of the experimental setup and some results concerning dust particle growth are given in Ref. 9. The growth process leads to various shapes of the dust cloud (few layers, domelike shape, three-dimensional dense cloud) due to the fact that we do not control precisely the size and density of grown dust particles. Indeed, the growth process seems to be highly sensitive to gas purity. This effect is amplified by the fact that experiments are performed at static pressure (no gas flow). At least 1 h of pumping between each experiment is needed to eliminate species formed during the previous run and/or coming from the outgassing of the walls and/or from the sputtered matter. This behavior is well observed on successive runs by using emission spectroscopy. Impurities like N_2 and OH are observed and their effect on dust particle formation is under investigation. Until now it is not clear if their presence prevents the sputtering or if the sputtering occurs but the growth cannot takes place. This effect of the gas purity has been previously reported in similar experiments.[8] Possible precursors like carbon molecules C_2, CN, and CH appear and the C_2 molecule seems to be a good indicator of dust formation.[35]

A very high dust density is obtained when base pressure before an experiment is sufficiently low (few 10^{-6} mbar). A base pressure of few 10^{-5} mbar drastically reduces the amount of grown dust particles. This base pressure dependence is even more drastic on the instability appearance. Indeed, in our experimental conditions, they are observed only if the base pressure is lower than 4×10^{-6} mbar. Consequently, unstable conditions depend on gas purity and/or on dust particle density.

III. DUST PARTICLE GROWTH INSTABILITIES

Dust particle growth instabilities (DPGI) typically appear a few tens of seconds after plasma ignition. Their appearance is well observed on both electrical and optical measurements.[36,37] Due to their low frequency and strong amplitude, the beginning of DPGI is also well detected by the naked eye looking at the plasma glow.

When dust particles are growing in a plasma, the amplitude of the discharge current fundamental harmonic is decreasing due to the electron attachment on the dust particle surface. This decrease is well observed in Fig. 1 from around 20 s (plasma ignition) to 800 s. The appearance of DPGI is also clearly evidenced by an increase of the fluctuation amplitude becoming a real oscillation. DPGI can last several minutes (more than 12 min in Fig. 1) and different regimes are evidenced. Their starting time is slightly changing from one experiment to another due to differences in dust particle density, which is strongly dependent on gas purity. Nevertheless, statistics performed on several experiments allow to deduce some general behavior. For example, the pressure dependence is shown in Fig. 2. A decreasing exponential variation of DPGI appearance time as a function of pressure is observed: the higher the pressure, the shorter the appearance time. This variation underlines the relation between the instability appearance and dust particle density. Indeed, DPGI are observed only when a huge dust particle density is obtained. From our previous experiments,[35] we define the threshold pressure permitting dust particle growth at around 1.2 mbar. At higher pressures, a shorter delay before formation of a dense cloud is measured. This delay is well evidenced in Fig. 2. At 1.4 mbar, nearly 2 min are necessary to initiate DPGI while only 40 s are required at 1.8 mbar. Two possibilities can explain this delay at low pressures: either a longer time is required to attain the critical dust density necessary to initiate DPGI or the dust density is lower and for DPGI to begin it needs bigger dust particles (i.e., longer

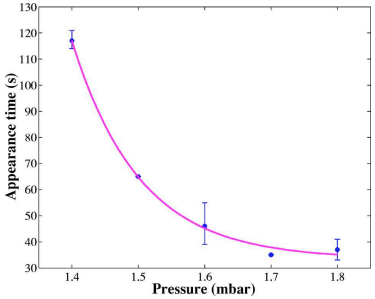

FIG. 2. (Color online) Instability appearance time as a function of argon pressure.

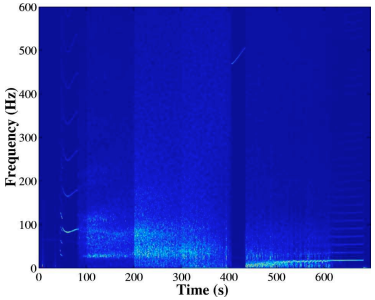

FIG. 4. (Color online) Spectrogram of electrical measurements corresponding to Fig. 3 and describing the frequency evolution of DPGI as a function of time.

time). These explanations are consistent with another observation: the lower the rf power, the longer the appearance time.

IV. PHASE IDENTIFICATION: ELECTRICAL AND OPTICAL MEASUREMENTS

As can be seen in Fig. 1, different regimes characterize DPGI. These different phases are easily brought to light by performing the same electrical measurements but in ac mode in order to improve oscilloscope vertical resolution. The resulting curve is presented in Fig. 3. The beginning of DPGI is detected around 40 s and clear phases, numbered from 1 to 7, are observed. These different phases are better evidenced by performing Fourier analysis of the electrical signals. A typical spectrogram is given in Fig. 4. In order to emphasize small ordered domains, the spectrogram intensity has been normalized inside each 100 s range (from 0 to 100 s intensity has been normalized to its maximum value inside this time domain and so on). The same Fourier analysis performed on spatially resolved optical measurements shows roughly the same spectrogram features and phases. From Figs. 3 and 4 we can identify seven different regimes (a precise analysis of these different phases will be presented in the following sections):

- Three ordered phases P1, P2, P3 (from ≃40 s to ≃80 s).
- Chaotic phase P4 (from ≃80 s to ≃405 s).
- High frequency phase P5 (from ≃405 s to ≃435 s).
- Chaotic phase becoming more and more regular P6 (from ≃435 s to ≃600 s).
- Regular oscillation phase P7 (from ≃600 s to ≃680 s).

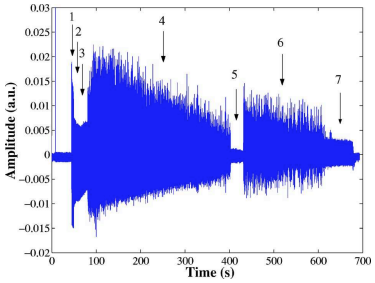

FIG. 3. (Color online) Time evolution of the amplitude of the discharge current fundamental harmonic during dust particle growth (ac component). Instabilities appear around 40 s after plasma ignition. Successive phases are numbered from 1 to 7.

All these phases are observed on both electrical and optical measurements, confirming their real correlation to an unstable state of the plasma-dust particle system. The global scheme of these instabilities is different from the one describe in Refs. 7 and 8, where a filamentary mode (that could be related to our chaotic regime) is followed by a regular phase (great void mode). In our experiment, instabilities begin with regular oscillations (P1, P2, P3) followed by a long chaotic regime (P4). This chaotic phase (P4) suddenly ends with a high-frequency phase (P5) and starts again (P6), becoming more and more ordered. Finally, the system reaches a regular phase (P7) that can be sustained for a long time (in the example given here the plasma has been switched off at 680 s).

A. First three ordered phases

DPGI begin with a succession of three ordered phases separated by clear transitions (Fig. 5). The P1 and P2 phases are short and are not detected in all experiments while the P3 phase lasts longer and is regularly observed. The three phases are well separated and evolve as a function of time. To explain the observed transitions between phases, it is necessary to also analyze the corresponding time series. As an example, Fig. 6 represents an electrical measurement obtained with a very short P2 phase in order to illustrate on the

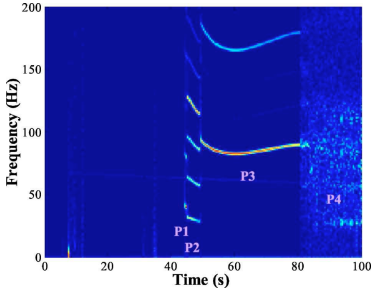

FIG. 5. (Color online) First three ordered phases of DPGI and transition to a chaotic regime.

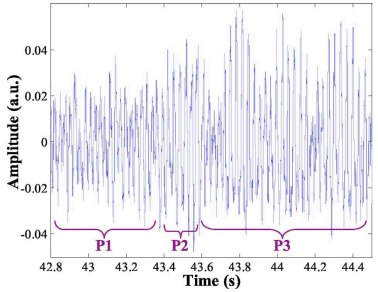

FIG. 7. (Color online) Transitions between the first three ordered phases observed on optical measurements performed near the plasma edge.

same figure the P1–P2 and P2–P3 transitions. In Fig. 6, the P1 phase is characterized by wide separated peaks with a mean frequency of about 40 Hz. The transition from P1 to P2 corresponds to the growth of two small peaks between these higher amplitude patterns. The Fourier analysis traduces this change by a frequency decrease from about 40 Hz in P1 to about 30 Hz in P2. The small peaks continue to grow (P2 phase) and the higher amplitude ones decrease. Finally, all peaks reach the same amplitude characterizing the P3 phase. The frequency of the P3 phase is then approximately three times the P2 frequency (around 94 Hz). The P3 phase is robust (nearly always observed in our experiments) and lasts a sufficiently long time to evolve with dust particle growth (Fig. 5). Its frequency time evolution is always the same, it decreases, reaches a minimum value, and then slightly increases until DPGI enter in the chaotic regime. Furthermore, the frequency range of the P3 phase seems to be linearly dependent on the phase duration: the higher the frequency, the shorter the time duration. The time evolution

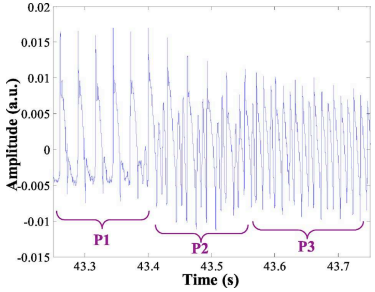

FIG. 6. (Color online) Transitions between the first three ordered phases observed on electrical measurements.

of these three ordered phases is better observed on the frequency harmonics appearing due to the nearly sawtooth shape of the electrical signals (Fig. 6).

Optical measurements recording the plasma light (integrated on all wavelengths) at different positions also show three ordered phases (Fig. 7). Nevertheless, these P1, P2, and P3 phases have different characteristics than the ones observed on electrical measurements. Concerning the oscillation shape, the transition between the P1 and P2 phases is here revealed by an increase of oscillation amplitude (Fig. 7). The P3 phase is strongly marked by a clear amplitude modulation, which is better evidenced near the plasma edge than in the plasma center. Concerning the oscillation frequency, some small discrepancies with electrical measurements are also observed, especially on the P3 phase (Figs. 5 and 8). Indeed, the P1 and P2 phases are similar but when DPGI enter in the P3 phase, the typical frequency is not tripled, like in electrical measurements, but remains around the same value than during the P2 phase. Furthermore, optical measurements of this P3 phase are slightly different depending on the observed plasma region. The signal recorded by the optical fiber watching the plasma center [Figs. 8(a) and 8(c)] is not exactly the same as the one recorded near the plasma edge [Figs. 8(b) and 8(d)]. Indeed, the central fiber gives a main frequency around 26 Hz and a small amplitude component around 31 Hz [Fig. 8(c)]. The near plasma edge fiber gives the same frequencies but also additional ones: one in between 26 and 31 Hz and another one around 3 Hz [Fig. 8(d)] that corresponds to the strong modulation observed in Fig. 7. These observations underline that some spatial considerations must be made to interpret this P3 phase. The first local indication concerns the frequency that is three times lower than for electrical measurements. This point seems to signify that a phenomenon oscillating at around 94 Hz affects the plasma, and consequently the electrical measurement, but is detected only one time out of three by the optical fibers. One possible explanation is that a plasma modification either appears successively in different places, or moves and comes back in front of an optical fiber with a frequency of about 30 Hz. This plasma modification appears successively

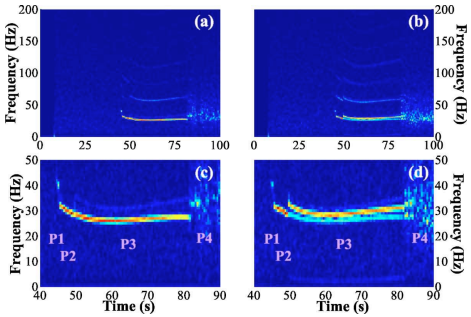

FIG. 8. (Color online) Spectrogram of optical measurements recorded (a) in the plasma center, (b) near the plasma edge. (c) Zoom of (a), (d) zoom of (b).

in distinct locations of the plasma because it is not detected at 94 Hz by any optical fiber looking at the plasma center or edge. Investigations concerning this hypothesis are currently underway using a high speed camera. The second local indication giving credit to this hypothesis is the difference between observations given by each optical fiber. Indeed, even if their Fourier spectrum is nearly similar and shows only small discrepancies, the recorded time series bring more information. Optical measurements performed by the near plasma edge fiber is in phase opposition with the ones in the center. This behavior, coupled with the fact that a stronger modulation is observed near the plasma edge, could confirm a possible motion, or appearance in different places, of a modified plasma region.

B. Chaotic regime

After three different ordered phases, DPGI enter in a chaotic regime P4 (Fig. 5 after 80 s) with a strong increase in DPGI amplitude (Fig. 3). Then, the amplitude slowly decreases during the whole phase. P4 is also characterized by structured oscillations appearing in a transient manner. These structured regions are identified by some bright spots on electrical and optical spectrograms. On time series they appear as bursts of order. In Fig. 9(a), electrical signals reveal a clear transition between the P3 phase and the chaotic regime. This regime change is indicated by an arrow and a burst of order is encircled. A zoom of this burst of order is shown in Fig. 9(b). During the chaotic regime, structured oscillations in electrical signals always appear following a three peak structure [see, for example, between 94 s and 94.04 s in Fig. 9(b)] that could be related to the three peaks observed in the P2 or P3 phases. Indeed, it could be a reemergence of these phases during the chaotic regime. To compare our observations with the filamentary mode,[7,8] a Fourier spectrum of the whole chaotic regime (from 80 to 405 s) has been performed in Fig. 10. For electrical signals [Fig. 10(a)], a noisy main frequency around 28 Hz is observed and is equal to the frequency at the end of the P2 phase, confirming the possible reemergence of this phase. This frequency corresponds to the occurrence frequency of the three peak structure regularly appearing during the chaotic regime [Fig. 9(b)]. Due to these structures, multiple frequencies (54 Hz, 83 Hz, and 107 Hz corresponding to the frequency between two successive peaks of one single three peak structure) are also detected in Fig. 10(a). For optical measurements [Fig. 10(b)], differences with electrical ones are the same than in the P3 phase: one optical oscillation corresponds to a three peak structure and consequently only the 28 Hz frequency appears [Fig. 10(b)]. These spectra are very similar to the one obtained for the filamentary mode[8] even if in our experiments the presence of more ordered domains is observed. Thus, we can surmise that the chaotic regime we observe could be similar to this filamentary mode.

C. High-frequency phase

In some experiments, the chaotic regime is suddenly interrupted by a strong frequency change (at 405 s in Figs. 3 and 4). Indeed, this phase P5 is not always observed but when it is present, its general characteristics are nearly always the same. This new phase appears after a continuous

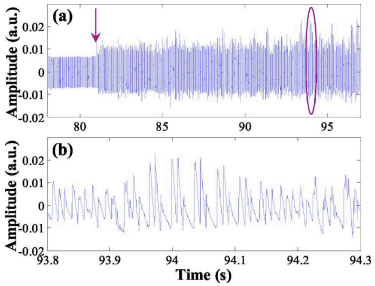

FIG. 9. (Color online) Electrical measurements: (a) transition between P3 and P4 phases and encircled burst of order, (b) zoom of the encircled part of (a).

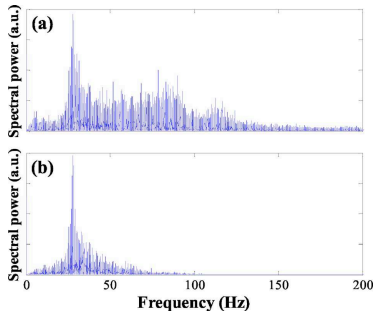

FIG. 10. (Color online). Fourier spectrum of the first chaotic regime on (a) electrical measurements, (b) central optical fiber measurements

decrease of the P4 phase amplitude and is defined by a radical change in DPGI amplitude and frequency. Indeed, DPGI turn into a low-amplitude and high-frequency (around 500 Hz) oscillations as shown in Fig. 11. This change happens suddenly when no fast modifications in dust particle size and density are expected. Furthermore, the phase frequency increases with time. In Fig. 4, this increase is nearly linear but nonlinear behaviors have also been observed in certain cases. As previously mentioned, this phase is not always observed, which means relatively precise conditions must be fulfilled for its existence. This effect is well confirmed in the experiment described in Fig. 12, where this phase is interrupted before starting again. Small modifications in plasma or dust particle properties can easily turn the system from the high-frequency phase to the chaotic one. Furthermore, this P5 phase can also be transformed in regular oscillations as shown in Fig. 12 at $t=294$ s. From these experimental results it can be assumed that this high-frequency phase is a particular case of DPGI, obtained in a tight set of parameters and that can be easily turned in ordered or chaotic regimes.

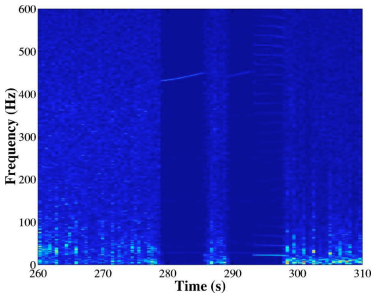

FIG. 12. (Color online) Spectrogram of a particular case of the high-frequency phase. This phase is interrupted by a chaotic regime and is transformed in regular oscillations just before turning again in a chaotic regime.

D. Second chaotic regime

After the high-frequency phase, a second chaotic regime is usually observed. Two different types of this P6 phase are observed. The most usual is presented in Fig. 4 between 435 and 600 s. It corresponds to a phase similar to P4 but with more and more ordered regions. Figure 4 clearly shows that DPGI tend to stabilize to regular oscillations ($\simeq$600 s). This transition appears as a small and continuous increase in DPGI frequency. Nevertheless, some experiments show a slightly different behavior as in Fig. 13. Instead of slowly increasing, the frequency decreases and enters (still decreasing) in a regular oscillation phase. This behavior corresponds to void rotation in a horizontal plane, which is clearly evi-

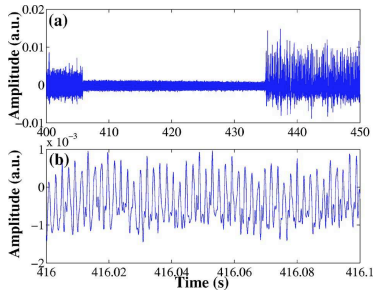

FIG. 11. (Color online) (a) Appearance of the high-frequency phase in between two chaotic regimes. (b) Zoom of (a).

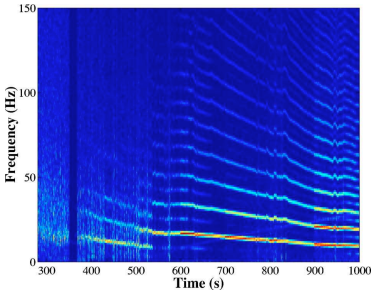

FIG. 13. (Color online) Spectrogram of a particular case of the second chaotic regime corresponding to void rotation in a horizontal plane.

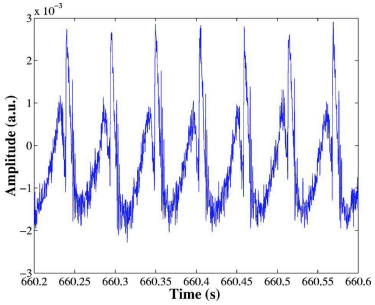

FIG. 14. (Color online) Electrical measurements corresponding to the final regular oscillation phase.

denced thanks to CCD camera images. The corresponding spectrogram is nearly similar to the one obtained in Ref. 8 and related to the great void mode.

E. Final regular oscillation phase

The final step of DPGI often corresponds to a regular oscillation phase characterized by a spectrogram with a typical frequency around 18 Hz (Fig. 4) and its harmonics. The corresponding electrical signal is shown in Fig. 14. The signal shape is in particular marked by a sharp peak appearing at each period. This shape is similar to what is obtained during the "heartbeat" instability,[23,38] which corresponds to regular contractions and expansions of the void size. At this stage of DPGI, this regular oscillation phase can last for minutes and is robust, meaning that once it is set up it does not turn in another regime. Optical measurements performed in the plasma center show an evolution similar to the electrical one except near the sharp peak region as observed in Ref. 36. Furthermore, the near edge optical fiber signal is in phase opposition with the central one (as in Ref. 36), emphasizing the similarity with the heartbeat instability.

V. DISCUSSION AND CONCLUSIONS

In this paper, self-excited instabilities induced by the formation of submicrometer dust particles are investigated. These instabilities appear when a sufficiently high dust particle density is reached. Instability frequency and shape change during the growth process and direct correlation with dust particle size and density cannot be easily deduced. Indeed, effects of both parameters on discharge behavior are difficult to separate: a high density of small particles can have roughly the same effect than a lower density of bigger particles, assuming that the total collection surface is identical and consequently the same amount of electrons can be captured. The only way to conclude on this point is to measure dust particle size and density but most commonly used *in situ* diagnostics cannot be implemented on our experimental setup. Furthermore, an easy systematic collection of dust particles coming from one and only one experiment is not possible in our reactor. DPGI reproducibility can be obtained only with very low base pressures not reached in the case of regular reactor opening. By comparing Fig. 1 with electrical characteristics obtained in silane based discharges,[39] we can speculate that DPGI occur during the "coalescence phase" and last during the so-called "surface deposition phase." These phases[40] are characterized by a significant amount of negatively charged dust particles strongly impacting on plasma stability. This comparison with dust particle growth process in silane based chemistry must be taken carefully because the analogy has not been strictly proven yet. From visual observations we know that when DPGI occur, dust particles are not detected yet by our video system and are certainly smaller than 100 nm. When instabilities stop, the dust particle size could be of a few hundreds of nanometers. The instability development follows a well-defined succession of phases that can be ordered or chaotic. At least seven different regimes have been evidenced and their occurrence is strongly dependent on plasma and dust particle properties. Complex transitions between different ordered phases or between ordered and chaotic ones have been evidenced and underline the nonlinear behavior of these instabilities. Two observed phases seem to correspond to the ones reported in previous papers.[7,8] These phases, called the filamentary mode and the great void mode, can be a part of a more general behavior described in this paper. The new phases described here underline the complexity of the phenomena behind observations and their high sensitivity to plasma and dust particle properties. Indeed, the complete scheme with seven phases can be observed in very specific experimental conditions usually encountered in this work. Striations (in our case, enhanced ionization regions appearing as bright spots or filaments) seem to be responsible for the different observed phases. The various regimes could be related to the way striations appear. Indeed, we can surmise that the ordered regimes could be striations appearing periodically and nearly at the same places. Following this hypothesis, the often observed three peak structure can correspond to three different striations. By analogy, chaotic regimes can be due to randomly appearing (in time and in space) striations. Optical measurements performed in different plasma positions bring to the fore that these instabilities need to be analyzed with spatial considerations. Differences with works reported in Refs. 7 and 8 can be the consequence of different plasma and/or dust particle properties, geometrical considerations, or gas flow. Furthermore, our observations show that void formation is not a consequence of these instabilities as proposed in Ref. 24. The void can be formed with or without instabilities preceding its appearance. In some conditions, the void is formed before instability begins. In this case, the instability evolution scheme does not describe all the phases presented here. Similarities between the final regular oscillation phase and the heartbeat instability concerning the void region have been observed. It could indicate that dust particle growth instabilities and the heartbeat instability could be different aspects of the same physical phenomena.

ACKNOWLEDGMENTS

The PKE-Nefedov chamber has been made available by the Max-Planck-Institute for Extraterrestrial Physics, Germany, under the funding of DLR/BMBF under Grant No. 50WM9852. The authors would like to thank S. Dozias for electronic support, J. Mathias for optical support, and Y. Tessier for experimental support.

This work was supported by CNES under contract No. 793/2000/CNES/8344.

[1] A. Bouchoule, A. Plain, L. Boufendi, J.-P. Blondeau, and C. Laure, J. Appl. Phys. **70**, 1991 (1991).
[2] Y. Watanabe, M. Shiratani, Y. Kubo, I. Ogawa, and S. Ogi, Appl. Phys. Lett. **53**, 1263 (1988).
[3] A. Howling, C. Hollenstein, and P. Paris, Appl. Phys. Lett. **59**, 1409 (1991).
[4] G. Jellum and D. Graves, J. Appl. Phys. **67**, 6490 (1990).
[5] W. Yoo and C. Steinbrüchel, J. Vac. Sci. Technol. A **11**, 1258 (1993).
[6] B. Ganguly, A. Garscadden, J. Williams, and P. Haaland, J. Vac. Sci. Technol. A **11**, 1119 (1993).
[7] G. Praburam and J. Goree, Phys. Plasmas **3**, 1212 (1996).
[8] D. Samsonov and J. Goree, Phys. Rev. E **59**, 1047 (1999).
[9] M. Mikikian, L. Boufendi, A. Bouchoule, H. Thomas, G. Morfill, A. Nefedov, V. Fortov, and the PKE-Nefedov Team, New J. Phys. **5**, 19.1 (2003).
[10] R. Roth, K. Spears, G. Stein, and G. Wong, Appl. Phys. Lett. **46**, 253 (1985).
[11] G. Selwyn, J. Singh, and R. Bennett, J. Vac. Sci. Technol. A **7**, 2758 (1989).
[12] L. Boufendi and A. Bouchoule, Plasma Sources Sci. Technol. **11**, A211 (2002).
[13] P. Roca i Cabarrocas, P. Gay, and A. Hadjadj, J. Vac. Sci. Technol. A **14**, 655 (1996).
[14] S. Tiwari, F. Rana, H. Hanafi, A. Hartstein, and E. Crabbé, Appl. Phys. Lett. **68**, 1377 (1996).
[15] C. Szopa, G. Cernogora, L. Boufendi, J. Correia, and P. Coll, Planet. Space Sci. **54**, 394 (2006).
[16] B. Walch, M. Horanyi, and S. Robertson, IEEE Trans. Plasma Sci. **22**, 97 (1994).
[17] A. Melzer, T. Trottenberg, and A. Piel, Phys. Lett. A **191**, 301 (1994).
[18] C. Arnas, M. Mikikian, and F. Doveil, Phys. Rev. E **60**, 7420 (1999).
[19] L. Boufendi, J. Gaudin, S. Huet, G. Viera, and M. Dudemaine, Appl. Phys. Lett. **79**, 4301 (2001).
[20] M. Cavarroc, M. Jouanny, K. Radouane, M. Mikikian, and L. Boufendi, J. Appl. Phys. **99**, 064301 (2006).
[21] J. Dorier, C. Hollenstein, and A. Howling, J. Vac. Sci. Technol. A **13**, 918 (1995).
[22] G. Morfill, H. Thomas, U. Konopka, H. Rothermel, M. Zuzic, A. Ivlev, and J. Goree, Phys. Rev. Lett. **83**, 1598 (1999).
[23] M. Mikikian and L. Boufendi, Phys. Plasmas **11**, 3733 (2004).
[24] J. Goree, G. Morfill, V. Tsytovich, and S. Vladimirov, Phys. Rev. E **59**, 7055 (1999).
[25] M. Akdim and W. Goedheer, Phys. Rev. E **65**, 015401 (2001).
[26] V. Tsytovich, V. Vladimirov, G. Morfill, and J. Goree, Phys. Rev. E **63**, 056609 (2001).
[27] G. Gozadinos, A. Ivlev, and J.-P. Boeuf, New J. Phys. **5**, 32.1 (2003).
[28] K. Avinash, A. Bhattacharjee, and S. Hu, Phys. Rev. Lett. **90**, 075001 (2003).
[29] C. Zafiu, A. Melzer, and A. Piel, Phys. Plasmas **10**, 1278 (2003).
[30] A. Ivlev, S. Zhdanov, S. Khrapak, and G. Morfill, Phys. Rev. E **71**, 016405 (2005).
[31] M. Kretschmer, S. Khrapak, S. Zhdanov, H. Thomas, G. E. Morfill, V. Fortov, A. Lipaev, V. Molotkov, A. Ivanov, and M. Turin, Phys. Rev. E **71**, 056401 (2005).
[32] S. Vladimirov, V. Tsytovich, and G. Morfill, Phys. Plasmas **12**, 052117 (2005).
[33] V. Land and W. Goedheer, New J. Phys. **8**, 8 (2006).
[34] A. Nefedov, G. Morfill, V. Fortov, H. Thomas, H. Rothermel, T. Hagl, A. Ivlev, M. Zuzic, B. Klumov, A. Lipaev, *et al.*, New J. Phys. **5**, 33.1 (2003).
[35] M. Mikikian, L. Boufendi, and A. Bouchoule, in *Proceedings of the 30th EPS Conference on Controlled Fusion and Plasma Physics*, St. Petersburg, edited by R. Koch and S. Lebedev (2003), Vol. 27A of ECA, pp. O–3.1B, http://epsppd.epfl.ch/StPetersburg/PDF/O3-001B.PDF.
[36] M. Mikikian, M. Cavarroc, N. Chaumeix, and L. Boufendi, in *Proceedings of the 31st EPS Conference on Plasma Physics*, London, edited by P. Norreys and H. Hutchinson (European Physical Society, Petit-Lancy, 2004), Vol. 28G of ECA, pp. O–2.13, http://epsppd.epfl.ch/London/pdf/02_13.pdf.
[37] M. Mikikian, M. Cavarroc, and L. Boufendi, in *New Vistas in Dusty Plasmas*, edited by L. Boufendi, M. Mikikian, and P. Shukla, AIP Conf. Proc. No. 799 (AIP, Melville, NY, 2005), p. 319.
[38] M. Mikikian, M. Cavarroc, and L. Boufendi, in *New Vistas in Dusty Plasmas*, edited by L. Boufendi, M. Mikikian, and P. Shukla, AIP Conf. Proc. No. 799 (AIP, Melville, NY, 2005), p. 323.
[39] M. Cavarroc, M. Mikikian, G. Perrier, and L. Boufendi, Appl. Phys. Lett. **89**, 013107 (2006).
[40] A. Bouchoule, L. Boufendi, J. Hermann, A. Plain, T. Hbid, G. Kroesen, and W. W. Stoffels, Pure Appl. Chem. **68**, 1121 (1996).

Plasma Emission Modifications and Instabilities Induced by the Presence of Growing Dust Particles

Maxime Mikikian, Lénaïc Couëdel, Marjorie Cavarroc, Yves Tessier, and Laïfa Boufendi

***Abstract*—Formation of dust particles in a plasma can strongly change its properties due to electron attachment on dust surface. An easy way to detect dust formation is to analyze modifications of the plasma emission. In this paper, changes in the plasma emission are related to the growth of dust particles. We particularly show that dust formation induces low-frequency plasma instabilities. Another interesting induced effect is the formation of an enhanced emission region which is dust free and usually named "void."**

***Index Terms*—Complex plasma, dust particle growth, dusty plasma, instabilities, oscillations, plasma emission, void.**

PLASMAS ARE widely encountered in nature and industries. In many environments, these plasmas also contain dust particles (i.e., solid bodies from a few nanometers to centimeters) and are thus called dusty (or complex) plasmas. In astrophysics, these media are found in comet tails or planetary atmospheres. In artificial plasmas, these dust particles are fatal for processes in microelectronics (where cleanliness is needed) and for fusion devices like ITER (International Thermonuclear Experimental Reactor). Nevertheless, in nanotechnology, these media are useful in building nanostructured films or nanometer-size devices. Dust particles can be produced from reactive gases (silane and methane) or material sputtering injecting molecular precursors or solid bodies in the plasma. Molecular precursors coming from reactive gases or sputtering thus initiate a complex succession of chemical and physical reactions, leading to the growth of dust particles. As these dust particles are growing, they attach plasma electrons, leading to a disturbance of plasma equilibrium when the dust particle density is high [1]–[3].

In this paper, modifications of plasma emission and self-excited instabilities induced by the growing particles are visually analyzed. These experiments are performed in the PKE-Nefedov reactor [4] where dust particles are grown by sputtering a polymer layer exposed to a low-pressure radio-frequency (13.56 MHz) argon plasma. The capacitively coupled discharge is maintained by parallel electrodes of 4 cm in diameter separated by 3 cm. The typical pressure is about 1.4 mbar, and the injected power is 3.5 W. Plasma emission is recorded by using a standard color charge-coupled device camera at 25 frames/s. Simultaneously, the discharge current is monitored to identify the growing step and the occurring instability type.

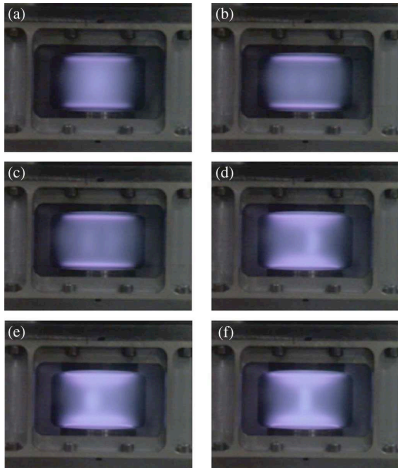

Fig. 1. Plasma emission evolution induced by the presence of dust particles: (a) 5 s after ignition (AI): No dust particles; (b) 1 min AI: Beginning of instabilities (striationlike) induced by the growing dust particles; (c) 2 min AI: Instabilities with increasing intensity; (d) 7 min AI: Plasma emission enhancement due to the presence of bigger dust particles; instabilities consist of a single enhanced emission region (void) rotating around the vertical axis of symmetry; (e) 15 min AI: Plasma emission enhancement and less off-centered rotation; and (f) 16 min AI: Centered void region with oscillating size.

Fig. 1 shows the plasma emission at different instants after plasma ignition. Fig. 1(a) has been taken 5 s after plasma ignition and is considered to be representative of a dust-free plasma as the growing kinetics is slow in our experimental conditions. This figure is thus our reference for the following discussion. It clearly shows the two presheath regions of enhanced emission and the plasma column. Fig. 1(b) corresponds to the beginning of self-excited instabilities induced by the high density of negatively charged dust particles [5] disturbing the plasma electrical equilibrium. These dust particle growth instabilities [1] are composed of a complex succession of well-defined phases. In Fig. 1(b), the instability is characterized by a striationlike behavior [1], [6], and two slightly brighter regions appear on both sides of the center. In this regime, bright regions appear alternatively in different places of the discharge. On electrical measurements, the instability signature corresponds to regular oscillations of a few tens of hertz. Even if the sampling rate of the camera is not sufficient to finely analyze this oscillation, it gives important information on plasma evolution as a major complement of electrical measurements. After this relatively regular regime, a chaotic phase occurs with bright regions appearing in a more erratic manner. This chaotic regime is partly characterized by a slight increase in the intensity of the bright regions, as shown in Fig. 1(c). This regime can last a few minutes and slowly tends toward a more and more ordered phase described by a single bright region that can be, at this stage, easily linked to a dust-free region called "void." This region, which can appear with or without precursory instability, is related to the competition of an inward electrostatic force and an outward ion drag force acting on dust particles. Once a clear void region exists in a dusty plasma, different kinds of instabilities are observed. In Fig. 1(d), taken around 7 min after plasma ignition, this void rotates around the vertical symmetry axis of the discharge. The void is clearly identifiable slightly on the right-hand side. The dust cloud at this instant is made of a high density of big dust particles (a few hundreds of nanometers). Their influence on the plasma is important and results in a strong increase of the plasma emission as observed in the void and above the presheath regions. The rotation slows down, and the rotation radius decreases [Fig. 1(e)]. Then, the enhanced emission void region stabilizes its position in the discharge center. At this time, another type of instability is able to disturb the plasma and the dust cloud. It consists of successive contraction and expansion of the void size [7] [Fig. 1(f)]. Due to its characteristic behavior, this instability has been named the "heartbeat" instability.

In this paper, we presented an easy visual indicator of the presence of a high dust particle density in a plasma. Changes in plasma emission intensity and appearance of self-excited instabilities easily detected by cameras are consequences of the drastic loss of free electrons to the dust particle surface.

Manuscript received November 28, 2007; revised February 4, 2008. This work was supported by the CNES under Contract 02/CNES/4800000059.

M. Mikikian, M. Cavarroc, Y. Tessier, and L. Boufendi are with the Groupe de Recherches sur l'Energétique des Milieux Ionisés, UMR6606, CNRS/Université d'Orléans, 45067 Orléans Cedex 2, France (e-mail: maxime.mikikian@univ-orleans.fr).

L. Couëdel is with the Groupe de Recherches sur l'Energétique des Milieux Ionisés, UMR6606, CNRS/Université d'Orléans, 45067 Orléans Cedex 2, France, and also with the School of Physics, A28, The University of Sydney, Sydney, N.S.W. 2006, Australia.

Color versions of one or more of the figures in this paper are available online at http://ieeexplore.ieee.org.

Digital Object Identifier 10.1109/TPS.2008.920946

This article has been accepted for inclusion in a future issue of this journal. Content is final as presented, with the exception of pagination.

ACKNOWLEDGMENT

The PKE-Nefedov chamber was made available by the Max-Planck-Institute for Extraterrestrial Physics, Germany, under the funding of DLR/BMBF under Grants No. 50WM9852.

REFERENCES

[1] M. Mikikian, M. Cavarroc, L. Couëdel, and L. Boufendi, "Low frequency instabilities during dust particle growth in a radio-frequency plasma," *Phys. Plasmas*, vol. 13, no. 9, p. 092 103, Sep. 2006.

[2] M. Cavarroc, M. C. Jouanny, K. Radouane, M. Mikikian, and L. Boufendi, "Self-excited instability occurring during the nanoparticle formation in an Ar-SiH_4 low pressure radio frequency plasma," *J. Appl. Phys.*, vol. 99, no. 6, p. 064 301, 2006.

[3] M. Cavarroc, M. Mikikian, G. Perrier, and L. Boufendi, "Single-crystal silicon nanoparticles: An instability to check their synthesis," *Appl. Phys. Lett.*, vol. 89, no. 1, p. 013 107, 2006.

[4] A. P. Nefedov *et al.*, "PKE-Nefedov: Plasma crystal experiments on the international space station," *New J. Phys.*, vol. 5, no. 3, pp. 33.1–33.10, 2003.

[5] L. Couëdel, M. Mikikian, L. Boufendi, and A. A. Samarian, "Residual dust charges in discharge afterglow," *Phys. Rev. E, Stat. Phys. Plasmas Fluids Relat. Interdiscip. Top.*, vol. 74, no. 2, p. 026 403, 2006.

[6] G. Praburam and J. Goree, "Experimental observation of very low-frequency macroscopic modes in a dusty plasma," *Phys. Plasmas*, vol. 3, no. 4, pp. 1212–1219, Apr. 1996.

[7] M. Mikikian, L. Couëdel, M. Cavarroc, Y. Tessier, and L. Boufendi, "Self-excited void instability in dusty plasmas: Plasma and dust cloud dynamics during the heartbeat instability," *New J. Phys.*, vol. 9, no. 8, p. 268, 2007.

D.2 Publications related to Chapter 5

- Mikikian, M.; Couëdel, L.; Cavarroc, M.; Tessier, Y. & Boufendi, L., "Self-excited void instability in dusty plasmas: plasma and dust cloud dynamics during the heartbeat instability", New J. Phys., **9**, 268 (2007)
- Mikikian, M.; Cavarroc, M.; Couëdel, L.; Tessier, Y. & Boufendi, L. "Mixed-Mode Oscillations in Complex-Plasma Instabilities" Physical Review Letters, **100**, 225005 (2008)

New Journal of Physics
The open–access journal for physics

Self-excited void instability in dusty plasmas: plasma and dust cloud dynamics during the heartbeat instability

M Mikikian, L Couëdel, M Cavarroc, Y Tessier and L Boufendi
GREMI, Groupe de Recherches sur l'Energétique des Milieux Ionisés,
UMR6606, CNRS/Université d'Orléans, 14 rue d'Issoudun,
BP6744, 45067 Orléans Cedex 2, France
E-mail: maxime.mikikian@univ-orleans.fr

New Journal of Physics **9** (2007) 268
Received 30 March 2007
Published 15 August 2007
Online at http://www.njp.org/
doi:10.1088/1367-2630/9/8/268

Abstract. When a three-dimensional dust cloud is present in a plasma, a dust-free region, called a void, is usually obtained in the plasma centre. Under certain conditions, this region exhibits a self-excited unstable behaviour consisting of successive contractions and expansions of its size. In this paper, this low frequency instability (few Hz), called a 'heartbeat', is characterised by various diagnostics. Electrical and optical measurements both correlated with high speed imaging brought to the fore the main features of this instability. Forces involved in the void existence are an inward electrostatic force and an outward ion drag one. The force balance ensures an open void but this equilibrium can be disturbed, leading to the observed instabilities. As these forces are strongly dependent on local ionisation conditions, correlations between physical processes in the plasma volume and the dust cloud motion are investigated through experimental results.

PII: S1367-2630(07)47353-0

Contents

1. Introduction

Dusty plasmas are relatively complex systems where new phenomena arise from the presence of solid dust particles trapped inside the plasma. Usually, this trapping is a consequence of the negative charge acquired by the dust particles [1]–[6] immersed in a medium partly composed of free electrons. The full dust particle dynamics is then described by charge dependent forces (mainly electric and ion drag forces) and other ones like gravity, neutral drag and thermophoresis. Relative amplitudes of these forces are strongly dependent on the dust particle size. In the micrometre range, dust particles are usually directly injected in the plasma volume. Their weight is non-negligible and some phenomena are only observed under microgravity conditions [7, 8]. Nevertheless, their big size allows an easy and precise visualisation in laboratory experiments. In the submicrometre range, dust particles are usually grown in the plasma using methods based on reactive gases or material sputtering.

Reactive gases are used due to their ability to form dust particles by following a rather complicated succession of growth phases. One of the most studied and well-known reactive gas is silane (SiH_4) [9]–[15]. The interest for silane based chemistry is mainly due to its implication in microelectronics and/or nanotechnology. Indeed, in the late 1980s, dust particle formation in the gas phase has been evidenced in reactors used for silicon based device fabrication [9, 16]. In some processes, cleanliness is a major requirement and a lot of studies began for understanding dust particle formation and growth in order to avoid their deposition. More recently, silicon nanocrystal formation [17] became of high interest for their incorporation in thin films in order to improve their properties. Indeed, their use in solar cell technology enhances optoelectronic properties of deposited films [18]. Single electron devices (SED) like transistors [19] or memories [20] can also be built, thanks to these silicon nanocrystals. Dust particle formation in hydrocarbon based gases like methane (CH_4) [21]–[23] or acetylene (C_2H_2) [21, 22, 24, 25] has also been studied. Indeed, CH_4 and C_2H_2 are used for deposition

of diamond-like carbon (DLC) films [26] or nanocrystalline diamond [27] used in industry for their unique properties like extreme hardness. Hydrocarbon gases are also of great interest for the astrophysical community dealing with planet atmospheres like Titan, where dust particles are created from a mixture of methane and nitrogen [28].

Another process for dust particle production is material sputtering [29]–[32]. This phenomenon can appear in industrial reactors and also in fusion devices [33] like Tore Supra [34] where graphite walls can be severely eroded by ion bombardment. Produced dust particles can strongly limit performances of the fusion plasma. This aspect is of great importance for the future ITER reactor.

Dust particles levitating in the full plasma volume can be obtained under microgravity (for micrometre dust particles) or in the laboratory (for submicrometre dust particles). Usually, the three-dimensional dust cloud exhibits a specific feature consisting of a centred egg-shaped region free of dust particles. This region, called a 'void' [7, 31, 32], [35]–[47], seems to be controlled by an equilibrium between the charge dependent forces (inward electrostatic and outward ion drag forces). This stable state is sometimes disturbed and void size oscillation can occur. This self-excited instability is named the 'heartbeat' instability [36, 46, 48, 49]. It has been previously observed during microgravity experiments with injected micrometre dust particles and has since also been studied in the laboratory with grown submicrometre dust particles [49]–[52]. In these last experiments, investigations of the heartbeat instability have been performed using both electrical and spatially resolved optical diagnostics. These measurements allowed to identify complex behaviours in recorded signals roughly related to dust particle motion. Furthermore, the threshold behaviour of this self-excited instability has been brought to the fore [51, 52]. Nevertheless, the presence of a sharp peak in electrical measurements and its absence in optical ones was still unclear. Further investigations have been conducted using high speed imaging to record dust particle cloud motion. These preliminary results gave first insights concerning dust cloud motion and void size evolution correlated with electrical signals [51, 52]. In the present paper, new results on the heartbeat instability are obtained thanks to a second high speed imaging experiment. Behaviour of both dust cloud and plasma glow is investigated and correlations between both types of data are deduced. These results are compared to electrical measurements and previous spatially resolved optical ones. The void dynamics during the instability is now better characterised and, for example, the sharp peak presence can be correlated with plasma glow changes.

2. Experimental set-up

2.1. Reactor

Experiments are performed in the Plasma Kristall Experiment (PKE)-Nefedov chamber [8, 32]. The plasma is produced by a capacitively coupled radio frequency (rf) discharge operating in push–pull mode at 13.56 MHz. The planar parallel electrodes are 4 cm in diameter and are separated by 3 cm. In this chamber, argon is introduced to a typical pressure of 1.6 mbar and the plasma is ignited with a rf power of typically 2.8 W. Dust particles are grown by sputtering a polymer layer deposited on the electrodes and constituted of previously injected melamine formaldehyde dust particles.

2.2. Diagnostics

Grown dust particles are observed by laser light scattering using a thin laser sheet produced by a laser diode at 685 nm and three standard charge coupled device (CCD) cameras (25 frames per second) equipped with narrow-bandwidth interference filters. Two of these cameras record the scattered light at 90° with different magnifications. The third one looks at the cloud with an angle lying approximately between 20° and 30° with respect to the incident laser direction. This camera allows the observation of grown dust particles when their size is too small to observe them at 90°.

Plasma and dust particle cloud behaviours are strongly linked and a modification in one of these media is usually reflected in the other. Therefore, diagnostics able to analyse both systems are used in order to better characterise the heartbeat instability.

The first one consists of the measurement of the time evolution of the amplitude of the discharge current fundamental harmonic. Indeed, this diagnostics is representative of global changes in plasma properties and can be related to electron density variations. It allows to monitor the total current during the various phases of the instability very easily. Thus, it is used as our reference diagnostics. It shows that the heartbeat instability has different signatures depending on the pressure, power and dust particle density [49].

The second diagnostics is based on spatially resolved optical measurements performed in two different ways. The time evolution of either the intensity of an argon line or the total plasma light is recorded in different plasma regions. For the total plasma light recording, five optical fibres are horizontally aligned (separated by 5 mm) with a spatial resolution of about 3 mm. This diagnostic is complementary to the electrical one because it can detect any plasma motion or local behaviours that cannot be evidenced by a global measurement.

The third diagnostics consists of high speed imaging. The observed instability oscillates at relatively low frequencies (10–200 Hz) but too high to be finely characterised by standard CCD cameras at 25 frames per second. Indeed, as previously observed [49], some features of the instability, like the sharp peak, take place during a typical time scale of about 1 ms. A high speed video camera system with 1789 frames per second (Mikrotron MC 1310) is used to observe either the plasma glow or the dust cloud. Thus, two successive frames are separated by around 560 μs. For the last observation, the high speed camera takes the place of the third standard CCD camera in order to record more light scattered by the dust cloud.

As already mentioned, the heartbeat instability has different signatures and measurements show a wide variety of frequencies and shapes. In the following sections, both dust cloud and plasma glow will be analysed in two different cases considered as sufficiently different to cover a wide range of experimental observations: a low repetition rate one (contraction–expansion sequences are well separated and original conditions, i.e. stable void, are nearly restored between each sequence) and a high repetition rate one (continuous motion of the void). The high repetition rate occurs when the instability is well established (higher values of injected rf power) whereas low repetition rate occurs at lower powers when the instability tends to slow down before stopping. Plasma glow will be mainly discussed through its intensity (thus 'glow intensity' is referred as 'glow' in the following), except when spatial concerns are well specified. Following results will mainly concern the fully developed instability. Another interesting phenomenon, consisting of failed contractions [51, 52] appearing near the instability existence threshold, will be analysed in a further article.

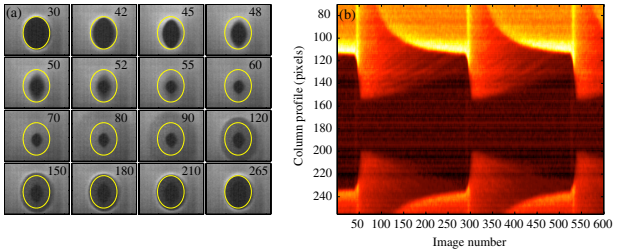

Figure 1. Heartbeat instability for a low repetition rate observed on the dust cloud. (a) Some images of the void region during one contraction–expansion sequence. The yellow ellipse delineates position of the stable open void. (b) Time evolution of central column profile (vertical line passing through the void centre) constructed from the entire video in false colours (from dark red to bright yellow) (see also movie 1, 3.9 MB MPEG).

3. Dust cloud and plasma glow behaviours near the void region

In order to characterise the heartbeat instability, a first approach consists of a direct visualisation of the void with its surrounding dust cloud. Typical unstable voids have a size of about a few millimetres. Beyond a certain size, voids are usually stable and no instability has been observed in the explored parameter range. Indeed, in this case, their stability is not disturbed even by decreasing the pressure or increasing the power (these changes are known to be able to initiate the heartbeat instability [49]).

3.1. Sequences with a low repetition rate

A video corresponding to a low repetition rate and showing three successive contraction–expansion sequences is available in figure 1. Some extracted images from the first sequence are shown in figure 1(a). Image aspect ratio is distorted due to the view angle compressing the horizontal direction. Image numbers appear on the top right part of each image. The drawn ellipse represents the position of the stable open void determined from image 30. Small but detectable motion starts at image 40 (not shown) and clearly appears at image 42 where dust cloud boundaries are clearly inside the drawn ellipse. Contraction lasts up to image 55 where the void reaches its minimum size. From this instant, the empty inner part slowly increases in size while a light grey corona region (i.e. lower dust density region) starts to be detected in image 80 and slowly reduces in size. These two regions meet and the stable open void state is nearly reached anew in image 265.

In order to better depict this contraction–expansion sequence, the time evolution of a column profile is shown in figure 1(b). To construct this false colour image, the vertical line passing through the void centre is extracted from each video image. Time is represented by image number in the x-axis and column profile is given in the y-axis. Using the video as a reference, this representation is of interest in that it gives in one single image a clear

characterisation of the instability in both time and space. Low dust density regions appear dark while high dust density ones appear bright. Three contractions and two expansions are clearly evidenced and give a frequency of about 7 Hz. For the first sequence, images 1–40 show the higher dust density region usually observed in the void boundaries. Then, the contraction takes place and the void reaches its minimum size approximately 2.5 times smaller than the stable void size. At this moment, the two previously described phenomena (size increase of the dark inner part and size decrease of an intermediate grey corona region) are well resolved in time. The regular size increase of the inner part can be directly correlated to the void size increase assuming that the term 'void' stands for the null dust density region. From figure 1, the behaviour of the corona region seems to correspond to the motion of dust particles attracted to the plasma centre during the contraction and going back to their original stable position. This motion is characterised by a moving boundary between a region of high dust density and another one of low dust density. It appears that the speed of this moving boundary decreases as it approaches the original void position. The dust particles which are the closest to the centre, react last with the smallest speed. Furthermore, the corona region in its maximum extension is larger than the size of the stable void indicating that the instability affects the dust cloud over a long distance and not only in the close vicinity of the void. Collective motions can take place on long distances due to the strong interaction between dust particles and their strong coupling with plasma changes. Finally, figure 1(b) shows that inner and corona regions meet (around image 280) and the high dust density boundaries are restored just before another contraction occurs.

To complete these observations, the interference filter is removed from the high speed camera in order to record plasma glow evolution without changing the camera position. The obtained image series is acquired approximately 2 s after the one presented in figure 1, checking that the instability does not change neither in frequency nor in shape. In order to synchronise dust cloud images with plasma glow ones, small residual plasma glow signal passing through interference filter is used (slightly visible in figure 1(b) in the black inner part of the void but not allowing analysis). Electrical measurements are used to check that instability characteristics remain unchanged. Typical images are presented in figure 2(a). In order to bring out changes, a reference image is subtracted and false colours are used. Plasma glow images shown in figure 2(a) correspond to the dust cloud ones shown in figure 1(a). For comparison, the same ellipse as in figure 1(a) is superimposed on the glow images. By correlating both dust cloud and glow images, it clearly appears that the void contraction seems to correspond to a glow enhancement in the plasma centre. Intermediate images of the glow variation are shown in figure 2(b). It appears that the concerned plasma region is bigger than the original void region even if maximum glow values are inside the void. This aspect can explain why the light grey corona region observed in figure 1 has a maximum extension bigger than the stable void. In fact, the first image showing the glow increase is image 10 in figure 2(b), where the bright region is already bigger than the drawn ellipse. Due to camera speed limitation, some data are missing between images 9 and 10. Consequently it cannot be concluded if, at the early beginning, the enhancement is bounded by the void and then propagates, or if it concerns directly a bigger size region. After reaching its maximum value (around image 13), plasma glow decreases and reaches a minimum below the mean glow value (darker image 19 in figure 2(a)). Certainly due to dust particle inertia, the void continues to shrink (figure 1(a)) but when the central glow (i.e. ionisation and consequently ion drag force) starts to increase slowly (from image 26 in figure 2(a) corresponding to image 55 in figure 1(a)), the contraction stops and expansion occurs.

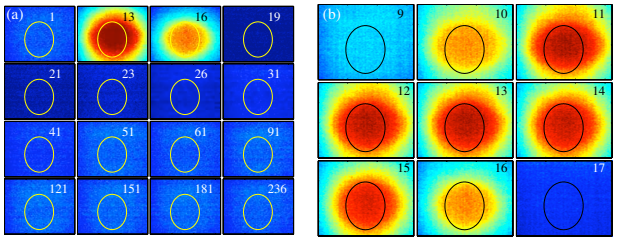

Figure 2. Heartbeat instability for a low repetition rate observed on the plasma glow. (a) Some images of the void region (in false colours from dark blue to red) during one contraction–expansion sequence (image 1 corresponds to image 30 of figure 1 and so on). The yellow ellipse delineates position of the stable open void. (b) Intermediate images of (a) during fast plasma glow modifications.

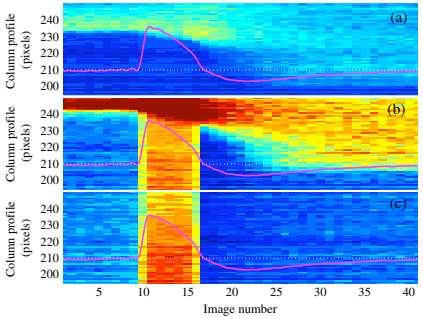

Figure 3. Heartbeat instability for a low repetition rate: electrical measurements superimposed on column profiles from (a) only dust cloud; (b) dust cloud and plasma glow, (c) only plasma glow. Parts (a), (b) and (c) in false colours (from dark blue to red).

Column profiles of these different series can be compared. Figure 3 shows synchronised profiles obtained from videos showing (a) the dust cloud (laser and camera with interference filter), (b) dust cloud and glow (laser and camera without interference filter) and (c) plasma glow (neither laser nor interference filter). Electrical measurements are superimposed with their mean value (dotted line) corresponding to the stable open void. In figure 3(c) it appears that there is a good correlation between plasma glow and electrical measurements as the main variations are related. The fast signal increase corresponds to glow enhancement. It is followed by a decrease in both sets of data. A small shoulder appearing in electrical measurements (slope change) is

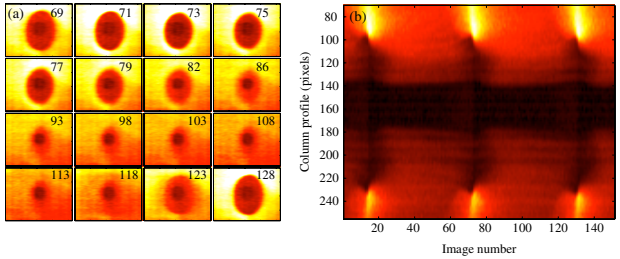

Figure 4. Heartbeat instability for a high repetition rate observed on the dust cloud: (a) some images of the void region (in false colours from dark red to bright yellow) during one contraction–expansion sequence; (b) time evolution of central column profile constructed from the entire video (see also movie 2, 2.3 MB).

related to a more drastic decrease of the central plasma glow. Then, the following minimum values of both data are close in time. After this point, the next plasma glow increase towards the mean state is well observed in electrical measurements slowly tending towards the mean value. As mentioned, global variations are similar but some discrepancies exist due to the fact that electrical measurements are integrated on all the plasma volume, and contain information on plasma variation occurring outside the plasma centre. This aspect will be explored in section 4, where a precise analysis of the entire plasma glow is performed. Concerning the dust cloud, the void contraction is related to glow and electrical signal increase (figures 3(a) and (b)), meaning that it corresponds to ionisation increase in the plasma centre. Nevertheless, it can be observed that contraction continues even when the electrical signal starts decreasing and is still not stopped when electrical measurements and plasma glow are below their original value. It confirms the direct comparison between dust cloud and plasma glow performed through figures 1 and 2.

3.2. Sequences with a high repetition rate

Analysis of a high repetition rate sequence is more fussy due to the fast and constant motion of the dust cloud without any clear stable position giving a fixed reference. A movie is available in figure 4 and in the same way as in the low repetition rate case, extracted images and column profile are given respectively in figure 4(a) and (b). In order to increase contrast, false colours are also used for extracted images. The constant motion clearly appears: no horizontal bright regions, corresponding to high dust density void boundaries, are observed in figure 4(b). This figure gives a frequency instability of about 31 Hz. Furthermore, the inner part of the void region, which is never filled with dust particles, exhibits only small variations. Indeed, all the motion takes place in the low dust density region between the dense dust cloud and the void inner part. From the nearly isolated case (figure 1), this region has been identified to consist of dust particles going back to their original position. In the high repetition rate case, the new

contraction occurs while dust particles from the previous contraction are still inside the void and try to reach their original position. Indeed, a new contraction starts around image 69 of figure 4(a) (complex motions do not allow precise determination) while dust particles are still inside the void region. At this time the plasma glow is close to its maximum value in the centre (determined from a plasma glow video correlated to the present one). This complex behaviour leads to the relatively constant regions (black inner part and grey intermediate part) observed in figure 4(b). The dust cloud is always moving even so spatial dust density appears more or less constant.

3.3. Asymmetry in void contraction

Another interesting phenomenon concerning dust cloud motion during the heartbeat instability, is the observable delay appearing in the response of horizontal and vertical directions. Indeed, in some conditions (currently not clearly defined) the dust cloud shrinks horizontally before shrinking vertically [51, 52]. As an example, a record containing both dust cloud and plasma glow information has been performed for a sequence where a stable open void suddenly starts a size oscillation. First and second contraction–expansion sequences are shown in figure 5 where a movie can also be found. Image 135 clearly shows the stable open void with the corresponding drawn ellipse. In image 142 plasma glow starts increasing and reaches its maximum value at 144. In this last image, it appears that the plasma glow enhancement affects a region bigger than the void size and correlation with the corona region well observed in figure 1 can be suggested again. This hypothesis is correct assuming that the intensity increase in the surrounding dust cloud is entirely due to plasma glow changes and not due to any dust density modification. Thanks to the drawn ellipse, it clearly appears that the void shrinks first in the horizontal direction (starting from image 143) and then in the vertical one (starting around image 147). As images are already compressed in the horizontal direction, a detectable motion in this direction clearly indicates a real dust cloud response and cannot be an optical illusion. The plasma glow reaches its minimum value in image 148 and, as already observed, the void continues to shrink to its minimum size in image 155. From this point, the void inner part slowly increases in size and the grey intermediate region, constituted of dust particles going back to their original position, becomes gradually visible. The next contraction occurs before the original state has been completely reached again (image 241).

These various steps are well observed on the column profile shown in figure 6(a). For better understanding, temporal evolution of plasma glow in the central pixel of the void is superimposed at the bottom of the image. The stable open void is accurately defined with its constant size and its high dust density boundaries (between images 100 and 142). When plasma glow increases, the void shrinks. Its minimum size is reached while plasma glow in the centre has already reached its minimum value and has started to slowly increase again. Then, the glow stays relatively constant in the void centre while dust particles are expelled to their original position. It clearly appears that the void did not reach its original size when the new glow increase occurs. This effect is traduced, firstly by the dark inner part which does not rejoin the position of the stable void and secondly by the intermediate corona region which is bigger than the original void size. This last point means that the 'wave front' formed by returning dust particles is still moving towards the original void boundaries. The speed of this wave front appears to slow down when approaching the original conditions. Furthermore, it is clearly visible that the instability is in a setting up phase. Indeed, starting from a stable open void,

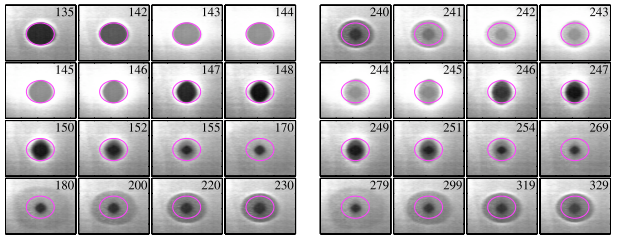

Figure 5. Simultaneous record of dust cloud and plasma glow in the void region during the setting up of the heartbeat instability. From image 135: stable open void (delineated by a pink ellipse) followed by a first contraction, and new contraction at image 241 while original conditions are not restored (see also movie 3, 2.6 MB).

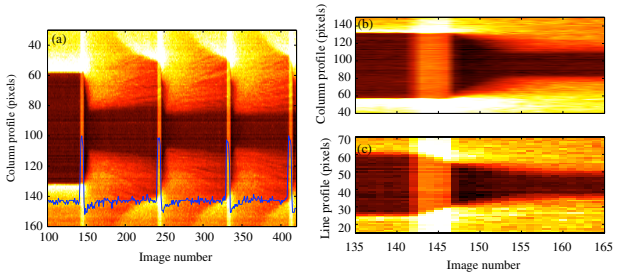

Figure 6. (a) Column profile (in false colours from dark red to bright yellow) calculated from image series presented in figure 5 with central plasma glow evolution superimposed (blue curve corresponding to line 95 of figure 6(a)), (b) zoom of (a), (c) corresponding line profile.

the characteristics of first and second contraction–expansion sequences are slightly different in terms of minimum void size and re-opening time duration. Concerning the time delay appearing in the vertical direction (as observed in figure 5) it can also be evidenced by comparing column and line profiles extracted from the video. These two profiles are shown respectively in figures 6(b) and (c). Previous results also showed that some correlation can be found between the different times of collapse and different slopes in electrical measurements [52]. Reasons why this effect appears in some cases are unclear due to a lack of statistics and spatiotemporal limitations of video acquisition. Nevertheless, one possible explanation is related to reactor geometry where confining conditions are different in the two directions. The electrode diameter is around 4 cm and glass boundaries are at approximately 3 cm of the electrode edges.

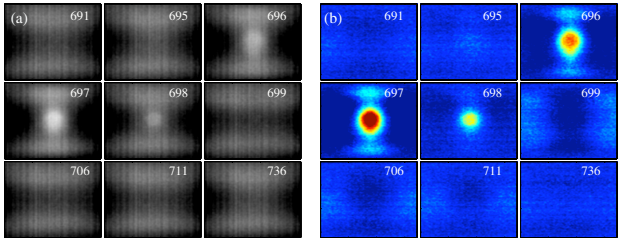

Figure 7. Heartbeat instability for a low repetition rate observed on the total plasma glow: (a) some images in true colours during one contraction–expansion sequence, (b) same images as in (a) with post-processing and false colours (from dark blue to red).

Consequently, the plasma usually extends beyond the electrodes towards the lateral sides. The plasma width is then nearly twice as large as the height and it is nearly the same for the trapped dust cloud and the void. No strong electrostatic barrier exists due to the distance to the glass boundaries, thus, plasma and void modifications in these directions are relatively free. On the contrary, the electrodes imposed a strong electrostatic barrier and vertical modifications and motions are then drastically controlled by the sheaths.

4. Plasma glow behaviour in the whole discharge

Plasma glow in the whole interelectrode volume is recorded during the instability in the two different cases (low and high repetition rate). This analysis is performed in order to understand global evolution of the plasma and not only central part behaviour as in the previous section. It can identify some side effects already suggested (relation between a sharp peak in electrical measurements and brighter glow regions near plasma horizontal boundaries [49, 51]) and that are inaccessible through the analysis presented in section 3.

4.1. Sequences with a low repetition rate

The total plasma glow recorded by fast imaging during a contraction–expansion sequence is shown in figure 7(a). Both bright presheath regions are clearly evidenced on the upper and lower parts of the images (electrodes are not visible). Before the contraction–expansion sequence (stable situation with an open void), the central plasma region is relatively uniform and not very bright (image 691). Then, the glow increases fast and concentrates in the discharge centre before disappearing and leaving a darker region in the centre as observed in the previous section. This scheme is better evidenced by representing the same images in false colours and by subtracting a reference image (stable situation) as shown in figure 7(b). The relatively homogeneous glow (image 691) changes into a bright (i.e. higher ionisation) central region and dark (i.e. lower ionisation) edges during the contraction (image 697). A reverse situation (dark centre and bright

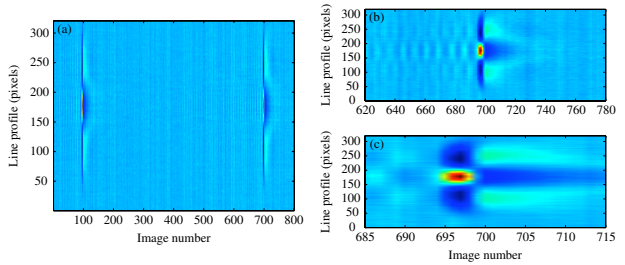

Figure 8. (a) Line profile (in false colours from dark blue to red) calculated from the image series presented in figure 7; (b) and (c) are different magnifications of (a).

edges) starts just before the re-opening (image 699). Then, the glow becomes slowly uniform again (image 736).

Time evolution of a line profile is presented in figure 8(a) and magnified in figures 8(b) and (c). To construct this false colour image, the horizontal line passing through the middle of the discharge is extracted from each video image. This line has been chosen because it passes through the region of biggest changes. In order to extract changes occurring during the instability, a temporal average value is subtracted. A smoothing filter is also applied for noise reduction and better delimitation of changing regions. Column profiling has also been performed for the plasma glow analysis but no original information has been extracted partly due to the limiting conditions imposed by electrodes.

Nearly isolated contraction–expansion sequences often have a short time duration. Figure 8 shows an instability frequency of about 3 Hz. In between each sequence, original conditions have time to be restored. From figures 8(b) and (c), plasma glow behaviour is well observed and its complete evolution analysis is more easily performed than from direct images like in figure 7. First, some small oscillations are observed before the real sequence. This phenomenon has already been observed [51, 52] and corresponds to failed contractions appearing sometimes near the instability existence threshold. This behaviour does not change the following analysis and will be described in a future article. Figure 8 confirms that when the void contracts, the plasma glow suddenly concentrates in the centre leaving dark border regions. The void re-opening occurs during the reverse situation with two symmetrical bright regions surrounding the plasma centre. Then, these regions seem to diffuse slowly to the centre until a homogeneous glow is obtained once again.

In the previous section, only the central part of the plasma was observed when the interference filter was removed. Indeed, the observed region was too small and due to the viewing angle, out of focal plane information was lost. The whole plasma recording allows to identify the dark (during contraction) and bright (during expansion) plasma edge regions. These observations show that the increase of plasma glow in the centre is really a concentration of the plasma towards the centre at the expense of the plasma edges. After that, the reverse situation occurs with plasma edges brighter than in the stable void situation.

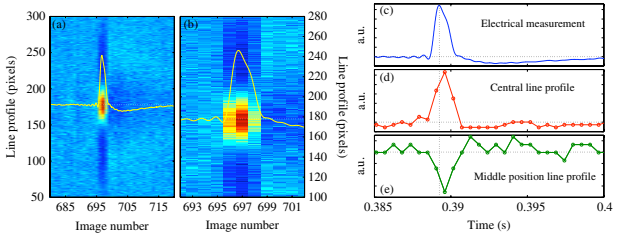

Figure 9. (a) Line profile (in false colours from dark blue to red) calculated from the image series presented in figure 7 with electrical measurements superimposed; (b) zoom of (a); (c) electrical measurements; (d) central line (line 178) profile of (a); (e) middle position line (line 105) profile of (a).

Correlation with electrical results is presented in figures 9(a) and (b) with non smoothed images in order to get pixel precision. The dotted curve is the current continuous component. From this superimposition it can be deduced that the contraction corresponds to an increase in the global ionisation (i.e. electron density). Indeed, increase of central plasma glow corresponds to an increase of electrical signal amplitude meaning that this central increase is not compensated by the decrease in the near plasma edge. Then, when the reverse situation occurs, ionisation appears to be below the stable situation value (as indicated by electrical measurements). Indeed, the dark central region is not balanced by the larger but slightly brighter near edge regions. Finally, these regions tend to rejoin in the centre following the slow increase observed in electrical measurements. These behaviours are also visible by comparing electrical measurements with line profiles (figures 9(c)–(e)) extracted from figure 9(a) (not to be confused with temporal evolution of line profile extracted from video images) and physically corresponding to the time evolution of individual pixels taken in (d) plasma centre and in (e) the near edge.

4.2. Sequences with a high repetition rate

When the heartbeat instability frequency increases, contraction–expansion sequences are closer in time, and no exact return to original stable conditions is achieved. Indeed, the next sequence happens while the void size has not reached its stable state. The case presented here is quite similar to the one shown in figures 5 and 6. The corresponding video is presented in figure 10 showing three successive contraction–expansion sequences. Images extracted from one sequence appear in figure 10(a). Figure 10(b) is obtained from figure 10(a) in the same way as figure 7(b). As the sequence lasts longer, better time resolution is obtained and variation of plasma glow is well evidenced. In comparison with the low repetition rate case, the change from bright centre and dark edges to the reverse is here more strongly marked. The different phases of the contraction–expansion sequence that have been already described, are highly visible here.

The deduced line profile is very significant and summarises nearly all results concerning plasma glow evolution during the heartbeat instability (figure 11). Indeed, starting from a void

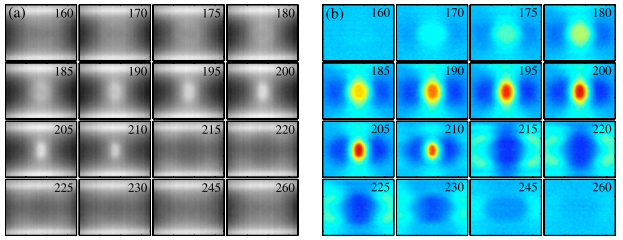

Figure 10. Heartbeat instability for a high repetition rate observed on the total plasma glow: (a) some images in true colours during one contraction–expansion sequence; (b) same images as in (a) with post-processing and false colours (from dark blue to red) (see also movie 4, 2.7 MB).

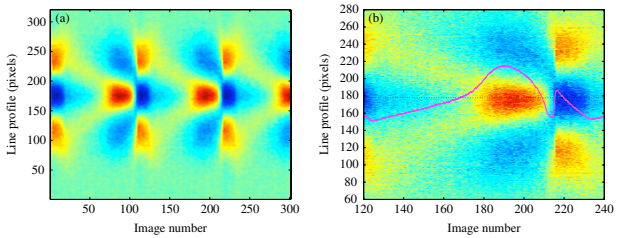

Figure 11. (a) Line profile (in false colours from dark blue to red) calculated from image series presented in figure 10; (b) zoom of (a) with electrical measurements superimposed.

expansion (dark inner part and bright plasma edges), slow concentration of the glow from the plasma edge towards the centre takes place. This motion can be correlated to the grey corona region observed in the dust cloud and presented in section 3. Furthermore, it clearly appears that the two brighter edge regions do not meet completely and no homogeneous plasma is restored as in figure 8. Indeed, the central glow increases at the expense of plasma edges before the brighter glow regions fully converge towards the plasma centre. This central enhancement is then followed by a strong and fast reversal. Electrical measurements are superimposed on the line profile in figure 11(b). The bright region moving from the plasma edge towards the plasma centre corresponds to a continuous increase of the current. Then, it appears that the strong brightness reversal is related to the presence of a sharp peak in the current. Measurements without peak certainly correspond to cases where the brightness reversal between plasma centre and edges exists, but is not strongly marked (figure 9). This sharp peak is an interesting feature already observed but not fully explained. Indeed, in [49], preliminary results suggested that this peak could be correlated to a strong glow decrease in the centre and increase in the

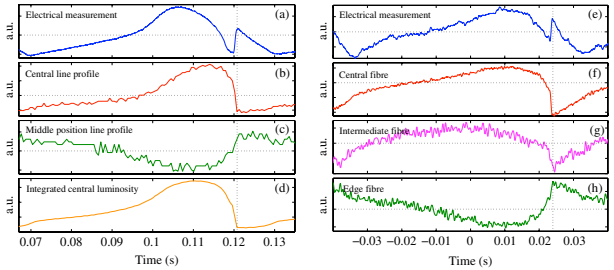

Figure 12. Extracted data from figure 11: (a) electrical measurements; (b) central line profile; (c) line profile in the glow reversal region. (d) Plasma glow integrated on a small central volume from complete image series of figure 10. Previous measurements in similar conditions for (e) electrical measurements; (f) light recorded by a centred optical fibre; (g) intermediate fibre; (h) edge fibre (same observed region as (c)).

plasma edge. These measurements were performed thanks to a spatially resolved (four different positions) analysis of an argon line emission at 750.4 nm. Further results with five optical fibres (also used for characterisation of dust particle growth instabilities [53]) and integrating all plasma wavelengths gave similar results [51] but no complete description was available. Present results greatly enhance spatiotemporal resolution of this phenomenon and clearly correlate the sharp peak with an enhancement of the plasma glow outside the central region. Variations of electrical measurements are representative of global changes of the plasma (spatially integrated measurement). From the present analysis it appears that electrical measurements are not only dominated by the plasma core.

These effects are also evidenced in figure 12 by direct comparison of (a) electrical measurements, with data extracted from figure 11: (b) central line profile (i.e. physically corresponding to central pixel variation), (c) middle position line profile (i.e. variation of a pixel in the glow reversal zone) and from the video in figure 10: (d) integrated central luminosity (i.e. variation integrated in a small centred volume assumed to represent plasma core). Comparison of figure 12(a), (b) and (d) shows that the main central plasma changes are observed in electrical measurements. Nevertheless, it appears that the maximum value of central glow occurs while electrical measurements have already decreased. In fact, at this time, electrical measurements are affected by the edge plasma glow decrease as observed in figure 12(c). Finally, the sharp peak region is well understood thanks to figure 11(b) and figure 12(a)–(d). Opposite behaviour of electrical measurements and central glow is directly related to the strong and fast enhancement of plasma edges while the centre becomes the less luminous part.

In order to show consistency of the new results, previous measurements performed in similar instability conditions (i.e. similar electrical measurements) with the optical fibre diagnostics, are presented in figure 12(e)–(h). Here, the edge fibre (figure 12(h)) observes the region corresponding to the middle line profile of figure 12(c). The intermediate fibre observes

a region in between the centre and the edge. Its maximum value appearing before the one of figure 12(f) traduces the plasma concentration towards centre. Main features concerning the sharp peak region are observed: the peak corresponds to a glow reversal between the centre and the edge. This comparison is of major interest because it confirms that no artefacts, neither in the way measurements are performed nor in data retrieval from images, are implied for explanation of the sharp peak region.

5. Discussion and conclusion

From the different analyses, several features of the heartbeat instability can be brought to the fore: the void contraction corresponds to an increase of the central plasma glow. These observations tend to show that a sudden higher ionisation in the plasma centre enhances the ratio between the inward electrostatic force and the outward ion drag force. Then, the void centre becomes darker but dust particles continue to move towards the centre due to their inertia. Their motion seems more or less continuous (at relatively constant speed) and is stopped suddenly (see for example figure 1). The void is not entirely filled by dust particles meaning that a force prevents further motion towards its centre. This force also exceeds gravity that should induce void collapse by acting on, among others, dust particles constituting the upper part of the void. At this time the central glow is not very bright. Furthermore, it appears more or less homogeneous, a property usually associated with a weak electric field. The force stopping dust particles is then supposed to be the ion drag.

Dust particles located near the plasma centre are then nearly immobile while a dust particle 'wave front' coming from the plasma edge starts to be detected. At this time, a corona region of higher ionisation is observed in plasma glow images. This region surrounds the plasma centre and moves slowly towards it. Correlating dust cloud images with plasma glow ones, this moving region seems to correspond to the dust particle wave front. Darker centre and brighter edge can create an outward electrostatic force near the corona region. This hypothesis is assumed by analogy with the contraction phase when an enhanced glow region attracts dust particles. Thus, central dust particles are immobile (far from this interface) and the wave front corresponds to dust particles close to the corona region and moving towards it. As dust particles move, local conditions change and the corona region moves towards the centre attracting inner dust particles one after the other. As the plasma becomes more and more homogeneous, the wave front speed decreases and the last dust particles to move are finally the closest to the plasma centre.

In the case of low repetition rate sequences, the original stable position of the void is restored between each sequence that can be considered as isolated and independent. On the contrary, high repetition rate conditions lead to a continuous motion of the dust particles. Indeed, while central dust particles return to their original position, a new contraction occurs.

An asymmetry in void contraction has been evidenced in some cases. This behaviour can find its origin in the discharge geometry, confined by electrodes in the vertical direction and more free to diffuse in the horizontal one. It is confirmed by the observed corona region in plasma glow images. Indeed, it is better observed near the horizontal edges than near the vertical ones where it is merged with the bright presheath regions.

The sharp peak in electrical measurements can be associated with the glow reversal from bright centre and dark edges to bright edges and dark centre. It appears when this phenomenon is strongly marked. It is replaced by a change in signal slope in other cases. This reversal is very fast and our camera system does not allow to resolve this phenomenon in time. The optical

fibre diagnostics have a high time resolution but noise is relatively important and the data do not show if there is a wave propagation between centre to edge during the reversal. The reversal seems to be instantaneous and its physical origin is under investigation.

Acknowledgments

The PKE-Nefedov chamber has been made available by the Max-Planck-Institute for Extraterrestrial Physics, Germany, under the funding of DLR/BMBF under grants No. 50WM9852. We would like to thank S Dozias for electronic support and J Mathias for optical support. ESA and Kayser-Threde GmbH are acknowledged for providing the high speed camera system in the framework of the IMPACT programme. This work was supported by CNES under contract 02/CNES/4800000059.

References

[1] Walch B, Horanyi M and Robertson S 1994 *IEEE Trans. Plasma Sci.* **22** 97
[2] Melzer A, Trottenberg T and Piel A 1994 *Phys. Lett.* A **191** 301
[3] Arnas C, Mikikian M and Doveil F 1999 *Phys. Rev.* E **60** 7420
[4] Samarian A A and Vladimirov S V 2003 *Phys. Rev.* E **67** 066404
[5] Ratynskaia S *et al* 2004 *Phys. Rev. Lett.* **93** 085001
[6] Couëdel L, Mikikian M, Boufendi L and Samarian A A 2006 *Phys. Rev.* E **74** 026403
[7] Morfill G E, Thomas H M, Konopka U, Rothermel H, Zuzic M, Ivlev A and Goree J 1999 *Phys. Rev. Lett.* **83** 1598
[8] Nefedov A P *et al* 2003 *New J. Phys.* **5** 33
[9] Roth R M, Spears K G, Stein G D and Wong G 1985 *Appl. Phys. Lett.* **46** 253
[10] Watanabe Y, Shiratani M, Kubo Y, Ogawa I and Ogi S 1988 *Appl. Phys. Lett.* **53** 1263
[11] Bouchoule A, Plain A, Boufendi L, Blondeau J P and Laure C 1991 *J. Appl. Phys.* **70** 1991
[12] Howling A, Hollenstein C and Paris P J 1991 *Appl. Phys. Lett.* **59** 1409
[13] Bouchoule A, Boufendi L, Hermann J, Plain A, Hbid T, Kroesen G, Stoffels E and Stoffels W W 1996 *Pure Appl. Chem.* **68** 1121
[14] Boufendi L, Gaudin J, Huet S, Viera G and Dudemaine M 2001 *Appl. Phys. Lett.* **79** 4301
[15] Cavarroc M, Jouanny M C, Radouane K, Mikikian M and Boufendi L 2006 *J. Appl. Phys.* **99** 064301
[16] Selwyn G S, Singh J and Bennett R S 1989 *J. Vac. Sci. Technol.* A **7** 2758
[17] Cavarroc M, Mikikian M, Perrier G and Boufendi L 2006 *Appl. Phys. Lett.* **89** 013107
[18] Roca i Cabarrocas P, Gay P and Hadjadj A 1996 *J. Vac. Sci. Technol.* A **14** 655
[19] Dutta A, Lee S P, Hayafune Y, Hatatani S and Oda S 2000 *Japan. J. Appl. Phys.* **39** 264
[20] Dutta A, Hayafune Y and Oda S 2000 *Japan. J. Appl. Phys.* **39** L855
[21] Deschenaux C, Affolter A, Magni D, Hollenstein C and Fayet P 1999 *J. Phys. D: Appl. Phys.* **32** 1876
[22] Hong S, Berndt J and Winter J 2003 *Plasma Sources Sci. Technol.* **12** 46
[23] Pereira J, Géraud-Grenier I, Massereau-Guilbaud V and Plain A 2005 *Thin Solid Films* **482** 226
[24] Stefanović I, Kovačevic E, Berndt J and Winter J 2003 *New J. Phys.* **5** 39
[25] De Bleecker K, Bogaerts A and Goedheer W 2006 *Phys. Rev.* E **73** 026405
[26] Robertson J 2002 *Mater. Sci. Eng.* R **37** 129
[27] Zhou D, McCauley T G, Qin L C, Krauss A R and Gruen D M 1998 *J. Appl. Phys.* **83** 540
[28] Szopa C, Cernogora G, Boufendi L, Correia J J and Coll P 2006 *Planet. Space Sci.* **54** 394
[29] Selwyn G S, McKillop J S, Haller K L and Wu J J 1990 *J. Vac. Sci. Technol.* A **8** 1726
[30] Ganguly B, Garscadden A, Williams J and Haaland P 1993 *J. Vac. Sci. Technol.* A **11** 1119
[31] Praburam G and Goree J 1996 *Phys. Plasmas* **3** 1212

[32] Mikikian M, Boufendi L, Bouchoule A, Thomas H M, Morfill G E, Nefedov A P, Fortov V E and PKE-Nefedov Team 2003 *New J. Phys.* **5** 19
[33] Winter J 1998 *Plasma Phys. Control. Fusion* **40** 1201
[34] Arnas C, Dominique C, Roubin P, Martin C, Brosset C and Pégourié B 2006 *J. Nucl. Mater.* **353** 80
[35] Dorier J L, Hollenstein C and Howling A 1995 *J. Vac. Sci. Technol.* A **13** 918
[36] Goree J, Morfill G E, Tsytovich V N and Vladimirov S V 1999 *Phys. Rev.* E **59** 7055
[37] Samsonov D and Goree J 1999 *Phys. Rev.* E **59** 1047
[38] Akdim M R and Goedheer W J 2001 *Phys. Rev.* E **65** 015401
[39] Jovanović D and Shukla P K 2003 *Phys. Lett.* A **308** 369
[40] Gozadinos G, Ivlev A V and Boeuf J P 2003 *New J. Phys.* **5** 32
[41] Avinash K, Bhattacharjee A and Hu S 2003 *Phys. Rev. Lett.* **90** 075001
[42] Tsytovich V N, Morfill G, Konopka U and Thomas H 2003 *New J. Phys.* **5** 66
[43] Zafiu C, Melzer A and Piel A 2003 *Phys. Plasmas* **10** 1278
[44] Schauer J C, Hong S and Winter J 2004 *Plasma Sources Sci. Technol.* **13** 636
[45] Kretschmer M, Khrapak S A, Zhdanov S K, Thomas H M, Morfill G E, Fortov V E, Lipaev A M, Molotkov V I, Ivanov A I and Turin M V 2005 *Phys. Rev.* E **71** 056401
[46] Vladimirov S V, Tsytovich V N and Morfill G E 2005 *Phys. Plasmas* **12** 052117
[47] Land V and Goedheer W J 2006 *New J. Phys.* **8** 8
[48] Goree J, Quinn R A, Morfill G E, Thomas H M, Hagl T, Konopka U, Rothermel H and Zuzic M 1998 *Proc. 4th Microgravity Fluid Physics and Transport Phenomena Conf.* (*Cleveland*)
[49] Mikikian M and Boufendi L 2004 *Phys. Plasmas* **11** 3733
[50] Mikikian M, Boufendi L and Bouchoule A 2003 *Proc. 30th EPS Conf. on Contr. Fusion and Plasma Phys.* (*St Petersburg*) (ECA vol 27A) ed R Koch and S Lebedev pp O–3.1B online at http://epsppd.epfl.ch/StPetersburg/pdf/O3_001b.pdf
[51] Mikikian M, Cavarroc M, Chaumeix N and Boufendi L 2004 *Proc. 31st EPS Conf. on Plasma Phys.* (*London*) (ECA vol 28G) ed P Norreys and H Hutchinson (Petit-Lancy: European Physical Society) pp O–2.13. Online at http://epsppd.epfl.ch/London/pdf/O2_13.pdf
[52] Mikikian M, Cavarroc M and Boufendi L 2005 *New Vistas in Dusty Plasmas* ed L Boufendi, M Mikikian and P K Shukla *AIP Conf. Proc.* vol 799 p 323
[53] Mikikian M, Cavarroc M, Couëdel L and Boufendi L 2006 *Phys. Plasmas* **13** 092103

Mixed-Mode Oscillations in Complex-Plasma Instabilities

Maxime Mikikian,* Marjorie Cavarroc, Lénaïc Couëdel, Yves Tessier, and Laïfa Boufendi

GREMI, Groupe de Recherches sur l'Energétique des Milieux Ionisés, UMR6606, CNRS/Université d'Orléans, 14 rue d'Issoudun, BP6744, 45067 Orléans Cedex 2, France

(Received 11 February 2008; published 6 June 2008)

Instabilities in dusty plasmas are frequent phenomena. We show that some instabilities can be described by mixed-mode oscillations often encountered in chemical systems or neuronal dynamics and studied through dynamical system theories. The time evolution of these instabilities is studied through the change in the associated waveform. Frequency and interspike interval are analyzed and compared to results obtained in other scientific fields concerned by mixed-mode oscillations.

DOI: 10.1103/PhysRevLett.100.225005 PACS numbers: 52.27.Lw, 05.45.−a, 52.25.Gj, 52.35.−g

Solid dust particles from a few nanometers to centimeters are often present in plasmas and are at the origin of a wide variety of new phenomena. Plasmas containing dust particles are called dusty or complex plasmas. These media are encountered in many environments such as astrophysics, industrial processes, and fusion devices. Dust particles can come from regions in the plasma vicinity or can be formed in the plasma due to the presence of molecular precursors. In most cases, they acquire a negative charge by attaching plasma free electrons. In plasma reactors, dust clouds are often characterized by a central dust-free region. This region, usually named "void" [1–6], is considered to be maintained by an equilibrium between inward electrostatic and outward ion drag forces. Under certain conditions, this equilibrium can be disturbed, resulting in self-excited low frequency oscillations of the void size. The obtained instability, consisting of successive contractions and expansions of the void, is named "heartbeat" [1,4,7,8] due to its apparent similarity with a beating heart. Nevertheless, the dust cloud behavior is more complex than it could be supposed [7,8]. This self-excited instability can stop by its own through an ending phase characterized by failed contractions that appear more and more numerous as the end approaches. The phenomena sustaining the instability evolve progressively until a new stable state is reached. This phase can be studied by analyzing the discharge current or the plasma glow emission. These signals have a well-defined shape that seems similar to mixed-mode oscillations (MMOs).

MMOs are complex phenomena consisting of an alternation of a varying number of small amplitude oscillations in between two larger ones (also named spikes). Small and large amplitude oscillations are often considered as, respectively, subthreshold oscillations and relaxation mechanisms of the system. These MMOs are encountered in a wide variety of fields. In chemistry, reaction kinetics can take the form of MMOs [9,10] like in the intensively studied Belousov-Zhabotinskii reaction [11,12]. In natural sciences, MMOs are the subject of an intense research [13–15] since their observation in the Hodgkin-Huxley model of neuronal activity [15,16]. In this context, they are strongly related to spiking and bursting activities in neurons [17,18]. In plasma physics, MMOs have been reported in dc glow discharge [19,20] but to the best of our knowledge, no evidence of MMOs in dusty plasmas have been reported yet. Because of the broad diversity of scientific domains concerned by MMOs, they induced a lot of researches and several approaches have been explored. These studies are based on dynamical system theories, like, for example, canards [13,15,21], subcritical Hopf-homoclinic bifurcation [16,22] or Shilnikov homoclinic orbits [23,24].

In this Letter, we report for the first time on the existence of MMOs in dusty plasmas. An example is analyzed and its main characteristics, like typical frequencies and evolution of interspike interval, are explored. Particular attention is paid to the evolution of the number of small amplitude oscillations in between consecutive spikes. We thus underline very close similarities with typical MMOs observed in neuronal activity and chemistry.

Experiments are performed in the PKE-Nefedov reactor [2,25]. A capacitively coupled radiofrequency (rf at 13.56 MHz) discharge is created between two planar parallel electrodes. The static argon pressure is comprised between 0.5 and 1.6 mbar and the applied rf power is around 2.8 W. Dust particles are grown by sputtering a polymer layer deposited on the electrodes and constituted of previously injected melamine formaldehyde dust particles. A few tens of seconds after plasma ignition, a three-dimensional dense cloud of visible grown dust particles (size of a few hundreds of nanometers) is formed. This observation is performed by laser light scattering with standard CCD cameras. The discharge current (related to electron density) is measured on the bottom electrode. Plasma emission in the center is recorded thanks to an optical fiber with a spatial resolution of a few millimeters [8]. These two diagnostics give rather similar results and are used to characterize the ending phase of the heartbeat instability. When void contraction occurs, a high amplitude peak is observed in the signals [8]. Failed void contractions appear as small amplitude oscillations, i.e., failed peaks.

The first two oscillations in Fig. 1(a) are representative of a typical fully developed heartbeat signal [7] without any failed peak. The observed shape is the one used as reference, with a main peak corresponding to the fast contraction and a slowly increasing signal (like a shoulder) during the slow void reopening [8]. Then, a transition between this regime and a regime with one failed contraction [arrow in Fig. 1(a)] occurs. At the instant where a large amplitude oscillation is expected, a decrease in the signal occurs. The spike occurrence is then delayed. A similar behavior is obtained in the optical signal, as observed in Fig. 1(b) for a transition between one and two failed peak regimes. Signal shape clearly corresponds to typical MMOs and is remarkably similar to waveforms measured or modeled in chemical systems [9,10,12,24] or in neuronal dynamics [13,15,18,26,27]. For the sake of simplicity, classical notation for MMOs [9,12] will be used in the following. Thus, a pattern characterized by L high amplitude oscillations and S small amplitude ones will be noted L^S. As an example, Fig. 1(a) is a transition between 1^0 and 1^1 states, whereas Fig. 1(b) corresponds to a 1^1–1^2 transition. A closer look to this last transition is shown in Fig. 1(c) where the first 1^2 state is superimposed on the last 1^1 state. A vertical dotted line marks the place where signals differ. As it can be observed, signals are nearly identical until this time and no clear indication announces this next change. In dynamical systems, noise can induce drastic changes in system behavior. In the present study, due to a low signal to noise ratio, analyses cannot be performed on raw data. Thus, data in Fig. 1 have been processed using wavelet techniques (checking that no signal distortion was added) in order to remove noise and thus its effect will not be investigated.

As the similarity between our signals and MMOs is established, a more complete study can be performed. For that purpose, electrical signal evolution has been recorded until the complete end of the instability. A typical sequence is shown in Fig. 2(a). The signal mean value is almost constant and the instability consists of a succession of high amplitude spikes separated by an interspike interval (ISI) increasing as one goes along. As in Fig. 1, low amplitude oscillations appear in between these spikes giving the classical shape of MMOs. The increase in the ISI is thus a consequence of the occurrence of more and more failed peaks. As an example, the insert in Fig. 2(a) shows a 1^4–1^5 transition (this time series starts during the 1^3 state). Just after the transition, the memory that a transition occurred is visible. Indeed, the new failed peak [Fig. 2(a) inset] has a higher amplitude than the other ones, keeping partly the characteristics of a spike. Then, its amplitude decreases during the next few patterns until reaching the same amplitude as the other failed peaks. These MMOs can be also characterized by their corresponding phase space. Figures 2(b) and 2(c) are, respectively, 3D and 2D phase spaces of a representative part of the time series presented in Fig. 2(a). To obtain these attractors, an appropriate time delay τ has been calculated using the mutual information method proposed in [28] in the framework of the Belousov-Zhabotinskii reaction. The main large trajectory in phase space corresponds to the large amplitude variation during spikes. A smaller loop (indicated by an arrow labeled 1) corresponds to a short additional peak sometimes observed on the right part of the main spikes [7,8]. This phenomenon is observed in Fig. 1(a) and does not alter the present study. Small amplitude oscillations are represented by loops in a tiny region indicated by an arrow labeled 2 [Figs. 2(b) and 2(c)]. In this region, the number of loops corresponds to the number of failed peaks (3 loops for the 1^3 state, for example) like observed in [15]. The analysis through ISIs is often used in neuroscience for

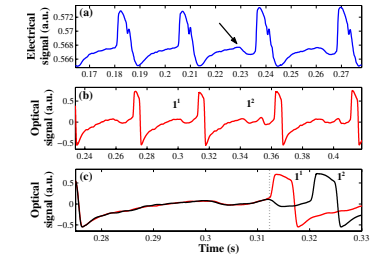

FIG. 1 (color online). (a) Electrical signal with a transition between 1^0 and 1^1 states (arrow: failed peak). (b) Optical signal with a transition between 1^1 and 1^2 states. (c) Superimposition of the two consecutive states shown in (b).

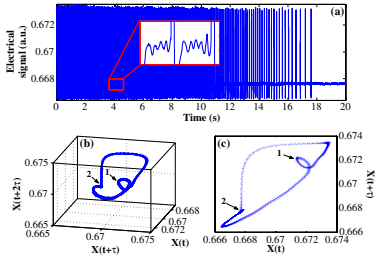

FIG. 2 (color online). (a) Evolution of the electrical signal during the instability ending phase. The insert is a zoom of a transition between 1^4 and 1^5 states. Corresponding phase space is represented in (b) 3D and (c) 2D. Arrows labeled 1 and 2 show, respectively, the loop due to the additional peak observed on the right-hand side of spikes [see Fig. 1(a)] and the region containing the loops corresponding to failed peaks.

characterizing neural activity [18,29]. Figure 2(a) shows that the ISI increases by the progressive addition of failed peaks until the instability stops. This behavior is better observed by performing a spectrogram, i.e., a time-resolved fast Fourier transform (FFT) of this time series [Fig. 3(a)]. This analysis clearly shows a step-by-step decrease of the characteristic frequencies until no more oscillations are observed (at ~17.7 s). The main frequency corresponding to the spike occurrence is indicated by an arrow labeled 1. Because of the shape of the time series, harmonics are also obtained. Figure 3(a) clearly shows that the frequency jumps become smaller as time increases. Moreover, the duration of a given L^S state decreases with time. These last two properties are also brought to the fore by performing a global FFT of the time series [Fig. 3(b)]. Clearly separated peaks are observed, confirming the step-by-step evolution of the frequency. The main peaks are located at 20.5, 17.5, 15.1, 13.3, and 11.8 Hz. Their amplitude is proportional to the duration of each L^S state. As in Fig. 3(a), it is observed that this duration decreases with time (as the frequency). The amplitude of the first peak at 20.5 Hz is not representative because the time series started to be recorded during the 20.5 Hz phase (1^3 state) and part of this phase is thus missing. Another correlation that can be made with Fig. 3(a), is the decrease of the frequency jumps. Indeed, the frequency jumps are equal to $\Delta f = 3$, 2.4, 1.8, and 1.5 Hz. Finally, Fig. 3(a) gives also the frequency of the failed peaks (arrow labeled 2). It is interesting to note that this frequency does not strongly evolve but only slightly decreases with time (variation of about 10%).

In order to improve the analysis of ISI, the occurrence time of each spike is deduced from the time series presented in Fig. 2(a). Spike position is obtained by detecting points exceeding a correctly chosen threshold. The direct time evolution of the ISI can thus be obtained as shown in Fig. 4(a) (blue dots). A very clear step-by-step behavior, as in [14,16], is obtained with ISIs varying from ~0.05 s (~20.5 Hz, 1^3 state) to ~0.4 s (~2.5 Hz, 1^{40} state). Each step corresponds to the occurrence of a new failed peak, i.e., transition from a L^S to a L^{S+1} state. Close to the end of the instability (after 15 s), the system evolves faster and faster with transitions between L^S and L^{S+n} states with n increasing from 2 to 5. The global time dependence (without taking into account the steps) of ISI evolves as $a + b/(t_0 - t)$ as in [16,22]. Parameters a, b and t_0 are fitted to the experimental data and the corresponding curve is superimposed in Fig. 4(a) (orange curve). The parameter t_0 corresponds to the time of the asymptotic limit (~19 s) where ISI tends to infinity which is often considered to be characteristic of a homoclinic transition [16,30]. Figure 4(a) also shows that the ISI during a L^S state is not perfectly constant and slightly increases (left hand side insert). This increase is nonlinear (like, for example, in [16]) and seems to become faster close to the transition between L^S and L^{S+1} states. Thus, it appears that this transition is the consequence of a progressive increase of the ISI. It can be noted that this ISI increase during a given L^S state can also be fitted by a function $a + b/(t_0 - t)$ (blue curve in left hand side insert) with different a, b, and t_0 than the ones obtained from the fit of the global curve. This behavior was not so clearly marked in Fig. 3(a) due to the smoothing induced by the time window used for calculating the time resolved FFT. Nevertheless, a slight decrease in frequency during each L^S state can be observed on the high order harmonics. As in Fig. 3(b), the duration of each L^S state can also be analyzed by performing a histogram of ISIs [Fig. 4(b)]. This histogram is characterized by a clear multimodal pattern that can be fitted by a decreasing exponential function [green curve, first bar is not taken into account due to missing data as in Fig. 3(b)]. Same conclusions can be drawn: when ISI increases, duration of the corresponding state decreases.

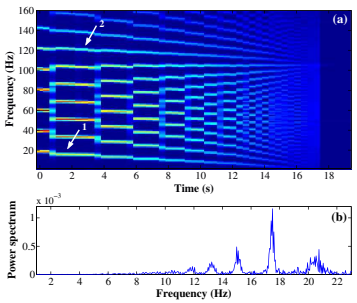

FIG. 3 (color online). (a) Spectrogram of the time series presented in Fig. 2(a). Arrows labeled 1 and 2 show the occurrence frequency of, respectively, spikes and small amplitude oscillations. (b) Power spectral density of the same signal.

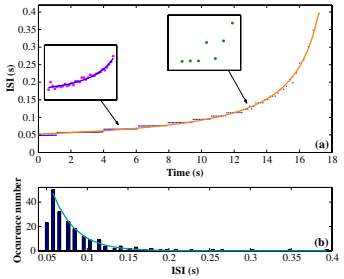

FIG. 4 (color online). (a) Evolution of the ISI during the instability ending phase: measurements (blue dots) and corresponding fit (orange curve). The two inserts are zooms showing, Left: slight evolution of ISI during a L^S phase, Right: unstable transition between two phases. (b) Corresponding histogram of ISIs with an exponential fit (green curve).

This ISI analysis reveals also a particular behavior which is the unstable transition between a L^S and a L^{S+1} state [right-hand side inset in Fig. 4(a)]. The system changes from a L^S state to a L^{S+1} one but returns to the L^S state once again before changing of state definitively. Experimental observations, not presented here, show that an alternation of two states differing by one failed peak can be observed during several periods. Thus, transitions can take place through the progressive occurrence of L^{S+1} patterns during a L^S state. It suggests that the step-by-step evolution of Fig. 4(a) could be compared to the devil's staircase which is an infinite self-similar staircase structure. This specific structure has been observed in chemistry in the framework of MMOs [9,10,12,31] but also in a wide range of other fields like in physiology [32] or in wave-particle interaction [33]. In chemical systems, this structure is often obtained by representing the firing number $F = L/(L + S)$ as a function of the control parameter. The number of steps is then nearly infinite and in between two parent states, an intermediate state exists with a firing number related to the ones of the parent states by the Farey arithmetic [9,12,31]. Thus, the structure obtained in Fig. 4(a) can be an incomplete devil's staircase with an unidentified control parameter evolving with time and not perfectly flat plateaus. More intermediate states could be obtained with a more slowly varying system and thus it can be speculated that the staircase could be partly completed.

In this Letter, we evidenced and characterized mixed-mode oscillations in dusty plasmas. This work highlights new situations of MMOs that can be of interest for improving dynamical system theories related to these structures. The obtained structures are very similar to what is observed in oscillating chemical systems and in neuronal activity. These fields use well-known sets of equations giving rise to MMOs. This scientific background can thus be used to explore and develop new theoretical approaches in dusty plasma dynamics.

M. Lefranc is acknowledged for helpful discussions. The PKE-Nefedov chamber has been made available by the Max-Planck-Institute for Extraterrestrial Physics, Germany, under the funding of DLR/BMBF under Grants No. 50WM9852. This work was supported by CNES under Contract No. 02/CNES/4800000059.

*maxime.mikikian@univ-orleans.fr

[1] J. Goree, G.E. Morfill, V.N. Tsytovich, and S.V. Vladimirov, Phys. Rev. E **59**, 7055 (1999).
[2] M. Mikikian, L. Boufendi, A. Bouchoule, H.M. Thomas, G.E. Morfill, A.P. Nefedov, V.E. Fortov, and the PKE-Nefedov Team, New J. Phys. **5**, 19 (2003).
[3] K. Avinash, A. Bhattacharjee, and S. Hu, Phys. Rev. Lett. **90**, 075001 (2003).
[4] S.V. Vladimirov, V.N. Tsytovich, and G.E. Morfill, Phys. Plasmas **12**, 052117 (2005).
[5] V. Land and W.J. Goedheer, New J. Phys. **9**, 246 (2007).
[6] M. Cavarroc, M. Mikikian, Y. Tessier, and L. Boufendi, Phys. Rev. Lett. **100**, 045001 (2008).
[7] M. Mikikian and L. Boufendi, Phys. Plasmas **11**, 3733 (2004).
[8] M. Mikikian, L. Couëdel, M. Cavarroc, Y. Tessier, and L. Boufendi, New J. Phys. **9**, 268 (2007).
[9] F.N. Albahadily, J. Ringland, and M. Schell, J. Chem. Phys. **90**, 813 (1989).
[10] V. Petrov, S.K. Scott, and K. Showalter, J. Chem. Phys. **97**, 6191 (1992).
[11] J.L. Hudson, M. Hart, and D. Marinko, J. Chem. Phys. **71**, 1601 (1979).
[12] J. Maselko and H.L. Swinney, J. Chem. Phys. **85**, 6430 (1986).
[13] H.G. Rotstein, T. Oppermann, J.A. White, and N. Kopell, J. Comput. Neurosci. **21**, 271 (2006).
[14] G. Medvedev and Y. Yoo, Physica (Amsterdam) **228D**, 87 (2007).
[15] J. Rubin and M. Wechselberger, Biol. Cybern. **97**, 5 (2007).
[16] J. Guckenheimer, R. Harris-Warrick, J. Peck, and A. Willms, J. Comput. Neurosci. **4**, 257 (1997).
[17] E.M. Izhikevich, Int. J. Bifurcation Chaos Appl. Sci. Eng. **10**, 1171 (2000).
[18] A.L. Shilnikov and N.F. Rulkov, Phys. Lett. A **328**, 177 (2004).
[19] T. Braun, J.A. Lisboa, and J.A.C. Gallas, Phys. Rev. Lett. **68**, 2770 (1992).
[20] T. Hayashi, Phys. Rev. Lett. **84**, 3334 (2000).
[21] A. Milik, P. Szmolyan, H. Löffelmann, and E. Gröller, Int. J. Bifurcation Chaos Appl. Sci. Eng. **8**, 505 (1998).
[22] J. Guckenheimer and A. Willms, Physica (Amsterdam) **139D**, 195 (2000).
[23] P. Gaspard and X.-J. Wang, J. Stat. Phys. **48**, 151 (1987).
[24] M.T.M. Koper, Physica (Amsterdam) **80D**, 72 (1995).
[25] A.P. Nefedov, G.E. Morfill, V.E. Fortov, H.M. Thomas, H. Rothermel, T. Hagl, A. Ivlev, M. Zuzic, B.A. Klumov, and A.M. Lipaev *et al.*, New J. Phys. **5**, 33 (2003).
[26] G.S. Medvedev and J.E. Cisternas, Physica (Amsterdam) **194D**, 333 (2004).
[27] M.A. Zaks, X. Sailer, L. Schimansky-Geier, and A.B. Neiman, Chaos **15**, 026117 (2005).
[28] A.M. Fraser and H.L. Swinney, Phys. Rev. A **33**, 1134 (1986).
[29] G.S. Medvedev, Phys. Rev. Lett. **97**, 048102 (2006).
[30] U. Feudel, A. Neiman, X. Pei, W. Wojtenek, H. Braun, M. Huber, and F. Moss, Chaos **10**, 231 (2000).
[31] K.-R. Kim, K.J. Shin, and D.J. Lee, J. Chem. Phys. **121**, 2664 (2004).
[32] S. De Brouwer, D.H. Edwards, and T.M. Griffith, Am. J. Physiol. Heart Circ. Physiol. **274**, 1315 (1998).
[33] A. Macor, F. Doveil, and Y. Elskens, Phys. Rev. Lett. **95**, 264102 (2005).

D.3 Publications related to Chapter 6

- Couëdel, L.; Mikikian, M.; Boufendi, L. & Samarian, A. A., "Residual dust charges in discharge afterglow Phys. Rev. E, **74**, 026403 (2006)
- Couëdel, L.; Samarian, A.; Mikikian, M.& L.Boufendi, "Dust-Cloud Dynamics in a complex plasma afterglow", IEEE Trans. Plasma Sci., In press (2008)
- Couëdel, L.; Samarian, A.; Mikikian, M. & L.Boufendi, "Influence of the ambipolar-to-free diffusion transition on dust particle charge in a complex plasma afterglow", Phys. Plasmas, **15**, 063705 (2008)
- Couëdel, L.; Samarian, A.; Mikikian, M. & L.Boufendi, "Dust density influence on complex plasma decay", Phys. Lett A, In press (2008)

Residual dust charges in discharge afterglow

L. Couëdel,* M. Mikikian, and L. Boufendi
GREMI (Groupe de Recherches sur l'Énergétique des Milieux Ionisés), CNRS/Université d'Orléans, 14 rue d'Issoudun, 45067 Orléans Cedex 2, France

A. A. Samarian
School of Physics A28, University of Sydney, NSW 2006, Australia
(Received 24 May 2006; published 22 August 2006)

An on-ground measurement of dust-particle residual charges in the afterglow of a dusty plasma was performed in a rf discharge. An upward thermophoretic force was used to balance the gravitational force. It was found that positively charged, negatively charged, and neutral dust particles coexisted for more than 1 min after the discharge was switched off. The mean residual charge for 200-nm-radius particles was measured. The dust particle mean charge is about $-5e$ at a pressure of 1.2 mbar and about $-3e$ at a pressure of 0.4 mbar.

DOI: 10.1103/PhysRevE.74.026403 PACS number(s): 52.27.Lw

I. INTRODUCTION

Dusty or complex plasmas are partially ionized gas composed of neutral species, ions, electrons, and charged dust particles. In laboratory experiments, these particles can be either injected or grown directly in the plasma. Injected dust particles are usually micron-size particles. Due to their mass, they are confined near the bottom electrode where the electric force counterbalances gravity. The microgravity condition is necessary to study dust clouds of micrometer-size particles filling the whole plasma chamber [1]. In the laboratory, dense clouds of submicron particles light enough to completely fill the gap between the electrodes can be obtained using reactive gases such as silane [2,3] or using a target sputtered with ions from plasma [4–7].

Dust-particle charge is a key parameter in complex plasma. It determines the interaction between a dust particle and electrons, ions, its neighboring dust particles, and electric field. The determination of the dust-particle charge is thus one of the basic problems in any complex plasma experiments. Knowledge of dust charge will allow us to understand the basic properties of dusty plasma, particle dynamics in dust clouds, and methods to manipulate the particles.

The particle charge controls the dust dynamics both in laboratory and technological plasma reactors, and also in space plasmas. Thus one of the main dusty plasma challenges is to understand the dust charging in a wide range of experimental conditions, which simulates industrial and space plasmas. For example, in most industrial processes in the microelectronics industry which uses silane as the reactive gas, dust contamination is a vital problem [8]. The dust dynamics and coagulation in space plasma are also phenomena governed by dust-particle charges [9,10].

There are many publications reporting on the investigation of dust charging in discharge plasma; see [11–18] and references therein. However there are only a few papers devoted to dust charging, or decharging to be more specific, in the discharge afterglow. In [19] a diffusion of fine dust particles (8–50 nm) in the afterglow of a dusty plasma has been studied. From the afterglow decay of dust number density the charged fraction of particles has been measured. It was found that some particles carried a very small residual charge and some were neutral. A model has been proposed to explain charges on particles in the late afterglow of a dusty plasma. An observation of decay, or "decharging," of an rf plasma with dust particles after switching off the discharge power was reported in [20]. Experiments were performed in the PKE-Nefedov reactor [1] under microgravity conditions on board the International Space Station. The existence of negative residual charges has been shown. A simple theoretical model that describes data obtained was proposed. The residual charges were attributed to the presence of an excitation electric field that was used for dust charge measurements. The limitations of the Space Station experiment routine could not prove this hypothesis. Theoretical predictions on an effect of rf plasma parameters on residual charges has also not been verified.

So any new experimental evidence of residual dust charges in afterglow plasma will lead to a better understanding in the decharging of complex plasma. Indeed the value and nature of residual charges after plasma extinction is of great importance. The dust-particle charge in afterglow plasma could induce a problem in future single-electron devices where a residual charge attached on deposited nanocrystals would be the origin of dysfunction. It could make easier industrial plasma processing reactor decontamination thanks to the use of specially designed electric fields. The residual charges on dust particles in fusion reactors (such as ITER) also can make the cleaning process much easier.

In this paper, we report an on-ground experiment on the residual charge measurement of dust particles after the decay of a dusty plasma. The experiment was performed in the PKE-Nefedov reactor where the dust particles were physically grown in the plasma. A temperature gradient was introduced in the chamber to create an upward thermophoretic force to balance gravity. The residual charges were determined from an analysis of dust oscillations, which were excited by applying a sinusoidal bias to the bottom electrode. A coexistence of positively and negatively charged dust particles as well as noncharged ones was found for more than 1 min after the discharge was switched off. The residual charges for 200-nm-radius particles have been measured for two different pressures. It was revealed that dust particles kept the residual charges only when the discharge was abruptly switched off. In the case when the discharge power is decreased slowly until the plasma disappeared, there was no residual charge on the dust particles. It was also shown that the presence of the low-frequency excitation electric field did not play any role in keeping the charge on dust particles in the afterglow plasma.

The article is organized as follows. Section II is devoted to a general description of the experimental setup. In Sec. III we analyze the forces acting on dust particles, paying most attention to the thermophoretic force. In Sec. IV we discuss a procedure of residual charge measurement and present experimental data obtained, and in Sec. V we analyze discharging of dust particle in afterglow plasma. Section VI is the conclusion.

*Electronic address: lenaic.couedel@univ-orleans.fr

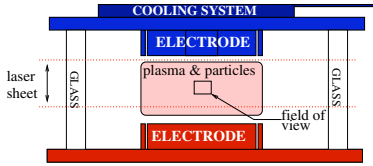

FIG. 1. (Color online) Schematic of the experimental apparatus.

II. EXPERIMENTAL SETUP

The work presented here is performed in the PKE-Nefedov (Plasma Kristall Experiment) chamber designed for microgravity experiments [1]. It is an rf discharge operating in push-pull excitation mode. It consists of 4-cm-diam parallel electrodes separated by 3 cm. The injected power varies in the range 0–4 W. Dust particles are grown in an argon plasma (0.2–2 mbar) from a sputtered polymer layer deposited on the electrodes and coming from previously injected dust particles (3.4 μm, melamine formaldehyde). A detailed description of this experiment and previous results are presented in Refs. [1,4,5].

For the study concerning residual charges, the top electrode was cooled (Fig. 1). An upward thermophoretic force was applied to dust particles in order to counterbalance gravity [21] when the plasma is off. To study particle charges, a sinusoidal voltage produced by a function generator with amplitude ±30 V and frequency of 1 Hz was applied to the bottom electrode. The induced low-frequency sinusoidal electric field $\boldsymbol{E}(\boldsymbol{r},t)$ generated dust oscillations if they kept a residual electric charge.

A thin laser sheet perpendicular to the electrodes illuminates dust particles and the scattered light is recorded at 90° with standard charge coupled device (CCD) cameras with 25 images per second. Video signals were transferred to a computer via a frame-grabber card with 8-bit gray scale and 560×700 pixel resolution. In order to avoid edge effect, a field of view over 8.53×5.50 mm^2 restrained to the center of the chamber was used for residual charge measurement. By superimposition of video frames particle trajectories have been obtained. The coordinates of the particles were measured in each third frame. The amplitude of the oscillations was figured out from the measured particle positions. Absolute values for the oscillation amplitude were obtained by scaling the picture pixels to the known size of the field of view.

III. FORCES ACTING ON DUST PARTICLES

Dust particles in laboratory plasmas are subjected to various forces that confine them in the plasma or drag them out (to the walls or pump outlet) [8]: the confining electrostatic force, the gravity, the thermophoretic force, the ion drag force, and the neutral drag force.

After the discharge is switched off, the forces still acting on dust particles are the gravity F_g, the thermophoretic force F_T, the neutral drag force F_{dn}, and, if dust particles keep residual charges, the electric force F_E due to the electric field induced by the sinusoidal voltage applied to the lower electrode. In this experiment the thermophoretic force balanced the gravity force and the electrostatic force was the reason for the dust oscillations while the neutral drag force dampens the last ones.

The expression for the gravity force is

$$\boldsymbol{F}_g = \frac{4}{3}\pi r_d^3 \rho \boldsymbol{g}, \tag{1}$$

where $\boldsymbol{g}$ is the gravity acceleration, r_d the dust particle radius, and ρ its mass density.

The neutral drag force was taken as [22]

$$\boldsymbol{F}_{dn} = -\frac{8}{3}\sqrt{2\pi} r_d^2 m_n n_n v_{Tn}\left(1+\alpha_{ac}\frac{\pi}{8}\right)(\mathbf{v}_d - \mathbf{v}_n), \tag{2}$$

where m_n is the neutral atom mass, n_n the neutral atom density, $v_{Tn}=\sqrt{8k_BT_n/\pi m_n}$ the thermal speed with $T_n=T$ the neutral gas temperature, k_B the Boltzmann constant, α_{ac} the accommodation coefficient, $\mathbf{v}_d$ dust particle speed, and $\mathbf{v}_n$ a mean speed of neutral atoms. In our experiment $\mathbf{v}_n$ can be taken as 0 because there is no gas flow.

The electric force can be written as

$$\boldsymbol{F}_E(\boldsymbol{r},t) = Q_d \boldsymbol{E}(\boldsymbol{r},t), \tag{3}$$

where Q_d is the dust particle electric charge and $\boldsymbol{E}(\boldsymbol{r},t)$ is the electric field between the electrodes after the plasma is switched off. In the late afterglow the plasma density is very small and $\boldsymbol{E}(\boldsymbol{r},t)$ can be approximated by the vacuum field above a charged disk. Taking into account the size of the camera field of view, the size of the electrode, and the fact that camera was directed to the region near center of the chamber, we are interested in the electric field vertical component $\boldsymbol{E}(\boldsymbol{r},t)\approx E_z(z,t)\vec{e}_z \equiv E(z,t)\vec{e}_z$ only. The calculated value of $E(z,t)$ at the central axis is presented in Fig. 2.

The expression for the thermophoretic force must be chosen carefully. Indeed, it depends strongly on the Knudsen

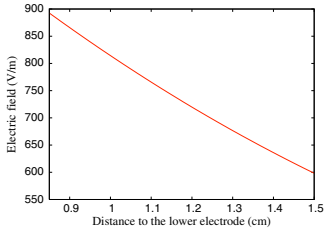

FIG. 2. (Color online) Vertical component of the electric field in the camera field of view.

number $\mathrm{Kn}=l/r_d$ [23] where l is the mean free path of buffer gas species. In our experiment, we work at an operating pressure around 1 mbar. In a previous paper [4], the size of grown dust particles was reported between 200 nm and 800 nm. It gives, using results from Varney [24] for an atom-atom cross section, Knudsen number $250<\mathrm{Kn}<1000$. Consequently we operate in a free molecular regime where a dust particle is similar to a very large molecule. Many theories have been developed [23,25–28] and used [21,23,29] for thermophoresis in the free molecular regime. The most commonly used equation is the Waldmann equation [28] which has been verified experimentally [30,31]:

$$\boldsymbol{F}_T = -\frac{32}{15} r_d^2 \frac{k_{tr}}{v_{Tn}} \nabla T, \tag{4}$$

where ∇T is the temperature gradient in the gas and k_{tr} the translational part of the thermal conductivity given for a monoatomic gas by [32]

$$k_{tr} = \frac{15 k_B}{4 m_n} \mu_{ref} \left(\frac{T}{T_{ref}}\right)^{\nu}, \tag{5}$$

where μ_{ref} is the reference viscosity at reference temperature $T_{ref}=273$ K and the exponent ν results from a best fit of experimental viscosity near the reference temperature. For argon, $\mu_{ref}=2.117\times10^{-5}$ Pa s and $\nu=0.81$ [32].

Another important effect that must be considered in the estimation of thermophoretic force is the influence of a finite volume of gas. If the pressure is low enough, the gas mean free path can become comparable to a length scale of experimental apparatus and the gas can no longer be treated as a continuous medium. Under such a condition, an additional Knudsen number must be added [23], $\mathrm{Kn}_L=l/L$, where L is the length scale of the reactor. In this experiment, the length between electrodes is $L=3$ cm giving $\mathrm{Kn}_L\sim5\times10^{-3}$ which means the gas can be considered as a continuous medium.

The temperature gradient between the electrodes was calculated with FEMLAB (steady-state analysis of heat transfer through convection and conduction with heat flux, convective and temperature boundary conditions using the Lagrange-Quadratic element). The temperatures on the electrodes were measured by a thermocouple and used as boundary conditions for the problem. The contour plot obtained is

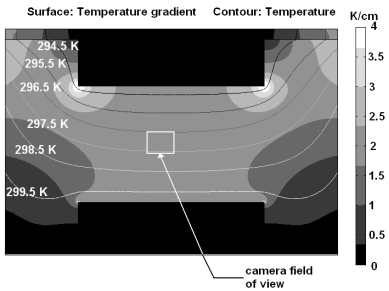

FIG. 3. Temperature profile and gradient.

presented in Fig. 3. It shows that the vertical component of the temperature gradient is constant near the reactor center. The value of temperature gradient is about 2 K/cm for our experiment. There is also a small horizontal component of the temperature gradient. This is the reason for particle drift in the horizontal direction. Such a drift allowed us to resolve particle trajectories (see next section) and made particle charge measurement more convenient.

IV. EXPERIMENTAL PROCEDURE AND RESULTS

In this section, dust-particle size estimation and residual charge measurement are presented. The residual charge measurements have been performed by the following routine. First the chamber was pumped down to lowest possible pressure (base pressure $\sim2\times10^{-6}$ mbar) and the cooling system was turned on. After this, argon was injected up to the operating pressure, the discharge was started, and particles were grown, forming familiar structures such as a void (see, for example, [5]). Then, the discharge was switched off and the bottom electrode was biased by sinusoidal voltage.

In afterglow plasma, the dynamics of dust particles is determined by a temperature gradient and excitation electric field. Figure 4 presents a superimposition of images taken after discharge had been switched off. There are two different types of motion observable. Dust particles drift upwards, downwards, and to the side due to existing temperature gradients and they oscillate due to electrostatic force. It is obvious that the thermophoretic force acts on any dust particle in the chamber, while the electrostatic force acts only if particles have charge in afterglow. Thus the presence of oscillating particles (see Fig. 4) clearly indicates that dust particles do have residual charges after the discharge has been switched off. Dust particles oscillating in opposite phases as well as nonoscillating dust grains have been observed, indicating that negatively charged, positively charged, and noncharged dust particles coexist after plasma extinction. It is worth mentioning that in order to observe dust oscillations the discharge must be switched off abruptly. It was shown that if the power was decreased slowly until the plasma dis-

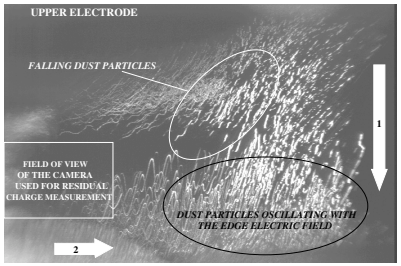

FIG. 4. Superimposition of video frames taken with a large-field-of-view CCD camera. Arrows 1 and 2 represent, respectively, the vertical and horizontal components of the temperature gradient. Edge effects as well as falling dust particles can be seen.

appears, there are no residual charges (no oscillations of dust particles in the sinusoidal electric field were observed). Another interesting fact is that the residual charge on dust particles has a long relaxation time and does not depend on time when the excitation electric field was applied. Dust oscillations were observed for more than 1 min after plasma extinction and in both cases when the function generator was switched on during the discharge or a few seconds after the discharge is turned off.

As can be seen in Fig. 4, there are dust particles falling after the discharge is switched off. These particles are too big to be sustained by the thermophoretic force. Other particles are horizontally adrift at constant height; this means that for these particles the gravity force is balanced by the thermophoretic force. These particles have been used to measure residual charges. It is clear from Fig. 4 that use of a large-field-of-view camera gives us a nice overall picture of decaying dusty plasma but it is not suitable for residual charge measurement because edge effects cannot be neglected. Thus a camera with a small field of view was used for the charge measurement (see Fig. 4). The superimposition of images from this camera is presented in Fig. 5. These images give us a clear track of the dust oscillations, so dust grain trajectories can be reconstructed (Fig. 6).

A. Size and mass of levitating dust grains in discharge afterglow

Particle size (mass) and residual charge measurement are strongly related in this experiment. Charge, size, and mass of dust particles have to be determined. Considering that dust particles levitating in a reactor at a constant height after plasma extinction are the ones for which the gravity is exactly balanced by the thermophoretic force, the dust particle radius can be found using Eqs. (1) and (4):

$$r_d = -\frac{8}{5\pi\rho g} \frac{k_{tr}}{v_{th}} \nabla T. \tag{6}$$

Dust grains are supposed to be spherical and mainly made of carbon (sputtering of a carbonaceous polymer material) [4]

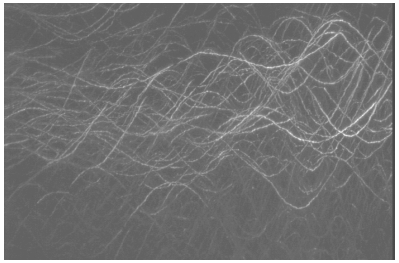

FIG. 5. Superimposition of video frames 10 s after plasma extinction. Dust-particle oscillations can clearly be seen. The temperature gradient has a slight horizontal component. Therefore, oscillations are in the two-dimensional laser plane.

so that the mass m_d can be deduced from Eq. (6):

$$m_d = \frac{4}{3}\pi r_d^3 \rho, \tag{7}$$

where ρ is the mass density of graphite. In our experimental condition, the radius of levitating dust grains is estimated to $r_d\simeq190$ nm and their mass is $m_d\simeq6.5\times10^{-17}$ kg.

B. Dust-charge measurement

From the measurement of oscillation amplitude, the residual charge on a dust particle can be obtained. As the gravity is compensated by the thermophoretic force, the equation of motion for one dust particle, neglecting its interactions with other dust particles, can be reduced to

$$m_d \ddot{z} = F_E(z,t) + F_{nd}(z). \tag{8}$$

Taking $E(t)=E_0(z_{mean})\cos(\omega t)$ (the amplitude of the electric field E_0 is the one at the mean dust levitation height z_{mean}) and using Eqs. (3), (2), and (8), the dust-particle oscillation amplitude b can be obtained [33]:

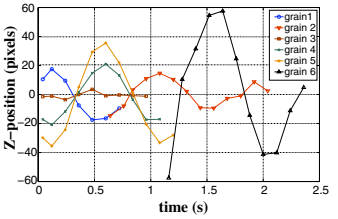

FIG. 6. (Color online) Oscillation of six dust grains 10 s after plasma extinction. Nonoscillating dust grains and opposite phase oscillations are observed.

TABLE I. Measured maximum, minimum, and mean dust-particle residual charges for the two operating pressures.

	$P=1.2$ mbar	$P=0.4$ mbar
∇T	-190 K m^{-1}	-177 K m^{-1}
r_d	194 nm	180 nm
m_d	6.9×10^{-17} kg	5.4×10^{-17} kg
γ	1.36×10^{-13} kg s^{-1}	0.39×10^{-13} kg s^{-1}
$Q_{d_{res}max}$	$+2e$	$+2e$
$Q_{d_{res}min}$	$-12e$	$-4e$
$Q_{d_{res}mean}$	$-5e$	$-3e$

$$b(\omega,Q_d,E_0)=\frac{Q_dE_0(z_{mean})}{m_d\omega\sqrt{\omega^2+4\gamma^2/m_d^2}}, \tag{9}$$

where $\gamma=(4/3)\sqrt{2\pi}r_d^2m_nn_nv_{Tn}[1+\alpha_{ac}(\pi/8)]$ is the damping coefficient and $\omega=2\pi f$ where f is the frequency imposed by the function generator. Equation (9) can easily be inversed to derive the dust residual charge:

$$Q_{d_{res}}=\frac{m_db(\omega,Q_d,E_0(z_{mean}))\omega\sqrt{\omega^2+4\gamma^2/m_d^2}}{E_0(z_{mean})}. \tag{10}$$

The sign of the dust-particle charge is deduced from the phase of the dust-particle oscillation with respect to the excitation electric field. Oscillation amplitudes up to 1.1 mm have been measured (depending on the operating pressure) and charges from $-12e$ to $+2e$ are deduced where e is the elementary charge. It has been found that at high pressure dust particles keep a higher mean residual charge (Table I) but uncertainties are of $\sim 2e$ for each measurement.

V. DISCUSSION

The charging (discharging) process of dust particles in a plasma is governed by the contributions of all currents entering (or leaving) the dust surface, involving plasma electrons and ion currents, photoemission and thermionic emission currents, etc.

$$\frac{dQ_d}{dt}=\sum I_a+\sum I_l, \tag{11}$$

where I_a and I_l are currents absorbed and emitted by the particle (with appropriate sign). In most cases for discharge plasmas we can ignore the emission current and the kinetics of the particle charge can be expressed as

$$\frac{dQ_d}{dt}=J_i-J_e=-\pi er_d^2[n_ev_{T_e}e^{-\varphi}-n_iv_{T_i}(1+\tilde{T}_e\varphi)], \tag{12}$$

where J_e and J_i are the fluxes of electrons and ions onto the particle, $v_{T_{i(e)}}=\sqrt{8k_BT_{i(e)}/\pi m_{i(e)}}$ the thermal velocity of ions (electrons), $\tilde{T}_e=T_e/T_i$ is the electron to ion temperature ratio, $n_{i(e)}$ is the density of ions (electrons), and $\varphi=-eQ_d/4\pi\epsilon_0k_Br_dT_e$ is the dimensionless surface potential of a dust particle where ϵ_0 is the vacuum dielectric permittivity. According to Eq. (12), charge on a dust particle depends on the electron-ion masses, temperatures, and density ratios m_e/m_i, n_e/n_i, and T_e/T_i. Thus to analyze the decharging of dust particle in afterglow plasma one needs to consider the kinetics of plasma decay.

The plasma diffusion loss and electron temperature relaxation determine the kinetics of the discharge plasma decay [34]. In the presence of dust particles, plasma loss is due to diffusion onto the walls completed by surface recombination on dust particles. The equations for the plasma density and electron temperature relaxation are [34,35]

$$\frac{d\tilde{n}}{dt}=-\frac{\tilde{n}}{\tau_L}, \tag{13}$$

$$\frac{d\tilde{T}_e}{dt}=-\frac{\tilde{T}_e-1}{\tau_T}, \tag{14}$$

where $\tilde{n}=n_{i,e}/n_0$ with n_0 the initial plasma density, τ_L the time scale of the plasma loss, and τ_T the time scale for electron temperature relaxation. The expressions for the time scales are [34,35]

$$\tau_L^{-1}=\tau_D^{-1}+\tau_A^{-1}, \tag{15}$$

$$\tau_D^{-1}\simeq\frac{l_{in}v_{T_i}}{3\Lambda^2}(1+\tilde{T}_e)\equiv\frac{1}{2}(1+\tilde{T}_e)\frac{1}{\tau_D^\infty}, \tag{16}$$

$$\tau_A^{-1}\simeq\pi r_d^2n_dv_{T_i}(1+\varphi\tilde{T}_e)\equiv\left(\frac{1+\varphi\tilde{T}_e}{1+\varphi}\right)\frac{1}{\tau_A^\infty}, \tag{17}$$

$$\tau_T^{-1}=\sqrt{\frac{\pi}{2}}\sqrt{\frac{m_e}{m_i}}\frac{v_{T_i}}{l_{en}}\sqrt{\tilde{T}_e}\equiv\frac{\sqrt{\tilde{T}_e}}{\tau_T^\infty}, \tag{18}$$

where τ_D is the ambipolar diffusion time scale onto the walls, τ_A the particle absorption time scale, $l_{i(e)n}$ the mean free path of the ion- (electron-) neutral collision, and Λ the characteristic diffusion length ($\Lambda\sim1$ cm in this experiment). The ∞ exponent stands for the limit at very long time.

For a charging time scale lower than the plasma decay or temperature relaxation time scales the charge on the dust particle is in equilibrium—i.e., ion and electron fluxes balance each other—$\varphi\simeq\varphi_{eq}$, and using Eq. (12), φ_{eq} is given by

$$\frac{n_e}{n_i}\sqrt{\tilde{T}_e}e^{-\varphi_{eq}}=\sqrt{\frac{m_e}{m_i}}(1+\tilde{T}_e\varphi_{eq}). \tag{19}$$

In this case, the expressions for the charge fluctuation and charge fluctuation time scale τ_Q are

$$\frac{dQ_d}{dt}\simeq-\frac{Q_d-Q_{deq}}{\tau_Q}, \tag{20}$$

$$\tau_Q^{-1}\simeq\frac{v_{T_i}r_d}{4\lambda_{i0}^2}(1+\varphi_{eq})\tilde{n}\equiv\frac{\tilde{n}}{\tau_Q^0}, \tag{21}$$

where $\lambda_{i0}=\sqrt{\epsilon_0k_BT_i/n_0e^2}$ is the initial ion Debye length.

It should be noted that the time scale for dust charge fluctuations strongly depends on the plasma density and can

TABLE II. Values of the different time scales for the two operating pressures.

	$P=0.4$ mbar	$P=1.2$ mbar
τ_D^0	30 μs	90 μs
τ_D^∞	1.5 ms	5 ms
τ_A^0	0.4 ms	0.4 ms
τ_A^∞	30 ms	30 ms
τ_L^0	30 μs	90 μs
τ_L^∞	1.4 ms	4.3 ms
τ_T^0	100 μs	34 μs
τ_T^∞	1 ms	340 μs
τ_Q^0	4 μs	4 μs
t_c	20 ms	60 ms
$\tau_Q(t_c)$	1.4 s	1.4 s

vary from microseconds for the initial stages of plasma decay up to seconds in the case of almost extinguished plasma. Taking into account Eqs. (13) and (21), the time dependence of τ_Q can be expressed as [20]

$$\tau_Q^{-1}=\frac{1}{\tau_Q^0}\exp(-t/\tau_L). \tag{22}$$

To understand the dusty plasma decharging dynamics we have to compare different time scales. In Table II, the time scales for this experiment are presented. It can be seen that the initial charge fluctuation time scale is the shortest. The temperature relaxation time scale is shorter or becomes comparable (for 0.4 mbar) to the plasma density decay time scale and plasma losses mainly determined by diffusion. The latest means that for our experimental conditions dust particles did not affect the plasma decay at the initial stage. Figure 7 presents the qualitative dependence of the main plasma and

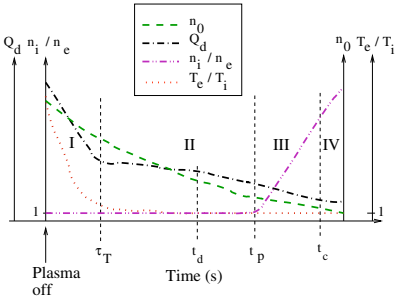

FIG. 7. (Color online) Qualitative time evolution of dust charge, plasma density, and electron temperature during the afterglow. Four stages of the dust plasma decay can be identified: I: temperature relaxation stage up to t_T. II: plasma density decay stage up t_p. III: dust charge volume stage t_c. IV: frozen stage.

dust particle parameters during the afterglow. Four stages of the dust plasma decay can be labeled. As we can see, the first stage of the plasma decay ($t<\tau_T$) is characterized by the electron temperature T_e drop down to room temperature, while the plasma density (especially in case $\tau_T^0<\tau_L^0$) is slightly decreased. As the charging time scale is almost independent of $\tilde{T}_e$ [Eq. (21)], the charge is still determined by its equilibrium value [Eq. (12)]. During the temperature relaxation stage the particle charge should decrease to the value [20]

$$Q_{rT}=\frac{1}{\tilde{T}_{e0}}\left(\frac{\varphi_{eq}(1)}{\varphi_{eq}(\tilde{T}_{e0})}\right)Q_0\simeq\frac{Q_0}{62}\simeq-15e, \tag{23}$$

where Q_0 is the initial dust charge in the plasma and Q_{rT} the value of the dust residual charge at the end of the first decay stage. The dust charge in the plasma Q_0 was estimated as $Q_0=-950e$, solving numerically Eq. (19), with the given parameters $T_i=300$ K and $T_e\simeq3$ eV, for argon plasma with $n_i\cong n_e$. At the next stage of decay, the electron temperature is stabilized while the plasma density is still decreasing (see Fig. 7). So τ_Q continues increasing according to Eqs. (12) and (21). When τ_Q becomes comparable to τ_L, the particle charge cannot be considered as in equilibrium and to determine particle charge we should use Eq. (12). The time scale when the particle charge starts sufficiently deviating from the equilibrium can be estimated as [Eqs. (15) and (22)]

$$t_d\sim-\tau_L^\infty\ln\left[\frac{8}{3}\left(\frac{\lambda_{i0}}{\Lambda}\right)^2\frac{l_{in}}{r_d}\right]\sim6\tau_L^\infty. \tag{24}$$

However, according to Eq. (12), as long as the plasma is neutral ($n_e=n_i$) the charge on the dust particle does not change. The plasma will keep quasineutrality until decaying rates for the electrons and ions are the same. It will be true in the case of ambipolar diffusion. When the nature of the diffusion changes, electrons and ions start to diffuse independently, which will lead to a changing n_e/n_i ratio and consequently the dust charge change.

The nature of the plasma diffusion changed when the particle volume charge cannot be ignored or when the plasma screening length becomes comparable to the chamber size. In the first case the ion diffusion will be influenced by the negatively charged dust particles, while the electrons will be free to go. In the second case, large density differences appear over distances less than the screening length and electrons and ions diffuse independently. Let us estimate the characteristic times for both cases.

The influence of the overall particle charge is determined by the value of the Havnes parameter $P_e=-NQ_d/en_e$. Based on the model discussed, the qualitative evolution of the Havnes parameter P_e in dusty plasma afterglow can be plotted as shown in Fig. 8. The initial value of P_e is small (~0.06 with an estimated dust density $N\sim2\times10^5$ cm^{-3} and $n_0\simeq n_{e0}\sim5\times10^9$ cm^{-3}) and there is no influence of dust. At the first stage of decaying (temperature relaxation stage) P_e decreases due to a dramatic decrease of the dust charge while the plasma density decreases by a factor of 1.1. At τ_T, P_e reaches its minimum value of about 1×10^{-3}. After this P_e starts increasing. During this stage the dust particle charge

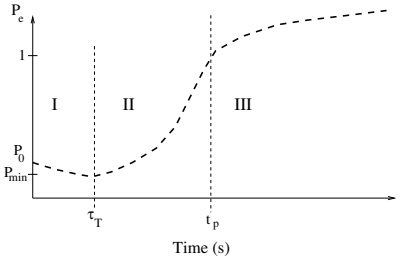

FIG. 8. Qualitative time evolution of the Havnes parameter after the power is switched off.

changes slowly while the plasma number density decays fast (see Fig. 7). The time at which P_e becomes ~ 1 can be estimated as [Eqs. (13)–(18)]

$$t_p \sim \tau_L^{\infty} \ln\left[\left(\frac{T_{e0}}{T_n}\right)\left(\frac{-en_0}{Q_d N}\right)\right] \sim 8\tau_L^{\infty}. \tag{25}$$

The screening length becomes comparable to the chamber size—i.e., $\lambda_i(\tilde{n}_c) \sim \Lambda$—when the density drops down to $\tilde{n}_c = \lambda_{i0}^2/\Lambda^2$. This occurs at [20]

$$t_c \sim \tau_L^{\infty} \ln \tilde{n}_c^{-1} \sim 10\tau_L^{\infty}. \tag{26}$$

At time $\min[t_p, t_c]$, electrons start running away faster than ions and the ratio n_i/n_e grows. For our experimental conditions $t_p < t_c$; thus, the neutrality violation due to the presence of dust particles happens before the Debye length exceeds the chamber size. So the third stage of dusty plasma decay starts at t_p. During this stage the charge on the dust particles is changed due to the changing of the n_e/n_i ratio. At this stage $t_d < t_p$, thus, the kinetic equation (12) should be used for estimations of the charge variation. The upper limit of the charge change can be estimated ignoring the electron current and considering the time interval between t_p and t_c,

$$\frac{dQ}{dt} < J_i \Big|_{t_p}^{t_c} \tag{27}$$

$$< \pi r_d^2 n_i(t_p) v_{T_i} \left(1 - \frac{e}{4\pi\epsilon_0 k_B r_d T_i} Q_d\right)\Big|_{t_p}^{t_c}. \tag{28}$$

Solving Eq. (28), the charge should evolve as follows:

$$Q_d = \left(Q_{dT} - \frac{1}{\alpha}\right)\exp(-K\alpha\Delta t) + \frac{1}{\alpha}, \tag{29}$$

where $\alpha = e/4\pi\epsilon_0 k_B r_d T_i \sim 0.28/e$, $K = \pi e r_d^2 n_i(t_p) v_{T_i} \sim 190e$, and thus $(K\alpha)^{-1} \sim 20$ ms $\sim \Delta t = (t_c - t_p)$.

Therefore, the charge during the third stage decreases to $-3e$. At the fourth stage of plasma decay, $t > t_c$, the plasma density decreases such that any further changes of the dust charge become negligible and the charge remains constant for a while. Thus the final residual charge for our condition is

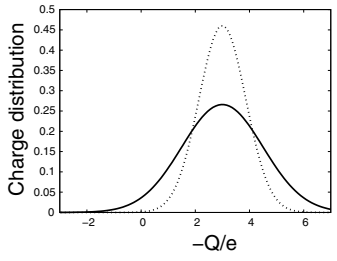

FIG. 9. Charge distribution with and without image force correction. The dotted line represents the distribution with $\Delta Q = 0.5\sqrt{Q}$. The solid line represents the distribution with $\Delta Q = 0.87\sqrt{Q}$ [37].

expected to be about $Q_{d_{res}} \sim -3e$ which is well correlated with the charges measured in the experiment (Table I).

The observation of neutral and positively charged particles in our experiments can be explained by the particle charge distribution. The charge distribution in a dust-particle ensemble is due to charge fluctuation on every individual dust particle. It has been shown [36–40] that the rms of stochastic charge fluctuations varies as $\delta\sqrt{\langle Q_d \rangle}$, where δ is a parameter depending on the plasma conditions and close to 0.5. Thus for mean charge around $-3e$ the charge distribution should lie mainly between $-1e$ and $-5e$. However, in our case we can expect a broader distribution, taking into account two reasons. First for small particles with a charge of about a few electrons the image force (polarizability) correction starts playing role; see [37]. And for electron temperature less then 0.1 eV the correction factor can be up to 3. That is a significantly broadened distribution, so dust particles can experience fluctuations to neutral and positive charges; see Fig. 9. Another reason for the broadened distribution could be the earlier freezing of the charge distribution so it remains the same while the mean charge decreases. Indeed as $t > t_d$ the charge is not in equilibrium with the surrounding plasma, so the existing charge distribution should remain unchanged or changed slightly during the later stages. Unfortunately, in this experiment the ratio between positively and negatively charged particles has not been measured due to experimental limitations concerned with the fact that dust grains do not stay in the laser sheet for a sufficiently long time due to their out-of-plane thermal motion. Thus to elaborate on the true reason for the presence of residual charges of different polarities one needs additional measurements of the charge distributions.

The considered decharging model predicts a higher residual charge for lower pressure. For low pressure the temperature relaxation time scale exceeds the plasma density decay time (see characteristic times for 0.4 mbar in Table II). This leads to a quick increase of the charging time and makes charge freezing at an early stage of decay keeping charge at a relatively high value. In fact larger charges were measured for the higher pressure. A possible explanation for

this is an electron reheating in late afterglow from metastable atoms [41]. The presence of a significant amount of argon metastables in PKE discharge have been established by plasma modeling [42] and by experimental measurements [43]. Due to reheating, the electrons can have temperatures a few times more than room temperature which will lead to an increase of the residual charge on dust particles. As reheating is more effective for high pressures, larger charges are thus expected.

VI. CONCLUSION

Residual dust-particle charges have been measured in the late afterglow of a dusty plasma. Dust particles have been grown directly in the plasma by sputtering of a polymer material previously deposited on electrodes. Dust particles with a radius of few hundreds of nanometers are levitating after the power of the discharge is switched off. The gravity was balanced by an upward thermophoretic force. Residual charges were determined from an analysis of dust oscillations, which were excited by applying a sinusoidal bias to the bottom electrode.

Positive, negative, and noncharged dust particles have been detected. The mean residual charge for 200-nm-radius particles was measured. The particle charge is about $-5e$ at a pressure of 1.2 mbar and about $-3e$ at a pressure of 0.4 mbar. A model for the dusty plasma decay was exploited to explain the experimental data. According to this model the dusty plasma decay occurs in four stages: temperature relaxation stage, density decay stage, dust-charge volume stage, and frozen stage (ice age IV). The main decrease of the dust charge happens during the first stage due to cooling of the electron gas. The final residual charge established during the third stage when the density of ions exceeds the density of electrons and the plasma density is still high enough to affect the charge. Measured values of the dust residual charges are in good agreement with values predicted by the model. However, the residual charge dependence on discharge conditions and the detection of positively charged particles show that a more detailed model taking into account various phenomena (electron reheating, electron release [44], afterglow chemistry) in decaying plasma has to be developed for a better understanding of dusty plasma afterglow.

ACKNOWLEDGMENTS

The authors would like to thank S. Dozias and B. Dumax for electronic support, J. Mathias for optical support, and Y. Tessier for experimental support. The PKE-Nefedov chamber has been made available by the Max-Planck-Institute for Extraterrestrial Physics, Germany, under the funding of DLR/BMBF under Grant No. 50WM9852. This work was supported by CNES under Contract No. 793/2000/CNES/8344. This work is partly supported by the French-Australian integrated research program (FAST) of the French foreign affairs ministry and the International Science Linkages established under the Australian Government's innovation statement, Backing Australia's Ability and University of Sydney Research and Development Scheme.

[1] A. P. Nefedov *et al.*, New J. Phys. **5**, 33.1 (2003).
[2] A. Bouchoule and L. Boufendi, Plasma Sources Sci. Technol. **2**, 204 (1993).
[3] M. Cavarroc, M. C. Jouanny, K. Radouane, M. Mikikian, and L. Boufendi, J. Appl. Phys. **99**, 064301 (2006).
[4] M. Mikikian, L. Boufendi, A. Bouchoule, H. M. Thomas, G. E. Morfill, A. P. Nefedov, V. E. Fortov, and the PKE-Nefedov team, New J. Phys. **5**, 19.1 (2003).
[5] M. Mikikian and L. Boufendi, Phys. Plasmas **11**, 3733 (2004).
[6] D. Samsonov and J. Goree, J. Vac. Sci. Technol. A **17**, 2835 (1999).
[7] A. A. Samarian and B. W. James, Phys. Lett. A **287**, 125 (2001).
[8] A. Bouchoule, *Dusty Plasmas: Physics, Chemistry and Technological Impacts in Plasma Processing* (Wiley, New York, 1999).
[9] I. A. Belov, A. S. Ivanov, D. A. Ivanov, A. F. Pal, A. N. Starostin, A. V. Filippov, A. V. Demyanov, and Y. V. Petrushevich, JETP **90**, 93 (2000).
[10] U. Konopka *et al.*, New J. Phys. **7**, 227 (2005).
[11] S. Vladimirov, K. Ostrikov, and A. Samarian, *Physics and Applications of Complex Plasmas* (Imperial Press, London, 2005).
[12] E. B. Tomme, D. A. Law, B. M. Annaratone, and J. E. Allen, Phys. Rev. Lett. **85**, 2518 (2000).
[13] C. Zafiu, A. Melzer, and A. Piel, Phys. Rev. E **63**, 066403 (2001).
[14] A. A. Samarian and S. V. Vladimirov, Phys. Rev. E **67**, 066404 (2003).
[15] O. S. Vaulina, A. A. Samarian, B. W. James, O. F. Petrov, and V. E. Fortov, JETP **96**, 1037 (2003).
[16] N. J. Prior, L. W. Mitchell, and A. A. Samarian, J. Phys. D **36**, 1249 (2003).
[17] S. Ratynskaia *et al.*, Phys. Rev. Lett. **93**, 085001 (2004).
[18] C. Arnas, M. Mikikian, and F. Doveil, Phys. Rev. E **60**, 7420 (1999).
[19] M. A. Childs and A. Gallagher, J. Appl. Phys. **87**, 1086 (2000).
[20] A. Ivlev *et al.*, Phys. Rev. Lett. **90**, 055003 (2003).
[21] H. Rothermel, T. Hagl, G. E. Morfill, M. H. Thoma, and H. M. Thomas, Phys. Rev. Lett. **89**, 175001 (2002).
[22] P. Shukla and A. Mamun, *Introduction to Dusty Plasma Physics* (IOP, Bristol, 2002).
[23] F. Zheng, Adv. Colloid Interface Sci. **97**, 255 (2002).
[24] R. N. Varney, Phys. Rev. **88**, 362 (1952).
[25] Z. Li and H. Wang, Phys. Rev. E **70**, 021205 (2004).
[26] I. Goldhirsch and D. Ronis, Phys. Rev. A **27**, 1616 (1983).
[27] I. Goldhirsch and D. Ronis, Phys. Rev. A **27**, 1635 (1983).
[28] L. Waldmann, Z. Naturforsch. A **14**, 589 (1959).
[29] K. DeBleecker, A. Bogaerts, and W. Goedheer, Phys. Rev. E

71, 066405 (2005).
[30] W. Li and E. J. Davis, J. Aerosol Sci. **26**, 1063 (1995).
[31] W. Li and E. J. Davis, J. Aerosol Sci. **26**, 1085 (1995).
[32] M. A. Gallis, D. J. Rader, and J. R. Torczynski, Aerosol Sci. Technol. **36**, 1099 (2002).
[33] L. Landau and E. Lifchitz, *Physique Théorique* (Édition Mir Moscou, 1982), Vol. 1.
[34] Y. P. Raizer, *Gas Disharge Physics* (Springer, Berlin, 1991).
[35] V. N. Tsytovich, Phys. Usp. **40**, 53 (1997).
[36] T. Matsoukas and M. Russell, J. Appl. Phys. **77**, 4285 (1995).
[37] T. Matsoukas, M. Russell, and M. Smith, J. Vac. Sci. Technol. A **14**, 624 (1996).
[38] O. S. Vaulina, S. A. Khrapak, A. P. Nefedov, and O. F. Petrov, Phys. Rev. E **60**, 5959 (1999).
[39] S. A. Khrapak, A. P. Nefedov, O. F. Petrov, and O. S. Vaulina, Phys. Rev. E **59**, 6017 (1999).
[40] C. Cui and J. Goree, IEEE Trans. Plasma Sci. **22**, 151 (1994).
[41] G. Wenig, M. Schulze, P. Awakowicz, and A. v. Keudell, Plasma Sources Sci. Technol. **15**, S35 (2006).
[42] M. R. Akdim and W. J. Goedheer, Phys. Rev. E **67**, 066407 (2003).
[43] M. Mikikian, L. Boufendi, and A. Bouchoule, in *Proceedings of the 30th EPS Conference on Controlled Fusion and Plasma Physics, St Petersburg, 2003*, edited by R. Koch and S. Lebedev, vol. 27A of *ECA* (European Physical Society, Paris, 2003), pp. O-3.1B.
[44] J. Berndt, E. Kovacevic, V. Selenin, I. Stefanovic, and J. Winter, Plasma Sources Sci. Technol. **15**, 18 (2006).

Dust-Cloud Dynamics in a Complex Plasma Afterglow

Lénaïc Couëdel, Alexandre A. Samarian, Maxime Mikikian, and Laïfa Boufendi

***Abstract*—The motion of a dust-particle cloud in the afterglow of a complex plasma is reported. It is shown that the dust-particle charges strongly affect the dynamic behavior of the dust cloud. Consequently, using the analysis of the whole cloud motion to deduce dust residual-charge and plasma-diffusion parameters is proposed.**

***Index Terms*—Charge, dust cloud, dusty plasma.**

A COMPLEX (dusty) plasma is a partially ionized gas in which there are some charged dust particles. They are very common media and can be either natural plasmas (such as comet tails, planetary ring, and near-Earth plasmas) or human-made plasmas (such as tokamak-edge plasma, etching plasmas, and plasma-enhanced chemical vapor deposition). In laboratory discharges, the dust particles are negatively charged due to a higher mobility of the electrons [1], [2].

The dust particles can be either grown or injected directly into the plasma. Injected dust particles are generally micrometer sized, and thus, they are confined in the sheath region above the lower electrode where the force due to the electric field can balance the gravity force. Consequently, microgravity conditions are needed to observe a cloud of injected particles filling up the whole discharge chamber [3]. On the other hand, dust particles grown directly in the plasma are light enough to fill the whole interelectrode space, and dense clouds of dust particles can be observed and can form structures, such as the dust void, in onground experiments [4]. Dust particles can be grown by using reactive gases (such as silane [5] or methane [6]) or by sputtering a target with the ions coming from the plasma [7], [8].

The dust-particle charge is a very important parameter for complex plasmas. It determines the interaction of a dust particle with its neighboring dust particles and the ions and electrons of the surrounding plasma. Consequently, the determination of the dust-particle charge is one of the most important measurements in any complex plasma experiment.

Manuscript received November 28, 2007; revised February 13, 2008. This work was supported in part by CNES under contract 793/2000/CNES/8344 and in part by the French–Australian integrated research program (FAST) under Contract FR060169.

L. Couëdel is with the School of Physics, The University of Sydney, Sydney, N.S.W. 2006, Australia, and also with the Groupe de Recherches sur l'Energétique des Millieux Ionisés, Centre National de la Recherche Scientifique–Université d'Orléans, 45067 Orléans Cedex 2, France.

A. A. Samarian is with the School of Physics, The University of Sydney, Sydney, N.S.W. 2006, Australia.

M. Mikikian and L. Boufendi are with the Groupe de Recherches sur l'Energétique des Millieux Ionisés, Centre National de la Recherche Scientifique–Université d'Orléans, 45067 Orléans Cedex 2, France.

Color versions of one or more of the figures in this paper are available online at http://ieeexplore.ieee.org.

Digital Object Identifier 10.1109/TPS.2008.920220

In a decaying complex plasma, the electrons and ions of the plasma are lost by diffusion to the walls of the reactor and by recombination on the dust-particle surfaces. Consequently, the charge carried by the dust particles evolves with the other plasma parameters during the plasma afterglow. As the dust-charging time depends strongly on the electron and ion densities [1], the dust-particle charging time becomes very long in the late plasma afterglow, and the dust-particle charges are considered frozen. It has thus been shown that in the late afterglow of a complex plasma, dust particles indeed keep a residual charge of a few elementary charges and that positively charged, negatively charged, and neutral dust particles coexist for several minutes after the power of the discharge is turned off [9], [10].

In a complex plasma afterglow, the dust-cloud motion will be affected by the dust residual charges due to the involved electrostatic interactions. By recording the motion of a dust cloud in the afterglow of a complex plasma, it is thus possible to deduce some important parameters such as the dust-particle mean charge and the remanent electric fields. In this paper, the motion of a dust-particle cloud in the afterglow of an RF discharge is reported.

The experiment has been done in the plasma kristal experiment (PKE)-Nefedov reactor [3]. It is an RF discharge operating in a push–pull excitation mode. The electrodes are parallel and are 4 cm in diameter. They are separated by a gap of 3 cm. The injected power is in the range of 0–4 W. The dust particles were grown in an argon plasma (0.2–2 mbar). A thin laser sheet that is perpendicular to the electrodes was used to illuminate the dust particles, and the scattered light was recorded at an angle $\Theta \sim 30^\circ$ with a fast charge-coupled device camera with 500 frames/s.

Frames from the video taken at different times of the complex plasma afterglow are shown in Fig. 1. As it can be seen when the discharge is on ($t < 0$), the interelectrode space is filled with a cloud of dust particles in which a dust-free region called a "void" can be observed. This void is a common feature of complex plasmas [1]–[4]. The intensity of the scattered light of the column going through the center of the void is also shown in Fig. 1 (3-D plot). It shows its evolution with time and, thus, the evolution of the dust density. A similar method was used in [4] to study dust-cloud dynamics in a running discharge. The void is clearly observed because it corresponds to a strong drop in the scattered light intensity. Video frames can also be used to extract dust-particle trajectories (not presented here).

When the discharge is turned off, the dust cloud starts to fall down due to the gravity (in Fig. 1, frames for $t > 0$). Nevertheless, it can be seen that in the first 20 ms after the discharge is switched off, the scattered light intensity increases drastically. As the scattered light is roughly proportional to the dust density, it indicates that the dust cloud contracts at the very beginning of the plasma decay. The time scale of this contraction ($t_c \leq 20$ ms) is too short to be explained by the gravity force. Consequently, it implies the action of the confining electric field. This electric field confines the dust cloud inside the plasma when the discharge is on while the dust particles tend to repel each other. When the RF generator is turned off, the RF field decreases, and the confining electric field evolves, too. During this time, the electron temperature relaxes to room temperature, leading to a drastic drop of the dust charge [9]. The dust-particle cloud thus contracts due to the changes in the repelling and confining forces. Knowing the dust-particle charge evolution and looking at the dust-cloud dynamics, an estimation of the evolution of the confining electric field may be done.

Another feature of the dust-cloud dynamics in the plasma afterglow is the evolution of the dust void. As it is shown in Fig. 1, the dust void remains well defined with a sharp boundary for a very long time.

To conclude, the analysis of the motion of the dust cloud could give information about dust residual charges, diffusion processes, and electric fields because the dust-cloud dynamics is strongly affected by the dust-particle charges.

This article has been accepted for inclusion in a future issue of this journal. Content is final as presented, with the exception of pagination.

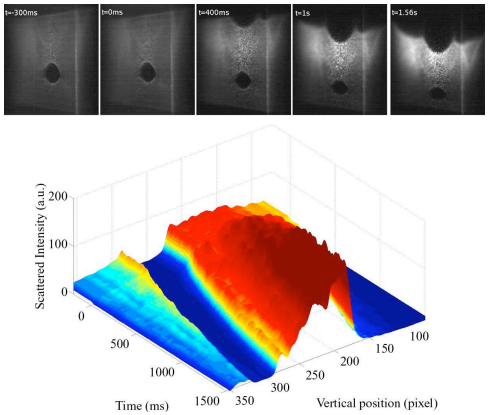

Fig. 1. (Top) Frames extracted from the video of the laser scattered light during the plasma afterglow. (Bottom) Evolution of the scattered intensity of the central column going through the center of the dust void. The zero coordinate in the vertical position corresponds to the top of the picture. The discharge was switched off at $t = 0$ ms.

Acknowledgment

The authors would like to thank S. Dozias and B. Dumax for the electronic support, J. Mathias for the optical support, and Y. Tessier for the experimental support. The PKE-Nefedov chamber has been made available by the Max-Planck-Institut für extraterrestrische Physik, Germany, under the funding of the Deutsches Zentrum für Luft- und Raumfahrt/Bundesministerium für Bildung und Forschung under Grant 50WM9852.

References

[1] S. Vladimirov, K. Ostrikov, and A. Samarian, *Physics and Applications of Complex Plasmas*. London, U.K.: Imperial Press, 2005.

[2] A. Bouchoule, *Dusty Plasmas: Physics, Chemistry and Technological Impacts in Plasma Processing*. New York: Wiley, 1999.

[3] A. P. Nefedov, G. E. Morfill, V. E. Fortov, and H. M. Thomas *et al.*, "PKE-Nefedov: Plasma crystal experiments on the international space station," *New J. Phys.*, vol. 5, p. 33, 2003.

[4] M. Mikikian, L. Couëdel, M. Cavarroc, Y. Tessier, and L. Boufendi, "Self-excited void instability in dusty plasmas: Plasma and dust cloud dynamics during the heartbeat instability," *New J. Phys.*, vol. 9, p. 268, 2007.

[5] M. Cavarroc, M. Mikikian, G. Perrier, and L. Boufendi, "Single-crystal silicon nanoparticles: An instability to check their synthesis," *Appl. Phys. Lett.*, vol. 89, no. 1, p. 013 107, Jul. 2006.

[6] H. T. Do, G. Thieme, M. Fröhlich, H. Kersten, and R. Hippler, "Ion molecule and dust particle formation in Ar/CH_4, Ar/C_2H_2 and Ar/C_3H_6 radio-frequency plasmas," *Contrib. Plasma Phys.*, vol. 45, no. 5/6, pp. 378–384, Aug. 2005.

[7] M. Mikikian *et al.*, "Formation and behaviour of dust particle clouds in a radio-frequency discharge: Results in the laboratory and under microgravity conditions," *New J. Phys.*, vol. 5, p. 19, 2003.

[8] D. Samsonov and J. Goree, "Particle growth in a sputtering discharge," *J. Vac. Sci. Technol. A, Vac. Surf. Films*, vol. 17, no. 5, pp. 2835–2840, Sep. 1999.

[9] L. Couëdel, M. Mikikian, L. Boufendi, and A. A. Samarian, "Residual dust charges in discharge afterglow," *Phys. Rev. E, Stat. Phys. Plasmas Fluids Relat. Interdiscip. Top.*, vol. 74, no. 2, p. 026 403, Aug. 2006.

[10] A. Ivlev *et al.*, "Decharging of complex plasmas: First kinetic observations," *Phys. Rev. Lett.*, vol. 90, no. 5, p. 055 003, Feb. 2003.

Influence of the ambipolar-to-free diffusion transition on dust particle charge in a complex plasma afterglow

L. Couëdel,[1,2,a)] A. A. Samarian,[1] M. Mikikian,[2] and L. Boufendi[2]
[1]*School of Physics A28, The University of Sydney, Sydney, NSW 2006, Australia*
[2]*GREMI (Groupe de Recherches sur l'Énergétique des Milieux Ionisés), CNRS/Université d'Orléans, 14 rue d'Issoudun, 45067 Orléans Cedex 2, France*

(Received 13 February 2008; accepted 12 May 2008; published online 27 June 2008)

The influence of diffusive losses on residual dust charge in a complex plasma afterglow has been investigated. The residual charge distribution was measured and exhibits a mean value $Q_{d_{\mathrm{res}}} \sim (-3e-5e)$ with a tail in the positive region. The experimental results have been compared with simulated charge distributions. The dust residual charges were simulated based on a model developed to describe complex plasma decay. The experimental and simulated data show that the transition from ambipolar to free diffusion in the decaying plasma plays a significant role in determining the residual dust particle charges. The presence of positively charged dust particles is explained by a broadening of the charge distribution function in the afterglow plasma. © *2008 American Institute of Physics*. [DOI: 10.1063/1.2938387]

I. INTRODUCTION

Dusty plasmas (also called complex plasmas) are ionized gases containing dust particles. These dust particles are electrically charged due to interaction with ions and electrons of the surrounding medium. In laboratory experiments, these particles can be either injected or grown directly in the plasma. Injected dust particles are usually micrometer-size particles. Due to their mass, they are confined in the sheath region where the electric force counterbalances gravity. Microgravity conditions are thus necessary to study dust clouds of micrometer-size particles filling the whole plasma chamber.[1] In the laboratory, dense clouds of submicrometer particles light enough to completely fill the gap between the electrodes can be obtained using reactive gases such as silane[2,3] or using a target sputtered with ions from the plasma.[4–9] The dust particles are also subject to other forces in the plasma such as the ion drag force, the neutral drag force, and the thermophoretic force.[10,11]

Dust particle charge is a key parameter in a complex plasma. It determines the interaction between a dust particle and electrons, ions, its neighboring dust particles, and electric field.[11,10] Data of the dust charge will allow us to understand the particle dynamics in dust clouds, and methods of manipulating the particles. The knowledge of the dust charge is very important in every dusty medium (complex plasmas, colloidal suspensions, fog). For example, in gas flow containing dust particles the dust charge and dust charge distribution are studied because of their consequences (safety hazard, dry coating, etc.);[12,13] the charging of fog particles is also studied as the electrical properties of fog are very important for the fog forecast and control; and aerosol and dust systems influence the electric fields and currents in the atmosphere.[14]

There are many publications reporting on the investigation of dust charging in a discharge plasma (see Refs. 10 and 15–22 and references therein). However, there are only a few papers devoted to dust charging, or discharging to be more specific, in the discharge afterglow.[23–25] These papers report that dust particles retain residual electric charges when the power of the discharge is switched off. Nevertheless, the discharging phenomenon was not totally understood. The models proposed do not predict accurately residual charge values observed in those experiments, nor do they explain the existence of positively charge particles.

One of the main reasons is that the models are working with simple assumptions. For example, it was assumed[24] that ambipolar diffusion continues until the ionic Debye length λ_{Di} reaches the diffusion length Λ, and then an abrupt transition to free diffusion of ions and electrons occurs. In contrast, it has been shown that diffusion of charged species in a plasma afterglow deviates from ambipolar diffusion as soon as the ratio $(\Lambda/\lambda_{De}) \sim 100$, where λ_{De} is the electron Debye length.[26–29] These results indicate that electrons and ions are lost at different rates very early in the decay process and one has to expect that this will strongly affect the value of residual dust charge. As the charge on dust particles is related to the ratio n_i/n_e, where $n_{i(e)}$ is the ion (electron) density,[10] this must result in a different dust particle charge evolution in the afterglow compared to the predictions based on previous assumptions.[24,25] For this reason, a model taking into account the actual transition from ambipolar to free diffusion of electrons and ions is vital for the correct calculation of dust charges in afterglow plasma.

In this paper we report numerical simulations of residual electric charge on dust particles in an afterglow plasma for various transitions from ambipolar to free diffusion. These numerical results are compared to the experimental data. The importance of the transition from ambipolar to free diffusion in the decaying plasma for determining the dust particle residual charges is shown. The broadening of the charge distribution function is found to be responsible for the presence of positively charged particles.

a)Electronic mail: lenaic.couedel@univ-orleans.fr.

1070-664X/2008/15(6)/063705/11/$23.00

II. MODELING OF DISCHARGE AFTERGLOW

In this section, we first describe a qualitative model that helps us to explain the existence of residual charges. Then we consider dust-free plasma decay taking into account the experimental transition from ambipolar to free diffusion. We then discuss the plasma decay in the presence of dust particles using a model for particle charging (discharging) in a afterglow plasma.

A. Four-stage model

The evolution of dust charge in afterglow plasma will depend on the evolution of plasma parameters. In a decaying plasma (afterglow plasma), the kinetics of plasma losses is mainly governed by the electron temperature relaxation process and plasma diffusion and recombination processes.[30] The proposed model in Ref. 25 predicts evolution of dust residual charge after the discharge is switched off. Based on the plasma decay kinetics we can define four stages in a discharge afterglow during which the different processes (electron temperature relaxation, ambipolar diffusion, free diffusion) govern the evolution of dust charge:

(1) Electron temperature relaxation stage: the electron temperature decreases to the gas temperature while the plasma density remains almost constant resulting in a strong decrease of dust particle charges ($t \sim 500\ \mu$s for an argon pressure $P_{\mathrm{Ar}} \sim 1.2$ mbar).
(2) Ambipolar diffusion stage: the dust particle charge stays almost constant while plasma particles (ions and electrons) are lost by ambipolar diffusion on to the walls of the reactor. The ambipolar diffusion of ions and electrons continues until the Debye length λ_D equals the diffusion length Λ of the reactor or until the Havnes parameter $P_H = |\tilde{Q}_d n_d / e n_e| \sim 1$ ($t \sim 40$ ms for an argon pressure $P_{\mathrm{Ar}} \sim 1.2$ mbar).
(3) Free diffusion stage: this stage begins when diffusion changes from ambipolar to free; i.e., electrons and ions start diffusing independently. As electrons diffuse faster than ions, the ratio n_i/n_e becomes more than 1, resulting in a decrease of the dust particle charge ($t \sim 60$ ms for an argon pressure $P_{\mathrm{Ar}} \sim 1.2$ mbar).
(4) Finally, ion and electron densities become too small to influence dust particle charges that can be considered as frozen (i.e., charging time tends to infinity).

This model predicts the existence of a negative residual charge of a few electrons but is unable to predict a positive residual charge. The limits of the model are the step transition from ambipolar to free diffusion and the failure to properly take account of the influence of dust particles. Indeed, the effect of the dust particles is ignored until the dust charge density is the same as the electron density, which leads to an abrupt change from ambipolar to free diffusion of ions and electrons. The assumption of the step transition from ambipolar to free diffusion is quite unphysical and contradicts existing experimental data.[26–29] These data indicate that electrons and ions are diffusing at different rates very early in the decay process. This smooth transition must lead to a change in dust charges as the ratio n_i/n_e will be modified early in the decaying process. Under the conditions of our experiments, the ratio $(\Lambda/\lambda_{De}) \sim 50$ when the discharge is switched off. Consequently, this must result in a different dust particle charge evolution in the afterglow compared to previous assumptions.[24,25] For this reason, in the next sections, a modified model taking into account the gradual transition from ambipolar to free diffusion is used to simulation of complex plasma afterglow.

B. Dust-free plasma decay

In a dust-free plasma of monoatomic gas, losses of the plasma are mainly due to diffusion to the walls. At the very beginning of the afterglow when the discharge is switched off, plasma density n as follows,

$$\frac{d\tilde{n}}{dt} = -\frac{\tilde{n}}{\tau_D}, \tag{1}$$

where $\tilde{n} = n/n_0$ with n_0 the initial plasma density and τ_D is the time scale for ambipolar diffusion given by[30]

$$\tau_D^{-1} = \frac{D_a}{\Lambda^2} \simeq \frac{l_{in} v_{T_i}}{3\Lambda^2}(1+\tilde{T}_e) \equiv \frac{1}{2}(1+\tilde{T}_e)\frac{1}{\tau_D^{\infty}}, \tag{2}$$

where D_a is the ambipolar diffusion coefficient, $\tilde{T}_e = T_e/T_i$ with T_e the temperature of electrons, $T_i = T$ the temperature of ions and T the temperature of neutral atoms, $v_{T_i} = \sqrt{8k_BT/\pi m_i}$ the thermal speed of ions with k_B the Boltzmann constant and m_i the ion mass and $l_{in} = 1/(n_n \sigma_{in})$ the mean free path for ion-neutral collisions, n_n the density of neutral atom, and σ_{in} the ion-neutral cross section.

Nevertheless, it has been shown that the plasma diffusion deviates from ambipolar diffusion as soon as the ratio $(\Lambda/\lambda_{De}) \sim 100$.[26–29] From this moment, ions and electrons must be treated separately. In our model, the deviation from ambipolar diffusion is derived from the results of Gerber and Gerardo[29] or Freiberg and Weaver.[26] Both experiments were performed in helium at different pressures exhibit similar evolution of the diffusion coefficients. Though these results were obtained with helium, they can be used to estimate the transition in an argon plasma. Indeed, the ambipolar diffusion coefficient is

$$D_a \propto \frac{(k_B T_i)^{3/2}}{P \sigma_{in} m_i^{1/2}}, \tag{3}$$

where P is the neutral gas pressure. As $\sigma_{in_{\mathrm{Ar}^+}} \sim 2.5\sigma_{in_{\mathrm{He}^+}}$ (Ref. 31) and $m_{i_{\mathrm{Ar}^+}} \sim 10 m_{i_{\mathrm{He}^+}}$, $D_{a_{\mathrm{Ar}}} \sim (1/8) D_{a_{\mathrm{He}}}$ for equal pressures. Consequently, it can be assumed that the diffusion of an argon plasma with argon pressure P_{Ar} is the same as a helium plasma with helium pressure $P_{\mathrm{He}} \simeq 8P_{\mathrm{Ar}}$. The experimental results obtained for helium are in the range of pressure 0.4–4 Torr (Ref. 26) or 9–22.8 Torr,[29] which correspond to 0.05–0.5 Torr and 1.13–2.85 Torr, respectively, in equivalent argon pressure. Consequently, these sets of data can be used for upper and lower estimation in the simulations that are performed in the range 0.3–1 Torr (0.4–1.3 mbar).

In the model, electron and ion densities are treated separately, and follow

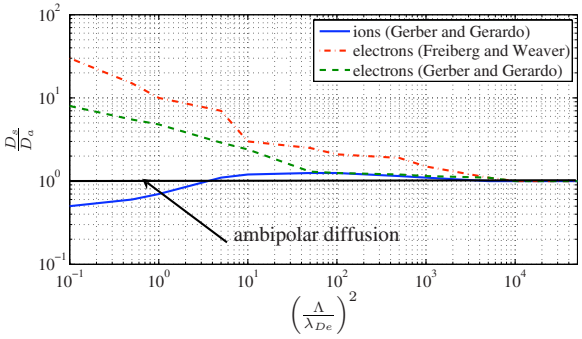

FIG. 1. (Color online) Evolution of the ratio D_s/D_a $(s=i,e)$ as a function of $(\Lambda/\lambda_{De})^2$. These data are extracted from Refs. 29 and 26.

$$\frac{dn_i}{dt} = -\frac{n_i}{\tau_{Di}}, \tag{4}$$

$$\frac{dn_e}{dt} = -\frac{n_e}{\tau_{De}}, \tag{5}$$

where $n_{i(e)}$ is the ion (electron) density and $\tau_{Di(e)}$ is the ion (electron) diffusion time. The diffusion times are function of the ratio $(\Lambda/\lambda_{De})^2$ and are calculated using experimental results from Gerber and Gerardo[29] or Freiberg and Weaver[26] (see Fig. 1). (Only results from Ref. 29 are available for ions and, consequently, they have been used.)

The electron temperature relaxes due to energy exchange in collisions with neutrals. At the initial stage of plasma decay, the electron temperature T_{e0} is much higher than the neutral temperature T and will decrease and tend asymptotically to T. The equation for electron temperature relaxation is[30]

$$\frac{d\tilde{T}_e}{dt} = -\frac{\tilde{T}_e - 1}{\tau_T}, \tag{6}$$

where $\tau_T^{-1} = \sqrt{\pi/2}\sqrt{m_e/m_i}v_{T_i}/l_{en}\sqrt{\tilde{T}_e} \equiv \sqrt{T_e}/\tau_T^{\infty}$, m_e is the electron mass, and l_{en} is the mean free path of electron-neutral collision. It can be deduced from Eq. (6) that the electron cooling time decreases when increasing the pressure.

C. Plasma decay in the presence of dust

In the presence of dust particles in the plasma, the temperature relaxation and diffusion losses could be different from dust-free plasma. However, no experimental data nor theoretical estimations of the transition from ambipolar to free diffusion in dusty plasma exist. Consequently, for our simulation we will assume that the electron temperature relaxation and diffusion processes of ions and electrons are not significantly affected by the presence of dust particles, allowing us to treat ion and electron diffusion in a similar way to dust-free plasma. This restricts the validity of our simulations to the case of low dust particle densities. In this case, the influence of dust particles can be restricted to plasma absorption losses on the particle surface. Indeed, when immersed in a plasma, a dust particle acquires a net electric charge due to ions and electrons "falling" on its surface.[10,11,32] In dusty plasmas, ions and electrons captured by dust particles can be considered as "lost" by the plasma and thus the charging process of dust particles is also a loss process.

In the orbital motion limited (OML) approach,[10,11,32] the charge on a dust particle can be calculated from the ion and electron currents ignoring emission currents,

$$\frac{dQ_d}{dt} = I_e + I_i, \tag{7}$$

where Q_d is the charge on the dust particle and $I_{e(i)}$ is the electron (ion) current. In a typical laboratory discharge, dust particles are negatively charged due to higher mobility of the plasma electrons. The ion current can be expressed as

$$I_i = 4\pi r_d^2 n_i q_i \left(\frac{k_B T_i}{2\pi m_i}\right)^{1/2}\left(1 - \frac{q_i\phi_d}{k_B T_i}\right), \tag{8}$$

and the electron current as

$$I_e = 4\pi r_d^2 n_e q_e \left(\frac{k_B T_e}{2\pi m_e}\right)^{1/2} \exp\left(-\frac{q_e\phi_d}{k_B T_e}\right), \tag{9}$$

where ϕ_d is the surface potential of the dust particle, r_d is the dust particle radius, and $q_{i(e)}$ is the ion (electron) charge. In steady state, the charge on a dust particle can be obtained:

$$Q_d = C\frac{4\pi\epsilon_0 r_d k_B T_e}{e}\ln\left[\frac{ni}{n_e}\left(\frac{m_e T_e}{m_i T_i}\right)^{1/2}\right]. \tag{10}$$

For typical argon plasma, $m_e/m_i \approx 1.4\cdot 10^{-5}$ and $1 < T_e/T_i < 100$, and the correction factor $C \sim 0.73$.[33]

A dusty afterglow plasma is not a steady case but the OML approach can be used to obtain the charge on dust particles. A Fokker–Planck model of dust charging due to the discreetness of the charge currents (ion and electron) can be used to obtain dust particle charge distributions. Indeed, the plasma particle absorption time interval as well as the sequence in which electrons and ions arrive at the dust particle surface vary randomly but observe probabilities that depend on the dust particle potential ϕ_d. The probability per unit of time for absorbing an electron $p_e(\phi_d)$ or an ion $p_i(\phi_d)$ are calculated from the OML currents:[34]

$$p_e = -I_e/e, \tag{11}$$

$$p_i = I_i/q_i. \tag{12}$$

The ion and electron currents can be calculated using Eqs. (8) and (9) only when the dust particle charge is negative. For positively charged dust particles, the ion current is calculated by Eq. (9) with all subscripts changed to i, and electron current is calculated by Eq. (8) with all subscripts changed to e. In the simulation, electron and ion densities are studied in a fluid manner solving numerically Eqs. (4) and (5) using the same constant time step $t_f \ll \tau_{Di(e)0}$, where $\tau_{Di(e)0}$ is the diffusion time for ions (electrons) at the beginning of the simulation (i.e., the very beginning of the decaying plasma).

The contribution of dust particles to plasma losses is taken into account in the following way.

The charges of N_d dust particles are computed. Knowing the dust density n_d in the plasma, an equivalent volume V_{eq} to these N_d dust particles can be calculated.

For a dust particle, a time step t_{p_j} for which the probability of collecting an ion or an electron of the plasma is computed:[34]

$$t_{p_j} = -\frac{\ln(1-R1)}{p_{\text{tot}}}, \tag{13}$$

where $0 < R1 < 1$ is a random number and $p_{\text{tot}} = p_e + p_i$ is the total probability per unit of time to absorb an ion or an electron.

While $\Sigma_j t_{p_j} \leq t_f$, an electron or an ion is absorbed during the time step t_{p_j}, and the nature of the absorbed particle is determined comparing a second random number $0 < R2 < 1$ to the ratio p_e/p_{tot}. If $R2 < p_e/p_{\text{tot}}$, then the collected particle is an electron; otherwise, it is an ion. The probability p_e and p_i are recalculated and a new time step $t_{p_{j+1}}$ is computed.

When $\Sigma_j t_{p_j} > t_f$, one more iteration is applied to the dust particle. Nevertheless, the probability of collecting an ion or an electron in the time interval $\Delta t = t_f - \Sigma_{k=1}^{j-1} t_{p_k}$ is $p(\Delta t) = 1 - \exp(-\Delta t p_{\text{tot}})$ [if $t_{p_1} > t_f$, then $p(t_{p_1})$ is computed]. A random number $0 < R3 < 1$ is then generated and if $R3 < p(\Delta t)$, a plasma particle (ion or electron) is absorbed. The choice between ion and electron is decided as previously described.

When all the N_d dust particles have been treated, the number of absorbed ions and electrons $N_{i\text{abs}}$ and $N_{e\text{abs}}$, respectively, by the N_d dust particles during the time step t_f is known and can be transformed using the equivalent volume V_{eq} into absorbed ion and electron densities $n_{i\text{abs}}$ and $n_{e\text{abs}}$, respectively, which are subtracted from the ion density n_i and electron density n_e before the next iteration of time step t_f.

For each iteration, the mean time $\bar{t_p}$ necessary for one particle to collect a plasma particle (i.e., an ion or an electron) as well as the ratio $r_{\text{loss}} = n_{e(i)_{\text{diff}}}/n_{e(i)_{\text{abs}}}$, where $n_{e(i)_{\text{diff}}}$ is the density of electron (ion) lost by diffusion. The program is stopped when $\bar{t_p} \gg \tau_{Di}$ ($\bar{t_p} > 10\tau_{Di}$ in this simulation) when the charge on dust particles can be considered as frozen due to a plasma loss time becoming faster than the particle charging time.

III. RESULTS AND DISCUSSION

In this section, the experimental dust charge distributions as well as the simulated ones are presented. We then discuss the validity of our results and role of the transition from ambipolar to free diffusion.

A. Experimental results

The experimental residual charge distributions have been obtained using the PKE-Nefedov reactor.[1] An upward thermophoretic force was applied to dust particles in order to counterbalance gravity[35] when the discharge is off. To study particle charges, a sinusoidal voltage produced by a function generator with amplitude ± 30 V and frequency of $f=1$ Hz was applied to the bottom electrode. The induced low frequency sinusoidal electric field generates dust oscillations if the dust particles have a residual electric charge. A thin laser sheet perpendicular to the electrodes illuminates the particles and the scattered light is recorded at 90° with standard charge coupled device (CCD) cameras. By superimposition of video frames, particle trajectories have been obtained. The coordinates of the particles were measured in each third frame and the amplitude of the oscillations was determined from the measured particle positions. Absolute values for the oscillation amplitude were obtained by scaling the image pixels to the known size of the field of view.

The charge of a dust particle Q_d can then be obtained from the oscillation amplitude b,[25]

$$Q_{d_{\text{res}}} = \frac{m_d b\omega\sqrt{\omega^2 + 4\gamma^2/m_d^2}}{E_0}, \tag{14}$$

where m_d is the mass of the dust particle, E_0 is the amplitude of the electric field at the mean height of the dust particle, $\omega = 2\pi f$ the angular frequency of the sinusoidal electric field, and γ the damping coefficient. The electric field E_0 was taken as the one above the axis of a polarized disk. For a levitation height of 1.5 cm, the electric field is $E_0 = 6$ V/cm.[25] The total error on the residual charge measurement (taking into account the error on the dust mass, dust size, E_0, and the damping force) is about ~49%. The sign of the dust particle charge is deduced from the phase of the dust particle oscillation with respect to the excitation electric field. A more detailed description of this experiment can be found in Ref. 25.

Following and measuring oscillations of many dust particles, the dust particle residual charge distribution in a afterglow plasma can be constructed. In Fig. 2, dust particle residual charge distributions are presented for two operating pressures. It can be seen that for both pressures the mean residual charge is negative and corresponds to a few elec-

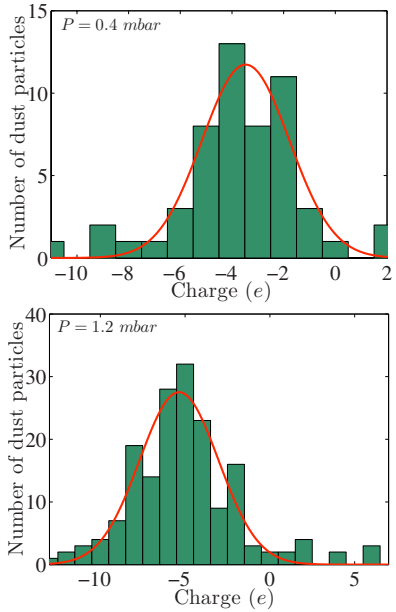

FIG. 2. (Color online) Experimental dust charge distribution. Top: $P=0.4$ mbar. Bottom: $P=1.2$ mbar. A Gaussian fit is superimposed to the experimental distributions.

trons ($-5e$ for 1.2 mbar and $-3e$ for 0.4 mbar). In both cases, the measured residual charge distribution has a tail that extends into positive residual charge region.

B. Numerical results

The numerical dust particle charge distributions are reconstructed simulating the charge of $N_d=500$ dust particles corresponding to a dust density $n_d=5\times10^4$ cm^{-3}. The dust particle radius was $r_d=190$ nm corresponding to the experimental ones. The initial ion density is $n_{i0}=5\times10^9$ cm^{-3} and the initial dust particle charge distribution is computed using a Cui–Goree algorithm[34] and the quasineutrality condition

$$Z_d n_d + n_e = n_i, \tag{15}$$

where $Z_d=|Q_d/e|$. The initial electron density n_{e0} is deduced from this calculation. Many iterations of the algorithm are necessary to obtain the initial dust charge distribution and the initial electron density: the first iteration assumes $n_{e0}=n_{i0}=5\times10^9$ cm^{-3}, and for the next iteration n_{e0} is calculated using Eq. (15) and the dust particle charges of the first iteration. A new dust particle charge distribution is then computed. This process is performed again and again until n_{e0} and the dust charge distribution are stabilized. The obtained dust particle charge distribution is presented in Fig. 3. The mean charge is $Q_{\text{mean}}\simeq-952e$ and the variance $\sigma(Q_d)\simeq17e$. Equation (10) predicts dust particle charges $Q_d=-950e$, which is in total agreement with our simulation results.

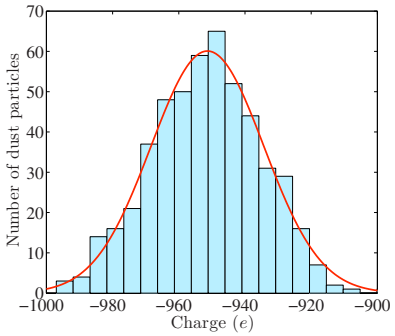

FIG. 3. (Color online) Dust charge distribution for 190 nm radius dust particles with $n_{i0}=5\times10^9$ cm^{-3} and $n_d=5\times10^4$ cm^{-3}.

The decay of a dusty argon plasma is then simulated using the algorithm previously described for two gas pressures [$P=0.4$ mbar and $P=1.2$ mbar (Fig. 4)]. The ion-neutral mean free path is calculated using the cross section from Varney[31] and the electron-neutral mean free path is calculated using the cross section from Kivel.[36] The initial electron temperature is taken as $T_{e0}=3$ eV and the ion temperature is supposed to be equal to the neutral temperature $T_i=T_n=T=0.03$ eV. The diffusion length is taken as $\Lambda=1$ cm, which is approximately the diffusion length of the PKE-Nefedov reactor in which experiments on residual dust charge have been performed.[24,25] The transition from ambipolar to free diffusion is based on either experimental results from Gerber and Gerardo[29] or experimental results from Freiberg and Weaver[26] (the former suggest a slower transition from ambipolar to free diffusion than the latter; see Fig. 1).

As it can be seen in Fig. 4, the first decrease of the dust particle charge corresponds to the electron temperature relaxation. While electrons and ions diffuse ambipolarly, the charge remains constant. Finally, when the transition occurs (after tens of milliseconds), electron and ions densities deviate from each other and the dust charge decreases until it freezes.

For a pressure $P=0.4$ mbar ($P=0.3$ Torr), the simulated final dust charge distributions (i.e., $\bar{t_p}>10\tau_{Di}$) are presented in Fig. 5. The residual charge is $Q_{d_{\text{res}}}\simeq-16e$ when no transition in the diffusion process is taken into account [Fig. 5(a)]. When using a model based on an abrupt transition from ambipolar to free diffusion at a Havnes parameter of $P_H=0.5$, the residual charge is smaller (in absolute value)

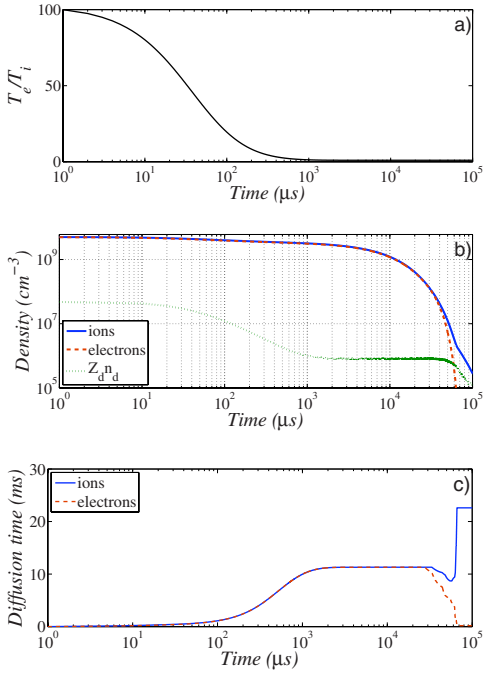

FIG. 4. (Color online) Decay of an argon plasma at $P=1.2$ mbar with a fast ambipolar-to-free diffusion transition. (a) Electron temperature relaxation; (b) density evolution; (c) evolution of diffusion time.

$Q_{d_{\text{res}}}\simeq-13e$ but still far from experimental value [Fig. 5(b)]. It should be noted that, typically, the Havnes parameter reaches 0.5; after 10 ms, it corresponds to a Λ/λ_{De} ratio close to unity. Using Gerber and Gerardo data (slow transition, lower curve in Fig. 1), the mean residual charge $Q_{d_{\text{res}}}\simeq-13e$ [see Fig. 5(c)], whereas it is $Q_{d_{\text{res}}}\simeq-1e$ [see Fig. 5(d)] using Freiberg and Weaver data (fast transition, higher curve in Fig. 1). In the slow transition case, there are no positive particles observed in the simulated dust particle charge distribution whereas there are ones in the case of the fast transition. The residual charge distribution for the fast transition is similar to the experimental results. (see Fig. 2).

For a pressure $P=1.2$ mbar ($P=0.9$ Torr), the simulated final dust particle charge distributions are presented in Fig. 6. The residual charge is $Q_{d_{\text{res}}}\simeq-16e$ when no transition in the diffusion process is taken into account [Fig. 6(a)]. When using a model based on an abrupt transition from ambipolar to free diffusion (at a Havnes parameter of $P_H=0.5$), the residual charge is smaller (in absolute value) $Q_{d_{\text{res}}}\simeq-7e$ but still far from experimental value [Fig. 6(b)]. A dependence on the ambipolar to free diffusion transition is again seen with $Q_{d_{\text{res}}}\simeq-14e$ for the slow transition and $Q_{d_{\text{res}}}\simeq-2e$ for the fast transition. The latest charge distribution is the closest to experimentally measured distribution.

The results for both pressures are summarized in Table I.

IV. DISCUSSION

We now discuss the results and limits of our model. In general, we found that the transition from ambipolar to free diffusion plays a major role in the discharging process of the dust particle. It is instructive to see how the transition affects the residual dust charge, in particular, the width of dust charge distribution. The fact that electrons and ions began to diffuse independently at an early stage of afterglow changes the dust charge distribution function drastically.

As we can see from data in Figs. 5(a)–5(c) for the pressure of 0.4 mbar the distributions for ambipolar diffusion, abrupt, and slow transitions do not differ significantly. Thus, any difference in diffusion in the late afterglow (low ratio of Λ/λ_{De}) has little effect on residual charge. In contrast, a slight difference at an early stage has a large influence on the

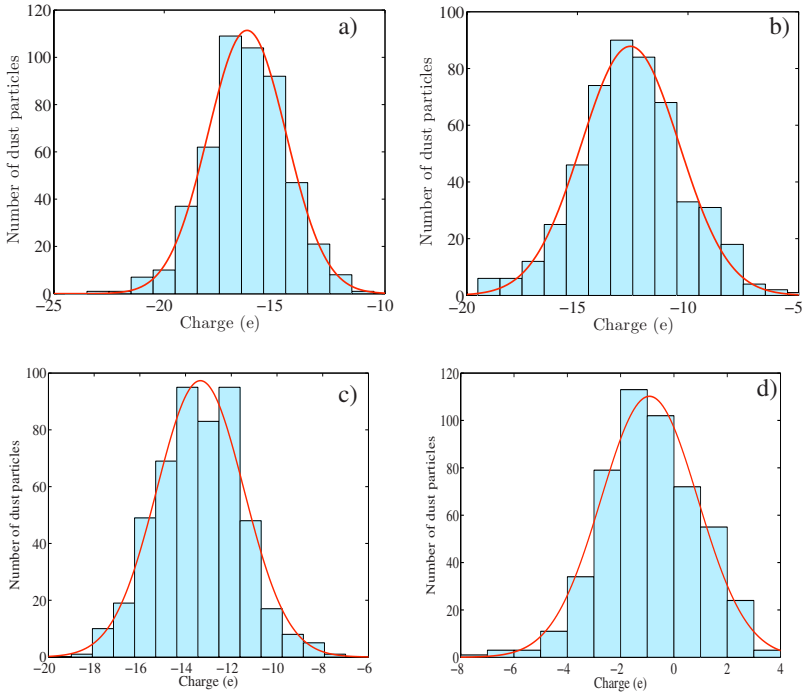

FIG. 5. (Color online) Numerical results for 190 nm radius dust particles with argon pressure $P=0.4$ mbar ($P=0.3$ Torr) and $n_d=5\times10^4$ cm^{-3}. (a) Ambipolar diffusion until the end of the decay process. (b) Abrupt transition from ambipolar to free diffusion when $P_H=0.5$. (c) Using data from Gerber and Gerardo for transition from ambipolar to free diffusion (Ref. 29). (d) Using data from Freiberg and Weaver for transition from ambipolar to free diffusion (Ref. 26).

final dust charge distribution and leads to the appearance of positively charge particles [Fig. 5(d)]. For the higher pressure (1.2 mbar) this effect is not so pronounced, and the diffusion in the late afterglow plays a noteworthy role. In this case an abrupt transition directed due to the influence of the dust charge particle volume effect tends to decrease the residual dust particle charge [Fig. 6(b)]. It does not, however, give us the experimentally observed value of residual charge or the positive tail of the charge distribution. Thus, the results obtained let us conclude that the four-stage model can be used only for the rough estimation of residual charge. For a more accurate calculation, one has to take into account the actual diffusive rates for the electrons and ions.

We now discuss the validity of the presented model. This model is valid only for low dust particle density. As the losses by diffusion are treated as in a dust-free plasma, the influence of dust particle has to be very small compared to the total process. Indeed, if losses on dust particles are similar or bigger than those by diffusion, this last process must be significantly affected. It has thus been shown that the presence of a high density of dust particles significantly reduces the plasma loss time.[37] Moreover, if the total dust charge is not negligible compared that of ions and electrons, the diffusion process must also be modified as the dust particles will repel the electrons and attract the ions.

Consequently, the influence of dust particles can be treated independently from the other loss processes only if the total charge carried by the dust particles is small compared to the charge carried by electrons or ions during the decay process. Furthermore, losses on dust particle surfaces must not be the main loss process (i.e., $r_{\text{loss}}\gg1$) to allow ion and electron diffusions to be treated in the same way as in dust-free plasma. This condition is definitely satisfied for a discharge plasma but could change during the afterglow so we have to calculate evolution of the ratio $n_{i_{\text{diff}}}/n_{i_{\text{abs}}}$ in dis-

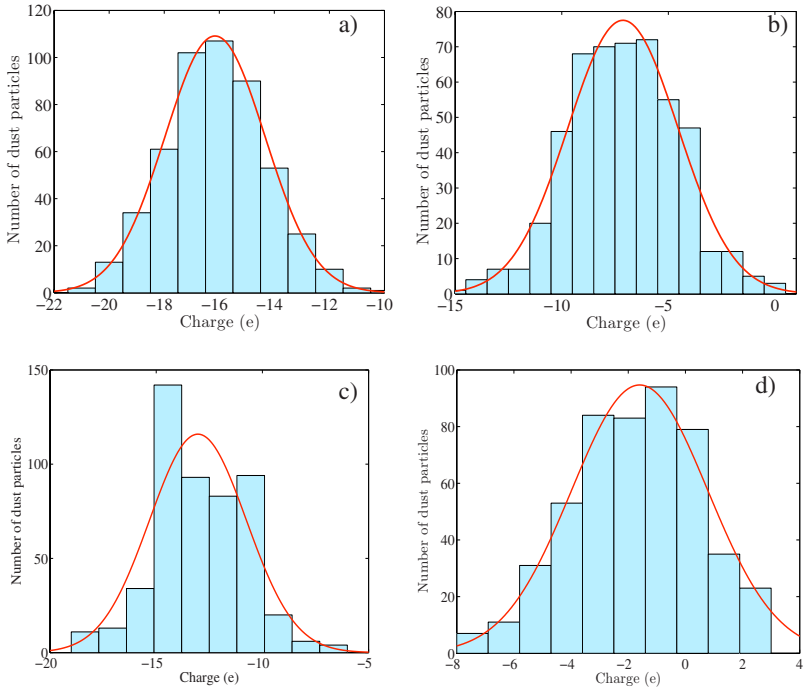

FIG. 6. (Color online) Numerical results for 190 nm radius dust particles with argon pressure $P=1.2$ mbar ($P=0.9$ Torr) and $n_d=5\times10^4$ cm^{-3}. (a) Ambipolar diffusion until the end of the decay process. (b) Abrupt transition from ambipolar to free diffusion when $P_H=0.5$. (c) Using data from Gerber and Gerardo for transition from ambipolar to free diffusion (Ref. 29). (d) Using data from Freiberg and Weaver for transition from ambipolar to free diffusion (Ref. 26).

charge afterglow where $n_{i_{\text{diff}}}$ is the ion density lost by diffusion and $n_{i_{\text{abs}}}$ the ion density lost by absorption onto the dust particle surfaces.

It shows that this ratio stay more or less above 5 during the whole decay process regardless of the conditions of pressure or data used to take into account the transition from ambipolar to free diffusion (only results using Gerber and Gerardo data are presented in Fig. 7). It means that during the plasma decay, losses on dust particles are very small compared to the losses to the reactor walls and our model for plasma decay is valid to the end of the afterglow. Furthermore, looking at the ratio $|\bar{Q}_d n_d/en_i|$ presented in Fig. 8, it can be seen that, except at the very end of the afterglow (i.e., a few milliseconds before the residual charges freeze), the total dust charge volume is much smaller than the total charge of ions. The charge onto the dust particles thus represents a negligible part of the total charge during the major part of the decay process.

TABLE I. Dust particle residual charges for two operating pressures.

	$P=1.2$ mbar	$P=0.4$ mbar
Experimental results	$-5e$	$-3e$
Ambipolar diffusion	$-16e$	$-16e$
Havnes transition	$-7e$	$-13e$
Slow transition (Ref. 29)	$-14e$	$-13e$
Fast transition (Ref. 26)	$-2e$	$-1e$

The data presented in Figs. 7 and 8 confirmed that, in our case, the overall influence of dust particles on the plasma decay can be neglected and, consequently, the assumption of dust-free plasma diffusion can be considered as valid for the whole decay process.

It should be noted that the transition from ambipolar to free diffusion is not the only process that influence the dust residual charge. Indeed, it has been shown that in reactive

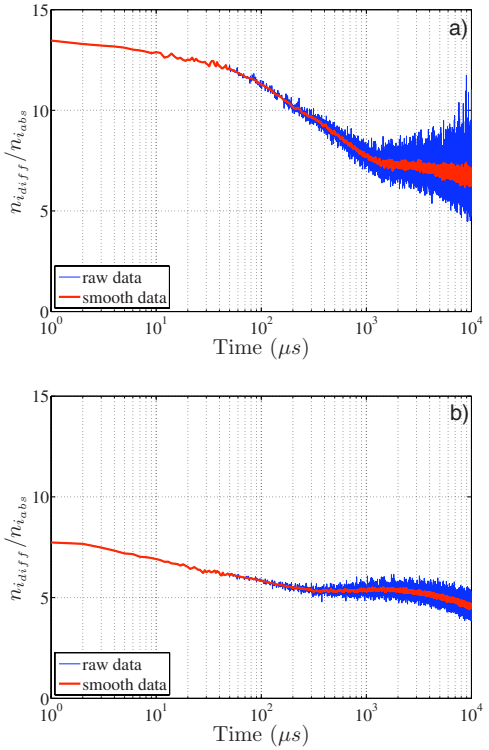

FIG. 7. (Color online) Evolution of $n_{i_{diff}}/n_{i_{abs}}$ using data from Gerber and Gerardo for transition from ambipolar to free diffusion (Ref. 29). (a) $P=0.4$ mbar. (b) $P=1.2$ mbar.

plasmas such as C_2H_4/Ar plasma,[38,39] in which the dust density can be very high ($n_d \simeq 4.5\times10^6$ cm^{-3}),[39] the afterglow electron density shows an unexpected increase at the very beginning of the decay process. Berndt *et al.* attributed this increase to an electron release by the dust particles.[38,39] However, as a such increase has already been observed in pulsed helium discharges and attributed to a re-ionization due to metastable-metastable collisions,[40,41] and as the presence of high dust particle density in a argon dilution plasma enhances the metastable density,[42] the increase of the electron density at the very beginning of the afterglow is still not clear. In all cases, these "extra electrons" must affect the charge on dust particles and consequently the residual charge distributions.

Moreover, it has been shown that the pressure in noble gases such as argon and neon significantly influences the diffusion coefficient.[43] Indeed, at low pressure the electron diffusion cooling process, i.e., the fast loss of energetic electrons to the walls of the reactor, which are imperfectly compensated through elastic collisions of the electrons with gas atoms, resulting in an electron temperature below that of the gas, causes a reduction of D_aP and thus an enhancement of the ambipolar diffusion time $\tau_D=\Lambda^2/D_a$. As mentioned previously, the dust particle charges are related to ion and electron density. Diffusion cooling can also affect dust particle charge distribution evolution. Nevertheless, the present model [see Eq. (6)] does not take into account the phenomena of diffusion cooling and its importance has to be investigated in a future article.

V. CONCLUSION

To conclude, the decharging process of dust particles is strongly dependent on the transition from ambipolar to free diffusion as their charges depend on the ratio n_i/n_e [see Eq. (10) for equilibrium charge]. In this article, it has been

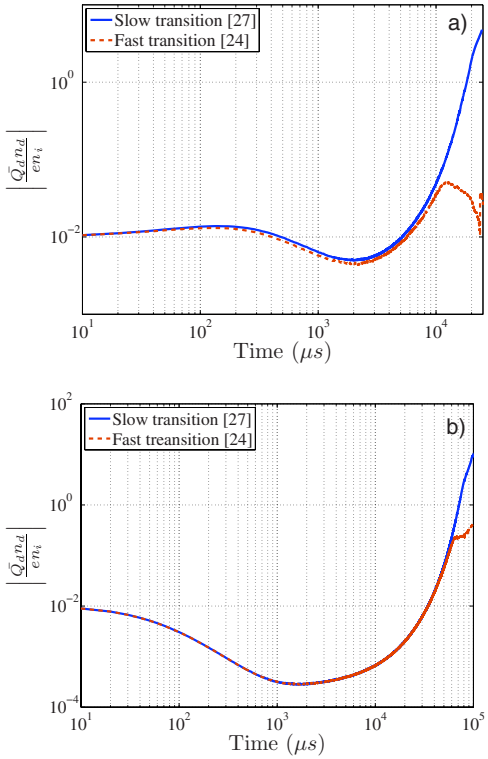

FIG. 8. (Color online) Evolution of $|\bar{Q}_d n_d/en_i|$. (a) $P=0.4$ mbar. (b) $P=1.2$ mbar.

shown that the character of the transition influences the final residual dust charge distribution in a strong manner. The faster the transition occurs (the earlier electrons and ions start to diffuse separately), the smaller the mean dust particle residual charge and a positive charge tail can even be obtained. Consequently, it may be possible to use the dust particle charge distribution as a probe to study the transition from ambipolar to free diffusion in decaying plasma as this distribution is strongly dependent on the transition. Further investigations are being carried on about this possibility.

It has to be noted that the proposed model is valid only in a limited range of parameters as some important issues such as the influence of dust particle charge volume, possible metastable re-ionization, low pressure diffusion cooling, have been ignored. Consequently, further studies are needed for a fuller understanding of the decay process in dusty plasmas.

ACKNOWLEDGMENTS

The authors would like to thank S. Dozias and B. Dumax for electronic support, J. Mathias for optical support, and Y. Tessier, C. Cuthbert, and J. Sisovic for experimental support. The authors would also like to thanks B. W. James for helpful discussions. The PKE-Nefedov chamber has been made available by the Max-Planck-Institute for Extraterrestrial Physics, Germany, under the funding of DLR/BMBF under Grant No. 50WM9852. This work was supported by CNES

under Contract No. 793/2000/CNES/8344. This paper is partially supported by the French–Australian integrated research program (FAST) under Contract No. FR060169.

[1] A. P. Nefedov, G. E. Morfill, V. E. Fortov, H. M. Thomas, H. Rothermel, T. Hagl, A. V. Ivlev, M. Zuzic, B. A. Klumov, A. M. Lipaev, V. I. Molotkov, O. F. Petrov, Y. P. Gidzenko, S. K. Krikalev, W. Shepherd, A. I. Ivanov, M. Roth, H. Binnenbruck, J. A. Goree, and Y. P. Semenov, New J. Phys. **5**, 33 (2003).
[2] A. Bouchoule and L. Boufendi, Plasma Sources Sci. Technol. **2**, 204 (1993).
[3] M. Cavarroc, M. C. Jouanny, K. Radouane, M. Mikikian, and L. Boufendi, J. Appl. Phys. **99**, 064301 (2006).
[4] M. Mikikian, L. Boufendi, A. Bouchoule, H. M. Thomas, G. E. Morfill, A. P. Nefedov, V. E. Fortov, and the PKE-Nefedov team, New J. Phys. **5**, 19 (2003).
[5] M. Mikikian and L. Boufendi, Phys. Plasmas **11**, 3733 (2004).
[6] M. Mikikian, M. Cavarroc, L. Couëdel, and L. Boufendi, Phys. Plasmas **13**, 092103 (2006).
[7] D. Samsonov and J. Goree, J. Vac. Sci. Technol. A **17**, 2835 (1999).
[8] A. A. Samarian and B. W. James, Phys. Lett. A **287**, 125 (2001).
[9] M. Mikikian, L. Couëdel, M. Cavarroc, Y. Tessier, and L. Boufendi, New J. Phys. **9**, 268 (2007).
[10] S. Vladimirov, K. Ostrikov, and A. Samarian, *Physics and Applications of Complex Plasmas* (Imperial Press, London, 2005).
[11] A. Bouchoule, *Dusty Plasmas: Physics, Chemistry and Technological impacts in Plasma Processing* (Wiley, New York, 1999).
[12] S. Matsusaka, M. Oki, and H. Masuda, Powder Technol. **135–136**, 150 (2003).
[13] K. Schonert, K. Eichas, and F. Niermoller, Powder Technol. **86**, 41 (1996).
[14] S. Anisimov, E. Mareev, N. Shikhova, A. Sorokin, and E. Dmitriev, Atmos. Res. **76**, 16 (2005).
[15] H. Kersten, H. Deutsch, and G. M. W. Kroesen, Int. J. Mass. Spectrom. **233**, 51 (2004).
[16] E. B. Tomme, D. A. Law, B. M. Annaratone, and J. E. Allen, Phys. Rev. Lett. **85**, 2518 (2000).
[17] C. Zafiu, A. Melzer, and A. Piel, Phys. Rev. E **63**, 066403 (2001).
[18] A. A. Samarian and S. V. Vladimirov, Phys. Rev. E **67**, 066404 (2003).
[19] O. S. Vaulina, A. A. Samarian, B. James, O. F. Petrov, and V. E. Fortov, JETP **96**, 1037 (2003).
[20] N. J. Prior, L. W. Mitchell, and A. A. Samarian, J. Phys. D **36**, 1249 (2003).
[21] S. Ratynskaia, S. Khrapak, A. Zobnin, M. H. Thoma, M. Kretschmer, A. Usachev, V. Yaroshenko, R. A. Quinn, G. E. Morfill, O. Petrov, and V. Fortov, Phys. Rev. Lett. **93**, 085001 (2004).
[22] C. Arnas, M. Mikikian, and F. Doveil, Phys. Rev. E **60**, 7420 (1999).
[23] M. A. Childs and A. Gallagher, J. Appl. Phys. **87**, 1086 (2000).
[24] A. Ivlev, M. Kretschmer, M. Zuzic, G. E. Morfill, H. Rothermel, H. Thomas, V. E. Fortov, V. I. Molotkov, A. P. Nefedov, A. M. Lipaev, O. F. Petrov, Yu. M. Baturin, A. I. Ivanov, and J. Goree, Phys. Rev. Lett. **90**, 055003 (2003).
[25] L. Couëdel, M. Mikikian, L. Boufendi, and A. A. Samarian, Phys. Rev. E **74**, 026403 (2006).
[26] R. J. Freiberg and L. A. Weaver, Phys. Rev. **170**, 336 (1968).
[27] M. A. Gusinow and R. A. Gerber, Phys. Rev. A **5**, 1802 (1972).
[28] R. A. Gerber, M. A. Gusinow, and J. B. Gerardo, Phys. Rev. A **3**, 1703 (1971).
[29] R. A. Gerber and J. B. Gerardo, Phys. Rev. A **7**, 781 (1973).
[30] Y. P. Raizer, *Gas Discharge Physics* (Springer, Berlin, 1991).
[31] R. N. Varney, Phys. Rev. **88**, 362 (1952).
[32] P. K. Shukla and A. A. Mamun, *Introduction to Dusty Plasma Physics* (IOP, Bristol, 2002).
[33] T. Matsoukas and M. Russell, J. Appl. Phys. **77**, 4285 (1995).
[34] C. Cui and J. Goree, IEEE Trans. Plasma Sci. **22**, 151 (1994).
[35] H. Rothermel, T. Hagl, G. E. Morfill, M. H. Thoma, and H. Thomas, Phys. Rev. Lett. **89**, 175001 (2002).
[36] B. Kivel, Phys. Rev. **116**, 926 (1959).
[37] K. Dimoff and P. R. Smy, Phys. Lett. A **32**, 13 (1970).
[38] J. Berndt, E. Kovacevic, V. Selenin, I. Stefanovic, and J. Winter, Plasma Sources Sci. Technol. **15**, 18 (2006).
[39] I. Stefanovic, J. Berndt, D. Maric, V. Samara, M. Radmilovic-Radjenovic, Z. L. Petrovic, E. Kovacevic, and J. Winter, Phys. Rev. E **74**, 026406 (2006).
[40] M. A. Biondi, Phys. Rev. **82**, 453 (1951).
[41] L. J. Overzet and J. Kleber, Plasma Sources Sci. Technol. **7**, 512 (1998).
[42] A. Bouchoule and L. Boufendi, Plasma Sources Sci. Technol. **3**, 292 (1994).
[43] M. A. Biondi, Phys. Rev. **93**, 1136 (1954).

Physics Letters A 372 (2008) 5336–5339

Contents lists available at ScienceDirect

Physics Letters A

www.elsevier.com/locate/pla

Dust density effect on complex plasma decay

L. Couëdel [a,b,*], A.A. Samarian [a], M. Mikikian [b], L. Boufendi [b]

[a] School of Physics A28, The University of Sydney, NSW 2006, Australia
[b] GREMI (Groupe de Recherches sur l'Énergétique des Milieux Ionisés), CNRS/Université d'Orléans, 14 rue d'Issoudun, 45067 Orléans Cedex 2, France

ARTICLE INFO

Article history:
Received 1 April 2008
Received in revised form 16 June 2008
Accepted 17 June 2008
Available online 27 June 2008
Communicated by F. Porcelli

PACS:
52.27.Lw

Keywords:
Complex plasma
Dust
Afterglow
Decay

ABSTRACT

In this Letter, the influence of dust particles on the plasma losses in a complex plasma afterglow is studied. It is shown that the dust particles can drastically shorten the plasma loss time by absorption-recombination onto their surfaces. The dust particle absorption frequency increases with the dust density but the dependence is not linear for high dust density. Finally, the possible use of dust absorption frequency measurements as a diagnostic for complex plasmas is mentioned and supported by comparison to existing experimental data.

1. Introduction

Complex plasmas (also called dusty plasmas) are partially ionised gases in which there are charged dust particles. They can be natural plasmas (such as near-Earth plasmas, combustion plasmas, comet tails, planetary rings, interstellar clouds, etc.) or human-made plasmas (PECVD, etching, fusion reactor, etc.). The dust particles are charged due to their interactions with the surrounding plasma electrons and ions [1,2]. The presence of this new charged species leads to interesting phenomena that distinguish complex plasmas from classic dust-free plasmas [3–5].

In laboratory discharges, the dust particles can be either grown directly in the plasma chamber (by sputtering [6,7] or using reactive gases [8,9]) or injected inside the plasma [10,11]. Due to a higher mobility of the electrons the dust particles are negatively charged. Consequently, in running discharges, dust particles act as a sink for the electrons of the plasma [2].

The loss of charged species in a complex plasma afterglow is of major importance as it determines the charge carried by the dust particles during the decay process and is fundamental to explain the dust particle residual charges observed experimentally in the late afterglow [12,13]. Dust particle residual charge can be useful (for example, the cleaning of industrial or fusion reactors using electrostatic techniques) or harmful (for example, future single electron devices where residual charge on deposited nanocrystal would be the origin of malfunction).

In a complex plasma afterglow, the dust particles will increase the plasma losses as ion and electron absorption-recombination can occur at their surface. When the dust particle density is high the particle absorption time τ_Q decreases. The plasma decay time τ_L can thus be drastically shortened. This effect has been observed by Dimoff and Smy in 1970 [14] but their results were not properly explained, especially the effect of high dust density on the particle absorption frequency that was far from their theoretical prediction.

In this Letter, the influence of dust particle density on plasma losses due to recombination on to dust particle surfaces is discussed. It is shown that the dust particle absorption frequency does not grow linearly with the dust density. This effect is visible when the ratio of the total charge carried by the dust particles to the charge carried by the ions (Havnes parameter) is close to 1. Finally, by comparison of the model with existing experimental data, the possibility of using plasma decay time in a complex plasma as a diagnostic is discussed.

2. Theoretical approach

When a discharge is switched off, the ions and electrons of the plasma start to diffuse and the plasma density decreases as follows:

$$\frac{dn}{dt} = -\frac{n}{\tau_L}, \tag{1}$$

* Corresponding author at: School of Physics A28, The University of Sydney, NSW 2006, Australia.
E-mail address: lcouedel@physics.usyd.edu.au (L. Couëdel).

0375-9601/$ – see front matter
doi:10.1016/j.physleta.2008.06.047

where n is the density of the plasma and τ_L the plasma decay time. In a complex plasma, plasma losses are due to the diffusion of the ions and the electrons toward the wall of the reactor and by recombination onto the dust particle surfaces. Consequently, the plasma decay time τ_L is:

$$\tau_L^{-1} = \tau_D^{-1} + \tau_Q^{-1}, \tag{2}$$

where τ_D is the plasma diffusion time and τ_Q the dust particle absorption time. As the dust particles are charged due to the fluxes of ions and electrons flowing to their surfaces, the dust particle absorption time will depend on the charge (and surface potential) of the dust particle. Using the orbital motion limited approach the charge on a dust particle is given by [2]:

$$\frac{dZ_d}{dt} = J_e - J_i = \pi r_d^2\left[n_e v_{T_e} e^{-\varphi} - n_i v_{T_i}\left(1+\frac{T_e}{T_i}\varphi\right)\right], \tag{3}$$

where Z_d is the dust particle charge number, $J_{i(e)}$ is the ion (electron) flux, r_d is the dust particle radius, $n_{i(e)}$ is the ion (electron) density, $v_{T_{i(e)}}$ is the ion (electron) thermal speed, $T_{i(e)}$ is the ion (electron) temperature and φ is the dimensionless dust surface potential. The latter can be linked do the dust charge number Z_d by:

$$\varphi = \frac{Z_d e^2}{4\pi\epsilon_0 r_d k_B T_e}, \tag{4}$$

where ϵ_0 is the vacuum dielectric permitivity and k_B is the Boltzmann constant. It sould be noted that the influence of trapped ions on the dust particle charge is neglected. It has been shown that when $T_i \ll T_e$ and $(r_d/\lambda_D)^2 \ll T_i/T_e$ where λ_D is the Debye length, the trapped ions play a significant role in the charging process of dust particles [15,16] and Eq. (3) has to be modified appropriately. However, for the conditions we are interested in, $(r_d/\lambda_D)^2 \sim T_i/T_e$.

In a complex plasma afterglow, recombination on dust particle surfaces is directly linked to the flux of ion onto the dust particles as the dust particles are negatively charged in a laboratory plasma ($Q_d = -Z_d e$ where Q_d is the dust particle charge and e is the elementary charge). Consequently, the dust particle absorption time τ_Q can be written as:

$$\tau_Q^{-1} = \pi r_d^2 n_d v_{Ti}\left(1+\frac{T_e}{T_i}\varphi\right). \tag{5}$$

In a dust-free plasma ($n_e = n_i$), the equilibrium surface potential of an isolated dust particle can be found by solving $dZ_d/dt = 0$ and thus by solving:

$$\left(\frac{T_i}{T_e}\frac{m_e}{m_i}\right)^{1/2}\left(1+\frac{T_e}{T_i}\varphi_0\right)\exp(\varphi_0) = 1. \tag{6}$$

In a complex plasma, however, the ion density n_i and the electron density n_e are different due to the charging of the dust particles. However, as the plasma is quasi-neutral, the electron density can be deduced using the neutrality equation:

$$n_e = n_i - Z_d \cdot n_d. \tag{7}$$

The ratio of the electron density to the ion density can be thus written as:

$$\frac{n_e}{n_i} = 1 - \frac{Z_d n_d}{n_i} = 1 - P_H, \tag{8}$$

where $P_H = Z_d n_d/n_i$ is the Havnes parameter. As it can be seen from Eqs. (7) and (8), for very low dust density, the electron density is very close to the ion density ($n_e \simeq n_i$ and $P_H \sim 0$). Consequently, the surface potential of the dust particle will be the same as for an isolated dust particle and the dust particle absorption time τ_{Q_0} is inversely proportional to the dust density:

$$\tau_{Q_0}^{-1} = \pi r_d^2 n_d v_{Ti}\left(1+\frac{T_e}{T_i}\varphi_0\right). \tag{9}$$

When the dust density increases, however, the electron and ion densities start to deviate from each other and the Havnes parameter increase. Consequently, solving $dZ_d/dt = 0$, the dust surface potential follows:

$$\left(\frac{T_i}{T_e}\frac{m_e}{m_i}\right)^{1/2}\left(1+\frac{T_e}{T_i}\varphi\right)\exp(\varphi) = 1 - P_H. \tag{10}$$

This equation has to be solved numerically and the value of the surface potential explicitly depends on the dust particle density. This will directly affect the dust particle absorption time. However, if the dust density is not too high, the deviation of the dimensionless dust surface potential from the isolated dust particle surface potential will be small so one can write $\varphi = \varphi_0 + \Delta\varphi$. Using a first order approximation, Eq. (10) can be rewritten as:

$$\left(\frac{T_i}{T_e}\frac{m_e}{m_i}\right)^{1/2}\left(1+\frac{T_e}{T_i}(\varphi_0+\Delta\varphi)\right)\exp(\varphi_0)(1+\Delta\varphi) = 1 - \frac{Z_d n_d}{n_i}. \tag{11}$$

From Eqs. (6) and (4), it can then be deduced that:

$$\Delta\varphi = -\left(1+\left(\frac{T_e}{T_i}\frac{m_e}{m_i}\right)^{1/2}\exp(\varphi_0) + \frac{4\pi\epsilon_0 r_d k_B T_e n_d}{e^2 n_i}\right)^{-1} \times \frac{4\pi\epsilon_0 r_d k_B T_e}{e^2}\frac{\varphi_0 n_d}{n_i}. \tag{12}$$

In typical laboratory plasma, $(T_e m_e/T_i m_i)^{1/2}\exp(\varphi_0) \sim 10^{-2}$ and $(4\pi\epsilon_0 r_d k_B T_e n_d)/(e^2 n_i) \sim 10^{-1}$, thus:

$$\Delta\varphi \simeq -\frac{4\pi\epsilon_0 r_d k_B T_e}{e^2}\frac{\varphi_0 n_d}{n_i} \sim -Z_{d0}\frac{n_d}{n_i}, \tag{13}$$

where Z_{d0} is the charge of an isolated dust particle. The dust particle absorption time can be rewritten as:

$$\tau_Q^{-1} \simeq \pi r_d^2 n_d v_{Ti}\left(1+\frac{T_e}{T_i}\varphi_0\right) - \pi r_d^2 n_d^2 v_{Ti}\cdot\frac{T_e}{T_i}\frac{4\pi\epsilon_0 r_d k_B T_e}{e^2}\frac{\varphi_0}{n_i}. \tag{14}$$

The dust particle absorption time is no longer inversely proportional to the dust density. There is a term in n_d^{-2} which tends to attenuate the effect of the dust particles on plasma losses. Indeed when the dust density is high the dust surface potential is lower as is the dust charge number Z_d. Consequently the ion flux is reduced and the dust particle absorption time is increased compared to the value it would have if the dust particles can be considered as isolated.

3. Numerical results

In this section, exact numerical solutions of Eqs. (5) and (10) are presented and compared to the approximate solution of Eq. (14).

In Fig. 1, the absorption frequency τ_Q^{-1} has been calculated for $n_i = 10^8$ cm^{-3}, $T_e = 0.3$ eV (close to experimental values of Ref. [14]) and a dust particle radius of $r_d = 10$ μm. As it can be seen in Fig. 1(a), for low dust densities the dust absorption frequency τ_Q^{-1} is increasing linearly as expected. On the contrary, for high dust density the absorption time τ_Q^{-1} deviates from linearity. The exact solution and the first order approximation are in agreement even though some small discrepancies are observed at high dust density. In Fig. 1(b), the exact solution is presented for different ratio T_e/T_i. As can be seen, the absorption frequency τ_Q^{-1} increases with increasing T_e/T_i. Indeed, when the electron temperature is higher than the ion temperature, ion and electron fluxes are greater at equilibrium (Eq. (3)) resulting in an increased dust

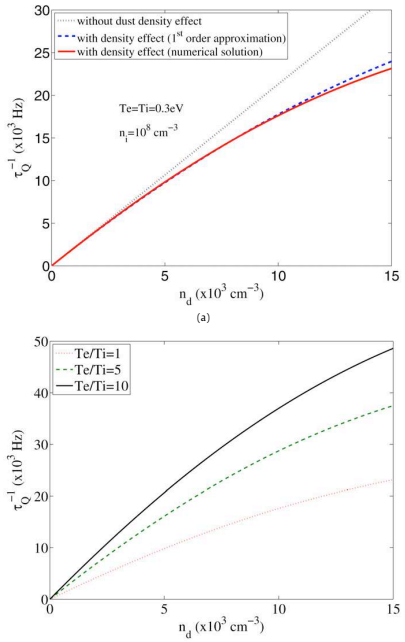

Fig. 1. (Color online.) Particle absorption frequency as a function of the dust density. (a) With or without taking into account the dust density effect. (b) Numerical solution for different Te/Ti.

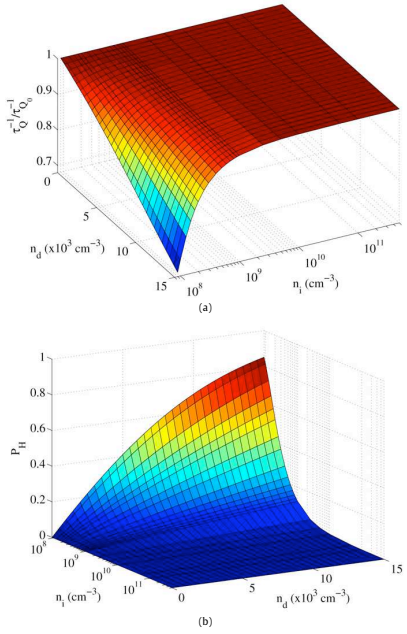

Fig. 2. (Color online.) (a) Ratio of the dust particle absorption frequency taking into account dust density effect τ_Q^{-1} over the dust particle absorption frequency not taking into account dust density effect $\tau_{Q_0}^{-1}$ for different dust density and plasma density. (b) Havnes parameter P_H for different dust density and plasma density.

particle absorption frequency. In Ref. [12], it is thus shown that the electron temperature relaxation in the plasma afterglow of a RF discharge results in a strong decrease of the dust particle charges.

In Fig. 2, the ratio $\tau_Q^{-1}/\tau_{Q_0}^{-1}$ as well as the Havnes parameter P_H have been calculated for different dust densities and ion densities. As can be seen in Fig. 2(a), the deviation from $\tau_{Q_0}^{-1}$ is marked at high dust density and low ion density. In Fig. 2(b) these conditions correspond to a Havnes parameter close to 1. For small Havnes parameters (i.e., small dust density and high ion density), it can be seen that $\tau_Q^{-1}/\tau_{Q_0}^{-1} \sim 1$. This confirms that when dust particles can be considered as isolated inside the plasma the absorption frequency is directly proportional to the dust density while for high dust density the charge carried by a dust particle is reduced as the dust density increases and consequently the dust absorption frequency does not evolve linearly with the dust density.

In a plasma afterglow, the plasma density decreases with time. Consequently the effect of the dust particles can become more and more important with time. In order to see this effect, the first moment of the decay of a complex plasma has been investigated using Eqs. (1), (2), (5) and (8). The results are presented in Fig. 3. The plasma diffusion loss is taken into account by choosing a plasma diffusion frequency $\tau_D^{-1} = 500$ Hz (which is a typical value for a laboratory discharge with an argon pressure around 1 Torr and these plasma parameters). As can be seen in Fig. 3(a), the dust particles enhance plasma losses and the larger the dust density, the larger the effect on plasma losses. In Fig. 3(b), it can be seen that at the very beginning of the plasma afterglow, the absorption frequency is roughly proportional to the dust density. This is due to the high value of the plasma density at this time which allows a small Havnes parameter and thus dust particles can be considered as isolated. However, as the density decreases, the effect of the dust particles become more and more important and the particle absorption frequency decreases. Indeed the Havnes parameter increases with time as the plasma density decreases. Consequently the dust particle charging is more and more affected by the presence of the other dust particles. The ion flux as well as the dust particle charge number decrease leading to a decrease of the dust absorption frequency. This effect is perfectly visible in Fig. 3(b) for high dust density.

4. Discussion and conclusion

As we demonstrated in Section 3, the dust density influences greatly the dust absorption–recombination process in an afterglow plasma. Thus, the dust absorption frequency does not increase linearly with the density, and for high density it is smaller than the absorption frequency that would occur if each dust particle could be considered as isolated in the plasma. Moreover, it was shown in Sections 2 and 3 that if the dust density is not too high, a first order approximation of the absorption frequency matches very well with the exact solution. In Eq. (14), there are only a few parameters to know (T_e, T_i, r_d, φ_0 and n_i). Consequently, it is possible to use the measurement of the absorption frequency in the afterglow of a complex plasma in parallel with other diagnostics to deduce some important parameters of the plasma.

For example, in Ref. [14], the dust particle absorption frequency has been measured in the afterglow of a linear pulsed discharge. The argon pressure was 1.9 Torr and the density of dust varied from 0 to 10^4 cm^{-3}. The dust particles had a mean radius $r_d \simeq 15$ μm. It is reported that the electron temperature was roughly equal to the ion temperature ($T_e \sim T_i$) [14]. Consequently, the influence of trapped ions on the dust particle charge can be neglected. In Fig. 4, experimental results from Ref. [14] are fitted using Eqs. (9) and (14). The fit gives $T_i \simeq 0.042$ eV, $(T_e/T_i)\varphi_0 = 4.4$ and thus assuming $T_i \leqslant T_e \leqslant 5T_i$ (depending when the measurement have been performed in the plasma afterglow), it gives 10^7 cm$^{-3} \leqslant n_i \leqslant 5 \times 10^7$ cm^{-3}. The range for the ion density and the ion temperature are much lower than those that were supposed in Ref. [14] but it could be due to the fact that their measurements were performed quite late in the plasma afterglow and temperature relaxation needed to be taken into account.

Author's personal copy

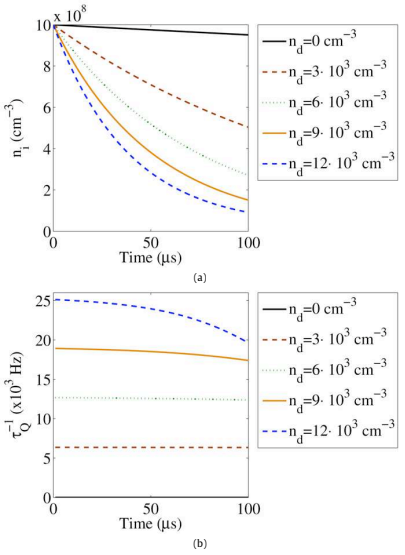

Fig. 3. (Color online.) Top: evolution of ion density n_i during the first microseconds of a plasma afterglow for different dust density. Bottom: evolution of the dust particle absorption frequency τ_Q^{-1} during the first microseconds of a plasma afterglow for different dust density. The plasma diffusion frequency is $\tau_D^{-1} = 500$ Hz and $T_e = T_i = 0.3$ eV.

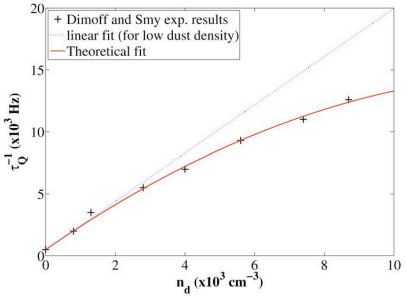

Fig. 4. (Color online.) Fit of experimental results of Ref. [14] using the first order approximation (Eq. (14)).

To conclude, the influence of the dust density on plasma losses has been studied. It has been shown that the presence of dust particles can drastically shorten the plasma loss time and that the increase of the dust absorption frequency does not depend linearly on the dust particle density. Finally, by comparing our results with existing experimental data, the possible use of absorption frequency measurement as a diagnostic for complex plasma is mentioned. Comparison with existing experimental data [14] supports this idea.

Acknowledgements

The authors would also like to thanks B.W. James for helpful discussions. This Letter is partially supported by the French–Australian integrated research program (FAST) under contract No. FR060169.

References

[1] A. Bouchoule, Dusty Plasmas: Physics, Chemistry and Technological impacts in Plasma Processing, Wiley, New York, 1999.
[2] S. Vladimirov, K. Ostrikov, A. Samarian, Physics and Applications of Complex Plasmas, Imperial Press, London, 2005.
[3] A. Barkan, R.L. Merlino, N. D'Angelo, Phys. Plasmas 2 (10) (1995) 3563.
[4] M. Cavarroc, M. Mikikian, Y. Tessier, L. Boufendi, Phys. Rev. Lett. 100 (4) (2008) 045001.
[5] M. Mikikian, L. Couëdel, M. Cavarroc, Y. Tessier, L. Boufendi, New J. Phys. 9 (8) (2007) 268.
[6] M. Mikikian, M. Cavarroc, L. Couëdel, L. Boufendi, Phys. Plasmas 13 (2006) 092103.
[7] D. Samsonov, J. Goree, J. Vac. Sci. Technol. A 17 (5) (1999) 2835.
[8] M. Cavarroc, M. Mikikian, G. Perrier, L. Boufendi, Appl. Phys. Lett. 89 (1) (2006) 013107.
[9] S. Hong, J. Berndt, J. Winter, Plasma Sources Sci. Technol. 12 (2003) 46.
[10] C. Arnas, M. Mikikian, F. Doveil, Phys. Rev. E 60 (1999) 7420.
[11] A.A. Samarian, B.W. James, Phys. Lett. A 287 (2001) 125.
[12] L. Couëdel, M. Mikikian, L. Boufendi, A.A. Samarian, Phys. Rev. E 74 (2) (2006) 026403.
[13] A. Ivlev, M. Kretschmer, M. Zuzic, G.E. Morfill, H. Rothermel, H. Thomas, V.E. Fortov, V.I. Molotkov, A.P. Nefedov, A. Lipaev, O.F. Petrov, Y. Baturin, A.I. Ivanov, J. Goree, Phys. Rev. Lett. 90 (2003) 055003.
[14] K. Dimoff, P.R. Smy, Phys. Lett. A 32 (1970) 13.
[15] M. Lampe, R. Goswami, Z. Sternovsky, S. Robertson, V. Gavrishchaka, G. Ganguli, G. Joyce, Phys. Plasmas 10 (5) (2003) 1500.
[16] A.V. Zobnin, A.P. Nefedov, V.A. Sinel'shchikov, V.E. Fortov, JETP 91 (2000) 483.

Bibliography

[1] W. Kleber and B. Makin, 1998, "Triboelectric powder coating: A practical approach for industrial use", *Part. Sci. Technol.*, vol. 16, no. 1, pp. 43–53.

[2] S. Anisimov, E. Mareev, N. Shikhova, *et al.*, 2005, "On the electro-dynamical characteristics of the fog", *Atmos. Res.*, vol. 76, no. 1-4, pp. 16–28.

[3] W. Borucki, R. Whitten, E. Bakes, *et al.*, 2006, "Predictions of the electrical conductivity and charging of the aerosols in titan's atmosphere", *Icarus*, vol. 181, pp. 527–544.

[4] G. S. Selwyn, J. Singh, and R. S. Bennett, 1989, "In situ laser diagnostic studies of plasma-generated particulate contamination", *J. Vac. Sci. Technol. A*, vol. 7, no. 4, pp. 2758–2765.

[5] A. Bouchoule, 1999, *Dusty Plasmas: Physics, Chemistry and Technological impacts in Plasma Processing*, Wiley, New York.

[6] O. Havnes and G. E. Morfill, 1984, "Effects of electrostatic forces on the vertical structure of planetary rings", *Adv. Space Res.*, vol. 4, no. 9, pp. 85–90.

[7] F. Li and O. Havnes, 2000, "Low frequency dust wave modes in planetary rings", *Planet. Space Sci.*, vol. 48, pp. 117–125.

[8] A. A. Mamun and P. K. Shukla, 2004, "Dust voids due to dust-phase-space vortices in plasma", *Phys. Plasmas*, vol. 11, p. 1757.

[9] C. Szopa, G. Cernogora, L. Boufendi, *et al.*, 2006, "Pampre: A dusty plasma experiment for titan's tholins production and study", *Planet. Space Sci.*, vol. 54, pp. 394–404.

[10] A. Pigarov, R. Smirnov, S. Krasheninnikov, *et al.*, 2007, "Transport of dust particles in tokamak devices", *J. Nucl. Mater.*, vol. 363-365, pp. 216–221.

[11] R. D. Smirnov, A. Y. Pigarov, M. Rosenberg, *et al.*, 2007, "Modelling of dynamics and transport of carbon dust particles in tokamaks", *Plasma Phys. Controlled Fusion*, vol. 49, no. 4, pp. 347–371.

[12] I. Langmuir, C. G. Found, and A. F. Dittmer, 1924, "A new type of electric discharge: the streamer discharge", *Science*, vol. LX, no. 1557, p. 392.

[13] R. V. M. D. Ghorain and A. Ltjyckx, 1950, "Spiraling in fluorescent lamps", *J. Electrochem. Soc.*, vol. 97, no. 5, pp. 159–165.

[14] E. G. Gibson, 1966, "Ionization phenomena in a gas-particle plasma", *Phys. Fluids*, vol. 9, no. 12, pp. 2389–2399.

[15] A. C. Breslin and K. G. Emeleus, 1971, "The distinction between negative ions and charged dust in plasmas", *Int. J. Electron.*, vol. 31, no. 2, pp. 189–190.

[16] K. G. Emeleus and A. C. Breslin, 1971, "Note on dust in positive columns", *Int. J. Electron.*, vol. 30, no. 3, pp. 273–273.

[17] K. G. Emeleus and A. C. Breslin, 1970, "Notes on the effects of dust in positive columns", *Int. J. Electron.*, vol. 29, no. 1, pp. 1–18.

[18] K. G. Emeleus, E. W. Gray, J. R. M. Coulter, *et al.*, 1968, "Notes on constricted and unstable positive columns in electronegative gases", *Int. J. Electron.*, vol. 25, no. 4, pp. 367–377.

[19] A. C. Breslin and K. G. Emeleus, 1970, "Effects of dust in a bounded positive column", *Phys. Lett. A*, vol. 31, pp. 23–24.

[20] M. A. Lieberman and A. J. Lichtenberg, 1994, *Principles of plasma discharges and materials processing*, Wiley, New York, ISBN 94-28954.

[21] K. Dimoff and P. R. Smy, 1970, "Dust induced quenching of an afterglow plasma", *Phys. Lett. A*, vol. 32, pp. 13–14.

[22] C. Kenty and E. J. Covington, 1968, "Sputtered particles in a $He - Ne$ laser tube", *J. Appl. Phys.*, vol. 39, no. 4, pp. 2160–2161.

[23] T. C. Anestos and C. D. Hendricks, 1974, "Injection of small macroscopic particles into plasmas as a diagnostic technique", *J. Appl. Phys.*, vol. 45, no. 3, pp. 1176–1178.

[24] C. K. Goertz and G. Morfill, 1983, "A model for the formation of spokes in saturn's ring", *Icarus*, vol. 53, no. 2, pp. 219–229.

[25] G. E. Morfill, E. Grun, C. K. Goertz, *et al.*, 1983, "On the evolution of Saturn's 'Spokes' - Theory", *Icarus*, vol. 53, pp. 230–235.

[26] J. R. Hill and D. A. Mendis, 1981, "On the braids and spokes in saturn's ring system", *Earth, Moon, and Planets*, vol. 24, no. 4, pp. 431–436.

[27] O. Havnes, 1984, "Charges on dust particles", *Adv. Space Res.*, vol. 4, pp. 75–83.

[28] O. Havnes, T. K. Aanesen, and F. Melandsø, 1990, "On dust charges and plasma potentials in a dusty plasma with dust size distribution", *J. Geophys. Res.*, vol. 95, no. A5, pp. 6581–6585.

[29] C. J. Mitchell, M. Horanyi, O. Havnes, *et al.*, 2006, "Saturn's Spokes: Lost and Found", *Science*, vol. 311, no. 5767, pp. 1587–1589.

[30] G. H. Jones, N. Krupp, H. Krüger, *et al.*, 2006, "Formation of Saturn's ring spokes by lightning-induced electron beams", *Geophys. Res. Lett*, vol. 33, p. 21202.

[31] K. G. Spears, T. J. Robinson, and R. M. Roth, April 1986, "Particle distributions and laser-particle interactions in an rf discharge of silane", *IEEE Trans. Plasma Sci.*, vol. 14, no. 2, pp. 179–187.

[32] G. S. Selwyn, J. E. Heidenreich, and K. L. Haller, 1990, "Particle trapping phenomena in radio frequency plasmas", *Appli. Phys. Lett.*, vol. 57, no. 18, pp. 1876–1878.

[33] A. Bouchoule and L. Boufendi, 1994, "High concentration effects in dusty plasmas", *Plasma Sources Sci. Technol.*, vol. 3, pp. 292–301.

[34] A. Bouchoule and L. Boufendi, 1993, "Particule formation and dusty plasma behaviour in argon-silane rf discharge", *Plasma Sources Sci. Technol.*, vol. 2, pp. 204–213.

[35] A. Bouchoule, A. Plain, L. Boufendi, *et al.*, 1991, "Particle generation and behavior in a silane-argon low-pressure discharge under continuous or pulsed radio-frequency excitation", *J. Appl. Phys.*, vol. 70, p. 1991.

[36] L. Boufendi, 1994, *Origine et comportement d'un nuage dense de particules submicroniques dans une décharge radiofréquence en milieu argon-silane basse pression*, Ph.D. thesis, Université d'Orléans.

[37] L. Boufendi and A. Bouchoule, 1994, "Particle nucleation and growth in a low-pressure argon-silane discharge", *Plasma Sources Sci. Technol.*, vol. 3, p. 262.

[38] L. Boufendi, A. Bouchoule, R. K. Porteous, *et al.*, 1993, "Particle-particle interactions in dusty plasmas", *J. Appl. Phys.*, vol. 73, p. 2160.

[39] L. Boufendi, J. Hermann, A. Bouchoule, *et al.*, 1994, "Study of initial dust formation in an $Ar - SiH_4$ discharge by laser induced particle explosive evaporation", *J. Appl. Phys.*, vol. 76, p. 148.

[40] L. Boufendi, A. Plain, J. P. Blondeau, *et al.*, 1992, "Measurements of particle size kinetics from nanometer to micrometer scale in a low-pressure argon-silane radio-frequency discharge", *Appl. Phys. Lett*, vol. 60, p. 169.

[41] E. Stoffels, W. W. Stoffels, G. M. W. Kroesen, *et al.*, 1996, "Dust formation and charging in an Ar/SiH_4 radio-frequency discharge", *J. Vac. Sci. Technol.*, vol. 14, no. 2, pp. 556–561.

[42] M. S. Barnes, J. H. Keller, J. C. Forster, *et al.*, 1992, "Transport of dust particles in glow-discharge plasmas", *Phys. Rev. Lett.*, vol. 68, no. 3, pp. 313–316.

[43] J. H. Chu and L. I, 1994, "Direct observation of coulomb crystals and liquids in strongly coupled rf dusty plasmas", *Phys. Rev. Lett.*, vol. 72, no. 25, pp. 4009–4012.

[44] Y. Hayashi and K. Tachibana, 1994, "Observation of coulomb-crystal formation from carbon particles grown in a methane plasma", *Jpn. J. Appl. Phys.*, vol. 33, pp. L804–L806.

[45] H. Thomas, G. E. Morfill, V. Demmel, *et al.*, 1994, "Plasma crystal: Coulomb crystallization in a dusty plasma", *Phys. Rev. Lett.*, vol. 73, no. 5, pp. 652–655.

[46] V. E. Fortov, A. P. Nefedov, V. M. Torchinsky, *et al.*, 1997, "Crystalline structures of strongly coupled dusty plasmas in dc glow discharge strata", *Phys. Lett. A*, vol. 229, no. 5, pp. 317–322.

[47] R. L. Merlino, A. Barkan, C. Thompson, *et al.*, 1998, "Laboratory studies of waves and instabilities in dusty plasmas", *Phys. Plasmas*, vol. 5, no. 5, pp. 1607–1614.

[48] V. Fortov, A. Nefedov, O. Petrov, *et al.*, 1996, "Experimental observation of coulomb ordered structure in sprays of thermal dusty plasmas", *JETP Letters*, vol. 63, no. 3, pp. 187–192.

[49] V. E. Fortov, A. P. Nefedov, O. F. Petrov, *et al.*, 1996, "Particle ordered structures in a strongly coupled classical thermal plasma", *Phys. Rev. E*, vol. 54, no. 3, pp. R2236–R2239.

[50] A. A. Samarian and O. S. Vaulina, 2000, "UV-induced coulomb structure in discharge plasma", *Phys. Lett. A*, vol. 278, no. 3, pp. 146–151.

[51] V. E. Fortov, A. P. Nefedov, V. I. Vladimirov, *et al.*, 1999, "Dust particles in a nuclear-induced plasma", *Phys. Lett. A*, vol. 258, no. 4-6, pp. 305–311.

[52] A. Barkan, R. L. Merlino, and N. D'Angelo, 1995, "Laboratory observation of the dust-acoustic wave mode", *Phys. Plasmas*, vol. 2, no. 10, pp. 3563–3565.

[53] M. Schwabe, M. Rubin-Zuzic, S. Zhdanov, *et al.*, 2007, "Highly resolved self-excited density waves in a complex plasma", *Phys. Rev. Lett.*, vol. 99, no. 9, p. 095002.

[54] G. E. Morfill, H. M. Thomas, U. Konopka, *et al.*, 1999, "The plasma condensation: Liquid and crystalline plasmas", *The 40th annual meeting of the division of plasma physics of the american physical society*, vol. 6, no. 5, pp. 1769–1780.

[55] H. M. Thomas and G. E. Morfill, 1996, "Melting dynamics of a plasma crystal", *Nature*, vol. 379, pp. 806–809.

[56] O. S. Vaulina, S. A. Khrapak, A. P. Nefedov, *et al.*, 1999, "Charge-fluctuation-induced heating of dust particles in a plasma", *Phys. Rev. E*, vol. 60, no. 5, p. 5959.

[57] F. Cheung, A. Samarian, and B. James, 2003, "The rotation of planar-2 to planar-12 dust clusters in an axial magnetic field", *New J. Phys.*, vol. 5, p. 75.

[58] J. Goree, G. E. Morfill, V. N. Tsytovich, *et al.*, 1999, "Theory of dust voids in plasmas", *Phys. Rev. E*, vol. 59, no. 6, p. 7055.

[59] D. Samsonov and J. Goree, 1999, "Instabilities in a dusty plasma with ion drag and ionization", *Phys. Rev. E*, vol. 59, p. 1047.

[60] M. Mikikian and L. Boufendi, 2004, "Experimental investigations of void dynamics in a dusty discharge", *Phys. Plasmas*, vol. 11, no. 8, p. 3733.

[61] M. Mikikian, L. Boufendi, A. Bouchoule, *et al.*, 2003, "Formation and behaviour of dust particle clouds in a radio-frequency discharge: results in the laboratory and under microgravity conditions", *New J. Phys.*, vol. 5, p. 19.

[62] V. E. Fortov, A. G. Khrapak, S. A. Khrapak, *et al.*, 2004, "Dusty plasmas", *Phys. Usp.*, vol. 47, no. 5, pp. 447–492.

[63] G. E. Morfill, H. M. Thomas, U. Konopka, *et al.*, 1999, "Condensed plasmas under microgravity", *Phys. Rev. Lett.*, vol. 83, no. 8, pp. 1598–1601.

[64] A. P. Nefedov, G. E. Morfill, V. E. Fortov, *et al.*, 2003, "PKE-nefedov: plasma crystal experiments on the international space station", *New J. Phys.*, vol. 5, p. 33.

[65] V. E. Fortov, A. P. Nefedov, O. S. Vaulina, *et al.*, 1998, "Dusty plasma induced by solar radiation under microgravitational conditions: An experiment on board the mir orbiting space station", *JETP*, vol. 87, p. 1087.

[66] M. Mikikian, L. Boufendi, and A. Bouchoule, 2003, "Spectroscopic analysis and instabilities observation during dust particle growth", R. Koch and S. Lebedev, eds., "30^{th} EPS Conf. on Contr. Fusion and Plasma Phys.", vol. 27A, pp. 0–3.1B.

[67] M. Mikikian, M. Cavarroc, N. Chaumeix, *et al.*, 2005, "Instabilities of the void region in a dense cloud of grown dust particles", L. Boufendi, M. Mikikian, and P. K. Shukla, eds., "NEW VISTAS IN DUSTY PLASMAS: Fourth International Conference on the Physics of Dusty Plasmas", AIP, vol. 799.

[68] M. Mikikian, M. Cavarroc, N. Chaumeix, *et al.*, 2004, "Instabilities in a dense cloud of grown dust particles", P. Norreys and H. Hutchinson, eds., "Proceedings of the 31st EPS Conference on Plasma Physics", vol. 28G of ECA, pp. 0–2.13.

[69] H. M. Thomas, G. E. Morfill, V. E. Fortov, *et al.*, 2008, "Complex plasma laboratory PK-3 plus on the international space station", *New J. Phys.*, vol. 10, no. 3, p. 033036.

[70] M. H. Thoma, H. Höfner, M. Kretschmer, *et al.*, 2008, "Parabolic flight experiments with PK-4", *Microgravity Sci. Technol.*, vol. 18, p. 47.

[71] P. R. i Cabarrocas, A. F. i Morral, S. Lebib, *et al.*, 2002, "Plasma production of nanocrystalline silicon particles and polymorphous silicon thin films for large-area electronic devices", *Pure Appl. Chem.*, vol. 74, p. 359.

[72] P. R. i Cabarrocas, T. Nguyen-Tran, Y. Djeridane, *et al.*, 2007, "Synthesis of silicon nanocrystals in silane plasmas for nanoelectronics and large area electronic devices", *J. Phys. D: Appl. Phys.*, vol. 40, no. 8, pp. 2258–2266.

[73] G. Praburam and J. Goree, 1996, "Experimental observation of very low-frequency macroscopic modes in a dusty plasma", *Phys. Plasmas*, vol. 3, no. 4, pp. 1212–1219.

[74] D. Samsonov and J. Goree, 1999, "Particle growth in a sputerring discharge", *J. Vac. Sci. Technol. A*, vol. 17, no. 5, p. 2835.

[75] M. Mikikian, M. Cavarroc, and L. Boufendi, 2005, "Dust Growth Instabilities in a Dense Cloud of Particles", L. Boufendi, M. Mikikian, and P. K. Shukla, eds., "AIP Conf. Proc. 799: New Vistas in Dusty Plasmas", pp. 319–322.

[76] S. V. Vladimirov, V. N. Tsytovich, and G. E. Morfill, 2005, "Stability of dust voids", *Phys. Plasmas*, vol. 12, p. 052117.

[77] A. Ivlev, M. Kretschmer, M. Zuzic, *et al.*, 2003, "Decharging of complex plasmas: First kinetic observations", *Phys. Rev. Lett.*, vol. 90, p. 055003.

[78] H. Rothermel, T. Hagl, G. E. Morfill, *et al.*, 2002, "Gravity compensation in complex plasmas by application of a temperature gradient", *Phys. Rev. Lett.*, vol. 89, p. 175001.

[79] T. Matsoukas and M. Russell, 1995, "Particle charging in low-pressure plasmas", *J. Appl. Phys.*, vol. 77, p. 4285.

[80] C. Arnas, M. Mikikian, and F. Doveil, 1999, "High negative charge of a dust particle in a hot cathode discharge", *Phys. Rev. E*, vol. 60, p. 7420.

[81] I. A. Belov, A. S. Ivanov, D. A. Ivanov, *et al.*, 2000, "Coagulation of charged particles in a dusty plasma", *JETP*, vol. 90, no. 1, pp. 93–101.

[82] U. Konopka, F. Mokler, A. V. Ivlev, *et al.*, 2005, "Charge-induced gelation of microparticles", *New J. Phys.*, vol. 7, p. 227.

[83] P. K. Shukla and A. A. Mamun, 2002, *Introduction to dusty plasma*, IOP Publishing, Bristol.

[84] J. E. Allen, B. M. Annaratone, and U. de Angelis, 2000, "On the orbital motion limited theory for a small body at floating potential in a Maxwellian plasma", *J. Plasma Phys.*, vol. 63, pp. 299–309.

[85] R. V. Kennedy and J. E. Allen, 2003, "The floating potential of spherical probes and dust grains. II: Orbital motion theory", *J. Plasma Phys.*, vol. 69, pp. 485–506.

[86] S. Vladimirov, K. Ostrikov, and A. Samarian, 2005, *Physics and Applications of Complex Plasmas*, Imperial Press, London.

[87] M. Lampe, R. Goswami, Z. Sternovsky, *et al.*, 2003, "Trapped ion effect on shielding, current flow, and charging of a small object in a plasma", *Phys. Plasmas*, vol. 10, no. 5, pp. 1500–1513.

[88] A. V. Zobnin, A. P. Nefedov, V. A. Sinel'Shchikov, *et al.*, 2000, "On the Charge of Dust Particles in a Low-Pressure Gas Discharge Plasma", *JETP*, vol. 91, pp. 483–487.

[89] G. E. Morfill, V. N. Tsytovich, and H. Thomas, 2003, "Complex plasmas: Ii. elementary processes in complex plasmas", *Plasma Phys. Rep.*, vol. 29, p. 1.

[90] T. Matsoukas, M. Russell, and M. Smith, 1996, "Stochastic charge fluctuations in dusty plasmas", *J. Vac. Sci. Technol. A*, vol. 14, no. 2, p. 624.

[91] T. Matsoukas and M. Russell, 1997, "Fokker-planck description of particle charging in ionized gases", *Phys. Rev. E*, vol. 55, no. 1, pp. 991–994.

[92] L. Couëdel, M. Mikikian, L. Boufendi, *et al.*, 2006, "Residual dust charges in discharge afterglow", *Phys. Rev. E*, vol. 74, no. 2, p. 026403.

[93] C. Cui and J. Goree, 1994, "Fluctiations of the charge on a dust grain in a plasma", *IEEE Trans. Plasma Sci.*, vol. 22, p. 151.

[94] S. A. Khrapak, A. P. Nefedov, O. F. Petrov, *et al.*, 1999, "Dynamical properties of random charge fluctuations in a dusty plasma with different charging mechanisms", *Phys. Rev. E*, vol. 59, no. 5, p. 6017.

[95] S. A. Maiorov, S. V. Vladimirov, and N. F. Cramer, 2002, "Calculation of the grain charge fluctuations in a dusty plasma", *Plasma Phys. Rep.*, vol. 28, p. 946.

[96] A. Melzer, T. Trottenberg, and A. Piel, 1994, "Experimental determination of the charge on dust particles forming coulomb lattices", *Phys. Lett. A*, vol. 191, no. 3-4, pp. 301–308.

[97] C. Arnas, M. Mikikian, and F. Doveil, 2001, "Micro-sphere levitation in a sheath of a low pressure continuous discharge", *Phys. Scr.*, vol. T89, pp. 163–167.

[98] A. A. Samarian and S. V. Vladimirov, 2003, "Charge of a macroscopic particle in a plasma sheath", *Phys. Rev. E*, vol. 67, p. 066404.

[99] S. Vladimirov and K. Ostrikov, 2004, "Dynamic self-organization phenomena in complex ionized gas systems: new paradigms and technological aspects", *Phys. Rep.*, vol. 393, pp. 175–380.

[100] M. R. Adkim and W. J. Goedheer, 2001, "Modeling of voids in colloidal plasmas", *Phys. Rev. E*, vol. 65, p. 015401.

[101] J. Perrin, P. Molinas-Mata, and P. Belenguer, 1994, "Ion drag and plasma-induced thermophoresis on particles in radiofrequency glow discharges", *J. Phys. D: Appl. Phys.*, vol. 27, no. 12, pp. 2499–2507.

[102] C. Zafiu, A. Melzer, and A. Piel, 2002, "Ion drag and thermophoretic forces acting on free falling charged particles in an rf-driven complex plasma", *Phys. Plasmas*, vol. 9, p. 4794.

[103] S. Khrapak, A. V. Ivlev, G. E. Morfill, *et al.*, 2002, "Ion drag force in a complex plasma", *Phys. Rev. E*, vol. 66, p. 046414.

[104] S. A. Khrapak, A. V. Ivlev, S. K. Zhdanov, *et al.*, 2005, "Hybrid approach to the ion drag force", *Phys. Plasmas*, vol. 12, p. 042308.

[105] F. Zheng, 2002, "Thermophoresis of spherical and non-spherical particles: a review of theories and experiments", *Adv. Colloid Interface Sci.*, vol. 97, pp. 255–278.

[106] R. N. Varney, 1952, "Drift velocities of ions in krypton and xenon", *Phys. Rev.*, vol. 88, no. 2, pp. 362–364.

[107] L. Waldmann, 1959, "Uber die kraft eines inhomogenen gases auf kleine suspendierte kugeln", *Z. Naturforsch*, vol. 14a, pp. 589–599.

[108] Z. Li and H. Wang, 2004, "Thermophoretic force and velocity of nanoparticles in the free molecule regime", *Phys. Rev. E*, vol. 70, p. 021205.

[109] I. Goldhirsch and D. Ronis, 1983, "Theory of thermophoresis. I. general considerations and mode-coupling analysis", *Phys Rev. A*, vol. 27, no. 3, p. 1616.

[110] I. Goldhirsch and D. Ronis, 1983, "Theory of thermophoresis. II. low density behaviour", *Phys. Rev. A*, vol. 27, no. 3, p. 1635.

[111] L. Talbot, R. K. Cheng, R. W. Schefer, *et al.*, 1980, "Thermophoresis of particles in a heated boundary layer", *J. Fluid Mech.*, vol. 101, p. 737.

[112] K. D. Bleecker and A. Bogaerts, 2005, "Role of the thermophoretic force on the transport of nanoparticles in dusty silane plasmas", *Phys. Rev. E*, vol. 71, p. 066405.

[113] W. Li and E. J. Davis, 1995, "Measurement of the thermophoretic force by electrodynamic levitation: Microspheres in air", *J. Aerosol Sci.*, vol. 26, pp. 1063–1083.

[114] W. Li and E. J. Davis, 1995, "The effects of gas and particle properties on thermophoresis", *J. Aerosol Sci.*, vol. 26, pp. 1085–1099.

[115] M. A. Gallis, D. J. Rader, and J. R. Torczynski, 2002, "Thermophoresis in rarefied gas flows", *Aerosol Sci. Technol.*, vol. 36, pp. 1099–1117.

[116] J. B. Pieper and J. Goree, 1996, "Dispersion of plasma dust acoustic waves in the strong-coupling regime", *Phys. Rev. Lett.*, vol. 77, no. 15, pp. 3137–3140.

[117] A. Barkan, N. D'Angelo, and R. L. Merlino, 1996, "Potential relaxation instability and ion acoustic waves in a single-ended Q-machine dusty plasma", *Phys. Lett. A*, vol. 222, pp. 329–332.

[118] Y. Nakamura, H. Bailung, and P. K. Shukla, 1999, "Observation of ion-acoustic shocks in a dusty plasma", *Phys. Rev. Lett.*, vol. 83, no. 8, pp. 1602–1605.

[119] M. Cavarroc, M. C. Jouanny, K. Radouane, *et al.*, 2006, "Self-excited instability occurring during the nanoparticle formation in an Ar/SiH_4 low pressure radio frequency plasma", *J. Appl. Phys.*, vol. 99, p. 064301.

[120] M. Cavarroc, M. Mikikian, G. Perrier, *et al.*, 2006, "Single-crystal silicon nanoparticles: An instability to check their synthesis", *Appl. Phys. Lett.*, vol. 89, no. 1, p. 013107.

[121] Y. P. Raizer, M. N. Shneider, and N. A. Yatsenko, 1995, *Radio-Frequency Capacitive discharges*, CRC Press LLC, Florida.

[122] H. R. Koenig and L. I. Maissel, 1970, "Application of rf discharges to sputtering", *IBM J. Res. Develop.*, vol. 14, no. 2, p. 168.

[123] L. Boufendi, J. Gaudin, S. Huet, *et al.*, 2001, "Detection of particles of less than 5 nm in diameter formed in an argon–silane capacitively coupled radio-frequency discharge", *Appl. Phys. Lett.*, vol. 79, no. 26, pp. 4301–4303.

[124] F. J. Gordillo-Vázquez, M. Camero, and C. Gómez-Aleixandre, 2006, "Spectroscopic measurements of the electron temperature in low pressure radiofrequency $Ar/H_2/C_2H_2$ and $Ar/H_2/Ch_4$ plasmas used for the synthesis of nanocarbon structures", *Plasma Sources Sc. Technol.*, vol. 15, no. 1, pp. 42–51.

[125] K. Kano, M. Suzuki, and H. Akatsuka, 2000, "Spectroscopic measurement of electron temperature and density in argon plasmas based on collisional-radiative model", *Plasma Sources Sci. Technol.*, vol. 9, pp. 314–322.

[126] X.-M. Zhu and Y.-K. Pu, 2007, "A simple collisional-radiative model for low-pressure argon discharges", *J. Phys. D: Appl. Phys.*, vol. 40, no. 8, pp. 2533–2538.

[127] B. James, 2007, "Spectroscopic investigation of a complex plasma during particle growth", Private communication.

[128] R. J. Freiberg and L. A. Weaver, 1968, "Microwave investigation of the transition from ambipolar to free diffusion in afterglow plasmas", *Phys. Rev.*, vol. 170, pp. 336–341.

[129] B. Agdur and B. Enander, 1962, "Resonances of a microwave cavity partially filled with a plasma", *J. Appl. Phys.*, vol. 33, no. 2, pp. 575–581.

[130] M. J. Mulcahy and J. J. Lennon, 1962, "Ambipolar diffusion measurements in low pressure rare gas afterglows", *Proc. Phys. Soc.*, vol. 80, no. 3, pp. 626–633.

[131] K. B. Persson, 1957, "Limitations of the microwave cavity method of measuring electron densities in a plasma", *Phys. Rev.*, vol. 106, no. 2, pp. 191–195.

[132] W. W. Stoffels, E. Stoffels, G. M. W. Kroesen, *et al.*, 1995, "Electron density fluctuations in a dusty Ar/SiH_4 rf discharge", *J. Appl. Phys.*, vol. 78, pp. 4867–4872.

[133] M. Haverlag, G. M. W. Kroesen, T. H. J. Bisschops, *et al.*, 1991, "Measurement of electron densities by a microwave cavity method in 13.56-MHz rf plasmas of Ar, CF_4, C_2F6, and CHF_3", *Plasma Chem. Plasma Process.*, vol. 11, no. 3, pp. 357–370.

[134] H. M. Mott-Smith and I. Langmuir, 1926, "The theory of collectors in gaseous discharges", *Phys. Rev.*, vol. 28, no. 4, pp. 727–763.

[135] V. A. Godyak, R. B. Piejak, and B. M. Alexandrovich, 1993, "Probe diagnostics of non-maxwellian plasmas", *J. Appl. Phys.*, vol. 73, no. 8, pp. 3657–3663.

[136] C. Dominique and C. Arnas, 2007, "Cathode sputtering and the resulting formation of carbon nanometer-size dust", *J. Appl. Phys.*, vol. 101, no. 12, p. 123304.

[137] Y. P. Raizer, 1991, *Gas Disharge Physics*, Springer, Berlin.

[138] V. Godyak, June 2006, "Nonequilibrium eedf in gas discharge plasmas", *IEEE Trans. Plasma Sci.*, vol. 34, no. 3, pp. 755–766.

[139] V. Godyak, R. Piejak, and B. Alexandrovich, Aug 1991, "Electrical characteristics of parallel-plate rf discharges in argon", *IEEE Trans. Plasma Sci.*, vol. 19, no. 4, pp. 660–676.

[140] I. Denysenko, M. Y. Yu, K. Ostrikov, *et al.*, 2004, "A kinetic model for an argon plasma containing dust grains", *Phys. Plasmas*, vol. 11, no. 11, pp. 4959–4967.

[141] M. Mikikian, M. Cavarroc, L. Couëdel, *et al.*, 2006, "Low frequency instabilities during dust particle growth in a radio-frequency plasma", *Phys. Plasmas*, vol. 13, p. 092103.

[142] A. Mamun, P. Shukla, and R. Bingham, 2002, "Plasma voids (holes) in a dusty plasma", *Phys. Lett. A*, vol. 298, pp. 179–184.

[143] M. Tribeche, K. Aoutou, , *et al.*, 2005, "Non linear dust phase-space vortices (holes) in charge-varying dusty plasmas", *Phys. Plasmas*, vol. 12, p. 32305.

[144] V. N. Tsytovich, 2001, "Evolution of voids in dusty plasmas", *Phys. Scr.*, vol. T89, pp. 89–94.

[145] V. N. Tsytovich, S. V. Vladimirov, and G. E. Morfill, 2004, "Theory of dust and dust-void structures in the presence of the ion diffusion", *Phys. Rev. E*, vol. 70, p. 066408.

[146] Y. Liu, Y. Song, Z.-X. Wang, *et al.*, 2007, "Dust void formation in complex plasmas with two various sizes of dust grains", *Phys. Plasmas*, vol. 14, no. 9, p. 094501.

[147] Y. H. Liu, Z. Y. Chen, M. Y. Yu, *et al.*, 2006, "Multiple void formation in plasmas containing multispecies charged grains", *Phys. Rev. E* , vol. 74, no. 5, p. 056401.

[148] Y. Liu, S. Mao, Z.-X. Wang, *et al.*, 2006, "A nonlinear theory of dust voids in cylindrical geometry with the convective effect", *Phys. Plasmas*, vol. 13, no. 6, p. 064502.

[149] M. Cavarroc, M. Mikikian, Y. Tessier, *et al.*, 2008, "Successive generations of dust in complex plasmas: A cyclic phenomenon in the void region", *Phys. Rev. Lett.*, vol. 100, no. 4, p. 045001.

[150] H. T. Do, G. Thieme, M. Fröhlich, *et al.*, 2005, "Ion molecule and dust particle formation in Ar/CH_4, Ar/C_2H_2 and Ar/C_3H_6 radio-frequency plasmas", *Contrib. Plasma Phys.*, vol. 45, pp. 378 – 384.

[151] M. Mikikian, L. Couëdel, M. Cavarroc, *et al.*, 2007, "Self-excited void instability in dusty plasmas: plasma and dust cloud dynamics during the heartbeat instability", *New J. Phys.*, vol. 9, no. 8, p. 268.

[152] M. Kretschmer, S. A. Khrapak, S. K. Zhdanov, *et al.*, 2005, "Force field inside the void in complex plasmas under microgravity conditions", *Phys. Rev. E*, vol. 71, p. 056401.

[153] M. Mikikian, M. Cavarroc, L. Couëdel, *et al.*, 2008, "Mixed-mode oscillations in complex-plasma instabilities", *Phys. Rev. Lett.*, vol. 100, no. 22, p. 225005.

[154] M. Krupa, N. Popović, N. Kopell, *et al.*, 2008, "Mixed-mode oscillations in a three time-scale model for the dopaminergic neuron", *Chaos*, vol. 18, no. 1, p. 015106.

[155] M. Moisan and J. Pelletier, 2006, *Physique des plasmas collisionnels: Application aux décharges haute fréquence*, Grenoble Sciences, Bonchamp-Lès-Laval, ISBN 2-86883-822-7.

[156] R. A. Gerber and J. B. Gerardo, 1973, "Ambipolar-to-free diffusion: The temporal behavior of the electrons and ions", *Phys. Rev. A*, vol. 7, no. 2, pp. 781–790.

[157] F. J. Mehr and M. A. Biondi, 1969, "Electron temperature dependence of recombination of O_2^+ and N_2^+ ions with electrons", *Phys. Rev.*, vol. 181, no. 1, pp. 264–271.

[158] J. Berndt, E. Kovacevic, V. Selenin, *et al.*, 2006, "Anomalous behaviour of the electron density in a pulsed complex plasma", *Plasma Sources Sci. Technol.*, vol. 15, pp. 18–22.

[159] I. Stefanovic, J. Berndt, D. Maric, *et al.*, 2006, "Secondary electron emission of carbonaceous dust particles", *Phys. Rev. E*, vol. 74, p. 026406.

[160] M. A. Biondi, 1951, "Ionization by the collision of pairs of metastable atoms", *Phys. Rev.*, vol. 82, no. 3, pp. 453–454.

[161] L. J. Overzet and J. Kleber, 1998, "Effect of metastable atom reactions on the electron energy probability functions in afterglows", *Plasma Sources Sci. Technol.*, vol. 7, pp. 512–523.

[162] E. B. Tomme, D. A. Law, B. M. Annaratone, *et al.*, 2000, "Parabolic plasma sheath potentials and their implications for the charge on levitated dust particles", *Phys. Rev. Lett.*, vol. 85, p. 2518.

[163] C. Zafiu, A. Melzer, and A. Piel, 2001, "Nonlinear resonances of particles in a dusty plasma sheath", *Phys. Rev. E*, vol. 63, p. 066403.

[164] O. S. Vaulina, A. A. Samarian, B. James, *et al.*, 2003, "Analysis of macroparticle charging in the near-electrode layer of a high-frequency capacitive discharge", *JETP*, vol. 96, no. 6, pp. 1037 – 1044.

[165] N. J. Prior, L. W. Mitchell, and A. A. Samarian, 2003, "Determination of charge on vertically aligned particles in a complex plasma using laser excitations", *J. Phys. D: Appl. Phys.*, vol. 36, pp. 1249–1253.

[166] S. Ratynskaia, S. Khrapak, A. Zobnin, *et al.*, 2004, "Experimental determination of dust-particle charge in a discharge plasma at elevated pressures", *Phys. Rev. Lett.*, vol. 93, p. 085001.

[167] L. Couedel and A. A. Samarian, 2005, "Particle charges determination for two vertically aligned dust particles in a complex plasma", L. Boufendi, M. Mikikian, and P. K. Shukla, eds., "NEW VISTAS IN DUSTY PLASMAS: Fourth International Conference on the Physics of Dusty Plasmas", AIP, vol. 799, pp. 549–552.

[168] M. A. Childs and A. Gallagher, 2000, "Plasma charge-density ratios in a dusty plasma", *J. Appl. Phys.*, vol. 87, no. 3, p. 1086.

[169] L. Landau and E. Lifpchitz, 1986, *Physique théorique: tome 1*, Mir, Moscou.

[170] M. Akdim and W. Goedheer, April 2004, "Modeling of dust voids in electronegative discharges under microgravity", *Plasma Science, IEEE Transactions on*, vol. 32, no. 2, pp. 680–690.

[171] I. Yasumoto, 1987, "Accommodation coefficients of helium, neon, argon, hydrogen, and deuterium on graphitized carbon", *J. Phys. Chem.*, vol. 91, no. 16, pp. 4298–4301.

[172] V. N. Tsytovich, 1997, "Dust plasma crystals, drops, and clouds", *Phys. Usp.*, vol. 40, p. 53.

[173] M. A. Gusinow and R. A. Gerber, 1972, "Space-charge-controlled diffusion in an afterglow", *Phys. Rev. A*, vol. 5, no. 4, pp. 1802–1806.

[174] R. A. Gerber, M. A. Gusinow, and J. B. Gerardo, 1971, "Transition from ambipolar to free diffusion of ions", *Phys. Rev. A*, vol. 3, no. 5, pp. 1703–1707.

[175] B. Kivel, 1959, "Elastic scatterring of low energy electrons by argon", *Phys. Rev*, vol. 116, no. 4, p. 926.

[176] M. A. Biondi, 1954, "Diffusion cooling of electrons in ionized gases", *Phys. Rev.*, vol. 93, no. 6, pp. 1136–1140.

[177] E. Belorizky, 1999, *Mathématiques d'usage courant pour scientifiques et ingénieurs*, Nathan, Paris, ISBN 2-09-191024-4.

[178] N. E. Huang, Z. Shen, S. R. Long, *et al.*, 1998, "The empirical mode decomposition and the Hilbert spectrum for nonlinear and non-stationary time series analysis", *Royal Soc. London Proc. Series A*, vol. 454, p. 903.

[179] A. Veltcheva and C. Soares, 2004, "Identification of the components of wave spectra by the hilbert huang transform method", *Appl. Ocean Res.*, vol. 26, no. 1-2, pp. 1–12.

[180] G. Rilling, P. Flandrin, and P. Goncalves, 2003, "On empirical mode decomposition and its algorithms", "IEEE-EURASIP Workshop on Nonlinear Signal and Image Processing NSIP-03", vol. Grado (I).

Lénaïc Gaël Hervé Fabien COUËDEL

Formation et dynamique de nanoparticules dans un plasma complexe (poussiéreux): de l'allumage du plasma à la phase post-décharge.

Les plasmas complexes (poussiéreux) sont un sujet d'intérêt croissant. Ce sont des gaz ionisés contenant des poudres chargées. Dans les décharges RF capacitives, deux méthodes peuvent être utilisées pour produire les poussières: les plasmas chimiquement actifs ou la pulvérisation. La croissance de poudres dans une décharge d'argon par pulvérisation ainsi que ses effets sur le plasma ont été étudiés depuis l'allumage de la décharge jusqu'à la phase post-décharge. Il a été montré que les paramètres du plasma et de la décharge sont grandement affectés par la présences de poudres. De plus, des instabilités du plasma peuvent être induites par la présence des poussières. Ces instabilités peuvent être dues à la croissance des poudres ou elles peuvent être des instabilités auto-excitées d'un nuage dense de poudres remplissant l'espace inter-électrode. Quand on éteint la décharge, les poudres agissent comme un piège pour les porteurs de charge et par conséquent modifient les mécanismes d'extinction du plasma. Il a aussi été montré que les poudres gardent une charge électrique résiduelle qui dépend fortement du processus de diffusion du plasma et notamment de la transition de la diffusion ambipolaire vers la diffusion libre.

Mots clés: plasma, décharge capacitive, poussières, instabilités, charge résiduelle, diffusion, post-décharge, croissance de poudres

Nanoparticle formation and dynamics in a complex (dusty) plasma: from the plasma ignition to the afterglow.

Complex (dusty) plasmas are a subject of growing interest. They areionized gases containing charged dust particles. In capacitively-coupled RF discharges, dust growth can occur naturally and two methods can be used to grow dust particles: chemically active plasmas or sputtering. The growth of dust particles in argon discharges by RF sputtering and the effect of dust particles on theplasma have been investigated from the plasma ignition to the afterglow. It was shown that plasma and discharge parameters are greatly affected by the dust particles. Furthermore, plasma instabilities can be triggered by the presence of the dust particles. These instabilities can be due to dust particle growth or they can be instabilities of a well established dust cloud filling the interelectrode space. When the discharge is switched off, the dust particles act like a sink for the charge carrier and consequently affect the plasma losses. It was shown that the dust particles do keep residual chargeswhich values are greatly affected by the diffusion of the charge carriers and especially the transition from ambipolar to free diffusion.

Keywords: plasma, capacitive discharge, dust, instabilities, residual charge, diffusion, afterglow, dust growth

GREMI, CNRS/Université d'Orléans, 14 rue d'Issoudun, BP 6744, 45067 Orléans Cedex 2

Complex Plasma Laboratory, School of Physics A28, The University of Sydney, NSW 2006, Australia